Liquid Jet Impingement Heat Transfer and Its Potential Applications at Extremely High Heat Fluxes

by

Xin Liu

Submitted to the Department of Mechanical Engineering
in partial fulfillment of the requirements for the degree of

Ph.D of Science in Mechanical Engineering

at the

MASSACHUSETTS INSTITUTE OF TECHNOLOGY

January 1992

Author .....
Department of Mechanical Engineering
January 29, 1992

Certified by....
.....
John H. Lienhard V
Associate Professor
Thesis Supervisor

Accepted by .....
Ain A. Sonin
Chairman
Department Committee on Graduate Studies

Liquid Jet Impingement Heat Transfer and Its Potential Application at Extremely High Heat Fluxes

Xin Liu

Submitted to the Department of Mechanical Engineering
on January 29, 1992 in partial fulfillment of the requirements
for the degree of Doctor of Philosophy in Mechanical Engineering

Abstract

The present thesis discusses the heat transfer for laminar and for turbulent jets, the hydraulic jump which limits the regions with thin liquid sheet, the stagnation flow and heat transfer, and the extremely high heat fluxes in stagnation zone of high speed jets impingement, and some suggestions on the jet impingement cooling design.

Jet impingement cooling of uniformly heated surfaces is investigated analytically for stable, unsubmerged, laminar jets and for fully developed turbulent jets. Experiments were performed to determine local Nusselt number from stagnation point to radii of up to 40 radius. Turbulent transition in the film flow for laminar incoming jets is measured experimentally. Numerical solutions are presented for stagnation point flow, using a simulation method for steady, inviscid, incompressible flow with surface tension. Integral method results are compared to numerical results for laminar film flow. Experiments on turbulent jet impingement were performed using a Phase Doppler Particle Analyzer to measure the size, velocity, and concentration of splattered droplets. A nondimensional group based on a capillary instability analysis of the circular jet was used to scale the splattering data, yielding predictions for the splattered mass. The hydraulic jump for circular jet impingement was investigated for downward and upward facing jets.

Experiments using high-speed jets were performed to determine the factors limiting heat fluxes in the stagnation zone. The results demonstrate a terrific potential to deal with extremely high heat fluxes. At present, the primary constraints on heat flux comes from material properties, particularly the melting point temperature and properties related to thermal stress. Jet impingement heat transfer at the stagnation zone can accommodate still higher heat fluxes if the heat flux barrier set by material limitations can be raised. Some suggestions and procedures for the design of jet impingement cooling systems are discussed.

Thesis Supervisor: John H. Lienhard V (Associate Professor of Mechanical Engineering)

to my dear wife

ACKNOWLEDGEMENT

In the years that were spent at MIT I have incurred a lots of debts of gratitude. I would like to thank all of the people, who have contributed to the completion of this work, from the bottom of my heart. My deepest is to Professor John H. Lienhard V, who is my thesis advisor supporting me financially during my these three and one half years. He not only gave me precious advice, but also solved problems personally with his great ability to make the focal points stand out. For my thesis he corrected my English one word by one word; for our papers, which are part of my thesis, he even rewrote. Thanks to Professor Borivoje Mikic, for letting me be his teaching assistant in "Conduction and Phase Change" for three terms, and for his humor and his encouraging words. To Professor Peter Griffith, for not only his valuable suggestions on my thesis, but also his thoughtfully reminding me of road condition for biking sometimes when weather was bad, since both of us were biking enthusiasts. To Professor Ain A. Sonin for his precious comments on my thesis and advice on my graduate studies.

To Joseph A. Caloggero, whom every one call 'Tiny', for teaching me how to do machine work, collecting comics from *Boston Globe* to help me improve my English, and our many interesting conversations from how to pronounce 'l' to his holiday hobby of going to New Hampshire and doing nothing. To Norman MacAskill, for both his strong muscles which helped me build experiment equipment, and the beautiful melody from his whistle, which brought happiness to the Lab.

To my dear wife Gao, Jinglin a special thanks, for her giving up her Ph.D. study at Tsukuba University of Japan to come to join me; a big hug and kiss to her for her understanding and accompanying me through this special period. To my mother, for her living without my company and help, and her encouraging words in every letter.

To all of my colleagues, especially Douglas Alexander Varela Cristales, Laurette A. Gabour and J. S. Lombara, for the happy times to work together and Sourav Bhunia for helping me to use the high speed jet equipment in my experiments. There are a lot of people I have not mentioned here, not because they may never read this dissertation but because of their different kindness, different smile, and different style beyond the ability of my pen.

This work was supported by the National Science Foundation under Grant number CBT-8858288 and by a grant from the Alfred P. Sloan Foundation.

PREFACE

This research stems from our interests in the cooling of a surface by liquid impinging jet, especially at extremely high heat flux. Although the impingement of circular, liquid jets provides a convenient method of cooling surfaces, the characteristics of liquid jets are quite complex. The present thesis discusses the heat transfer for laminar jets in Chapter 2 and for turbulent jets in Chapter 3. The hydraulic jump, which limits the regions with thin liquid sheet, in Chapter 4. The stagnation flow and heat transfer are discussed in Chapter 5, and efforts to achieve extremely high heat fluxes in the stagnation zone of high speed jets are discussed in Chapter 6. Finally, we give some suggestions on high flux jet impingement cooling design in Chapter 7.

In Chapter 2 jet impingement cooling of uniformly heated surfaces is investigated analytically and experimentally for stable, unsubmerged, laminar jets and in the absence of phase change. Analytical and numerical predictions are developed for a laminar radial film flow. Experiments using undisturbed laminar jets were performed to determine local Nusselt numbers from the stagnation point to radii of up to 40 diameters. Turbulent transition in the film flow is observed experimentally at a certain radius. Beyond this transition radius, a separate turbulent analysis is constructed. Integral method results are compared to numerical results, and Prandtl number effects are investigated. The predictions are found to agree well with the measurements for both laminar and turbulent flow. Predictive formulae are recommended for the entire range of radius.

Liquid jets often have surface disturbances. These disturbances are strongly

amplified when the jet strikes a surface perpendicular to its axis, and the film created will often break up, leading to splattering of liquid droplets. Turbulence in the jet is one common progenitor of such disturbances. Since the simplest implementation of liquid jet impingement cooling is to create a high Reynolds number jet at the outlet of a straight pipe, these cooling jets are often turbulent and susceptible to splattering. In Chapter 3, splattering and heat transfer due to impingement of an unsubmerged, turbulent liquid jet is investigated experimentally and analytically.

Experiments on turbulent jet impingement were performed using a Phase Doppler Particle Analyzer to measure the size, velocity, and concentration of splattered droplets. Heat transfer measurements were made along the uniformly heated surface onto which the jet impacted. The results show that splattering occurs within a certain range of radius, rather than being distributed along the entire film surface; the position of splattering was obtained experimentally. The total mass splattered is determined by the jet the Reynolds number, the jet Weber number, and the ratio of distance between the nozzle and the target plate. A nondimensional group based on a capillary instability analysis of the circular jet was used to scale the splattering data, yielding predictions for the onset of splattering beneath a turbulent jet and for the splattered mass.

Nusselt number was measured from the stagnation point to r/d as large as 40. The measurements of splattered mass and splattering position were incorporated into a momentum integral analysis to obtain the mean flow field beyond the radius of splattering, and the thermal law of the wall (Reynolds-Colburn analogy) was then

used to formulate a prediction of the local Nusselt number. The both the prediction and the experimental data reveal that the Nusselt number is enhanced for radial locations immediately following splattering. The extent of enhancement is determined by the ratio of the splattered mass to the total mass flow rate of the jet. At larger radii, the Nusselt number declines as a result of the slowing of the liquid sheet, and it finally falls below the Nusselt number for no splattering.

The hydraulic jump, which leads to a sudden increase of liquid sheet thickness, deteriorates the heat transfer dramatically. It is necessary to locate the position of hydraulic jump so as to correctly design cooling systems. In Chapter 4, the hydraulic jump for circular jet impingement is investigated for downward and upward facing jets. For downward jets, observations show that different jump patterns occur; a single jump, a double jump, and an unstable jump. Those patterns depend on the surface tension, the jump height, and other liquid properties. Immediately after jump, a back flow occurs on the free surface and the jump edge shows certain wave patterns related to its own instability. The standard theory of the hydraulic jump, which involves only the Froude number and the ratio of downstream depth to upstream depth, does not give good predictions for axisymmetric hydraulic jumps, because both viscosity and surface tension need to be taken into account. For upward jets, Taylor instability of the liquid sheet occurs at large radius. The liquid drips distribute in a circle with a certain azimuthal wavelength. A correlation is given to predict the radius at which the liquid drips down.

The fluid flow and heat transfer characteristics in the stagnation zone of an

impinging liquid jet are of particular importance, since the maximum heat transfer coefficient occurs in this region. In Chapter 5, the stagnation flow of an unsubmerged liquid jet is studied analytically and experimentally. Most available fluid flow and heat transfer results for the stagnation zone are based on results for a submerged jet, i.e., a single phase flow with uniform velocity at infinity. A few studies have examined an unsubmerged jet using a potential flow solution which neglects surface tension and viscosity. In this chapter, numerical solutions are presented for a laminar jet, using a simulation method for steady, inviscid, incompressible flow with surface tension. A series solution involving the surface tension is developed, and an iteration scheme is carried out. The solution is given by Legendre functions which satisfy the boundary conditions in an approximate manner. The numerical solution of the momentum equation shows that surface tension has an effect on the flow field at the stagnation point, especially for the case of small Weber number.

Stagnation zone heat transfer experiments for both laminar and turbulent jets were performed. The laminar jet was produced with a sharp-edged orifice with upstream disturbances damped elaborately. The fully-developed turbulent jets were produced using tube nozzles. Present results are compared with those of previous investigations. The overall understanding of unsubmerged, circular jet stagnation-point heat transfer is summarized.

The study of the heat transfer of impinging jets in stagnation zone shows its terrific potential to deal with extremely high heat fluxes. In Chapter 6, experiments using high-speed jets were performed to investigate the factors limiting heat fluxes

in the stagnation zone. A 1.9 millimeter jets at speeds up to 134 m/s (Re_d up to 1.69×10^6) were directed at thin metal sheets heated from the opposite side. A 20kW arc was used as heat source. The heat fluxes were determined from the temperature gradients in the target plates. The temperature on the jet side was determined using fusible temperature indicators; the melting temperature isotherm on the plasma side was located by looking at the crystal structure of the target plate. The results demonstrate the terrific potential of impinging jets to remove extremely high heat fluxes. The heat fluxes measured here range from 40.1 to 321 MW/m^2 for steel plate targets. The convection is an important portion of the total heat flux for high speed jets. A correlation is proposed for the present data. At present, the primary constraints on heat flux come from the material properties of the target plate, particularly its melting point temperature and properties related to thermal stress. Jet impingement heat transfer in the stagnation zone can accommodate still higher heat fluxes if the heat flux barrier set by material limitations can be raised. The issue of limiting heat fluxes is discussed. Two kinds of constraints limit heat flux. One arises from theoretical considerations related to transport mechanisms and the other comes from material constraints. At present, the primary constraints on heat flux come from material properties particularly the melting point and properties related to thermal stress. Extremely high heat flux raise questions regarding the validity of classical conductivity theory, which are discussed in Appendix A.

In Chapter 7, some suggestions and procedures for the design of jet impingement cooling are proposed in order to optimize the pumping power, which is one of the

main operational costs. At extremely high heat fluxes, material considerations are also discussed.

Contents

List of Figures

List of Tables

Nomenclature

Roman Letters

a liquid jet radius.

A disturbed diameter when jet strikes the plate.

A_{2n} constants in Equation 5.24

A_{rms} mean jet-radius disturbance-amplitude when jet strikes plate.

B_{2m} constants in Equation 5.25

C scaled nozzle-outlet turbulence intensity, $0.195\ \sqrt{2}(q'/u_f)^2$.

C_1, C_2 constant.

C_c contraction coefficient for liquid jets.

C_f friction factor.

c_p specific heat capacity.

C_s a constant.

C_v velocity coefficient for liquid jets.

d liquid jet diameter.

D temporal volumetric mean diameter of splattered droplets at a given height; or diameter of target tray.

e electronic charge.

$f'(\eta)$ similarity function.

$f_n(\theta)$ any continuous function of θ.

g gravitational acceleration.

$G(\mathrm{Pr})$ function of Prandtl number given by Equation 5.35.

g_m local mass transfer coefficient from liquid surface to environment.

h local thickness of liquid sheet; distance from a impinging plate; Plank's constant.

h_1 thickness of liquid sheet at a certain upstream position of jump.

h_2 thickness of liquid sheet at a certain downstream position of jump.

$\hat{h}$ local heat transfer coefficient from liquid surface to environment.

h^* mean thickness of liquid sheet at the position just after splatering occurs.

h_{fg} latent heat of vaporization.

$h(r)$ local thickness of liquid sheet.

h_c equivalent mean thickness of liquid sheet containing same momentum as actual sheet after splattering.

h_{r1} liquid sheet thickness at the position where thermal boundary layer reaches the free surface.

h_s mean liquid sheet thickness at the position just before splattering occurs.

h_t liquid sheet thickness at transition point from laminar to turbulence.

h_{T0} liquid sheet thickness at r_{T0}.

h_0 thickness of liquid sheet at which δ reaches the surface of the liquid sheet.

H distance between nozzle and target plate.

k thermal conductivity of the liquid.

k_w thermal conductivity of the heater.

l distance between nozzle and target.

m_w, m_∞ water vapor mass fractions at liquid surface, in environment.

M dimensionless group defined in Equation 4.30.

n number of particles per unit volume.

N total number of particles.

Nu_d Nusselt number, $q_w d/k(T_w - T_f)$.

Nu_r Nusselt number based on r, $q_w r/k(T_w - T_f) = \mathrm{Nu}_d(r/d)$.

Nu_x Nusselt number, $qx/k(T_w - T_f)$.

p local gauge pressure.

P_0 stagnation pressure.

P_{2n} Legendre function in $2n$ order.

p' rms turbulent fluctuation of liquid pressure.

p'_{max} pressure disturbance-amplitude at wavelength of maximum instability.

Pr Prandtl number.

q heat flux.

Q total flow rate of jet.

q' rms magnitutde of turbulent velocity vector at nozzle outlet.

q_w wall heat flux.

Q Volume flow rate of jet, $u_f \pi d^2/4$.

Q" volume flow rate of splattered liquid per unit height above the plate.

r radius coordinate in cylindrical coordinates, or radius coordinate in spherical coordinates.

r_h hump radius, at which turbulence is fully developed.

r_j radius at which hydraulic jump occurs.

r_m radius of droplet profile measurement.

r_o radius at which δ reaches the surface of the liquid sheet.

r_r radius where the flow relaminarises.

r_s effective radius of splattering region.

$r_{T,i}$ location of the initial temperature profile given.

r_{T0} radius where thermal boundary layer reaches the free surface for $\mathrm{Pr} < 1$.

$r_{u,i}$ location of the initial velocity profile given

r_t radius at transition point from laminar to turbulence.

r_1 radius where thermal boundary layer reaches the free surface for $\mathrm{Pr} > 1$.

r_2 radius at which T_w reaches the liquid saturation temperature.

R Reynolds number defined by Watson, $\frac{2Q}{d\nu} = (\pi/2)\,\mathrm{Re}_d$; or spherical radius coordinate of free surface.

R_1, R_2 principal radii of curvature for liquid surface.

Re_d Reynolds number of the jet, $u_f d/\nu$.

s liquid sheet thickness after hydraulic jump; or growth rate.

s, s_{max} growth rate of capillary disturbances, maximum growth rate.

Sc Schmidt number for water vapor in air.

St Stanton number $= q_w/(\rho c_p u_{max}(T_w - T_f))$.

t heater sheet thickness or time.

$T(r,y)$ liquid temperature distribution.

T_f incoming jet temperature at impingement.

$T_{f4}(r)$ jet surface temperature distribution in region 4.

T_m measured temperature on the back of the heater.

T_{sf} free surface temperature.

T_{sat} liquid saturation temperature.

T_w wall temperature on the liquid side of the heater.

u radial velocity distribution in liquid film.

u_o ideal jet velocity produced by stagnation pressure, $\sqrt{2P_o/\rho}$.

u_f velocity of impinging jet.

u_h supercritical velocity at the liquid sheet thickness is h.

u_{max} local maximum film velocity (liquid free surface velocity), equal to u_f in regions 2, 2l, and 3l.

u^*, u^*_max liquid velocity, liquid maximum velocity just after splattering.

u_s subcritical velocity at the liquid sheet thickness is s.

$U(r)$ radial velocity just outside boundary layer.

v mean radial velocity component of splattered droplets at a given height; or velocity in axial direction; particle speed, $\sqrt{v_x^2 + v_y^2 + v_z^2}$.

$\vec{v}$ velocity vector.

v_m mean incoming jet velocity.

v_n normal velocity in streamline coordinates.

v_t tangent velocity in streamline coordinates.

v_x, v_y, v_z velocity components of particles.

We_d jet Weber number, $\rho u_f^2 d/\sigma$.

x fraction of liquid sheet contained in boundary layer at given radius; or horizontal axis in planar coordinates.

y distance normal to the wall.

z distance between nozzle and target plate; or axial coordinate in cylindrical coordinates.

Greek Letters

α angle; or thermal diffusivity, $k/\rho c_p$.

β angle; or numerical relaxation factor.

γ_1 Fermi potential.

δ viscous boundary layer thickness.

δ_t thermal boundary layer thickness.

δ_0 the thickness of viscous boundary layer when it when reaches the liquid free surface.

Δ ratio of thermal boundary layer thickness to liquid sheet thickness, δ/h.

Δ_{T0} Δ at r_{T0}.

ϵ, ϵ_{max} amplitude, mean amplitude of initial surface displacement.

ε (t/d); ε^2 is the order of radial to vertical conduction in the heater sheet.

η similarity variable.

θ nondimensional temperature; or polar angle.

κ free surface curvature; Boltzman gas constant.

Θ constant in momentum balance.

λ wavelength.

λ_d most dangerous wavelength.

λ, λ_{max} capillary-disturbance wavelength for jet, most unstable wavelength.

μ dynamic viscosity.

ν kinematic viscosity.

ξ ratio of splattered-liquid volume flow rate to incoming jet volume flow rate.

ρ density.

ρ_g gas density.

ρ_l liquid density.

σ surface tension.

τ volume.

ϕ ratio of viscous boundary layer thickness to thermal boundary layer thickness, δ/δ_t; velocity potential; or velocity potential.

Φ constant in momentum balance.

ω nondimensional group, $\mathrm{We}\exp\left(\frac{l}{d}\frac{0.971}{\sqrt{\mathrm{We}}}\right)$.

$\partial/\partial n$ derivative normal to the solution domain boundary.

$\partial/\partial t$ derivative tangent to the solution domain boundary.

Superscripts

(n) result from the nth iteration.

$*$ dimensionless variable.

Chapter 1

INTRODUCTION

The jet dynamics have played an important role in the history of fluid mechanics. The application of jets may be traced back to the first water wheel built by man. These early jets were not driven by a pump, but by gravity. Systematic studies were not initiated until the Renaissance. A review of the history of hydraulics can be found in the reference by Rouse and Ince (1957).

After Galileo Galilei (1564-1642), the jet was viewed as a succession of freely falling particles obey "the law of fall". In 17th century, the father of the experimental method in France, Edme Mariotte (1620-1684) sought to derive a principle of jet impingement from Torricelli's principle of jet kinematics. He formulated the following rules for the deflection of a jet by a normal surface (Figure 1.1):

- Jets do not produce impact by the action of all their parts as do solid bodies.
- The water which is discharged from the bottom of a reservoir through a circular

opening will produce equilibrium by impact with a weight equal to that of a cylinder of water which has for base that opening and for height that between the center of the opening and the upper surface of the water.

- Two jets of water of equal size which emerge from small openings at the base of several pipes filled with water to different heights will produce equilibrium with weights which are in proportion to the heights.

- Jets of water of unequal velocities will support by their impact weights which are proportional to the square of these velocities.

- Jets of the same velocity from different openings will support by their impact weights which are in proportion to the squares of the diameter of the openings.

Mariotte was the first to indicate in the literature that the force exerted by flowing water varies with the square of its velocity. The errors in some of his statements stemmed in part from a lack of understanding of the jet contraction and in part from incomplete lateral deflection of a jet by the narrow surface of the balance system which he used.

Another French physicist, mathematician, and member of the Académie Royale des Sciences, Antoine Parent (1666-1716), sought to compute the peak operation of water wheels using a model of jet impinging on a target. His analysis was restricted to targets at rest, like that of Mariotte. Some of his erroneous statements and his solutions were accepted without question by several of his more famous successors.

Daniel Bernoulli became interested in the jet impingement at St. Petersburg in

1727, when he seemed to confirm experimentally Mariotte's conclusion that the force of jet on a normal surface was equal to the weight of the liquid column in the container directly above the orifice. Later Bernoulli modified his analysis by substituting the area of the contracted jet, the true force then becoming equal—in accordance with the momentum relationship—to the weight of a liquid column just twice as high.

John Smeaton (1724-1792), the first of the great English engineers, was entirely self-trained. In his gold-medal paper of 1759 about the evaluation of results on the water wheel, he concluded that the work done by the jet was proportional to the water expended, the height of the effective head, and nearly the cube of velocity of the water jet.

The total momentum and work produced by jet were at last understood, but without understanding the free surface behavior and viscous flow, it was impossible to predict the details of the fluid flow field for jet impingement. The subsequent history of viscous flow and boundary layer theory, which led to the modern fluid mechanics, are well known.

For the contraction of the free surface of the jet, we must mention Jean Charles Borda (1733-1799), a French engineering scientist, and Gustav Robert Kirchhoff (1824-1887), a German scientist. By means of momentum considerations, Borda found that for the two-dimensional case of a reentrant tube (the Borda mouthpiece) the jet would contract to one-half the area of the tube, and he verified the value experimentally. Hermann Ludwig Ferdinand von Helmholtz (1821-1894) formally analyzed the fluid flow from a Borda outlet and initiated to a succession of papers on

free surface flow. Kirchhoff extended Helmholtz' analysis to the case of flow from planar slot orifice. He gave the equation of the jet profile and calculated the limiting contraction coefficient to be $\pi/(\pi + 2) = 0.611$.

In the application of circular liquid jets, people observed the phenomena of a hydraulic jump. For a downward jet, when a jet of liquid strikes a flat surface, it normally spreads out in a thin layer which experiences a sudden increase in depth farther downstream. Past study of this kind of axisymmetric jumps followed the methods developed for planar jump, without checking their applicability to circular jump.

Hydraulic jump as a research topic was first mentioned in Leonardo da Vinci's collective (edited and published in 1924) writing "Del moto e misura dell'acqua". Giovanni Battista Venturi (Rouse and Ince, 1957) made the first successful effort to extend the hydraulic jump to a practical use. He suggested using the reduced depth of high-velocity flow from a spillway—just prior to the formation of a hydraulic jump—as a means of gaining head for drainage purposes.

Giorgio Bidone (1781-1839), a prfessor of hydraulics at University of Turin was the first to study the hydraulic jump systematically and to attempt its analysis. In Italy the hydraulic jump is known as the "jump of Bidone." Jean Baptiste Belanger (1784-1847) sought to improve upon Bidone's analysis of the hydraulic jump. His successor as professor of mathematics at the Ecole Polytecnique, Jacques Antoine Charles Bresse (1822-1883), found the correct formulation of momentum characteris-

tics of the hydraulic jump in his 1869 "Cours de meécanique appliquée":

$$Fr_h = \sqrt{\frac{1}{2}\frac{h_2^3}{h_1^3}\left(1+\frac{h_1}{h_2}\right)} \tag{1.1}$$

In the early 20th century an experimental laboratory of hydraulics was built at Polytechnic Institute of Karlsruhe by Theodor Rehbock (1864-1950). This laboratory introduced many innovations and model studies with particular emphasis on the depiction of the flow pattern. Figure 1.2 shows the flow pattern constructed by Rehbock in zone of eddy formation after an overfall dam due to hydraulic jump.

In the research on axisymmetric jumps, Bresse's formulation of the jump was still the basis used. Some investigators tried to prove experimentally its validity for circular jump, but the formulation was not as successful as for planar jets.

In 20th century, the application of jet impingement to manufacturing and other applications has greatly stimulated research on jets.

In metal rolling processes, recent technology in accelerated and controlled cooling has not only improved the metallurgical or physical properties in the rolled products (plates or strips), but has also reduced the manufacturing cost by eliminating the off-line heat treatment. For advanced materials, because the cooling rate and cooling history strongly affect overall mechanical properties (such as residual stresses, fracture toughness, fatigue resistance, formability, and weldability of the rolled products), not only the finishing and coiling temperature, but also the temperature profile and history of the strips during processing are nowadays increasingly demanded.

Jet impingement is used in heat treatment of metals. Several steels of different compositions may be hardened by quenching in exactly the same way but they will

be found to differ in both intensity and depth of hardness. Hardenability refers to the degree and depth of hardness obtained in a heat treatment. Jet impingement cooling, which called *Jominy end-quench test*, is a standard way to measure the hardenability (Figure 1.3).

The advancement of electronic technology calls for development of a new technology in heat dissipation methods. Very large scale integrated circuit chips have incorporated more and more components and heat dissipation in the circuits of such chips is continuously increasing. For these chips, the computer industry is gradually changing from air cooling to liquid cooling, in some cases with the coolant applied to the chip surface by jet impingement.

Other potential applications of jet impingement include cleaning surfaces, jet cutting, cooling laser mirrors, collecting solar energy, cooling spacecrafts reentering atmosphere, cooling in fission and fusion reactors, cooling high-efficiency (aircraft) generators, and so on. In particular, high-performance devices such as high-power-density fusion reactors, accelerator targets, advanced neutron sources, and rocket motors require removal of very high heat flux. For a Tokamak, heat fluxes as high as 7–200 GW/m^2 can be created during intervals 0.1–3 ms. The steady state cooling rate required is often more than $10MW/m^2$. Jet impingement cooling has terrific potential to achieve these very high cooling rates.

Knowledge of the total momentum and total force of the jet alone is unsatisfactory; the local behavior of jet impingement has become important. But information about it is still very limited. The relevant detailed review is divided into several topics

and presented sequentially in individual chapters.

REFERENCES

Bernoulli, D., Hydrodynamica, *sive de viribus et motibus fluidorum commentarii*, Strasboug, 1738.

Borda, J.C., "Mémoire sur l'écoulement des fluides par les orifices des vases," *Histoire de l'Académie Royale des Sciences*, 1779.

Leonardo de Vinci, *Del Moto e Misura dell'Acqua*, edited by E. Carusi and A. Favaro, Bologna, 1924.

Mariotte, E., *Traité du mouvement des eaux et des autres corps fluides*, Paris, 1686.

Rouse, H. and Ince, S., *History of Hydraulics*, State University of Iowa, 1957.

Smeaton, J., "An experimental inquiry concerning the natural powers of water and wind to turn mills, and other machines, depending on a circular motion," *Philosophical Transactions of the Royal Society of London*, Vol. 51, 1759.

Chen, S. and Kothari, J., "Temperature Distribution and Heat Transfer of a Moving Metal Strip Cooled by a Water Jet," *ASME paper 88-WA/NE-4*, 1988.

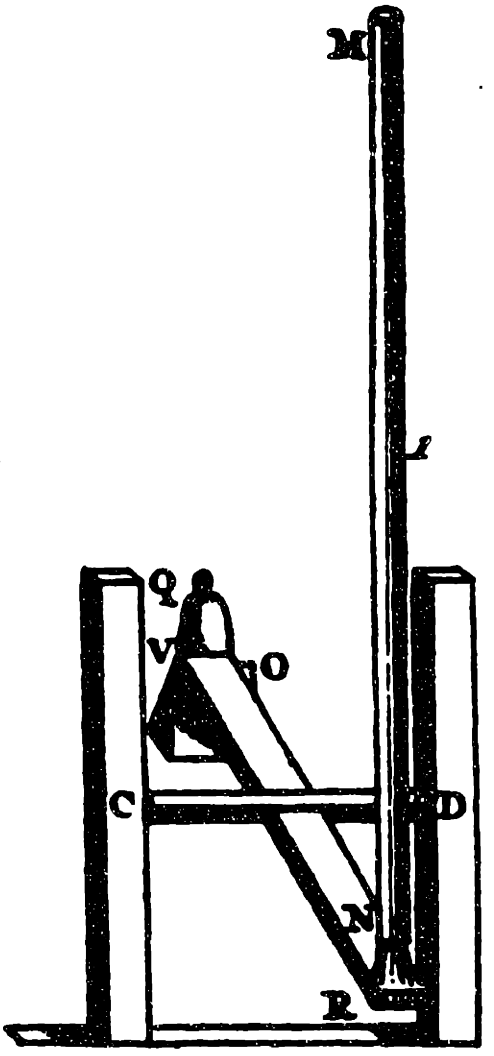

Figure 1.1: Apparatus used by Mariotte in studing jet impingement (Mariotte, 1686).

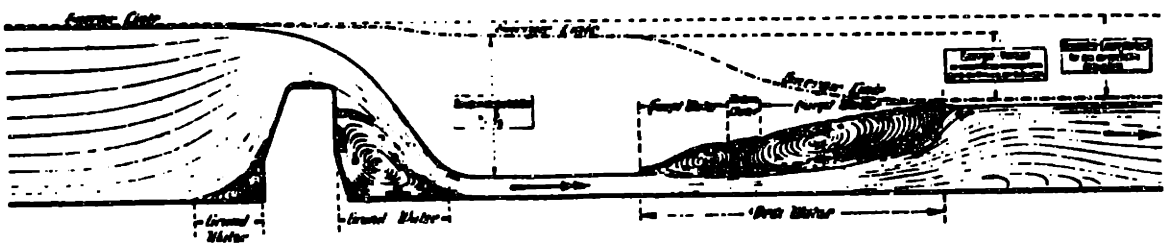

Figure 1.2: The flow pattern contructed by Rehbock in zone of eddy formation after an overfall dam due to hydraulic jump (Rouse and Ince, 1957).

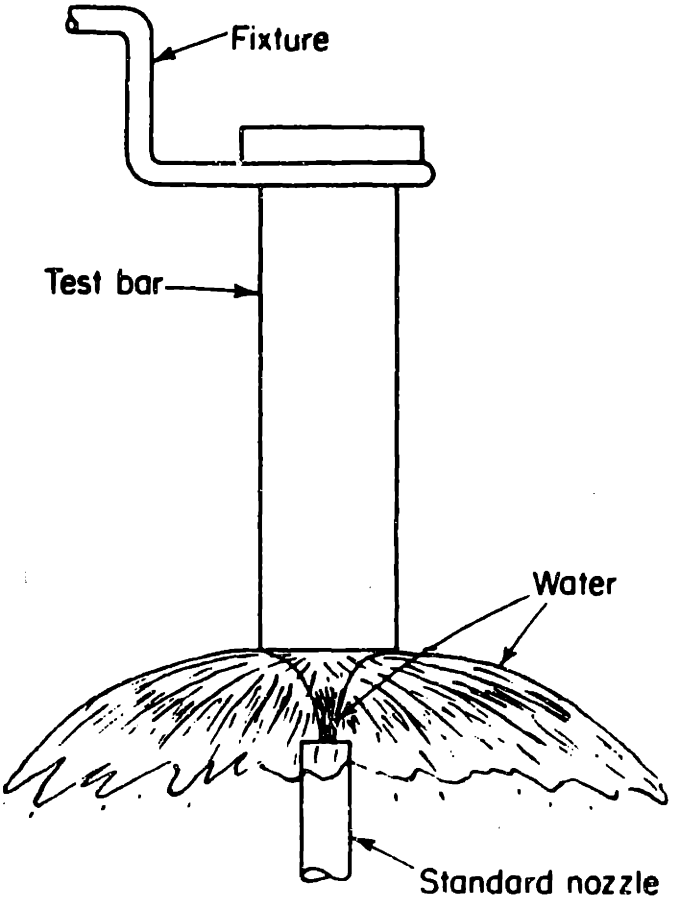

Figure 1.3: Jominy end-quench

Chapter 2

HEAT TRANSFER OF A LAMINAR JET

2.1 Introduction

Cooling a surface with an impinging liquid jet is an attractive technique because of its high efficiency and unsophisticated hardware requirements. Such jets lend themselves to either convective boiling or to nonevaporative convection, but in both situations the cooling efficiency varies with the radial distance from the point of impact. In this chapter, we consider the impingement of a circular, unsubmerged, laminar liquid jet on a surface of uniform heat flux. Convective transport, without change of phase, is analyzed theoretically and experimentally, taking account of both the initial laminar flow and the downstream turbulent flow.

An axisymmetric, laminar impinging jet spreads into a thin, laminar liquid film

when it impacts a plane surface normal to its axis (Figure 2.1). The hydrodynamics of this film have previously been studied theoretically by Watson (1964) and experimentally by Azuma and Hoshino (1984abcd) and by Olsson and Turkdogan (1966). Watson divided the flow radially into a stagnation region, a boundary layer region with surface velocity equal to jet speed, and a region of viscous similarity with decreasing surface velocity; he noted that the film flow would be terminated by a hydraulic jump at a location independently controlled by downstream conditions. The thickness of the film initially decreases and then increases with radius as viscous wall effects slow the spreading film. Watson employed both viscous similarity and momentum integral solutions.

Watson's theoretical expressions for the laminar boundary layer and similarity region velocity profiles and film thickness were experimentally verified by Azuma and Hoshino (1984bc) using laser doppler measurements. This is in contrast to the results of Olsson and Turkdogan (1966), who measured the surface velocity by dropping bits of cork onto the liquid. Olsson and Turkdogan found poor agreement with Watson's predictions, observing a constant surface velocity lower than the jet speed, and their results have sometimes been used to deny the presence of a similarity region. However, no conclusive evidence showed that the dropped, buoyant cork actually moved at the liquid surface speed. Since the experimental approach of Azuma and Hoshino is clearly more accurate, we are inclined to give their conclusions greater weight. For the details of Watson's flow field, the reader is referred to his paper. His expressions, and those of a later independent study by Sharan (1984), are quoted hereinafter when

needed.

Azuma and Hoshino measured the turbulent transition radius in their system (which used a circular orifice mounted on the plate, rather than an actual impinging jet) and also measured the subsequent velocity profiles. The turbulent film was well characterized by standard boundary layer results, but it did appear to show relaminarization further downstream as the film slowed and its stability increased.

Using Watson's similarity solution, Chaudhury (1964) analyzed the heat transfer from an isothermal wall in terms of a series solution for the similarity region and an integral solution for the boundary layer region; Carper (1989) has also presented a solution to that problem. Wang, Dagan and Jiji (1989abc) gave detailed theoretical solutions for heat transfer in the stagnation and boundary layer regions; these solutions account for variable wall conditions as well as for conjugate heat transfer between the jet and the wall. They did not consider the downstream similarity region, in which surface velocity declines with radius; at common Reynolds numbers, the stagnation zone and boundary layer regimes are confined to radii of 3 to 7 diameters from the point of impact. When a jet is used to cool large areas, the similarity region and turbulent transition must also be accounted.

Experimental studies have been few, particularly in regard to local, rather than average, heat transfer. Ishigai *et al.* (1977) measured local heat transfer coefficients in the hydraulic jump region and presented a limited, graphical set of data for the local heat transfer coefficient in the plane of impact. They mentioned that the data showed a downstream transition from laminar to turbulent flow; their jets were produced

by a short tube, three diameters in length. Stevens and Webb (1989) investigated turbulent impinging jet heat transfer experimentally and developed a correlation for Nu_d. Their data are confined to $r/d < 15$ and their correlation is accurate in a region $r/d < 5$ for $d = 2.2$ mm and a smaller region for larger diameter of jets. The radial transition from laminar to turbulent flow was not mentioned, but it must be noted that their jets were deliberately made turbulent prior to impact.

Nakoryakov, Pokusaev, and Troyan (1978) used electrodiffusion to obtain local mass transfer coefficients beneath a laminar jet and compared them to an appropriate boundary layer analysis. Their study applies to very high Schmidt number ($\mathrm{Sc} \gg 1$) and a boundary condition of uniform wall concentration, correspondent to the uniform wall temperature conditions at $\mathrm{Pr} \gg 1$. Their experiments showed the mass transfer coefficient to rise above the laminar prediction downstream, and they argued this to result from surface waves. However, the present results suggest that transition to turbulence is a more likely cause in their range of Reynolds number. The incoming jet velocities for their experiments were calculated on the basis of the apparently theoretical stagnation zone result

$$\mathrm{Nu}_l = 0.753\,\mathrm{Pr}^{1/3}\mathrm{Re}_l^{1/2} \tag{2.1}$$

where l is the radius of their electrodiffusion probe. However, this correlation was not independently corroborated in their paper.

The present paper develops radially complete results for the liquid film heat transfer with uniform heat flux; most of these results are analytically derived, and all are validated experimentally. Particular attention is devoted to the similarity region,

employing numerical solutions for the uniform flux condition (which is not self-similar) to investigate the role of wall boundary conditions, simplified correlations, and the integral method prediction of a critical Prandtl number above which the thermal boundary layer does not reach the free surface (*see* Appendix B). Our integral method solutions are extended to include $\mathrm{Pr} < 1$. The laminar predictions are then compared to new experimental data, from an experimental apparatus configured to achieve very clean, stable, laminar jets. The laminar predictions are generally found to agree very well with the data. In addition, turbulent transition is observed in the similarity region, and separate analytical predictions are developed to account for the turbulent augmentation of the heat transfer. A correlation is given for the turbulent transition point.

2.2 Predictions from the Laminar Theory

2.2.1 Integral Solutions for the Heat Transfer: $\mathrm{Pr} \geq 1$

We may obtaine integral solutions (*see* Appendix B for detail) for the heat transfer in the boundary layer and similarity regions for Prandtl number greater than unity. The regions identified and results found are as follow (*see* Figure 2.2a):

Region 1. *The stagnation zone.*

Region 2. $\delta < h$ *region*: Neither the thermal nor viscous boundary layer reach the free surface; surface temperature and velocity, T_{sf} and u_{max} are the inlet temperature and velocity, T_f and u_f.

Region 3. $\delta = h$ *and* $\delta_t < h$ *region*: The viscous boundary layer has reached the free surface. The velocity outside the viscous boundary layer decreases with radius,

but the surface temperature remains at the inlet temperature, T_f.

Region 4. $\delta = h, \delta_t = h$, *and* $T_w < T_{sat}$ *region*: In this region, the thermal boundary layer has reached the surface of the liquid sheet, and the temperature of the liquid surface increases with radius.

For region 2, the boundary layer region following the stagnation zone:

$$\mathrm{Nu}_d = 0.632\mathrm{Re}_d^{1/2}\mathrm{Pr}^{1/3}\left(\frac{d}{r}\right)^{1/2} \tag{2.2}$$

Region 2 ends and region 3 begins where the viscous boundary layer reaches the film surface at $r = r_0 = 0.1773\, d\, \mathrm{Re}_d^{1/3}$. In region 3:

$$\mathrm{Nu}_d = \frac{0.407\mathrm{Re}_d^{1/3}\mathrm{Pr}^{1/3}\left(\frac{d}{r}\right)^{2/3}}{\left[0.1713\left(\frac{d}{r}\right)^2 + \frac{5.147r}{\mathrm{Re}_d d}\right]^{2/3}\left[\frac{1}{2}\left(\frac{r}{d}\right)^2 + C_3\right]^{1/3}} \tag{2.3}$$

where

$$C_3 = \frac{0.267(d/r_0)^{1/2}}{\left[0.1713\left(\frac{d}{r_0}\right)^2 + \frac{5.147r_0}{\mathrm{Re}_d d}\right]^2} - \frac{1}{2}\left(\frac{r_0}{d}\right)^2 \tag{2.4}$$

Region 3 ends and region 4 begins where the thermal boundary layer reaches the liquid surface at $r = r_1$; equations defining r_1 are given in Appendix B. In region 4:

$$\mathrm{Nu}_d = \frac{0.25}{\frac{1}{\mathrm{PrRe}_d}\left(1 - \frac{r_1^2}{r^2}\right)\left(\frac{r}{d}\right)^2 + 0.130\frac{h}{d} + 0.0371\frac{h_{fg}}{d}} \tag{2.5}$$

where h is given by:

$$h = 0.1713\left(\frac{d^2}{r}\right) + \frac{5.147}{\mathrm{Re}_d}\left(\frac{r^2}{d}\right) \tag{2.6}$$

Note that region 4 will occur only for Pr less than a critical value near five (*see* Appendix B); otherwise, the thermal boundary layer does not grow fast enough to reach the surface of the liquid film, which thickens at increasing radius owing to

viscous retardation. This Prandtl number prediction is of particular interest, and we shall explore it further using numerical solutions for the viscous flow regime below. Regions 3 and 4 correspond to Watson's self-similar viscous flow regime.

2.2.2 Integral Solutions for the Heat Transfer: $Pr < 1$

As noted in Appendix B, the region map changes for small Prandtl number (*see* Figure 2.2b):

Region 1l. *The stagnation zone.*

Region 2l. $\delta_t < h$ *region*: Neither the thermal nor viscous boundary layer reach the free surface; surface temperature and velocity, T_{sf} and u_{max} are the inlet temperature and velocity, T_f and u_f.

Region 3l. $\delta_t = h$ *and* $\delta < h$ *region*: The thermal boundary layer has reached the free surface. The surface temperature increases with radius, but the velocity outside the viscous boundary layer is still the jet velocity, u_f.

Region 4l. $\delta = h, \delta_t = h$, *and* $T_w < T_{sat}$ *region*: In this region, the viscous boundary layer has reached the surface of the liquid sheet, and the velocity of the liquid surface decreases with radius.

In the boundary layer region, region 2l:

$$\mathrm{Nu}_d = 1.06\mathrm{Re}_d^{1/2}\mathrm{Pr}^{1/2}\left(\frac{d}{r}\right)^{1/2} \tag{2.7}$$

Region 2l ends where the thermal boundary layer reaches the surface of the liquid sheet at $r = r_{T0}$:

$$\frac{r_{T0}}{d} = \frac{0.1984\mathrm{Re}_d^{1/3}\mathrm{Pr}^{1/3}}{\left(1 - 0.7107\mathrm{Pr}^{1/2}\right)^{2/3}} \tag{2.8}$$

At r_{T0}, the beginning of region 3l, $\mathrm{Nu}_d = \mathrm{Nu}_{d,T0}$ and $h = h_{T0}$, where h can be computed from Sharan's equations (1984):

$$\frac{h}{d} = 0.125\left(\frac{d}{r}\right) + 1.005\left(\frac{r}{\mathrm{Re}_d d}\right)^{1/2} \tag{2.9}$$

In Region 3l:

$$\mathrm{Nu}_d = \frac{2}{\frac{r}{\mathrm{Re}_d \mathrm{Pr} h}\left(1 - \left(\frac{r_{T0}}{r}\right)^2\right) + 0.833\frac{h}{d} - 0.833\frac{h_{T0}}{d} + 2\frac{r_{T0}h_{T0}}{rh}\frac{1}{\mathrm{Nu}_{T0}}} \tag{2.10}$$

Region 4l begins at $r_0 = 0.1773 d\,\mathrm{Re}_d^{1/3}$, where the viscous boundary layer reaches the surface; here, the surface velocity decreases with radius.

$$h = 0.1713\left(\frac{d^2}{r}\right) + \frac{5.147}{\mathrm{Re}_d}\left(\frac{r^2}{d}\right) \tag{2.11}$$

In Region 4l:

$$\mathrm{Nu}_d = \frac{0.25}{\frac{1}{\mathrm{Re}_d \mathrm{Pr}}\left(\frac{r^2}{d^2} - \frac{r_0^2}{d^2}\right) + 0.130\left(\frac{h_0}{d} - \frac{h}{d}\right) + 0.25\frac{1}{\mathrm{Nu}_{d,0}}} \tag{2.12}$$

2.2.3 Numerical Integration in the Viscous Similarity Region

In the region of viscous similarity, we may solve the nonsimilar boundary-layer energy equation numerically in order to evaluation the accuracy of the integral method solutions for regions 3 and 4 ($\mathrm{Pr} > 1$) and for region 4l ($\mathrm{Pr} < 1$). In addition, we may probe the predicted critical Prandtl number for the occurrence of region 4 and the general differences between regions 3 and 4.

Chaudhury (1964) used Watson's velocity similarity to transform the energy equation in the film into the following form:

$$\frac{\partial^2 T}{\partial \eta^2} = Pr f' \frac{(r^3 + l^3)}{r^2} \frac{\partial T}{\partial r} \tag{2.13}$$

Here, the velocity similarity profile is (Watson, 1964)

$$\frac{2}{c^2} f'(\eta) = \sqrt{3} + 1 - \frac{2\sqrt{3}}{1 + \mathrm{cn}[3^{1/4} c(1 - \eta)]} \tag{2.14}$$

where cn is a Jacobi elliptic function, $c = 1.402$, the similarity coordinate is

$$\eta = \frac{y}{h} = \frac{3\sqrt{3} Q r}{2\pi^2 \nu (r^3 + l^3)} y \tag{2.15}$$

and the length l is

$$l = 0.3243 d Re_d^{1/3} \tag{2.16}$$

We may nondimensionalize r and l in equation (2.13) with r_0, the radius at which the viscous boundary layer reaches the liquid surface ($0.1833 d Re_d^{1/3}$, according to Watson's analysis [1]). Temperature is nondimensionalized as

$$\theta = \frac{T - T_f}{\Delta T} \tag{2.17}$$

where ΔT is chosen for convenience as $\Delta T = (2\pi^2 \nu q_w r_0^2)/(3\sqrt{3} k Q)$ for uniform wall heat flux and as $\Delta T = T_w - T_f$ for uniform wall temperature. The d.e. is then:

$$\frac{\partial^2 \theta}{\partial \eta^2} = Pr f'(\eta) \frac{\bar{r}^3 + \bar{l}^3}{\bar{r}^2} \frac{\partial \theta}{\partial \bar{r}} \tag{2.18}$$

[1] Watson found a Blasius velocity profile upstream of the similarity region. The integral method's algebraic velocity profile gives a constant of 0.1773, rather than 0.1833 (3.4% lower). To maintain consistency within each approach, we apply 0.1773 with our integral solutions and 0.1833 with the differential equations solutions.

The thermal boundary condition at the wall is

$$\frac{\partial\theta}{\partial\eta}|_{\eta=0} = -\frac{\bar{r}^3 + \bar{l}^3}{\bar{r}} \tag{2.19}$$

for uniform flux and

$$\theta|_{\eta=0} = 1 \tag{2.20}$$

for uniform temperature. The free surface is assumed to experience negligible evaporation or convection, so that

$$\frac{\partial\theta}{\partial\eta}|_{\eta=1} = 0 \tag{2.21}$$

This approximation is valid for low liquid surface temperatures (*see* Appensix B).

The numerical integration begins at $\bar{r} = 1$ ($r = r_0$). The temperature profile at this station is the initial condition for the solution; tests (see below) show that the initial profile is quickly damped and has little influence on the Nusselt number downstream. The following initial profile was employed:

$$\frac{T - T_f}{T_w - T_f} = 1 - \frac{3y}{2\delta_t} + \frac{1}{2}\left(\frac{y}{\delta_t}\right)^3 \qquad y \leq \delta_t \tag{2.22}$$

$$= 0 \quad \delta_t \leq y \leq \delta \tag{2.23}$$

which again satisfies the boundary conditions (no surface flux and matching to T_w). The wall temperature and boundary layer thickness were selected to match those of the upstream boundary layer as calculated from the integral solution. The differential equation was integrated using the Crank-Nicholson procedure.

2.3 Experiments

Experiments were performed to determine the wall temperature distribution and Nusselt number which actually occur in jet impingement cooling. The experimental arrangement is shown in Figure 2.3. The apparatus is in three primary parts: a water jet loop, a refrigerating system, and an electrical heating system.

To prevent splattering, a new apparatus was built specifically to produce laminar jets free of the surface disturbances which produce splattering (Vasista, 1989). A large plenum with an inlet momentum-breakup plate and turbulence dissipating honeycomb was used to create a pressurized liquid supply free of disturbances from the incoming flow. The jets studied were produced at the bottom of the plenum. The stability of liquid jets is very sensitive to the type of nozzle producing the jet. Pipe-like nozzles provide turbulent liquid to the jet when the Reynolds number exceeds a relatively small value (2000-4000); this turbulence generally leads to disturbances in the liquid surface which are unstable and which are strongly amplified when the jet impacts a flat surface (Errico, 1986). In the present experiments, carefully-machined sharp-edged orifice plates were used, rather than pipe-like nozzles. Sharp-edged orifices yield laminar, undisturbed jets of high stability. Thus, splattering was entirely suppressed in the present experiments.

The liquid supply was chilled by a mechanical refrigerator before being pumped to the plenum. The water was cooled to near 4°C. This cooling served two purposes. The first was to ensure that the liquid free-surface temperature would not become high enough to produce significant evaporative heat loss at any point along the heater

surface (*see* Appensix B). The second was to increase the accuracy of the experiments: the requirement of low evaporative loss necessitates relatively low heat fluxes and consequently small differences between wall and inlet temperatures. Subcooling the liquid supply maximized the measured ΔT, without creating evaporative loss, and thus decreased the uncertainty in the measured Nusselt number.

The liquid jets impinge on a heater made of 0.10 mm thick, 15.2 cm wide stainless steel sheet. The sheet is stretched over the open top of a 15.2 cm by 17.7 cm Plexiglass insulation box and over 2.54 cm diameter copper rods which serve as electrodes; springs maintain the tension in the sheet as it expands thermally and prevent its vibration or deflection. The insulation box keeps water away from the underside of the heater sheet, and restricts underside heat losses to a negligible natural convection loss. The box is slightly pressurized with compressed air to prevent liquid inflow. A 15 volt, 1200 ampere generator powers the sheet directly; the generator was run at up to 20% of full power.

The wall temperature distribution is measured by 0.076 mm J-type thermocouples attached to the underside of the sheet and electrically insulated from it by high-temperature Kapton tape. Starting at the stagnation point of the jet, the thermocouples are placed at radial increments of 1.27 cm along the arcs of circle centered at the stagnation point, within a sector of very small angle. The azimuthal symmetry of the flow is very high, and the mechanical convenience of this arrangement was found to introduce no error.

Radial conduction in the heater sheet may be shown to be of order $\epsilon^2 = (t/l)^2$ rel-

ative to vertical conduction, where l is the lengthscale associated with radial changes in the heat transfer coefficient. For the jet, l is essentially the jet diameter, d, so that $\varepsilon^2 \approx 0.001$. Radial conduction is thus negligible in comparison to vertical conduction; a formal perturbation solution of the heat equation substantiates this conclusion.

Convective backloss, via natural convection below the heater, is likewise negligible relative to the convective cooling at the upper surface of the heater: the back is essentially adiabatic. At the stagnation point, backloss is is less than 0.2% of the total flux, owing to the very high liquid-side Nusselt number. The backloss increases downstream, as the Nusselt number declines, but even in the worst case, at the largest radius, this loss is less than 4%. Because the backloss is so small, the temperature drop through the 0.06 mm thick Kapton tape (which electrically isolates the thermocouples) was entirely negligible and required no temperature correction.

The vertical conductive temperature drop through the electrical heater, however, can be appreciable in regions where the surface heat transfer coefficient becomes large, principally the stagnation zone. Solution of the heat equation, through terms of order $\varepsilon = t/d$, shows that the ratio of the true Nusselt number, based on liquid-side temperature, ($\mathrm{Nu}_t = q_w d/k(T_w - T_f)$) to the measured Nusselt number, based on temperature at the back of the heater, ($\mathrm{Nu}_m = q_w d/k(T_m - T_f)$) is

$$\frac{\mathrm{Nu}_t}{\mathrm{Nu}_m} = \frac{1}{1 - \zeta\,\mathrm{Nu}_m/2} \tag{2.24}$$

where $\zeta = tk/k_w d$ relates the Biot number to the true Nusselt number. This temperature correction was applied in reducing the measured data. For the majority of our measurements, the correction is less than 10% of the Nusselt number. However,

in the stagnation region, particularly when using the smallest orifice (3.18 mm), the correction could be as large $\approx$ 30%.

For each thermocouple measurement, a number of values were taken to reduce random error. These measured values were averaged to get the actual values for the calculations. The thermocouples were also calibrated under isothermal conditions before and after each run to reduce systematic errors. The wall temperature increases with radius and the local Nusselt number is based on the temperature differences between the wall and the incoming jets. At the stagnation point, the temperature differences are smallest and the uncertainty is largest. For 3/8 inch (9.5 mm) diameter orifice, the resulting Nusselt number uncertainty at this point is $\pm$10%, and for 1/8 inch (3.18 mm) diameter orifice, it is $\pm$30%. The uncertainty goes down very rapidly as radius increases and for most positions uncertainty is less than $\pm$5%. Further reduction of stagnation zone uncertainty, by increasing the heat flux, was untenable as a result of the requirement of minimizing downstream evaporation. The uncertainty for Re_d is less than $\pm$2% and that for r is less than $\pm$0.25 mm.

2.4 Discussion

2.4.1 Comparison of Integral and Differential Solutions

Numerical integration of the differential equation (2.13) requires the temperature distribution at the beginning of the similarity region. The exact temperature distribution depends on the upstream stagnation and boundary layer regions. In our

calculations, that distribution is based on the polynomial solution from the integral method. However, to test the effects of this initial condition, the computation was also run with an initially linear temperature distribution, between T_w and T_f, in the boundary layer and with a uniform initial temperature, at T_f. The bulk temperatures of these two profiles are larger and smaller, respectively, than the polynomial, while the initial slope of the profiles near the wall are smaller and larger, respectively. Thus, the linear profile gives a lower initial Nu_d and the uniform profile gives a higher initial Nu_d. Figure (2.4) compares the computations for the different initial temperature profiles. By $r/r_0 = 3$, the difference between the linear, polynomial, and constant initial temperature profiles has decreased to less than 10%, and the profiles are indistinguishable at larger r/r_0. Thus, the initial temperature distribution has minimal influence on the Nusselt number in the region far from the center, and results based on the polynomial initial distribution are clearly satisfactory. Moreover, these tests show that the heat transfer in the stagnation zone and boundary layer regimes have little effect on the wall temperature at large radii.

Figure (2.5) compares heat transfer coefficients for uniform wall heat flux (UHF) to those for uniform wall temperature (UWT) from the d.e. solution. In our previous paper, we noted that, in the boundary layer region, the heat transfer coefficient for UHF was 25% higher than that for UWT. By contrast, in the similarity region, the difference between boundary conditions increases with increasing radius. Once the thermal boundary layer reaches the free surface, the energy from the wall is absorbed by the entire film, a situation comparable to fully developed duct flow. However, the

UHF condition for the radial film differs markedly from the duct flow, in that the heat transfer surface increases linearly with radius. The UHF condition of the jet is akin to a duct flow with flux increasing linearly with axial position, and such a condition is known to produce a higher heat transfer coefficient. This conclusion is not altered by our definition of Nu_d in terms of incoming, rather than bulk, temperature.

The figure shows that, for small Prandtl numbers, the UWT Nusselt number decreases more rapidly than for large Prandtl number, since the driving temperature difference between wall and surface temperature dwindles much faster at low Pr. At $r/r_0 = 10$, the UWT Nusselt number for $Pr = 2$ is only 9% as large as that UHF, and that for $Pr = 6$ is only 40%.

Nusselt numbers from the integral and differential equations are compared in Figures (2.6ab) for $Pr > 1$ and $Pr < 1$ respectively.[2] For $Pr > 1$, the maximum difference between the integral and differential solutions is about 10%. The integral solution is lower than the d.e. solution as a result of the assumed shape of the temperature distribution. The integral solution neglects the higher order terms in δ_t/δ, which should cause more error as Pr decreases toward unity, but the comparison shows better agreement with the d.e. solution at lower Pr. Apparently, the neglect of higher order terms compensates for the somewhat smoother profile of the integral procedure. For $Pr < 1$, Figure 2.6b shows the simplified integral results, which neglect all terms in ϕ or Δ. In contrast to $Pr > 1$, for $Pr < 1$ the neglected terms are as large as the terms retained when Pr approaches unity. The comparison shows that for $Pr = 0.1$

[2]The ordinate $Nu_r/Re_d^{2/3}$ follows naturally from the scaling of the differential equation, but does not carry the full dependence on Re_d.

the disagreement between the integral and differential equations is more than 20%. Fortunately, most liquid metals have Pr near 0.01, and for this case the simplified integral results agree with the differential results to better than 5%. For larger Prandtl numbers, the higher order terms should be retained when calculating Nu_d.

From the integral analysis, we previously found that the thermal boundary layer would not reach the free surface for $Pr > 5.2$. Therefore, for $\mathrm{Pr} > 5.2$, the free surface temperature remains at T_f for all r according to the integral analysis. Of course, this is an approximation based on the assumption of a sharply defined boundary layer. Figure (2.7) shows the dimensionless free surface temperature from the d.e. solution as function of r/r_0 and illustrates the strong influence of the Prandtl number. For $\mathrm{Pr} = 2$, the surface temperature is more than 11 times higher than for $\mathrm{Pr} = 10$. For $\mathrm{Pr} > 5.2$, the free surface temperature increases much more slowly. However, the surface temperature does rise above the inlet value for $\mathrm{Pr} > 5.2$, and this is another cause of differences between integral and differential solutions for Nu_d.

For engineering purposes, it is convenient to construct a simplified version of the integral or differential predictions. First, we note that, in the Prandtl number range between 1 and 5.2 (for which region 4 is possible), the difference between the integral solutions for region 3 and region 4, if applied at the same Reynolds number and radius, amounts to less than 3%. Thus, the equation derived for region 3 can usually be applied as a good approximation in region 4 as well.

For further simplification, we may consider $r/d \gg 0.322\mathrm{Re}^{1/3}$ and neglect the

terms in d/r and C_3 in the integral result for region 3 (eqn. 2.3):

$$\mathrm{Nu}_d = 0.172\, Re_d\, Pr^{1/3} \left(\frac{d}{r}\right)^2 \tag{2.25}$$

Correlation of the differential equation solutions (accurate to ±9%) leads to the following, similar result for $1 \leq \mathrm{Pr} \leq 100$ and $2.5 \leq r/r_0 \leq 100$:

$$\mathrm{Nu}_d = 0.195\, Re_d^{0.98} Pr^{0.38} \left(\frac{d}{r}\right)^{1.95} \tag{2.26}$$

For the range $2.5 < r/r_0 < 10$, a slightly better fit (to ±5%) is

$$\mathrm{Nu}_d = 0.15\, Re_d^{0.93} Pr^{0.38} \left(\frac{d}{r}\right)^{1.80} \tag{2.27}$$

Since a turbulent transition and a hydraulic jump usually occur downstream, the latter equation is more useful. However, neither correlation is reliably accurate in the range $1 \leq r/r_0 \leq 2.5$; this range is important in practice, and we recommend use of the theoretical prediction, equation (2.3), in region 3. The integral prediction for region 2 is equation (2.2). For laminar flow, equations (2.2) and (2.3) can be used to estimate the local Nusselt number. These predictions are compared with our experimental data below.

The preceding results do not mean that the identification of regions 3 and 4 is unimportant. In region 4, liquid surface temperature increases rapidly with radius, and evaporation can become very significant. Conversely, in region 3, evaporation can be less important for low initial liquid temperature. Thus, for lower Prandtl numbers, the surface temperature should always be estimated, and, if necessary, the adiabatic surface condition should be dropped in favor of an evaporating surface

condition. Surface evaporation was carefully suppressed in the present experiments by cooling the incoming liquid and by limiting the heat flux, but in engineering applications, evaporation will almost always occur. Evaporation will tend to raise Nu_d (Appendix B), since it offers an additional heat sink, unless it leads to film dryout downstream, for which Nu_d will drop disastrously.

The numerical solutions with constant Prandtl number suggest Nusselt number is proportional to Prandtl number to 0.38th power over Prandtl number from 1 to 100. However, most liquids of high Prandtl number show rapid decrease in Prandtl number with increasing temperature. Streamwise variations in Pr, as bulk temperature rises, are certainly important and probably outweigh any finer adjustments of the Prandtl number exponents. Best agreement with experimental data was obtained when the values of viscosity (*viz.*, Re_d) and Pr used in the equations were those corresponding to temperatures at the radial midpoint of the film.

2.4.2 Turbulent Transition

The preceding analyses are based on laminar flow and consider neither surface waves nor turbulent transition. Plainly, it is important to know the location of transition from laminar to turbulent flow. If, in addition, turbulence significantly raises the Nusselt number above the laminar prediction, a separate analysis of the turbulent transport is necessary.

Figure (2.8) shows measurements of the turbulent transition radius in the present system. The transition point is easily identified, since the laminar liquid sheet is

smooth and transparent, while the turbulent liquid sheet has a rough surface which reflects light and appears bright. The associated surface waves are described by Azuma and Hoshino (1984a) as 'lattice-shaped' waves. A curve fit of our data (Gabour, 1990) gives the transition radius as

$$\left(\frac{r_t}{d}\right) Re_d^{0.422} = 1.2 \times 10^3 \tag{2.28}$$

In their own system, Azuma and Hoshino measured

$$\left(\frac{r_t}{d}\right) \mathrm{Re}_d^{0.315} = 0.73 \times 10^3 \tag{2.29}$$

which shows a slightly weaker dependence on Reynolds number, but turbulent transition points normally depend on the disturbances present in a specific system. Equation (2.28) suggests a coordinate of $\frac{r}{d} Re_d^{0.422}$. Using this coordinate, some of the present heat transfer data are shown in Figure (2.9). At the transition point, the figure shows a clear shift in the slope of the Nusselt number, which becomes more pronounced at higher Reynolds number. The Nusselt number increases above the laminar trend, as direct comparisons (below) illustrate. Note that the abscissa here is chosen to illustrate the turbulent transition, not the functional dependence of Nu_d on Re_d and Pr; thus, the curves do not collapse to a single line. Moreover, the streamwise changes in the Re_d and Pr dependencies make it impossible to present all of our data, for many different conditions, on a single graph. In this and following figures, we present enough data to illustrate the general behavior without attempting to be exhaustive.

The Nusselt numbers show a hump downstream of the turbulent transition point.

This hump corresponds to the point at which the turbulence has become fully developed (see heat transfer predictions below). As the Reynolds number increases, the hump becomes both more pronounced and occurs after shorter distance. The transition and hump radii are shown as a function of jet Reynolds number in Figure (2.10). The data for the hump position can be correlated as:

$$\left(\frac{r_h}{d}\right) Re_d^{0.68} = 2.86 \times 10^4 \tag{2.30}$$

Recall that the border of region 2 is $r_0/d = 0.1773 Re_d^{1/3}$. This implies that if $Re_d > 1.1 \times 10^5$, the transition will take place in region 2. For the present Reynolds number range, transition always occurs in the similarity region (region 3). Indeed, the stability analysis of Azuma and Hoshino (1984d) suggests that the flow will always be most unstable near the border of regions 2 and 3, with waves or turbulence commencing in the similarity region.

Figure (2.11) shows a comparison of the data to the integral solution (equation 2.2) in region 2. The agreement is generally within the uncertainty of the data. This region is relatively small. In this region, small concentric ripples can be observed (called 'disturbance' waves by Azuma and Hoshino). These waves do not develop significantly, and they appear to have no strong effect on the heat transfer.

In the similarity region, the heat transfer data show a clear transition from laminar to turbulent flow. Azuma and Hoshino (1984) report a critical (transition) discharge Reynolds number, based on the jet diameter, of 4.8×10^4. From our data this critical discharge Reynolds number is much lower (less than 2×10^4). This discrepancy may be caused by the definition of the critical discharge Reynolds number adopted

by Azuma and Hoshino. They regarded the flow to be turbulent when the so-called "sandpaper-like" waves are present over 50% of the azimuthal direction, and took that discharge Reynolds number as the critical value. That type of situation never occurs in the present experiments; here with increasing Reynolds number, waves and disturbances inside the liquid sheet intensify, but the transition circle stays essentially circular and symmetric at all Re_d.

The laminar analysis predicts that for a given Re_d, $\mathrm{Nu}_r = (r/d)\,\mathrm{Nu}_d$ reaches a peak value and then decreases. Figure (2.12), however, shows two features which differ from the prediction. The first is that the da' , break from the initially linear portion of the laminar prediction at a higher value of Nu_r than predicted. The other is a sharp peak in Nu_r downstream of the change in slope. The first feature suggests, from our observations and those of Azuma and Hoshino's (1984ad), the disturbance waves have intensified in this portion of the film. They appear to increase the heat transfer coefficients by up to 20% in this short region, which is just ahead of the transition radius where sandpaper-like waves occur (*see also* Figure 2.13b). The second feature, the peak, is simply the hump at full development of turbulence, as previously discussed.

The friction coefficient measurements and mass transfer data of Nakoryakov *et al.* show a very similar behavior. The primary difference is that turbulent transition, as deduced from their friction coefficient measurements, occurs in the boundary layer region (region 2). Their data show a single peak rather than the pair of features seen here. This suggests that the sheet has become turbulent before surface waves

can contribute significantly to the heat transfer. They attributed the peak to waves rather than turbulent transition. However, for their Reynolds number range, the turbulent transition is a more likely explanation.

2.4.3 Prediction of Turbulent Heat Transfer

The Nusselt number for turbulent flow may be calculated using the thermal law of the wall. The Stanton number is defined as

$$\mathrm{St} = \frac{q_w}{\rho c_p u_{max}(T_w - T_f)} \tag{2.31}$$

and the law of the wall may be written in the standard internal-flow form:

$$\mathrm{St} = \frac{C_f/2}{1.07 + 12.7(\mathrm{Pr}^{2/3} - 1)\sqrt{C_f/2}} \tag{2.32}$$

The skin friction coefficient is calculated from the Blasius law:

$$C_f = 0.945\left(\frac{\nu}{u_{max}h}\right)^{1/4} = 0.073 Re_d^{-1/4}\left(\frac{r}{d}\right)^{1/4} \tag{2.33}$$

where the one-seventh power turbulent velocity distribution produces a maximum velocity

$$u_{max} = \frac{1}{7}\frac{u_f d^2}{hr}, \tag{2.34}$$

and a film thickness h of

$$h = d\left[\frac{0.02091}{Re_d^{1/4}}\left(\frac{r}{d}\right)^{5/4} + C\frac{d}{r}\right] \tag{2.35}$$

with

$$C = 0.1713 + \frac{5.147}{Re_d}\frac{r_t}{d} - \frac{0.02091}{Re_d^{1/4}}\left(\frac{r_t}{d}\right)^{1/4} \tag{2.36}$$

From the above, the Nusselt number for turbulent flow may be calculated:

$$\mathrm{Nu}_d = 0.0052\mathrm{Re}_d^{3/4}\left(\frac{d}{h}\right)\left(\frac{d}{r}\right)^{3/4}\left(\frac{\mathrm{Pr}}{1.07+12.7(\mathrm{Pr}^{2/3}-1)\sqrt{\mathrm{C_f}/2}}\right) \tag{2.37}$$

When $r/d \gg 5.58 \times C\mathrm{Re}_d^{1/9}$, the equation may be simplified to

$$\mathrm{Nu}_d = 0.25\mathrm{Re}_d\left(\frac{d}{r}\right)^{2}\left(\frac{\mathrm{Pr}}{1.07+12.7(\mathrm{Pr}^{2/3}-1)\sqrt{\mathrm{C_f}/2}}\right) \tag{2.38}$$

The turbulent Nusselt number is substantially higher than the laminar Nu_d.

Figures (2.13ab) show the laminar and turbulent predictions together with experimental data for two runs at different Reynolds numbers. In both cases, agreement is excellent. The increasing strength of turbulent augmentation with increasing Reynolds number is also quite apparent. The only significant disagreement observed is in the stagnation zone for lower Reynolds number. Data and predictions for the stagnation zone are discussed in the next section.

2.4.4 Recommendations for Nusselt Number Estimation

Table 2.1 summarizes the suggested relations for estimating local Nusselt number for impinging, circular, free liquid jets. For most regions, deviations are less than 10%. For laminar convection in the similarity region, however, waves can enhance the heat transfer, and Nu_d may exceed the estimate by up to 20%; as the waves are damped, the heat transfer goes back down. The wavy region is relatively small, however, because it is limited by subsequent turbulent transition. In the region of transition from laminar to turbulent flow, between r_t and r_h, we tentatively recommend a line fit between the laminar predictions at r_t and the turbulent prediction at r_h. This fit

is shown in Figures (2.13ab), and can be seen not to account properly for the wave effects which occur in that region at larger Reynolds number. With the exceptions of this line fit and the correlation for r_t/d, all equations in Table 2.1 are analytical predictions; each is substantiated by experiment.

2.4.5 Additional Studies Required

In jet impingement cooling applications, turbulent incoming jets are likely to be produced, since upstream disturbances are not usually damped and the jets often issue from pipes. While turbulence may enhance stagnation point heat transfer, it is damped sharply as the film spreads. We are currently conducting experimental studies of turbulent jet heat transfer.

Impinging jets will splatter if the jet surface is even slightly disturbed or the thin liquid sheet is disturbed beyond a certain magnitude. Disturbances to the incoming jet are often caused by irregularities in the orifice or by turbulence in the liquid supply. Roughness of the target surface can also disturb the liquid film. Splattering removes liquid from the liquid film, and thus lowers the Nusselt number; Liu and Lienhard (1989) estimated reductions of 20% or more. We are also investigating the role of splattering in jet impingement cooling.

Finally, the behavior of the stagnation zone at lower Reynolds number will be further investigated, owing to a possible viscous decrease of the stagnation velocity gradient as Re_d becomes smaller.

2.5 Conclusions

Convective heat removal by liquid jet impingement has been investigated for uniform wall flux and circular, laminar jets. Both theoretical and experimental results are given.

- The radial distribution of Nusselt number is accurately predicted by the formulae in Table 1 for Prandtl number of order unity or greater.
- Laminar heat transfer in the film for $Pr \geq \mathcal{O}(1)$ may be calculated from Equation 2.2 in the boundary layer region (region 2) and by Equation 2.3 in the laminar portion of the similarity region (regions 3 and/or 4). These regions are described in Section 2.1.
- Laminar heat transfer predictions for $Pr < 1$ are developed in Section 2.2.
- Comparison of the integral predictions to numerical solutions in the similarity region supports conclusions previously drawn from the integral approach for $Pr > 1$ as well as the new results for $Pr < 1$.
- Turbulent transition occurs at a radius given by Equation 2.28. Turbulence becomes fully-developed at a radius given by Equation 2.30. Turbulent heat transfer in the film is given by Equation 2.37.

REFERENCES

Azuma, T. and Hoshino, T., 1984a, "The Radial Flow of a Thin Liquid Film, Part 1: Laminar-Turbulent Transition," *Trans. Japan Soc. Mech. Engrs*, 50-974.

Azuma, T. and Hoshino, T., 1984b, "The Radial Flow of a Thin Liquid Film, Part 2: Film Thickness," *Trans. Japan Soc. Mech. Engrs*, 50-982.

Azuma, T. and Hoshino, T, 1984c, "The Radial Flow of Thin Liquid Film, Part 3: Velocity Profile," *Trans. Japan Soc. Mech. Engrs*, 50-1126.

Azuma, T. and Hoshino, T., 1984d, "The Radial Flow of Thin Liquid Film, Part 4: Stability of Liquid Film and Wall Pressure Fluctuation," *Trans. Japan Soc. Engrs*, 50-1136.

Carper, H.J., 1989, "Impingement Cooling by Liquid Jet," presented at the ASME Winter Annual Meeting, San Francisco.

Chaudhury, Z.H., 1964, "Heat transfer in a radial liquid jet," *J. Fluid Mech.*, vol.20, pp.501-511.

Gabour, L.A., 1990, "Heat transfer to turbulent and splattering impinging liquid jets," S. B. Thesis in Mechanical Engineering, MIT.

Ishigai, S., Nakanishi, S., Mizuno, M., and Imamura, T., 1977, "Heat Transfer of the Impinging Round Water Jet in the Interference Zone of Film Flow along the Wall," *Bulletin of the JSME*, Vol.20, No. 139.

Lombara, J.S., 1990, "An experimental investigation of liquid jet impingement heat transfer theories", S.B. Thesis in Mechanical Engineering, MIT.

Nakoryakov, V. E., Pokusaev, B. G., and Troyan, E. N., 1978, "Impingment of an Axisymmetric Liquid Jet on a Barrier," *Int. J. Heat Mass Transfer*, Vol.21, pp.1175-1184.

Olsson, R. G. and Turkdogan, E. T., 1966, "Radial spread of a liquid stream on a horizontal plate", *Nature*, Vol.211, No.5051, pp.813-816.

Schach, W., 1935, "Umlenkung eines kreisförmigen Flussigkeitsstrahles an einer ebenen Platte senkrecht zur Strömungsrichtung, *Ing.-Arch.*, vol.6, pp.51-59.

Schlichting, H., 1979, *Boundary-Layer Theory*, 7th ed., McGraw-Hill Book Company.

Sharan, A., 1984,"Jet-disc boiling: burnout predictions and application to solar receivers," Master's Thesis in Mechanical Engineering, University of Houston.

Stevens, J. and Webb, B. W., 1989, "Local Heat Transfer Coefficients under an Axisymmetric, Single-phase liquid Jet," *Heat Transfer in Electronics - 1989*, ASME-HTD, Vol. 111, pp.113-119.

Vasista, V.K., 1989, "Experimental Study of the Hydrodynamics of an Impinging Liquid Jet," Bachelor's Thesis in Mechanical Engineering, M.I.T.

Wang, X. S., Dagan, Z., and Jiji, L. M., 1989a, "Heat transfer between a circular free impinging jet and a solid surface with nonuniform wall temperature or wall heat flux-1. solution for the stagnation region," *Int. J. Heat Mass Transfer*, Vol.32, No.7, pp.1351-1360.

Wang, X. S., Dagan, Z., and Jiji, L. M., 1989b, "Heat transfer between a circular free impinging jet and a solid surface with nonuniform wall temperature or wall heat flux-2. solution for the boundary layer region," *Int. J. Heat Mass Transfer*, Vol.32, No.7, pp.1361-1371.

Wang, X. S., Dagan, Z., and Jiji, L. M., 1989c, "Conjugate heat transfer between a laminar impinging liquid jet and a solid disk," *Int. J. Heat Mass Transfer*, Vol.32, No.11, pp.2189-2197.

Watson, E.J., 1964, "The radial spread of a liquid over a horizontal plane," *J. Fluid Mech.*, Vol.20, pp.481-499.

White, F. M., 1974, *Viscous Fluid Flow*, McGraw-Hill Book Company, New York.

Table 2.1: Suggested formulae for local Nusselt number for $\mathrm{Pr} \geq \mathcal{O}(1)$

Region	Range	Nu_d
Stagnation zone	$0 \leq r/d < 0.787, \quad 0.15 \leq \mathrm{Pr} \leq 3$ $\mathrm{Pr} > 3$	$0.715\,\mathrm{Re}_d^{1/2}\mathrm{Pr}^{0.4}$ $0.797\,\mathrm{Re}_d^{1/2}\mathrm{Pr}^{1/3}$
Transition: stagn. to b.l.	$0.787 < r/d < 2.23$	$\left(\frac{\frac{2I}{\pi\mu}\mathrm{Re}_d\mathrm{Pr}\frac{r}{d}}{\frac{1}{2}\left(\frac{r}{d}\right)^2-0.2535}\right)^{1/3}$
b.l. region (2)	$2.23 < r/d < 0.1773\,\mathrm{Re}_d^{1/3}$	$0.632\,\mathrm{Re}_d^{1/2}\mathrm{Pr}^{1/3}\left(\frac{d}{r}\right)^{1/2}$
Similarity region (3 & 4)	$0.1773\,\mathrm{Re}_d^{1/3} < r/d < 1200\,\mathrm{Re}_d^{-0.422}$ $(r_0/d < r/d < r_t/d)$	$\frac{0.407\,\mathrm{Re}_d^{1/3}\mathrm{Pr}^{1/3}\left(\frac{d}{r}\right)^{2/3}}{\left[0.1713\left(\frac{d}{r}\right)^2+\frac{5.147\,r}{\mathrm{Re}_d d}\right]^{2/3}\left[\frac{1}{2}\left(\frac{r}{d}\right)^2+C_3\right]^{1/3}}$ $\left(C_3 = \frac{0.267\,(d/r_0)^{1/2}}{\left[0.1713\left(\frac{d}{r_0}\right)^2+\frac{5.147\,r_0}{\mathrm{Re}_d d}\right]^2} - \frac{1}{2}\left(\frac{r_0}{d}\right)^2\right)$
Transition: laminar/turb.	$1200\,\mathrm{Re}_d^{-0.422} < r/d < 2.86\times10^4\,\mathrm{Re}_d^{-0.68}$	$\mathrm{Nu}_{lam}(r_t) + [\mathrm{Nu}_{turb}(r_h) - \mathrm{Nu}_{lam}(r_t)]\frac{(r-r_t)}{(r_h-r_t)}$
Turbulent region	$r/d > 2.86\times10^4\,\mathrm{Re}_d^{-0.68}$	$\frac{8\,\mathrm{Re}_d\mathrm{Pr}\,f(C_f,\mathrm{Pr})}{49(h/r)(r/d)+28(r/d)^{1/2}f(C_f,\mathrm{Pr})}$

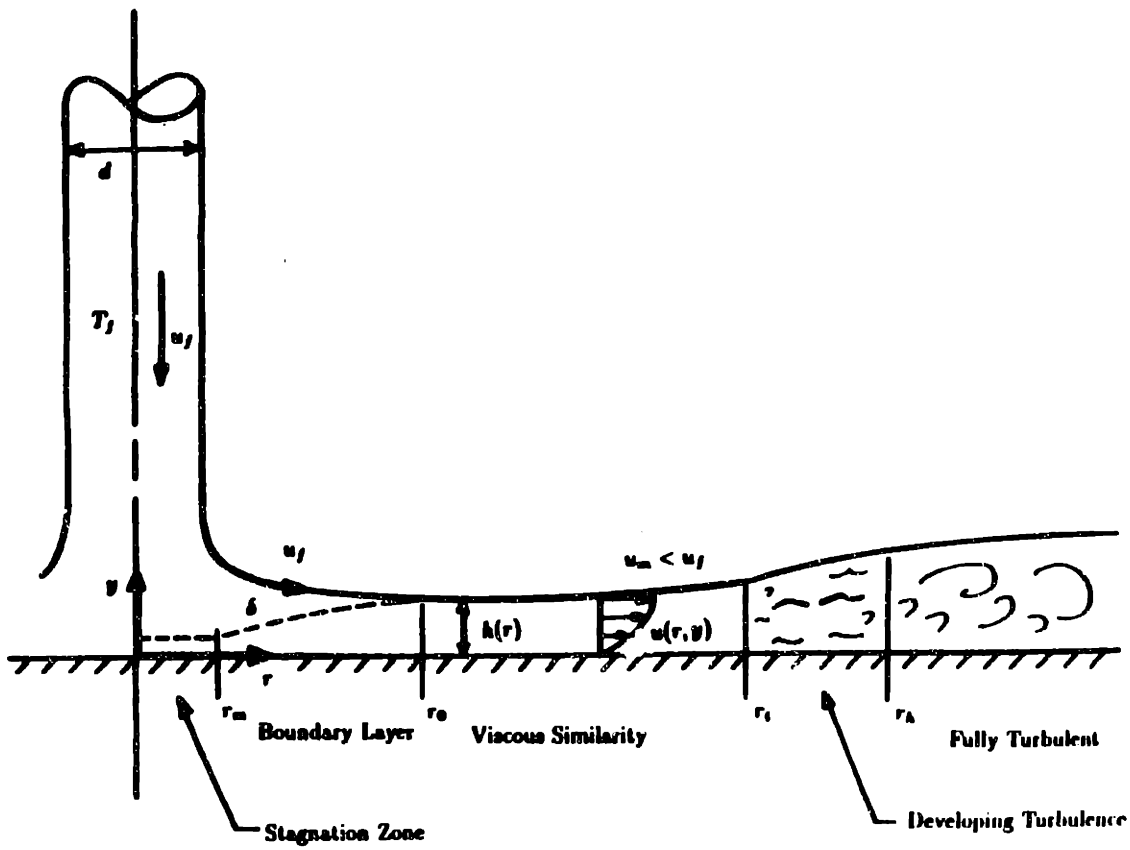

Figure 2.1: The Jet and Film Flow Field Showing Hydrodynamic Evolution. (Not to Scale)

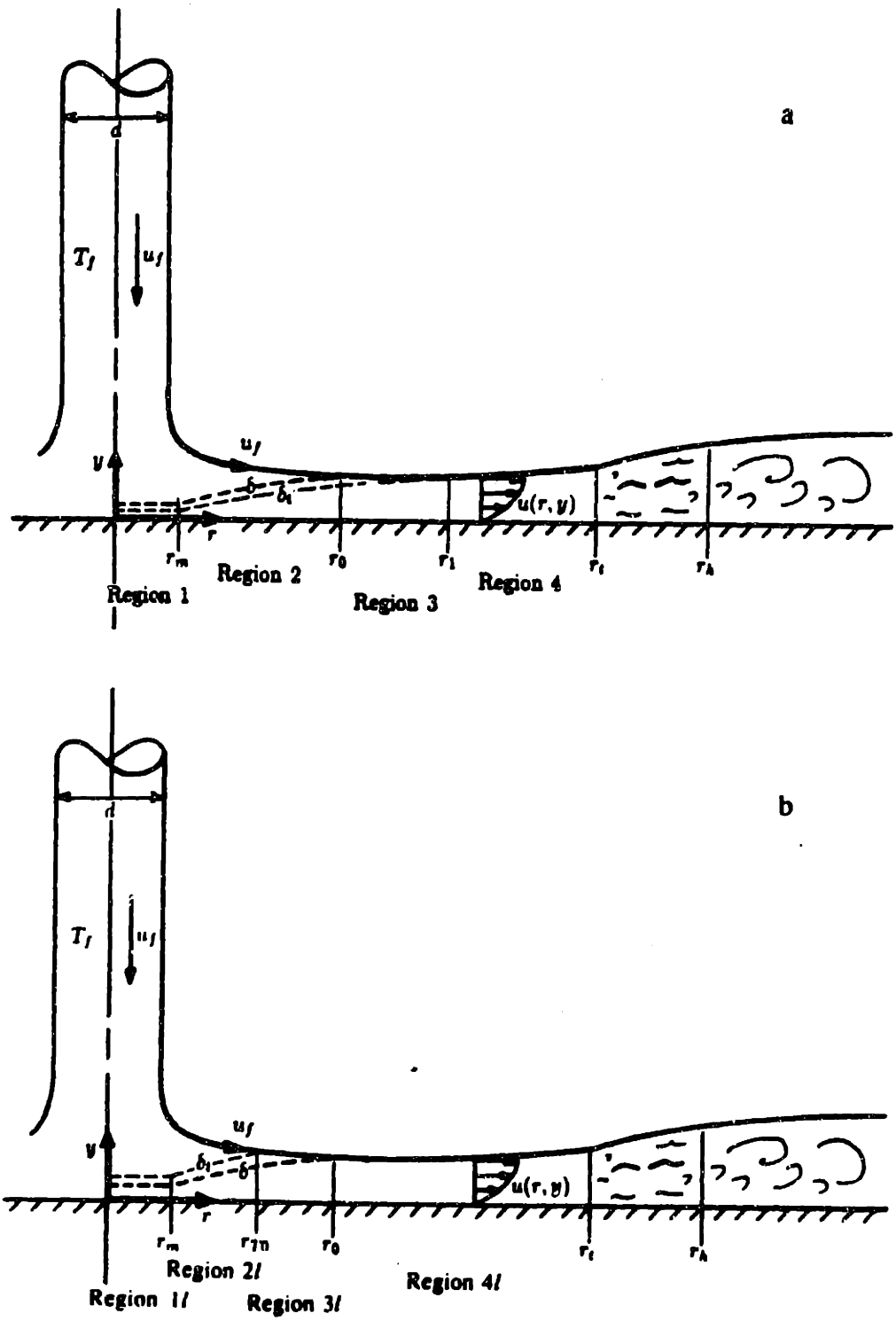

Figure 2.2: Development of the thermal boundary layer: (a) Pr > 1; (b) Pr < 1. (Not to Scale)

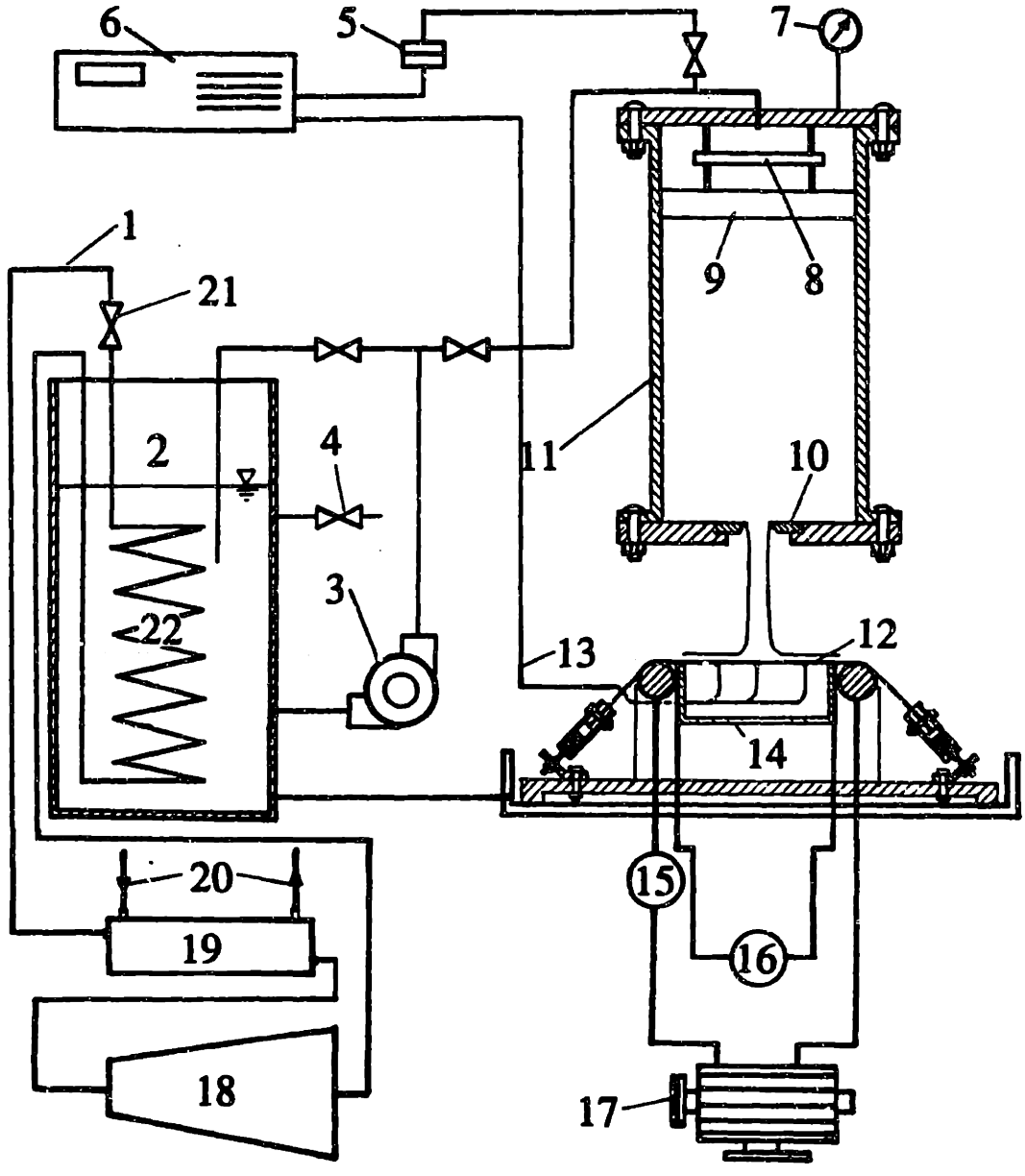

Figure 2.3: Experimental apparatus: 1. Freon line; 2. Chilled water tank; 3. Pump; 4. Water supply line; 5. Pressure transducer; 6. Digital Voltmeter; 7. Pressure gauge; 8. Momentum dissipating plate; 9. Honeycomb; 10. Sharp-edged orifice plate; 11. Plenum; 12. Steel heater sheet; 13. Thermocouple leads; 14. Pressurized plastic box; 15. Ammeter; 16. Voltmeter; 17. 30 kW Generator; 18. Compressor; 19. Heat exchanger; 20. Cooling water; 21. Throttling Valve; 22. Evaporator.

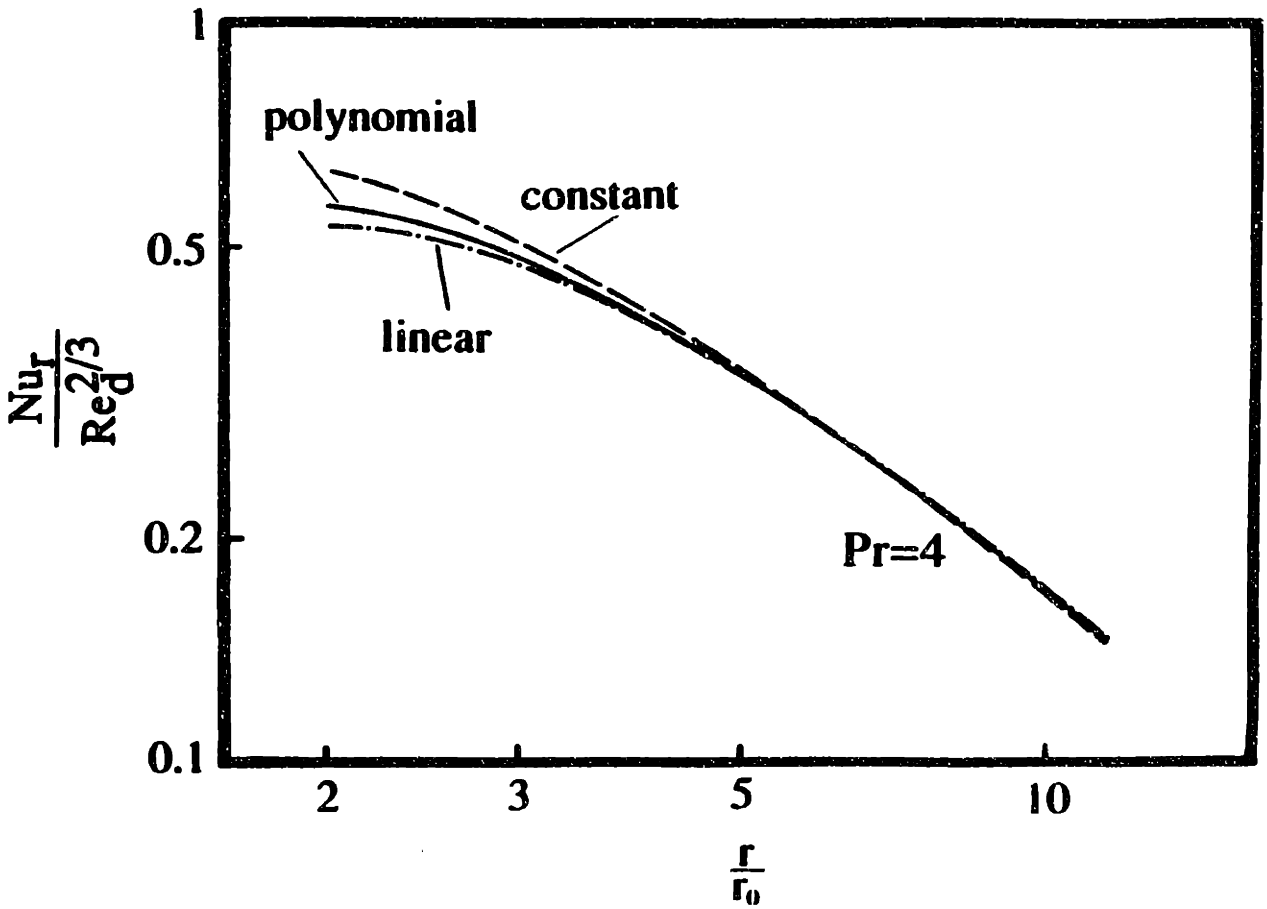

Figure 2.4: The effect of initial conditions on the solution of the differential equations in the viscous similarity region for Pr = 4.

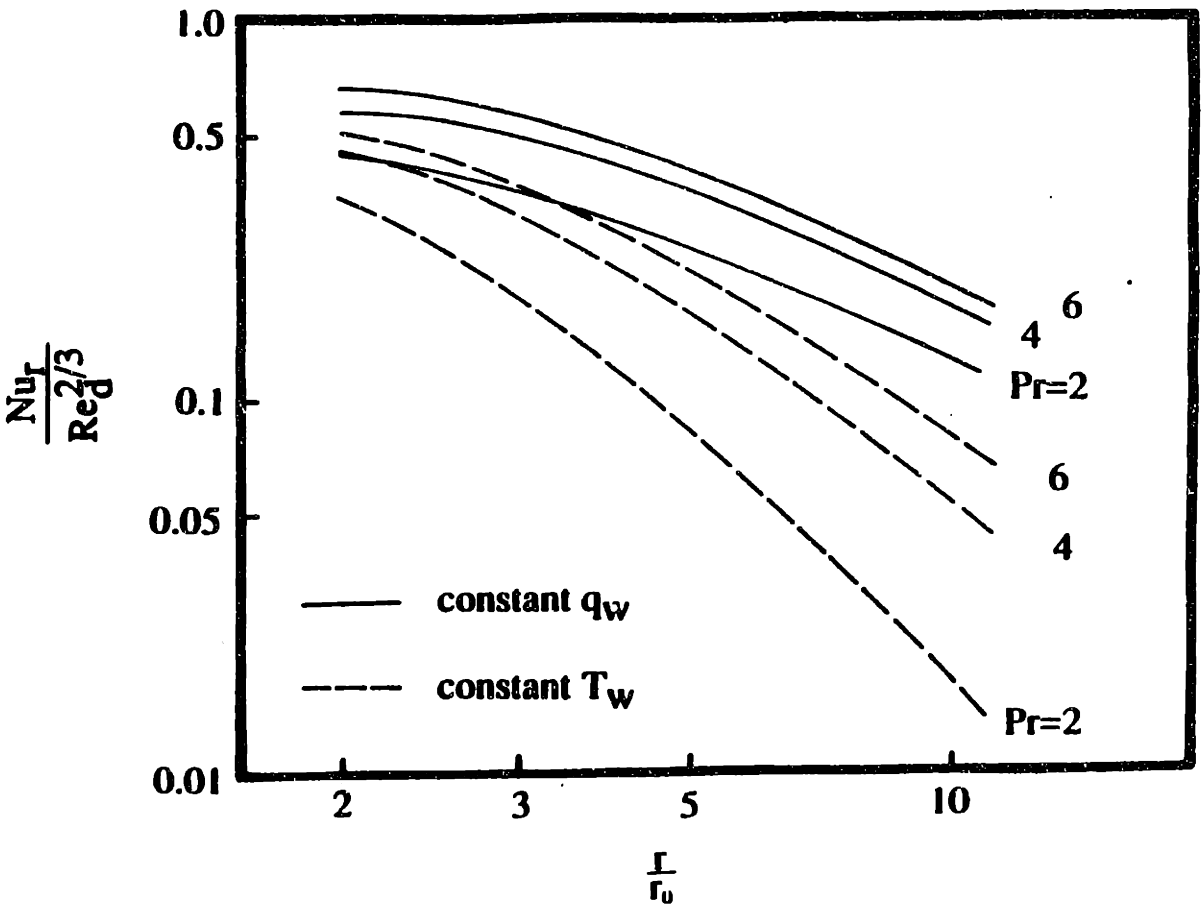

Figure 2.5: Comparison of uniform heat flux and uniform temperature wall conditions in the viscous similarity region (from d.e.).

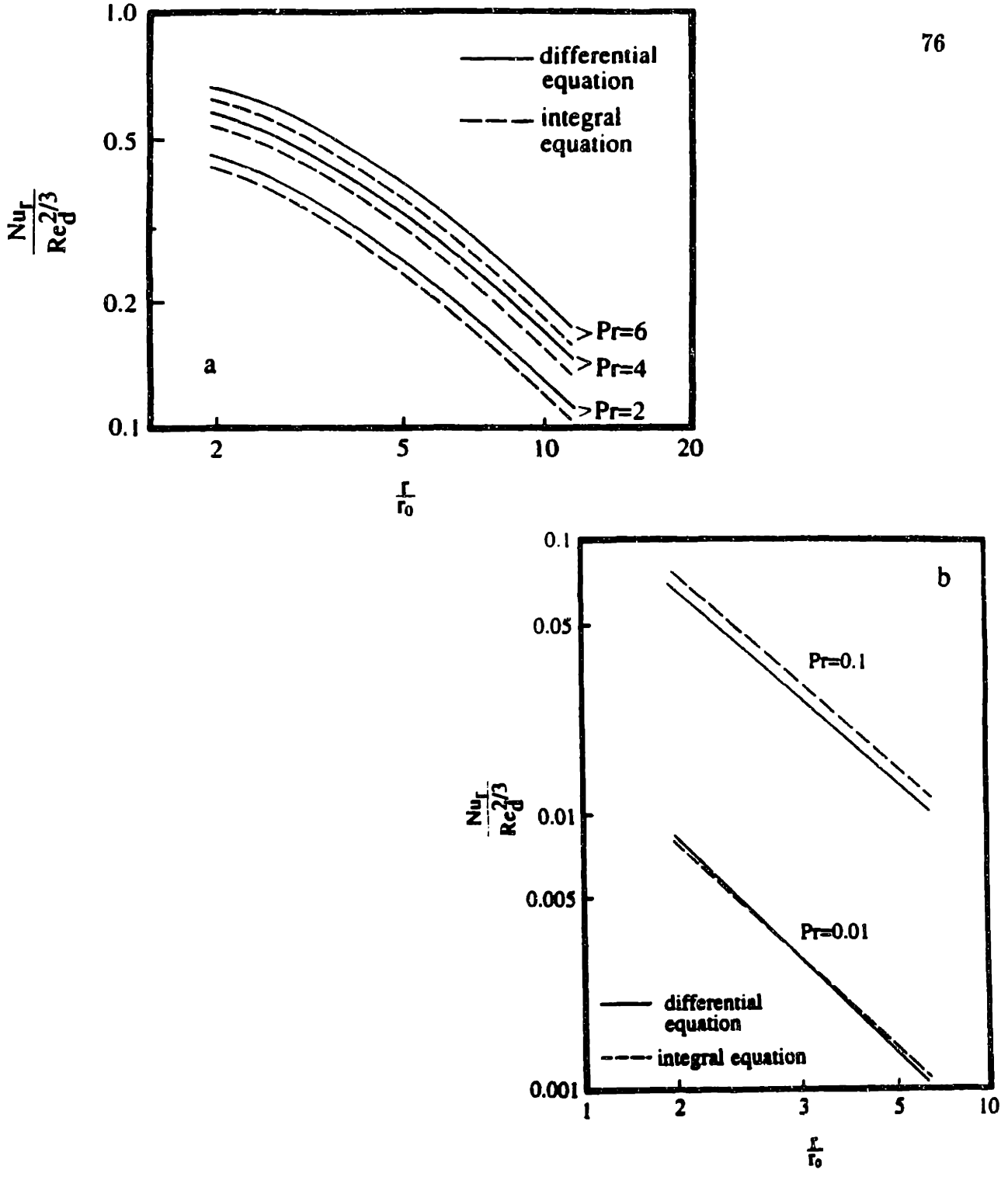

Figure 2.6: Comparison of the solutions from differential and integral analysis of the viscous similarity region at $Re_d = 10^4$ for: (a) $Pr > 1$; and (b) $Pr < 1$.

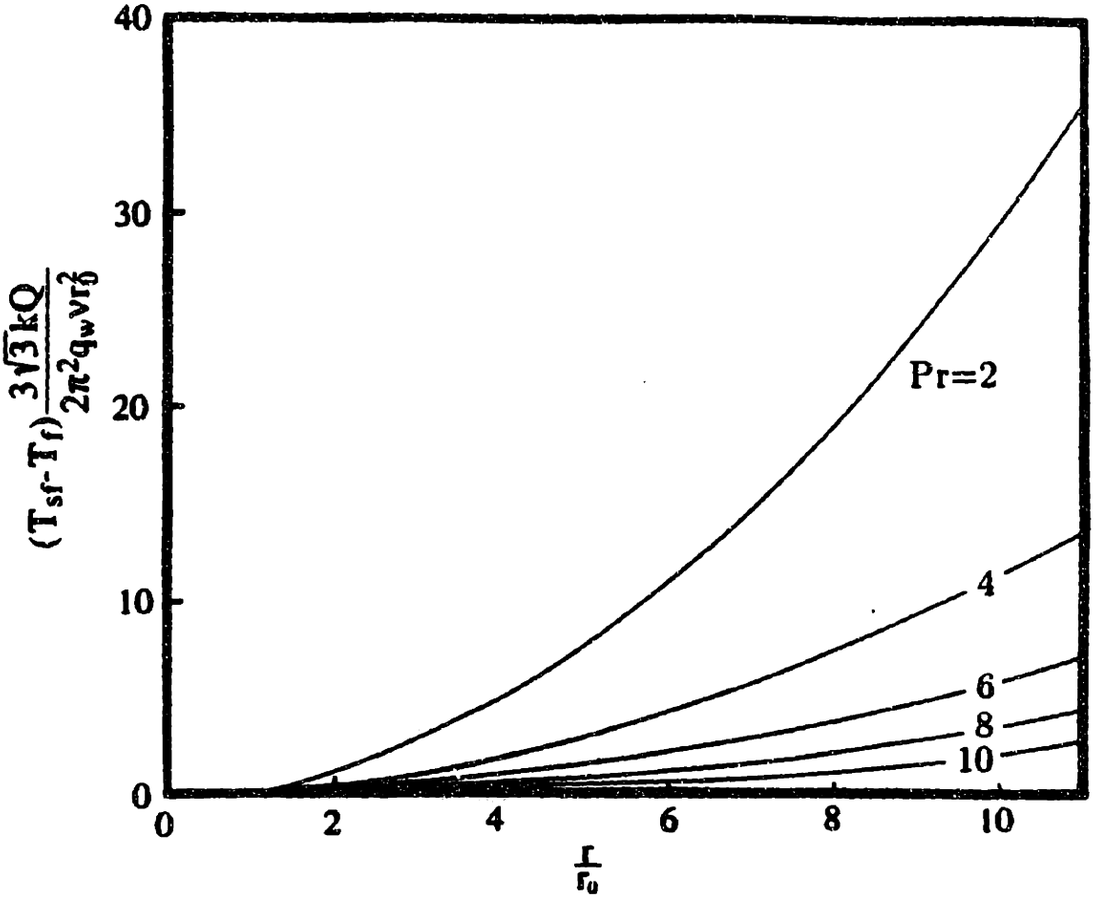

Figure 2.7: The effect of Prandtl number on the free surface temperature in the viscous similarity region (from d.e.).

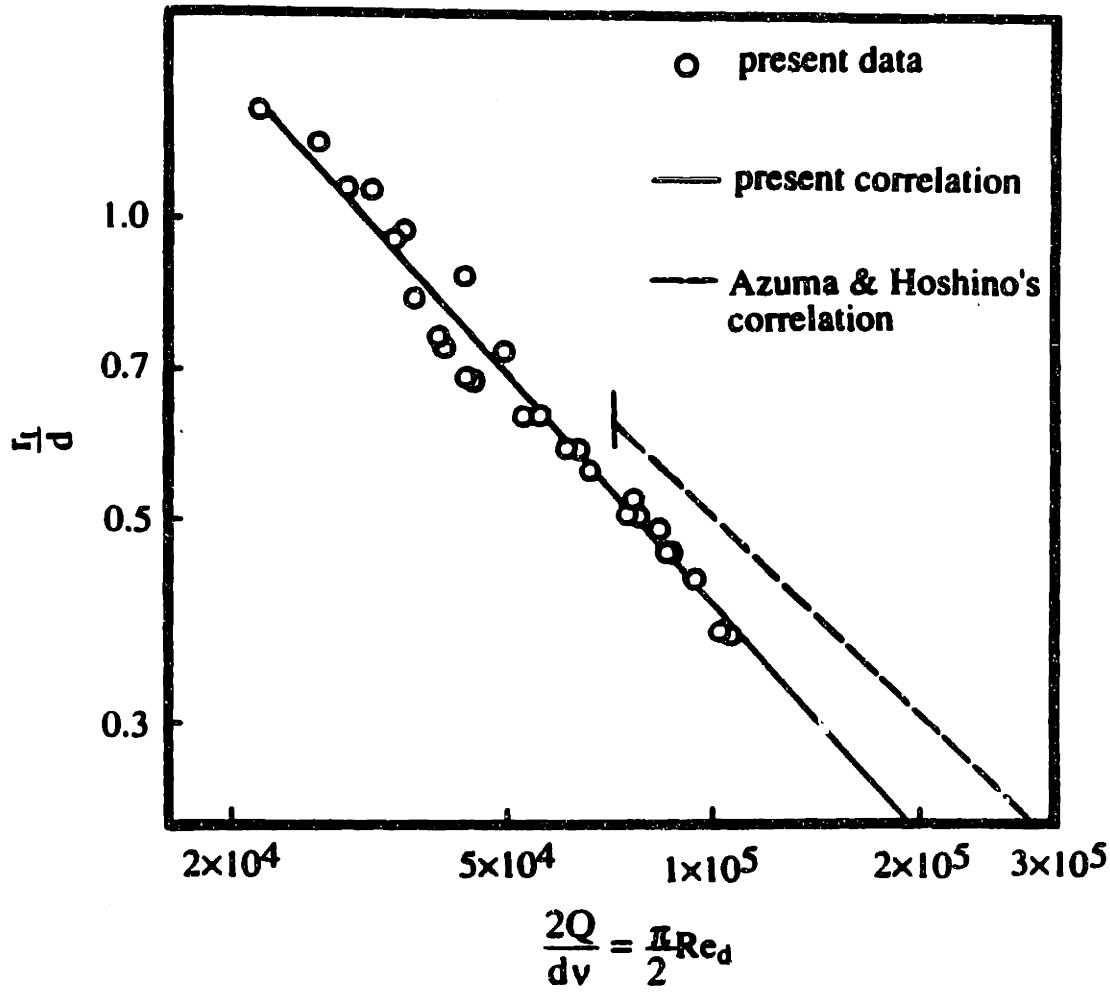

Figure 2.8: Radii for transition from laminar to turbulent flow.

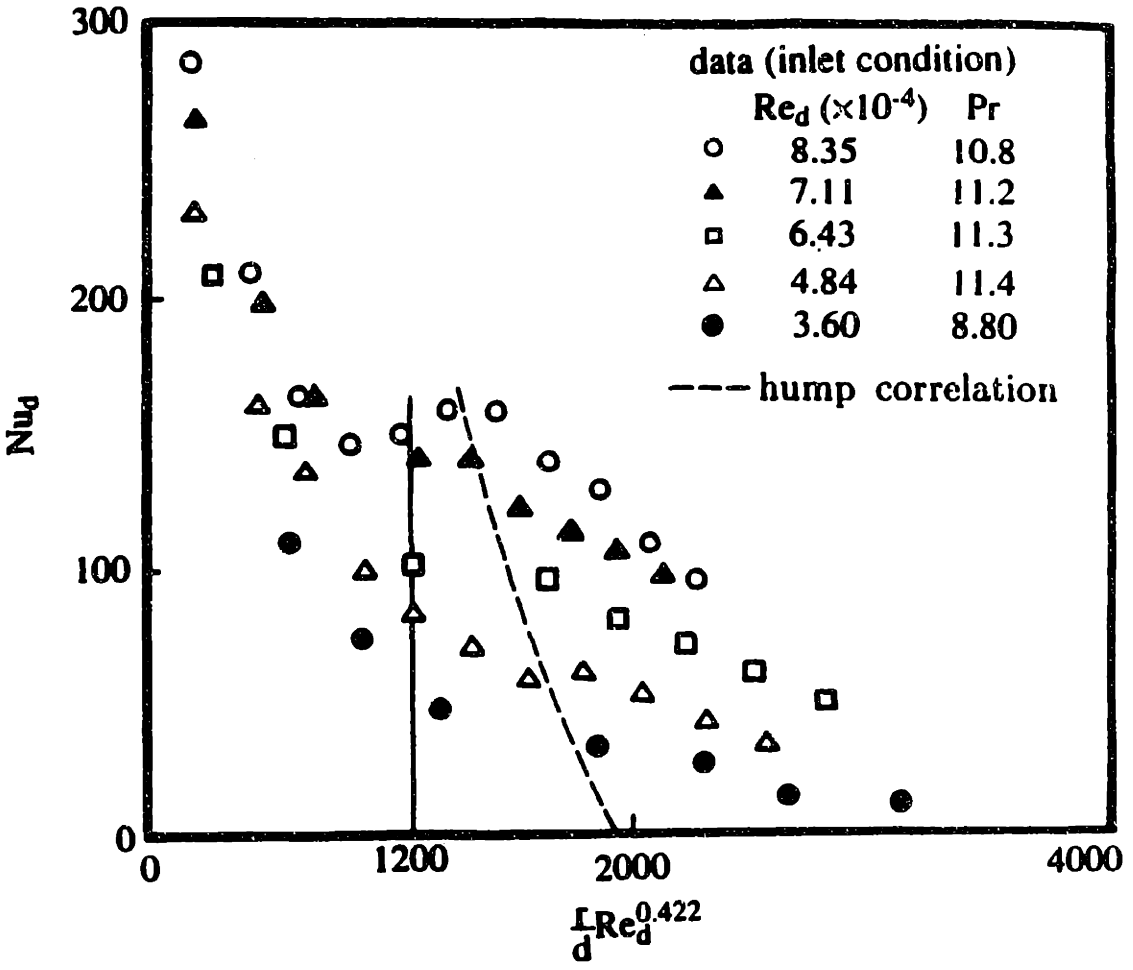

Figure 2.9: The turbulent transition as manifested in the Nusselt number.

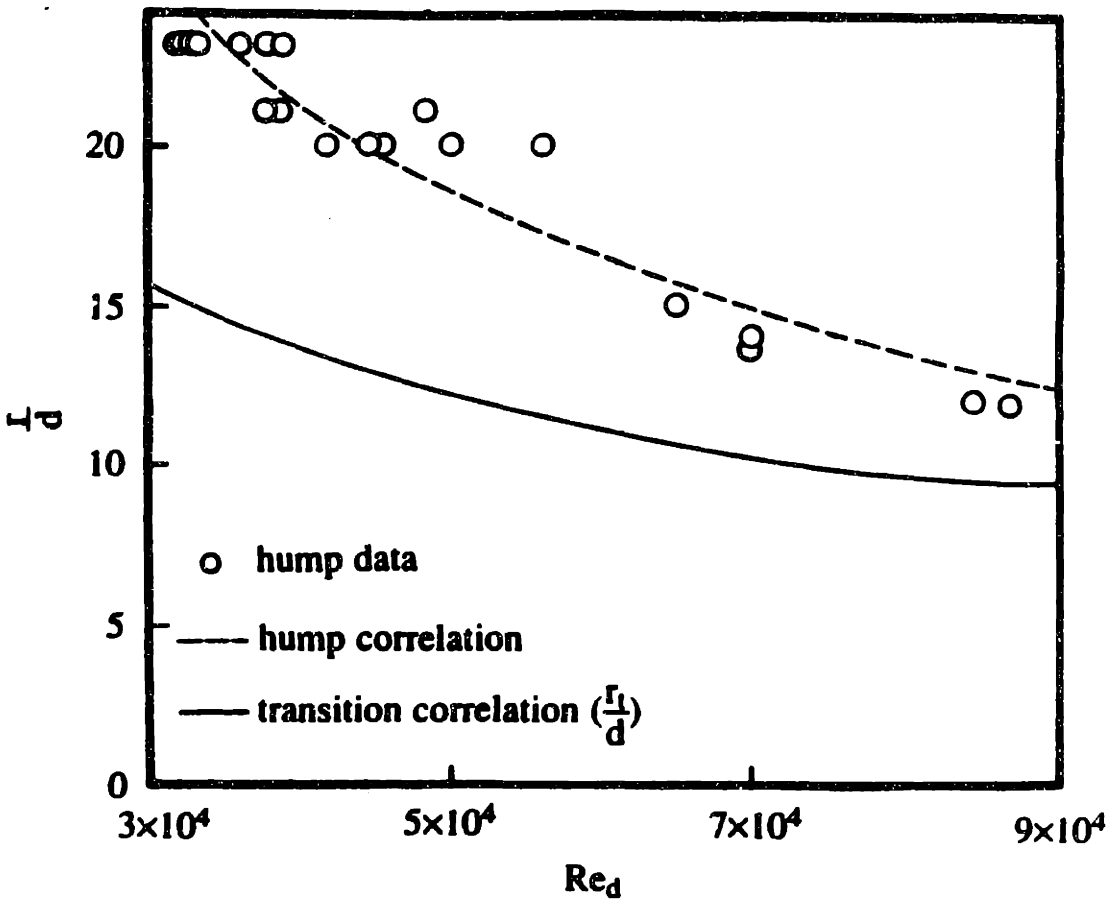

Figure 2.10: The transition and hump radii.

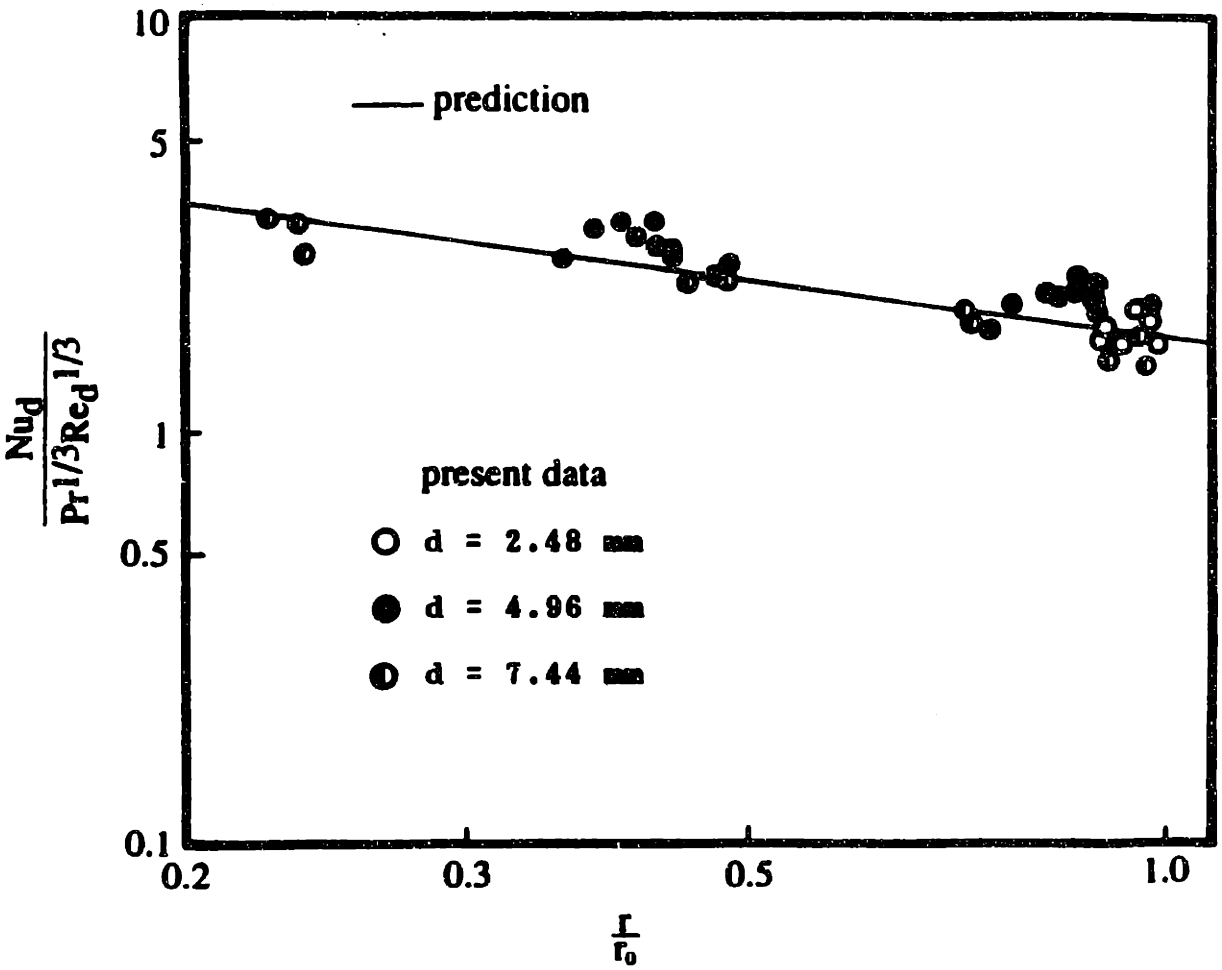

Figure 2.11: Measured and predicted Nusselt number in region 2. Data for several diameters of orifice.

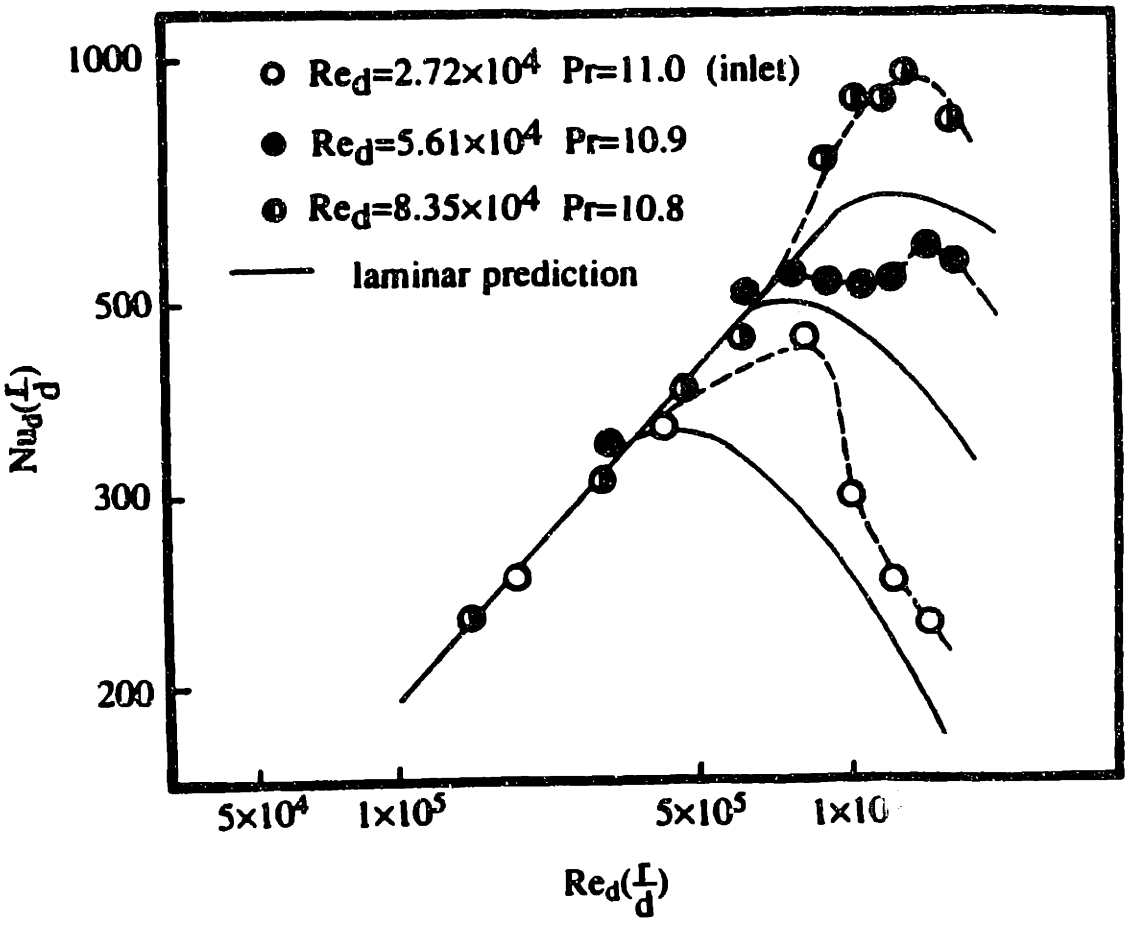

Figure 2.12: Nu_r from data and laminar theory for regions 2 and 3. (— — — : faired curves)

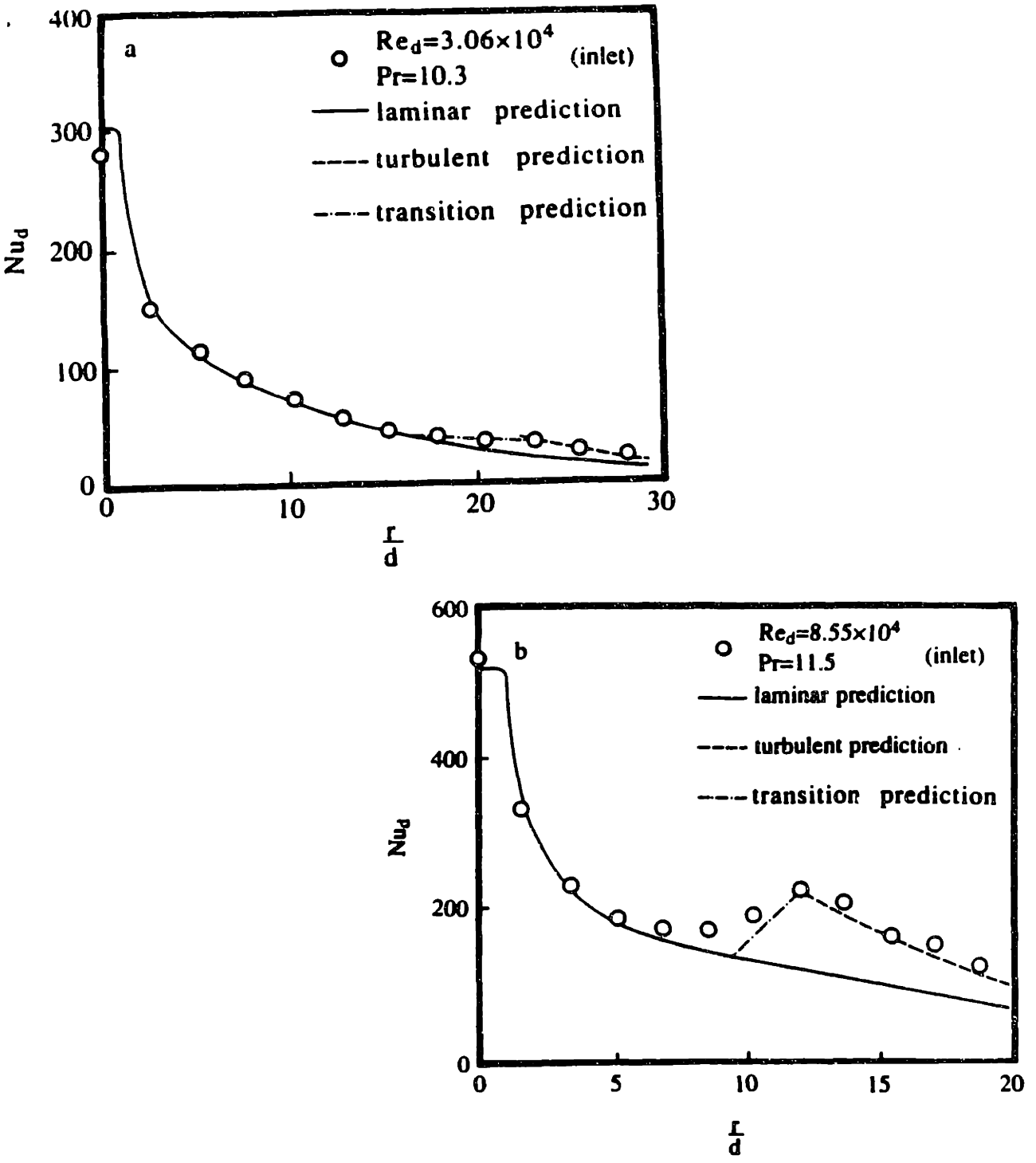

Figure 2.13: Comparison of data to the laminar and turbulent predictions (predictions follow Table 1).

Chapter 3

HEAT TRANSFER OF A TURBULENT JET

3.1 Introduction

Liquid jets are often directed onto hot surfaces to provide simple and efficient cooling. Such jets typically issue from a nozzle at the terminus of a pipe, or similar manifolding system. The corresponding piping systems have the added attraction of being inexpensive and easy to install.

In the previous chapter, the heat transfer characteristics of an unsubmerged, impinging laminar liquid jet which issued from a sharp-edged orifice were discussed. Disturbances to the experimental liquid supply were carefully damped so as to create uniform velocity-profile, laminar jets having very stable, undisturbed free surfaces. While that configuration is well-suited for examining the physical mechanisms of jet

impingement cooling, in applications such as mentioned above, the piping or manifolding systems are likely to generate turbulence in the liquid supply. The resultant liquid jets are turbulent and have heavily disturbed surfaces, which make them susceptible to the highly undesirable effect of splattering after they strike the target surface (Figure 3.1).

When a jet splatters, much of the incoming liquid can become airborne, as droplets, within a few jet diameters of the point of impact. Airborne liquid no longer contributes to the cooling of the liquid surface, and in consequence, cooling is far less efficient than it could be if splattering were suppressed. Understanding the causes and scaling of splattering is thus an essential element in jet cooling system design.

The basic physical mechanism of splattering has been described by Errico (1986). Disturbances to the surface of the incoming jet are strongly amplified as the jet spreads into a liquid film along a wall normal to the axis of the jet (Figure 3.1bc). The associated flow regimes along the surface can be characterized in an average sense as follows (Figure 3.2):

1. *stagnation zone.* A very thin wall boundary layer with a turbulent
2. *region before splattering:* Disturbances to the liquid sheet ar strongly amplified in this region. As in the stagnation zone, the wall boundary layer is affected by turbulent and capillary disturbances to the flow above it.
3. *region of splattering:* A portion of the liquid sheet breaks free as droplets, owing to the instability of the disturbed liquid sheet. The effective radial size of this zone is fairly small.
4. *region after splattering:* Having lost both mass and momentum in the splattering process, the remaining liquid sheet continues to flow outward. The liquid sheet is fully turbulent.

Errico's experiments on the splattering of impinging jets demonstrated that jet splatter is directly tied to the surface roughness or deformation of the incoming liquid jet, that jet splatter is reduced by making the jet shorter (so that disturbances to the liquid jet have less time to develop), and that jet stability is related to the specific nozzle design. Errico also found that onset of splattering in jets forced at their breakup frequency varies with Re_d, We_d, and the ratio of jet length to jet diameter.

Splattering and turbulence both produce additional mixing in the liquid sheet which will tend to enhance heat transfer relative to a laminar sheet. Conversely, the wall friction will be generally lower for laminar flow, which should result in larger velocities at a given downstream radius. The relative cooling efficiency of these cases is not obvious *a priori*, apart from the expectation that turbulence enhances heat transfer in the stagnation zone. Additionally, turbulence and splattering are closely related, with splattering both being driven by turbulence and adding fluctuating disturbances to the film, so that these effects must be accounted simultaneously in attempting to model the heat removal. Presumably, the jet Reynolds and Weber numbers will appear as controlling parameters.

Since the initial condition of the jet and the subsequent flow behavior are strongly dependent on the specific nozzle configuration, there arises the question of how best to explore the heat transfer performance of different nozzles. Most nozzle systems seek to minimize pressure drop by using a relatively large diameter liquid supply line followed by a contracting nozzle. The liquid supply may reasonably be assumed to have reached fully-developed turbulent flow, and this turbulence will be partially damped by the

nozzle. Actual nozzle conditions are thus bounded at one extreme by a stable laminar jet (as achieved by a sharp-edged orifice nozzle in previous chapter) and at the other extreme by a fully-developed turbulent jet (as achieved by a sufficiently long tube with no outlet contraction). Other types of nozzles will generally fall between these two, having a somewhat lower turbulence intensity than in fully-developed pipe flow, and their heat transfer behavior should be bounded by the laminar and fully-turbulent jets.

The mean velocity profile of the jet will also affect convective heat removal, particularly in the stagnation zone. The sharp-edged orifices used in our previous studies are known to produce a uniform velocity profile about one diameter downstream of the orifice. The turbulent pipe jets studied herein have a relatively flat velocity profile as well. A recent study of planar jets (Wolf *et al.*, 1990) concluded that velocity-profile effects on stagnation zone heat transfer were pronounced for laminar flows, but suggested that, for turbulent jets, the velocity profile was relatively unimportant in comparison to the stronger influence of turbulent mixing. In this light, we expect that velocity-profile effects are less important in what follows than are the effects of turbulence. However, measurements independently varying turbulence intensity and velocity profile are needed to fully resolve the role of mean velocity profile in turbulent jets, particularly for those jets having a large nonuniformity of mean velocity.

In this work, we investigate heat removal by fully-turbulent liquid jets both with and without splattering. Our method is to combine relatively simple models of the mechanism of liquid splattering with phase-doppler measurements of the splattered

droplets' size and velocity to create a predictive model for the mass lost to splattering and the radial location of splatter. We then use this information to model the consequences of splattering for the efficiency of convective heat removal by the jet-induced liquid sheet, and we compare the model's results to measurements of the local Nusselt number along the wall.

Our analysis employs the momentum integral procedure, reflecting our attention to the average behavior of a physical process which is far too complex for exact analytical solution. Moreover, the momentum integral procedure has been found to facilitate relatively clear and general descriptions of the varying radial characteristics of the film flow (*see* Chapter 2); alternative, numerical procedures cannot provide any useful generality for the whole range of radius, although they show some promise for the stagnation zone (*see* Chapter 5).

3.2 Experiments

Experiments were performed to measure the splattered mass and heat transfer for a fully-developed, turbulent liquid jet. The experimental jets were produced using long tubes (50 to 100 diam. long; 3.2 – 9.5 mm diam) which received liquid water from a pressurized plenum and issued into still air (Figure 3.3). The outlet of each pipe was carefully smoothed and deburred so that surface disturbances in the liquid jets were produced solely by the turbulence of the jets. The initial conditions for the jet should thus depend only on Reynolds number. Contraction of the turbulent jets causes less than a 1.5% reduction in diameter, in contrast to the large contraction for sharp-edged

orifice jets. Jet velocity was determined using a flow meter (primary calibration of the meter was performed). The jets struck a thin, uniformly electrically-heated plane target which was instrumented for local temperature measurement. The nozzle to plate separation was adjustable over the range $1.2 \leq l/d \leq 28.7$. The remainder of the experimental apparatus consists of the water jet loop, a refrigerating system, and an electrical heating system. Full details of this equipment, the heater, the instrumentation, and the error analysis are given by Chapter 2.

The distribution of the splattered droplets' velocities and diameters above the target plate were measured using a Phase Doppler Particle Analyzer (PDPA). The PDPA (Aerometrics, Inc.) is an advanced laser-Doppler velocimeter which produces concurrent measurements of an individual particle's diameter and velocity through an analysis of the measured amplitude and phase of the doppler burst. Since the splattered droplets travel at only a small angle with respect to the target surface (about 20° off horizontal), the PDPA was configured to record the radial component of velocity; this component is also that required in the momentum integral analysis below. Owing to ambiguities in the instrument's probe-area correction for the number density calculation, the measured volume flux was independently calibrated by direct measurement of the splattered mass (following Errico, 1986), as shown in Figure 3.4; the incoming-jet volume flow and the volume flow remaining in the liquid sheet after splattering were measured at radii corresponding to those used in the PDPA measurements.

The wall temperature increases with radius, and the local Nusselt number is

based on the difference between the local wall temperature and the temperature of the incoming jets. As in our previous experiments (*see* Chapter 2 and Appendix B), evaporative cooling was suppressed by limiting the maximum liquid temperature along the test heater. At the stagnation point, the temperature differences are the smallest and the uncertainty in Nusselt number is the largest when the previously mentioned heater is employed. Thus, a narrower heater strip (3.8 cm wide rather than 15.2 cm wide) was used for separate stagnation zone measurements. This enabled the use of higher heat fluxes (up to 300 kW/m^2) without concern for liquid surface temperature or burning of the test heater; the temperature differences were thus raised to accurately resolvable values for the stagnation point, providing stagnation Nusselt numbers with uncertainties of 10% or less. Downstream, the reported Nusselt numbers have uncertainties of only 5%. The estimated uncertainty for Re_d is 5% and that for r is 0.5 mm.

Both the wide and narrow heaters were made from 0.1 mm thick 304SS sheet. Corrections were applied for the conductive temperature difference across the sheet thickness, as described in Chapter 2. These corrections are quite important when Nu_d is large. Omitting them, as some authors apparently have (Faggiani and Grassi, 1990), may cause large errors.

3.3 Splattering

The vertical distribution of the radial volume flux of splattered droplets was measured for a variety of jet Reynolds numbers, Re_d, jet-to-plate separations, l/d, and radial

measuring stations, r_m/d. Representative profiles are presented in Figure 3.5(a); the droplet volume flow rate in the radial direction per unit height, Q'' (m^3/s m), is normalized with the total volume flow rate of the incoming jet, Q (m^3/s), and plotted as a function of the vertical distance from the plate surface at given radius. Decreasing the Reynolds number shifts the whole profile to the left. Decreasing the nozzle height has a similar effect, reducing the splattering at all vertical positions. When the profile is measured at larger radius, its basic shape changes; near the wall (small y) the splattered volume flux decreases with increasing radius, but farther from the wall (larger y), the flux decreases less and may even increase. The shape distortion occurs because the droplets travel at an angle relative to the plate, and at larger radius the droplets are spread over a larger area than at small radius.

In semilogarithmic coordinates (Figure 3.5b), the volume flux distribution is almost a straight line. A line fit may be applied to these curves, corresponding to an exponentially decaying vertical distribution of splattered mass, and the total volume flow rate of splattered droplets may then be obtained by integration. The total volume flow is then used to calibrate the volume flux measurements, as described above.

For the data shown in Figure 3.5b, the ratio of total splattered droplet volume flow to total incoming volume flow (which is 0.34) decreases by only about 2.6% when the measuring radius is increased from $r_m/d = 15$ to $r_m/d = 24$, holding other variables constant. This difference is within the uncertainty of the measurements, although some decrease may occur as a few large droplets fall back to the liquid sheet

under gravity. However, both these measurements and stroboscopic observations by Errico (1986) and by our group show that the actual splattering occurs within a certain radial band around the point of impact; beyond this band, splattering no longer occurs. Hence, the total splattered mass flow, as observed beyond the radius of splattering, will not depend on r/d, but only upon Reynolds number, Weber number, and l/d.

3.3.1 A Model for Splattering

The splattering of an impinging jet depends strongly upon the disturbances present on the incoming jet when it reaches the plate. These initial disturbances are sharply amplified when the fluid flows into the thin liquid film surrounding the point of impact, and their magnitude determines both whether or not the jet splatters and the magnitude of the actual splattering. The disturbances undergo substantial distortion upon entering the liquid sheet, with changes in amplitude, wavelength, and wavespeed; rigorous analysis of that development is beyond our present scope. However, we may make substantial progress by considering only the size of the disturbances which the jet delivers to the liquid sheet. Here, we present a model which relates the initial turbulence in the jet to the initial surface disturbances on the jet and their subsequent growth by capillary instability. In this way, we scale the disturbances reaching the liquid sheet which drive actual splattering.

Surface shape is related to the difference between liquid and gas phase pressure,

Δp, via the Laplace relation:

$$\Delta p = \sigma \left(\frac{1}{R_1} + \frac{1}{R_2} \right) \tag{3.1}$$

We assume that the surface disturbances at the nozzle outlet are due to primarily to turbulent pressure fluctuations within the jet, which have an rms value of

$$p' \cong \frac{1}{2} \rho (q')^2 = \frac{1}{2} \rho u_f^2 \left(\frac{q'}{u_f} \right)^2 \tag{3.2}$$

The turbulent pressure fluctuations will be distributed over a broad spectrum of wavelengths. The corresponding surface disturbances also show a range of wavelengths, some of which are more unstable than others. Rayleigh's normal mode analysis of circular jet capillary instability (Drazin and Reid, 1981) showed that a disturbance of wavelength λ evolves in time from an initial amplitude ε to an amplitude A given by

$$A = \varepsilon \exp \left(\imath [2\pi y/\lambda + m\theta] + st \right) \tag{3.3}$$

and that the disturbance of maximum growth rate has $\lambda_{max} = 4.51d$ and $m = 0$. From Equation 3.1, the associated initial pressure disturbance amplitude is (Drazin and Reid, 1981)

$$p'_{max} = -0.514 \frac{\sigma \varepsilon}{a^2} \tag{3.4}$$

and the corresponding growth rate may be shown to be

$$s_{max} = 0.3433 \sqrt{\frac{\sigma}{a^3 \rho}} \tag{3.5}$$

Thus, if we equate the rms turbulent pressure disturbance, p', to rms capillary pressure

disturbance, $|p'_{max}|/\sqrt{2}$, we obtain an rms initial surface displacement

$$\frac{\varepsilon_{rms}}{a} \cong 0.781\sqrt{2}\left(\frac{\rho u_f^2 a}{\sigma}\right)\left(\frac{q'}{u_f}\right)^2 \tag{3.6}$$

The spectral distributions of the turbulent pressure fluctuations and the surface disturbances have been lumped into a single mean disturbance amplitude, so no direct significance should be attached to coefficient $0.781\sqrt{2}$. However, the physical mechanism relating intensity of pressure fluctuations to the surface displacement should scale as shown irrespective of this approximation.

The liquid travels from the nozzle to the plate in a time $t = l/u_f$, during which the surface disturbance grows from the initial ε_{rms} to

$$A_{rms} = \varepsilon_{rms}\exp(s_{max}t) = \varepsilon\exp\left(0.3433\frac{l}{u_f}\sqrt{\frac{\sigma}{\rho a^3}}\right) \tag{3.7}$$

Nondimensionalizing yields

$$\frac{A_{rms}}{d} = C\,\mathrm{We}_d\exp\left(\frac{0.9710}{\sqrt{\mathrm{We_d}}}\frac{l}{d}\right) \tag{3.8}$$

where the jet Weber number is

$$\mathrm{We}_d = \frac{\rho u_f^2 d}{\sigma} \tag{3.9}$$

and

$$C = 0.195\sqrt{2}\left(\frac{q'}{u_f}\right)^2 \tag{3.10}$$

Hence, the disturbance reaching the point of impact, which drives subsequent splattering, should scale with the dimensionless group

$$\omega = \mathrm{We}_d\exp\left(\frac{0.971}{\sqrt{\mathrm{We_d}}}\frac{l}{d}\right) \tag{3.11}$$

and the fraction of the total incoming liquid flow which is splattered, ξ, is a function of ω which must be found experimentally.

The total turbulence intensity, q'/u_f, has an average value of approximately 0.080 in turbulent pipe flow (at $\mathrm{Re}_d = 5 \times 10^4$) and varies only weakly with Reynolds number (roughly as $\mathrm{Re}_d^{1/8}$; Laufer, 1954; Tennekes and Lumley, 1972). The Reynolds number range of the present splattering experiments (19,000 to 69,000) is narrow enough that a constant value of $C \approx 0.0018$ is an adequate initial condition for our jets. The turbulence decays under viscous influence as the jet travels to the plate; a homogeneous-turbulence decay estimate predicts a 50% drop in turbulence intensity if the jet is 20 diameters above the target. However, the capillary disturbances which turbulence induces at the jet outlet have grown exponentially during the journey to the target.

Figure 3.6 shows the ω at which we observed onset of splattering as a function of Reynolds number.* For all Reynolds numbers, the data show ω to be about 2120 at the onset of splattering. Thus, the jet disturbance found from the above analysis does control the stability of the liquid sheet, and ω is a good measure of that stability. From the definition of ω, this shows that splattering occurs whenever $\mathrm{We}_d > 2120$, irrespective of l/d, although splattering may occur at lower values of We_d when l/d is nonzero. This graph ends at Re_d of 30,000 because our higher Re_d jets all exceeded $\mathrm{We}_d = 2120$.

Figure 3.7 shows the total fraction of liquid splattered from the sheet as a function

*Our observations were both visual and tactile; "onset" is the point at which we observed *any* droplets to leave the liquid sheet.

of ω. The ratio of the splattered flow to the total flow increases monotonically with ω. The amount of splattering is very small in the range $2120 \leq \omega \leq 3000$, with $\xi \leq 2.5\%$; in engineering applications, splattering may be neglected in this range. For $2200 \leq \omega \leq 8500$, splattering increases rapidly; the splattering ratio is well represented by the curve fit

$$\xi = -0.0935 + 3.41 \times 10^{-5}\omega + 2.25 \times 10^{-9}\omega^2 \tag{3.12}$$

No data are available beyond $\omega = 8500$, but we can assume that ξ will flatten, since it is necessarily less than one. For these data, the uncertainty is 8% for ω and 1% for ξ.

The onset of splattering is fairly flat in the sense of ξ versus ω. Hence, the reported "onset" may vary among observers, depending on how much mass must be splattered before splattering is noticed. Little outside data is currently available for comparision to the present criterion. Womac *et al.* (1990) cite three observations of onset for tube nozzles 20 – 40 diameters length, which may be nondimensionalized using present terminology. For water, onset was noted for a 0.978 mm nozzle at $\omega \approx 2600 - 3800$ with $\mathrm{Re}_d = 13900$; for FC-77, onset was noted for a 0.978 mm nozzle at $\omega \approx 2900 - 4200$ with $\mathrm{Re}_d = 5800$ and for a 0.4 mm at $\omega \approx 6600 - 8300$ with $\mathrm{Re}_d = 5900$. The first pair of observations are consistent with the present results, given the smallness of ξ at those values of ω and the low [marginally turbulent] Reynolds numbers involved. The last observation is well above present results; however, the volume of splattered liquid at observed onset would have been roughly the same as for the larger nozzles, making an issue of the operating definition of "onset." From a

practical viewpoint, the curve $\xi(\omega)$ itself is of greatest importance, and onset may be best defined in terms of a threshold value of ξ below which splattering can be ignored.

Bhunia and Lienhard (1992) present more detailed results for the onset splattering and an improved version of Equation 3.12.

3.3.2 Droplet Departure Radius

The distribution of droplet diameter, D, typically ranges from a few microns to almost a millimeter. However, most droplets passing a particular point have essentially the same velocity irrespective of their size. Very small droplets (less than about 20 μm) suffer significant viscous drag and move slower, but these droplets contribute little to the mass-average velocity. The mean droplet velocity, v, near the plate is fairly represented by a linearly decreasing velocity profile (Figure 3.8a). The mean droplet diameter also decreases with increasing distance from the plate (Figure 3.8b).

We may infer the radial position at which the droplets separated from the liquid surface, r_s, by assuming that the large droplets near the liquid surface maintain the radial velocity they had at the point of departure from the liquid sheet (neglecting air drag) and that the departure velocity is equal to the mean surface velocity; the droplets' velocity then determines the radial position where the liquid surface had that velocity. This estimate sets the position of breakaway at about $r_s = 5.7d$. Since the wavelength of maximum capillary instability for a circular jet is $\lambda_{max}/d = 4.51$, the estimated breakaway position is slightly more than one λ_{max}. In his experiments, Errico (1986) observed that the radius where the disturbances to the liquid sheet

reach maximum height (droplet departure point) was between 0.73 cm and 1.46 cm, which appeared to be about 4 jet diameters.[†] The heat transfer data also verify this estimate indirectly, as will be discussed later. The present data do not clearly show a dependence of the breakaway radius upon Re_d, d, or ω, but more detailed measurements are unquestionably required to resolve such influences and to set a more precise value for r_s. For modelling purposes, we take $r_s \approx \lambda_{max}$ in what follows.

A few very fine droplets were observed around the incoming jet when the Reynolds number was large. These droplets appear to be generated at the jet nozzle, and are formed by a different mechanism than considered here. They have a very small contribution to the total liquid volume flow. In addition, aerodynamic drag on the jet will become increasingly important for Reynolds numbers above 50,000 and will alter the capillary growth as modelled here.

3.4 Mean Flow Field and Heat Transfer

For turbulent jets, and especially for those which splatter, the flow field of the liquid sheet is highly unsteady and irregular. However, for the purpose of modelling the jet heat convection, we may focus on the mean flow field and consider separately the region before splattering and the region after splattering.

Visual observation shows that the capillary disturbances create very large, highly-unsteady disturbances to the liquid film. Stroboscopic observations show that the

[†]Errico's water jet diameter was not specified, since he observed the splattering radius to be independent of jet size. From a Kelvin-Helmholtz instability analysis of the liquid sheet, Errico estimated that this radial position was one to two disturbance wavelengths.

disturbances grow larger up to the point of droplet separation where tall, sharp crests are observed; these crests break into a spray of droplets (Errico presents excellent photographs of the breakup). The capillary disturbances greatly exceed in magnitude the freestream turbulence in the incoming jet and will promote the rapid transition to a fully-turbulent film downstream.

In the region upstream of droplet breakaway, we may suppose the flow to be composed of a thin, *laminar* wall boundary layer and a turbulent, fluctuating freestream above it. We may further suppose that the capillary disturbances to the liquid surface have essentially the same effect on the boundary layer as does the freestream turbulence. This region extends to only about 5 jet diameters from the point of impact.

To gain some idea of freestream turbulence effects on wall boundary layer heat transfer, we can refer to previous studies of the problem. A general survey of freestream turbulence effects was given by Kestin (1966); the stagnation zone of a *submerged* jet was investigated numerically by Traci and Wilcox (1975). Local measurements in the laminar stagnation zone of a cylinder show an unexpectedly large effect of freestream turbulence, reaching an enhancement of more than 80% in $\mathrm{Nu}_d/\mathrm{Re}_d^{1/2}$ at the stagnation point for a change of turbulence intensity from 0% to only 2.7%. Laminar boundary layer heat transfer can be substantially increased if the pressure gradient is nonzero, but for zero pressure gradient (as in the present flow, *away* from the stagnation point), freestream turbulence does not affect the local heat transfer coefficient up to a turbulence intensity of at least 3.82%. The turbulence in-

tensities of these past experiments are similar to those estimated for the present case, in the absence of capillary contributions. The magnitude of the present capillary disturbances are not known precisely; however, we compare the present measurements to the undisturbed, laminar predictions (*see* Chapter 2) below, so as to gauge the magnitude of the combined turbulent and capillary augmentation.

The splattering region itself is relatively small and may be modelled as if splattering occurs at a single radius. The large disturbances associated with droplet departure may reasonably be presumed to induce fully-turbulent flow in the liquid sheet after splattering. We may estimate the thickness and velocity variation of the turbulent residual sheet by accounting for the loss of mass and momentum associated with splattering. Having the velocity and thickness of the turbulent liquid sheet, we may then use the thermal law of the wall to estimate the local Nusselt number.

We emphasize that the model which follows is directed at the average behavior of the sheet, rather than a precise prediction of velocity profile and film thickness.

3.4.1 Mass and Momentum Conservation

At the radial location just before splattering (here taken as $r_s/d = 4.51$), the ratio of mass in the boundary layer to total incoming mass in the jet is

$$x = \frac{2\pi r \int_0^\delta u dy}{\frac{\pi}{4} d^2 u_f} = 13.34 \left(\frac{r_s}{d}\right)^{3/2} \mathrm{Re}_d^{-1/2} = 128.3\, \mathrm{Re}_d^{-1/2} \tag{3.13}$$

where, from Sharan (1984),

$$u(y) = u_f \left[\frac{3}{2}\frac{y}{\delta} - \frac{1}{2}\left(\frac{y}{\delta}\right)^3\right] \tag{3.14}$$

and

$$\frac{\delta}{d} = 2.679 \left(\frac{r}{d\,\mathrm{Re}_d} \right)^{1/2} \tag{3.15}$$

These expressions assume a laminar wall boundary layer beneath a turbulent freestream with mean velocity u_f. Stevens and Webb (1991) measured radial surface speeds for a nonsplattering turbulent jet and found surface speeds near u_f (as would be expected from streamline momentum conservation); speeds up to 20% larger were measured for small diameter, low Reynolds number jets. As discussed below, this acceleration may be associated with surface tension effects on those small, slow jets.

If $(1 - \xi) \geq x$, the splattered liquid does not include fluid in the boundary layer. In this case, the liquid sheet remaining after splattering has an effective thickness, h_c (Figure 3.9), of

$$h_c = h_s - \frac{\xi d^2}{8 r_s} \tag{3.16}$$

where h_s is the mean film thickness prior to splattering and the second term is the loss of (inviscid) fluid due to splattering. The remaining mass flow, $(1 - \xi)\frac{\pi}{4} d^2 u_f$, carries momentum

$$2\pi r_s \rho \left[\int_0^{\delta} u^2 dy + \int_{\delta}^{h_c} u_f^2 dy \right] = 2\pi r_s \rho u_f^2 \Phi d \tag{3.17}$$

where

$$\Phi = 0.125(1 - \xi)\frac{d}{r_s} - 0.373 \left(\frac{r_s}{d Re_d} \right)^{1/2} \tag{3.18}$$

These results do not account for the transition to turbulent flow after splattering, which will change the velocity profile and alter the film thickness from h_c to another value, h^*.

Azuma and Hoshino (1984) measured the velocity distributions in the sheet for both laminar and turbulent flow; they showed that a $1/7th$ power law is a good approximation in the turbulent sheet:

$$u(y) = u_{max}\left(\frac{y}{h}\right)^{1/7} \tag{3.19}$$

for h the thickness of the turbulent sheet and u_{max} the free surface speed. We assume the adjustment from the laminar boundary layer to turbulent sheet velocity distributions occurs within a small radial region at the zone of splattering. In terms of the turbulent thickness just after splattering, h^*, the mass flow in the sheet after splattering is

$$2\pi r_s \rho \int_0^{h^*} u dy = \frac{7}{4}\pi r_s \rho h^* u^*_{max} \tag{3.20}$$

and the momentum flow in the sheet after splattering is

$$2\pi r \rho \int_0^{h^*} u^{*2} dy = \frac{14}{9}\pi r_s \rho h^* u^{*2}_{max} \tag{3.21}$$

for u^* the mean velocity distribution in the sheet just after splattering and u^*_{max} its maximum. Then, with equations (3.16 – 3.18), mass and momentum balances on the region of adjustment (at radius r_s) give

$$\frac{h^*}{d} = \frac{(1-\xi)^2 d^2}{63 r_s^2 \Phi} \tag{3.22}$$

At larger radii, solution of the momentum integral equation gives the variation of turbulent liquid sheet thickness as

$$\frac{h}{d} = \frac{0.02091}{[(1-\xi)\mathrm{Re}_d]^{1/4}}\left(\frac{r}{d}\right)^{5/4} + C_s\frac{d}{r} \tag{3.23}$$

where

$$C_s = \frac{h^* r_s}{d^2} - \frac{0.02091}{[(1-\xi)\mathrm{Re}_d]^{1/4}} \left(\frac{r_s}{d}\right)^{9/4} \tag{3.24}$$

Note that the above mass and momentum balances across the splattering region provided the initial conditions used in solving the momentum integral equation for $r > r_s$.

For the case $(1-\xi) < x$, the mass in the sheet after splattering is

$$(1-\xi)\frac{\pi}{4} d^2 u_f = 2\pi r \int_0^{h_c} \left(\frac{3}{2}\left(\frac{y}{\delta}\right) - \frac{1}{2}\left(\frac{y}{\delta}\right)^3\right) dy \tag{3.25}$$

so that

$$\frac{h_c}{\delta} \equiv \Theta = \sqrt{3 - 3\sqrt{1 - \frac{(1-\xi)d^2}{9 r_s \delta}}} \tag{3.26}$$

The momentum remaining within the liquid sheet is

$$2\pi r_s \rho \int_0^{h_c} u^2 dy = 2\pi r_s \rho u_f^2 \delta \left(\frac{3}{4}\Theta^3 - \frac{3}{10}\Theta^5 + \frac{1}{28}\Theta^7\right) \tag{3.27}$$

We obtain the same results for h^* and h, equations (3.22 and 3.23), except that Φ is not given as equation (3.18), but is instead

$$\Phi = \left(\frac{3}{4}\Theta^3 - \frac{3}{10}\Theta^5 + \frac{1}{28}\Theta^7\right)\frac{\delta}{d} \tag{3.28}$$

3.4.2 Heat Transfer

We may now apply the thermal law-of-the-wall to calculate the heat transfer in the film after splattering, following Chapter 2. According to the law of the wall

$$\mathrm{St} = \frac{q_w}{\rho c_p u_{max}(T_w - T_{sf})} = \frac{C_f/2}{1.07 + 12.7(\mathrm{Pr}^{2/3} - 1)\sqrt{C_f/2}} \tag{3.29}$$

The friction coefficient in the liquid sheet, from the Blasius law, is

$$C_f = 0.045 \left(\frac{\nu}{h u_{max}} \right)^{1/4} \tag{3.30}$$

and for a turbulent sheet,

$$u_{max} h = \frac{1}{7} \frac{u_f d^2 (1 - \xi)}{r} \tag{3.31}$$

If we define the local Nusselt number as

$$\mathrm{Nu}_d = \frac{q_w d}{k(T_w - T_f)} \tag{3.32}$$

then, letting $T_{sf} = T_f$ at $r = r_s$ and taking the free surface to essentially adiabatic (*see* Appendix II), a calculation yields

$$\mathrm{Nu}_d = \frac{8 \mathrm{Re}_d \, \mathrm{Pr} \, \mathrm{St}}{49(hr/d^2) + 28 (r/d)^2 \, \mathrm{St}} \tag{3.33}$$

This expression for Nu_d may be evaluated in conjunction with equations (3.23), (3.29), (3.30), (3.31), and (3.12).

Figure 3.10 shows the Nusselt number predicted above. The Nusselt number from the laminar prediction is also shown. As shown below (Figures 3.12ab), the turbulent prediction agrees reasonably well with our experimental results.

Splattering has a strong effect on the heat transfer, especially immediately after the breakaway radius. Increasing the amount of mass splattered (raising ξ) deteriorates the heat transfer. Splattering thins the film, and the resultant, increased skin friction creates a rapid decay in the Nusselt number with radius. Far downstream, the heat transfer is substantially worse than for the laminar case. Similarly, as more mass is splattered (ξ increasing), the remaining film has less momentum, and slows

more quickly. At radii close to the radius of splattering, however, the heat transfer is larger than for laminar flow; this results from the assumption that turbulent transition accompanies splattering. This enhancement is stronger when less mass is splattered, leaving more momentum in the film.

For the case without splattering, the prediction and data still show an enhancement from capillary disturbances which is caused by the turbulent transition. For $\omega < 5000$, the prediction overestimates the Nusselt number relative to measurements immediately after the 'splattering' radius (19% higher for $\omega \approx 2400$), but farther downstream the disagreement disappears (after about $5d$ for $\omega \approx 2400$). The overprediction may occur because turbulent transition is not completed at the splattering radius; Chapter 2 showed that turbulent transition can occur over a significant radial band. However, these estimates are still much closer to the data than is the laminar prediction; even in the absence of actual splattering, the liquid sheet is still highly disturbed by the capillary fluctuations.

Stevens and Webb (1989) and Jiji and Dagan (1988) present results for the turbulent stagnation zone of an unsubmerged jet. The parameter ω is generally small for both studies, given their low ranges of either Reynolds number or l/d; neither study appears to have used splattering jets. Jiji and Dagan's jets were confined to low Re_d and were produced by very short tubes, some six diameters in length. The turbulence intensity in their jets should thus be lower than for the fully-developed turbulence of the present, long tubes, leading to a somewhat lower stagnation point Nusselt number. Their results are shown for comparison in Chapter 5 (Figure 5.9a); their

data are in fact somewhat below the present data. Stevens and Webb's prediction is considered below.

For liquid jet impingement, the pressure gradient in the region between the stagnation zone and the splattering radius is negligible, and, as noted above, previous studies (Kestin, 1956) suggest that no turbulent augmentation of the boundary layer heat transfer should occur. However, the presence of strong capillary disturbances before the radius of droplet separation provides an alternative mechanism for heat transfer enhancement. To show the effect of capillary disturbances, the Nusselt number between stagnation and splattering was averaged, and the ratio between this average Nusselt number and the averaged laminar prediction (*see* Appendix II) was calculated. Figure 3.11 shows this ratio as a function of ω. The enhancement by capillary disturbances is apparent, in contrast to the stagnation zone heat transfer, and enhancement appears to be independent of Reynolds number. Capillary augmentation reaches a factor of three at $\omega = 9000$.

We may predict the Nusselt number over the entire range of radius by using Equation 3.33 for the region after splattering ($r/d > 5.7$), using Equation 5.41 for the stagnation zone ($r/d < 0.787$), and applying the augmentation factor (Figures 3.11) to the laminar prediction between the stagnation zone and the splattering radius. This composite prediction is compared to two sets of data in Figure 3.12ab, and the agreement is generally good. Many other cases are shown in Gabour (1991). In Figure 3.12a, in the region just after splattering, the data show a lower value than the prediction. The reason, as mentioned above, that for this case ω is about

4003 and the turbulent transition does not complete in the splattering region; this disagreement disappears downstream as the transition is completed. In the figure, the correlation of Stevens and Webb (1989) underestimates the Nusselt number for $r/d > 3$, consistent with its expected range of validity. Our data are somewhat higher than that correlation at small r. Figure 3.12b shows similar results at a larger ω.

3.5 Other Nozzles

Other nozzle configurations may have different outlet turbulence intensities. A tentative suggestion for adapting the present results to such nozzles is to rescale the present values of ω to values appropriate to such nozzles. Since the initial disturbance to the sheet is proportional to $C\omega$, the procedure is to determine the values of C and ω for the new nozzle and then find an effective value of ω as:

$$\omega_{eff} = \frac{(C\omega)_{new}}{C_{present}} \tag{3.34}$$

The value ω_{eff} may be used in calculations based on the present results.

Additional considerations for other nozzles include variations in the coefficient of contraction and nonuniform velocity profiles. While velocity-profile influence on heat transfer has been clearly established for laminar jets, Wolf *et al.* (1990) suggested that for planar, fully-developed turbulent jets, the velocity profile itself has far less effect on turbulent heat transfer than does turbulence. However, measurements which independently vary turbulence intensity and mean velocity profile are needed in order to quantify and settle this issue.

Likewise, the precise effect of a nonuniform velocity distribution on the evolution of surface disturbances has yet to be clearly identified, although the present results work well for the levels of nonuniformity found in turbulent pipe jets. Until further data are obtained, a tentative recommendation is to ignore velocity-profile effects on splattering, unless the nozzle produces a mean velocity profile markedly different than for normal pipe flow.

Nonunity contraction coefficients should be taken into account when calculating jet velocity and diameter, although they seem unlikely to have a strong influence on capillary or turbulent distrurbances such as are considered here. For low Reynolds number jets of small diameter, surface tension (and grvitational acceleration) can alter the flow field of the jet near the plate. Chapter 5 will show some evidence of such effects in the stagnation zone of laminar jets.

3.6 Conclusions

Splattering and heat transfer have been investigated for unsubmerged, circular, fully-turbulent impinging liquid jets. Predictive results have been developed for the local Nusselt number along a uniform heat flux surface and for the onset of splattering and the total mass splattered.

- The occurrence of splattering is well-characterized by the group ω (Eqn. 3.11) when: (a) the initial disturbances to the jet are produced by turbulence in the liquid exiting the nozzle; and (b) the jet Reynolds number is low enough

that capillary instability guides the growth of these disturbances. The present results validate ω for $19,000 < \mathrm{Re}_d < 69,000$; breakdown of the model is likely at higher Reynolds numbers due to aerodynamic drag. Differences are also expected when the turbulence is less than fully-developed, as at lower Reynolds numbers. The data cover jet-to-target separations of $1.2 < l/d < 28.7$, and $1000 < \mathrm{We}_d < 5000$; the present model is likely to fail if the jet is long enough to undergo breakup prior to impact.

- Splattering occurs within a narrow radial band, rather than being distributing at all radii in the liquid sheet. The breakup radius, r_s, is about one λ_{max} (roughly $4.51d$), although further study of the scaling of both r_s and splattered droplet profiles are needed. Splattering appears to be an inviscid phenomenon.

- Jets begin to splatter when $\omega > 2120$ (or for $\mathrm{We}_d > 2120$ for any l/d). The fraction of incoming mass splattered, ξ, is given by Eqn. 3.12 for $\omega < 8500$. These results apply for $1.2 < l/d < 28.7$ and $1000 < \mathrm{We}_d < 5000$.

- Local Nusselt number depends on Re_d, r/d, and ω for turbulent, splattering jets. The present results facilitate prediction of local wall temperature from the stagnation zone to radii well past the splattering radius.

- After droplet breakaway, heat transfer is further enhanced by complete turbulent transition of the viscous film. However, heat transfer drops quickly thereafter as a result of the higher skin friction in the film. Nusselt number may be estimated with Eqn. 3.33 for $r > r_s$ and is shown in Figures 3.10 and 3.12.

References

Azuma, T. and Hoshino, T, 1984, "The Radial Flow of Thin Liquid Film, Part 3: Velocity Profile," *Trans. Japan Soc. Mech. Engrs*, 50-1126.

Bhunia, S.K. and Lienhard V., J.H., 1992, "Splattering of Turbulent Liquid Jets Impinging on Solid Targets: Parametric Studies," *28th AIChE/ASME Nat. Heat Transfer Conf.*, San Diego, to appear.

Drazin, P.G. and Reid, W.H., 1981, *Hydrodynamic Stability*, Cambridge University Press.

Errico, M., 1986, *A Study of the interaction of liquid jets with solid surfaces*, Ph.D Thesis, University of California, San Diego.

Faggiani, S, and Grassi, W., 1990, "Round Liquid Jet Impingement Heat Transfer: Local Nusselt Numbers in the Region with Nonzero Pressure Gradient," *Proc. Ninth Intl. Heat Transfer Conf.*, Jerusalem, Vol. 4, pp.197-202.

Gabour, L.A., 1991, "Heat Transfer to Turbulent and Splattering Impinging Liquid Jets," S.B. Thesis in Mechanical Engineering, MIT.

Jiji, L.M. & Dagan, Z., 1988. "Experimental Investigation of Single-Phase Multijet Impingement Cooling of an Array of Microelectronic Heat Sources," *Cooling Technology for Electronic Equipment*, Hemisphere, New York.

Kestin, J., 1966, "The effect of free-stream turbulence on heat transfer rates," *Adv. Heat Transfer*, Vol.3, 1-32.

Laufer, J., 1954, "The Structure of Turbulence in Fully Developed Pipe Flow," NACA Tech. Report No.1174.

Lombara, J. S., 1990, "An experimental investigation of liquid jet impingement heat transfer theories", S.B. Thesis in Mechanical Engineering, MIT.

Sharan, A., 1984,"Jet-disc boiling: burnout predictions and application to solar receivers," Master's thesis, University of Houston.

Stevens, J. and Webb, B. W., 1989, "Local Heat Transfer Coefficients under an Axisymmetric, Single-phase Liquid Jet", *Heat Transfer in Electronics - 1989*, ASME HTD, Vol.111, pp.113-119.

Stevens, J. and Webb, B. W., 1991, "Measurements of the free surface flow structure under an impinging, free liquid jet," presented at the 3rd ASME/JSME Thermal Engineering Joint Conference, Reno, Nevada.

Tennekes, H. & Lumley, J.L., 1972 *A First Course in Turbulence*, MIT Press.

Traci, R.M. and Wilcox, D.C., 1975, "Freestream turbulence effects on stagnation point heat transfer," *AIAA J.*, Vol.13, 890-896.

Wolf, D.H., Viskanta, R., and Incropera, F.P., 1990, "Local Convective Heat Transfer from a Heated Surface to a Planar Jet of Water with a Nonuniform Velocity Profile," *J. Heat Transfer*, Vol.112, pp.899-905.

Womac, D.J., Aharoni, G., Ramadhyani, S., and Incropera, F.P., 1990, "Single Phase Liquid Jet Impingement Cooling of Small Heat Sources," *Proc. Ninth Intl. Heat Transfer Conf.*, Jerusalem, Vol. 4, pp.149-154.

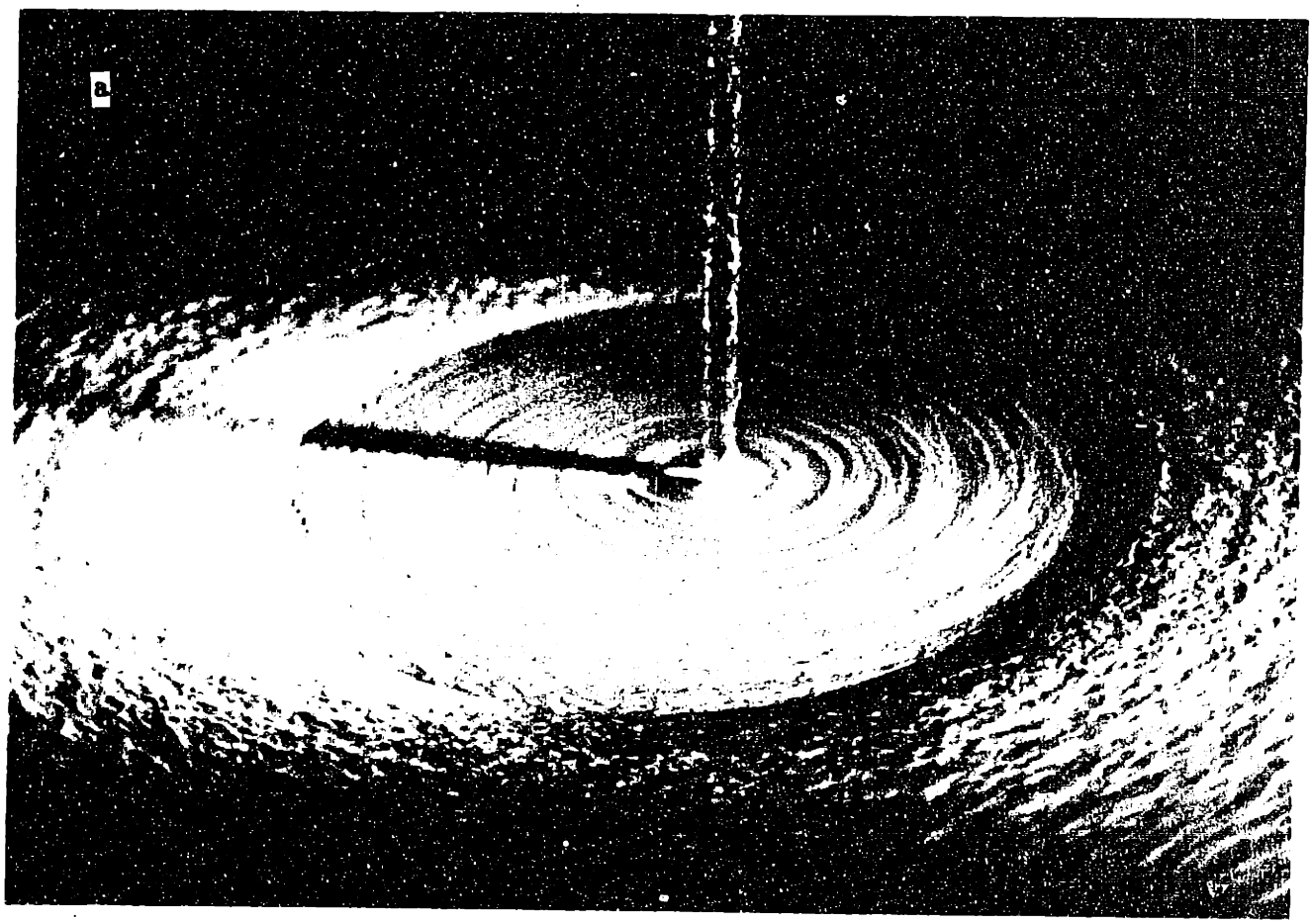

Figure 3.1: (a) Nonsplattering turbulent jet jump at $\mathrm{Re}_d = 14,500$, $\omega = 2080$, $\xi = 0$ (maximum depth of 3.2mm beyond hydraulic jump); (b) Splattering turbulent jet at $\mathrm{Re}_d = 28,400$, $\omega = 4550$, $\xi = 0.108$ (no jump); (c) Splattering turbulent jet at $\mathrm{Re}_d = 48,300$, $\omega = 8560$, $\xi = 0.311$ (no jump)

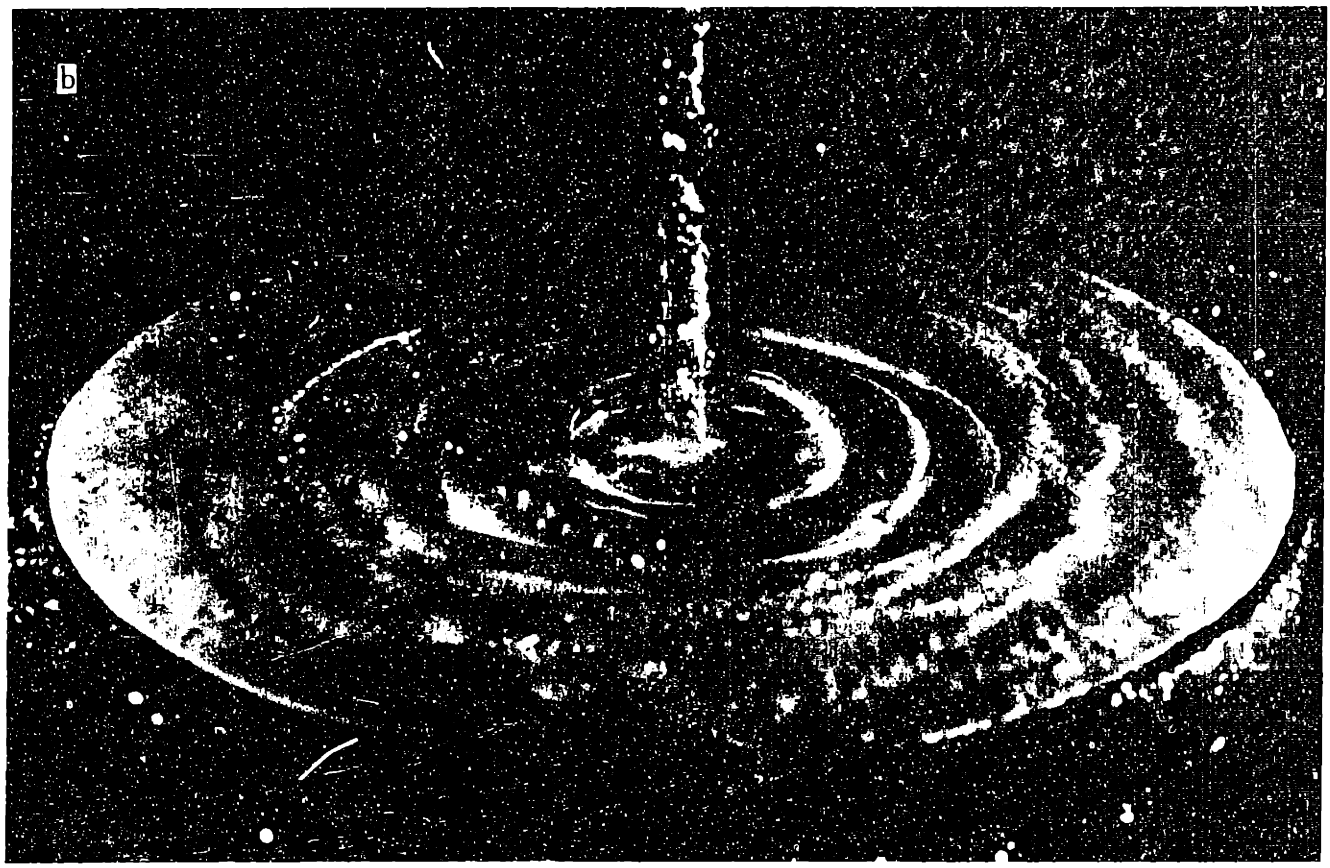
b

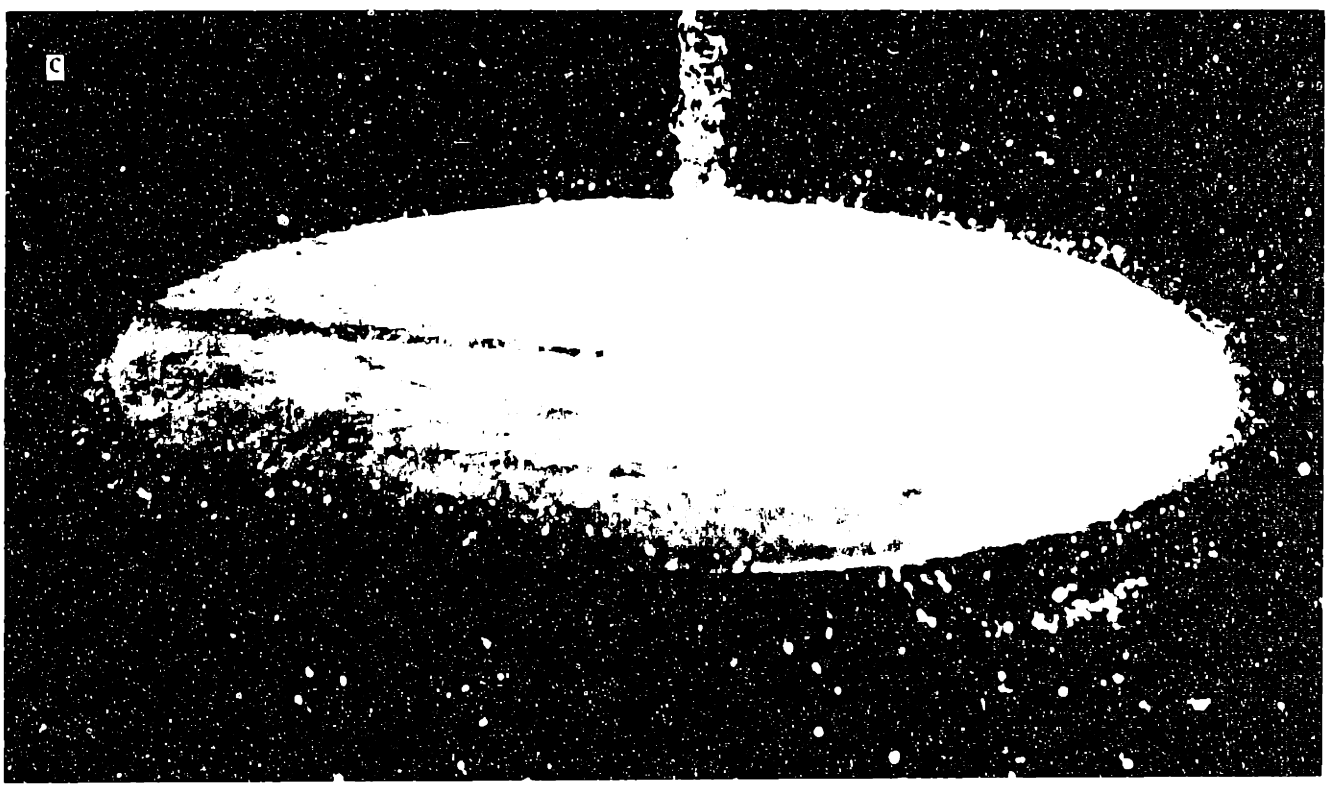
c

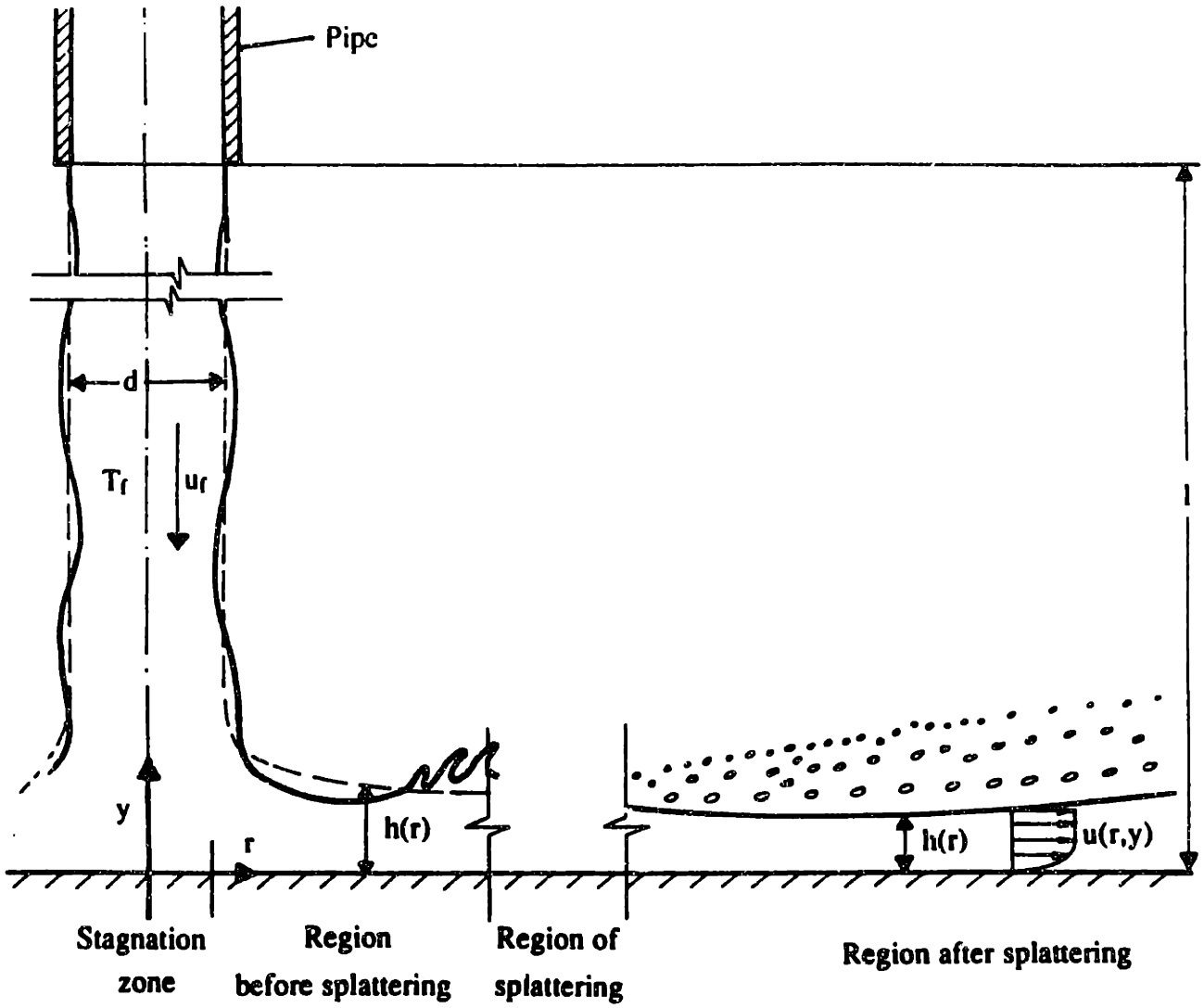

Figure 3.2: Regions for turbulent incoming jet: — instantaneous liquid surface; - - - mean liquid surface.

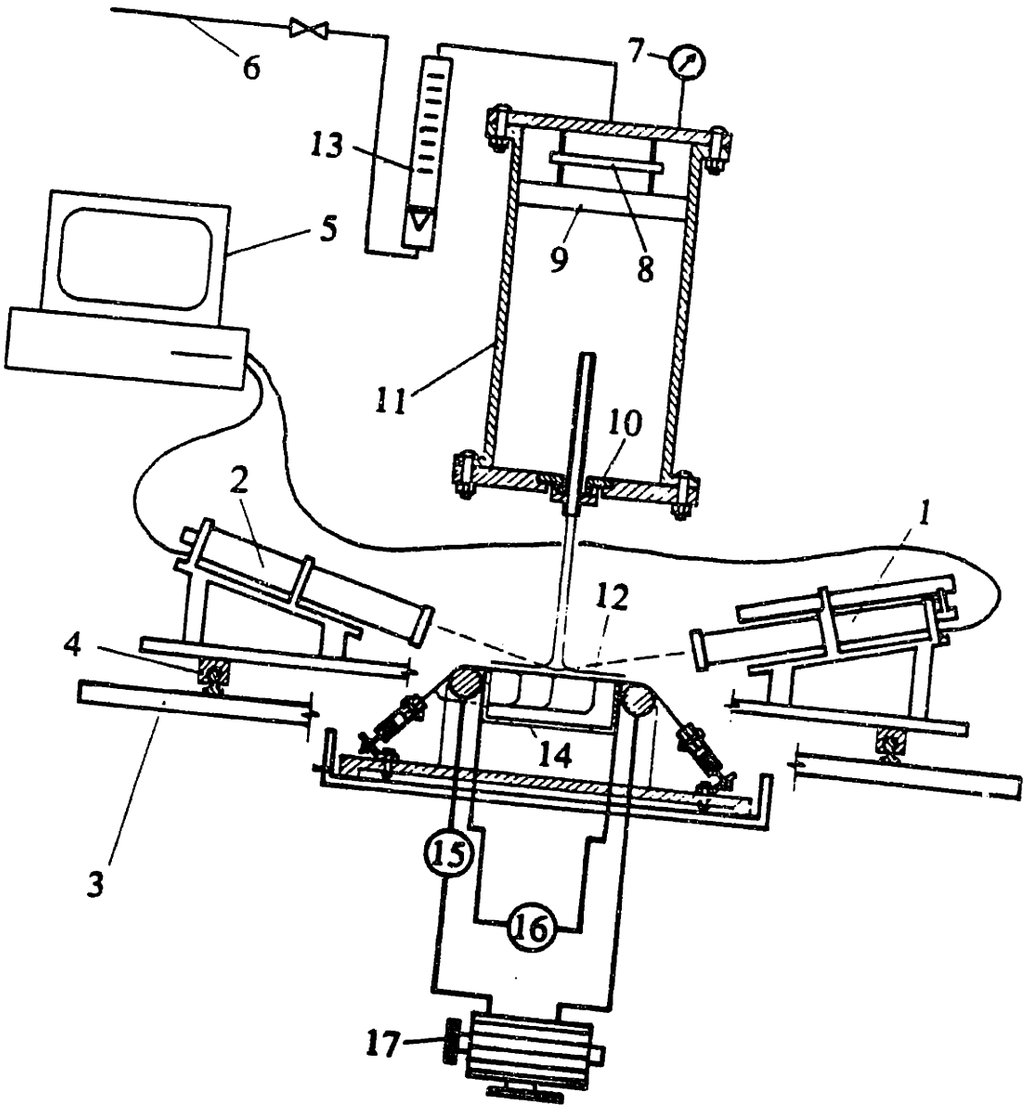

Figure 3.3: Experimental apparatus: 1. PDPA laser transmitter; 2. PDPA receiver; 3. Vertical traversing table; 4. Horizontal rail bearings; 5. PDPA electronics; 6. Water supply line; 7. Pressure gauge; 8. Strike plate; 9. Honeycomb; 10. Tube support plate; 11. Plenum; 12. Instrumented heater sheet; 13. Flowmeter; 14. Insulating box; 15. Electrical leads; 16. Voltmeter; 17. High-current, low-voltage electric generator, 25 kW.

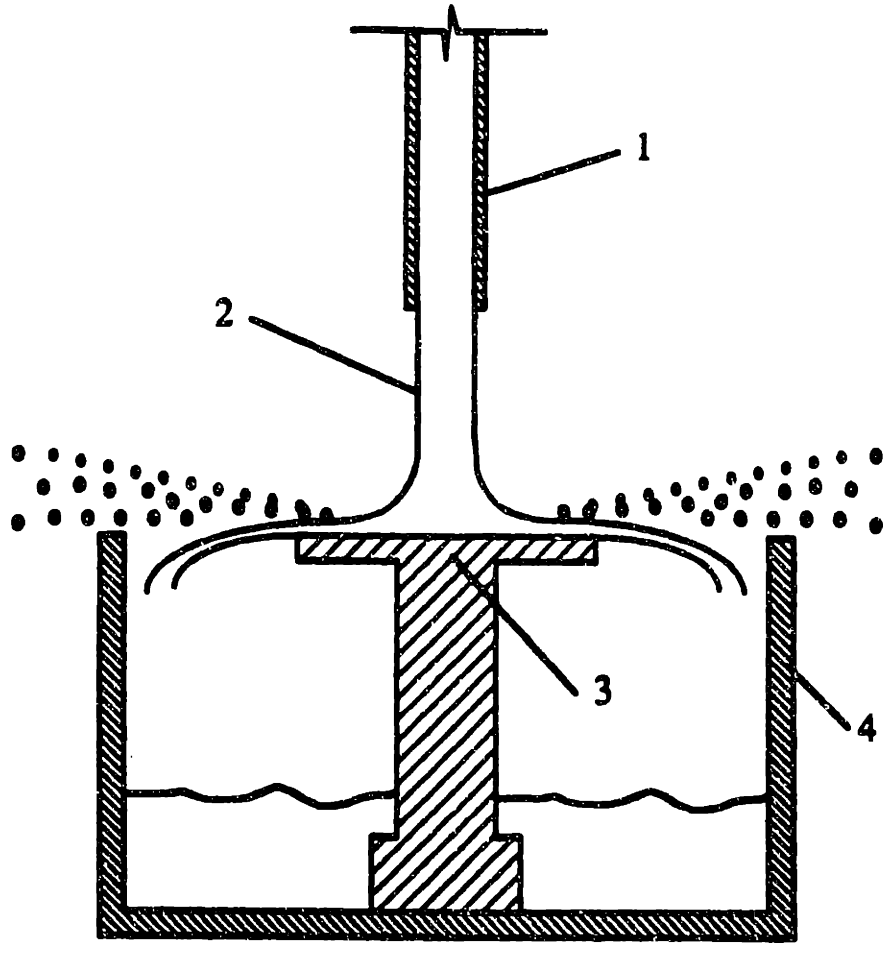

Figure 3.4: Direct measurement of splattered mass: 1. Tube; 2. Liquid jet; 3. Target disk; 4. Capture tank for unsplattered liquid.

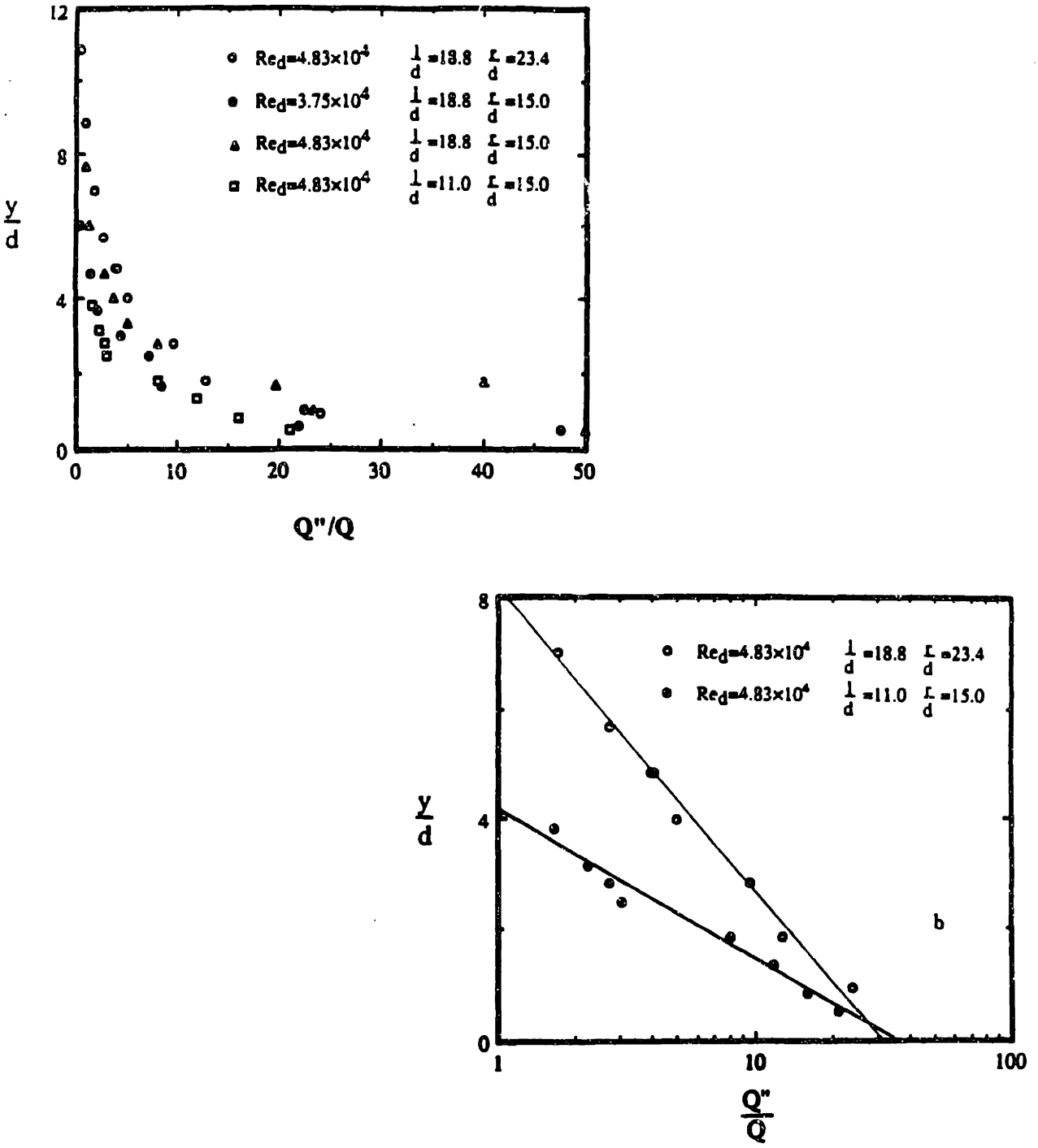

Figure 3.5: Vertical distribution of splattered radial liquid volume flow rate divided by total jet volume flow rate, Q''/Q (m^{-1}). (a) linear coordinates; (b) semilogarithmic coordinates.

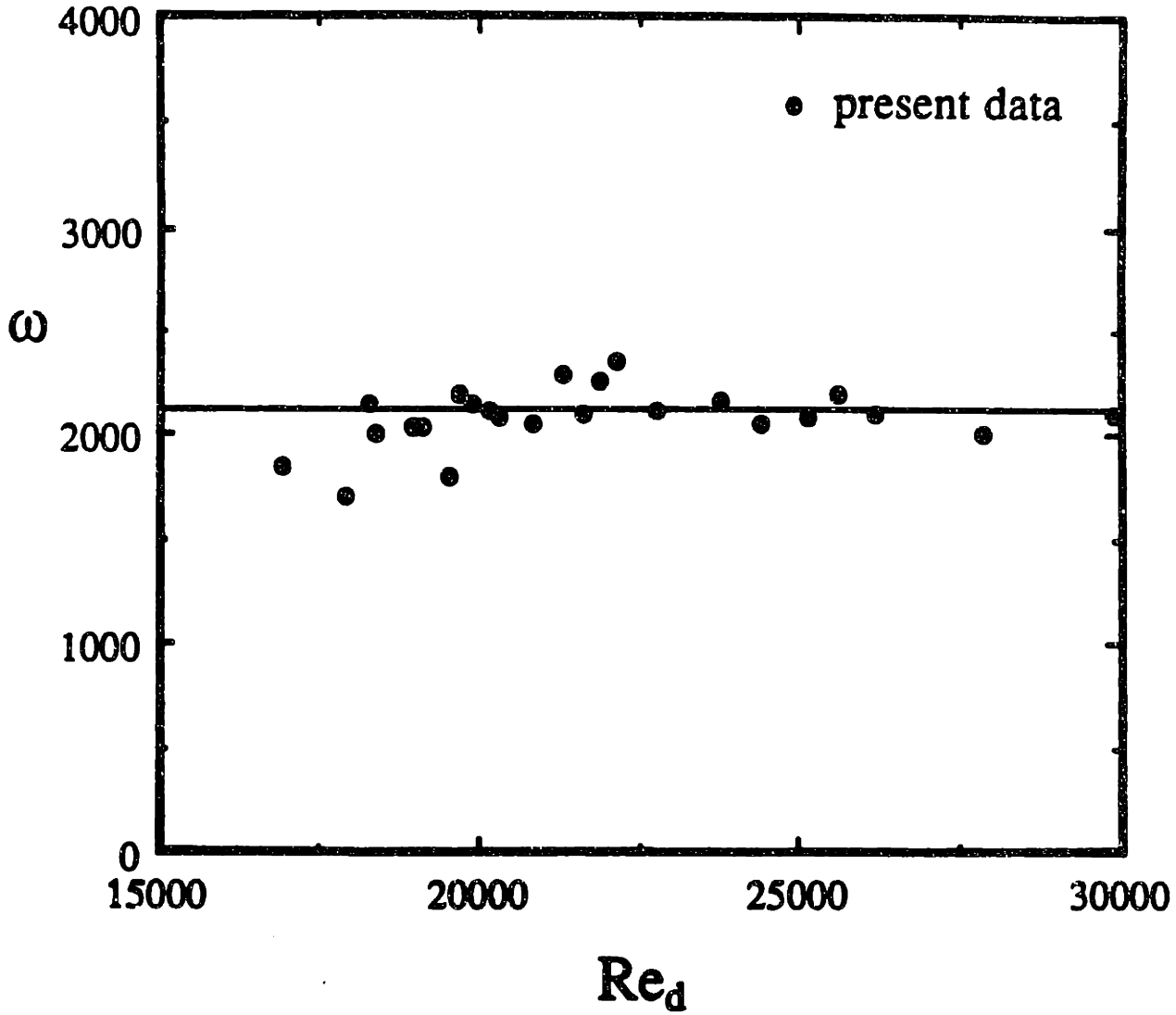

Figure 3.6: The critical ω for onset of splattering as a function of Reynolds number.

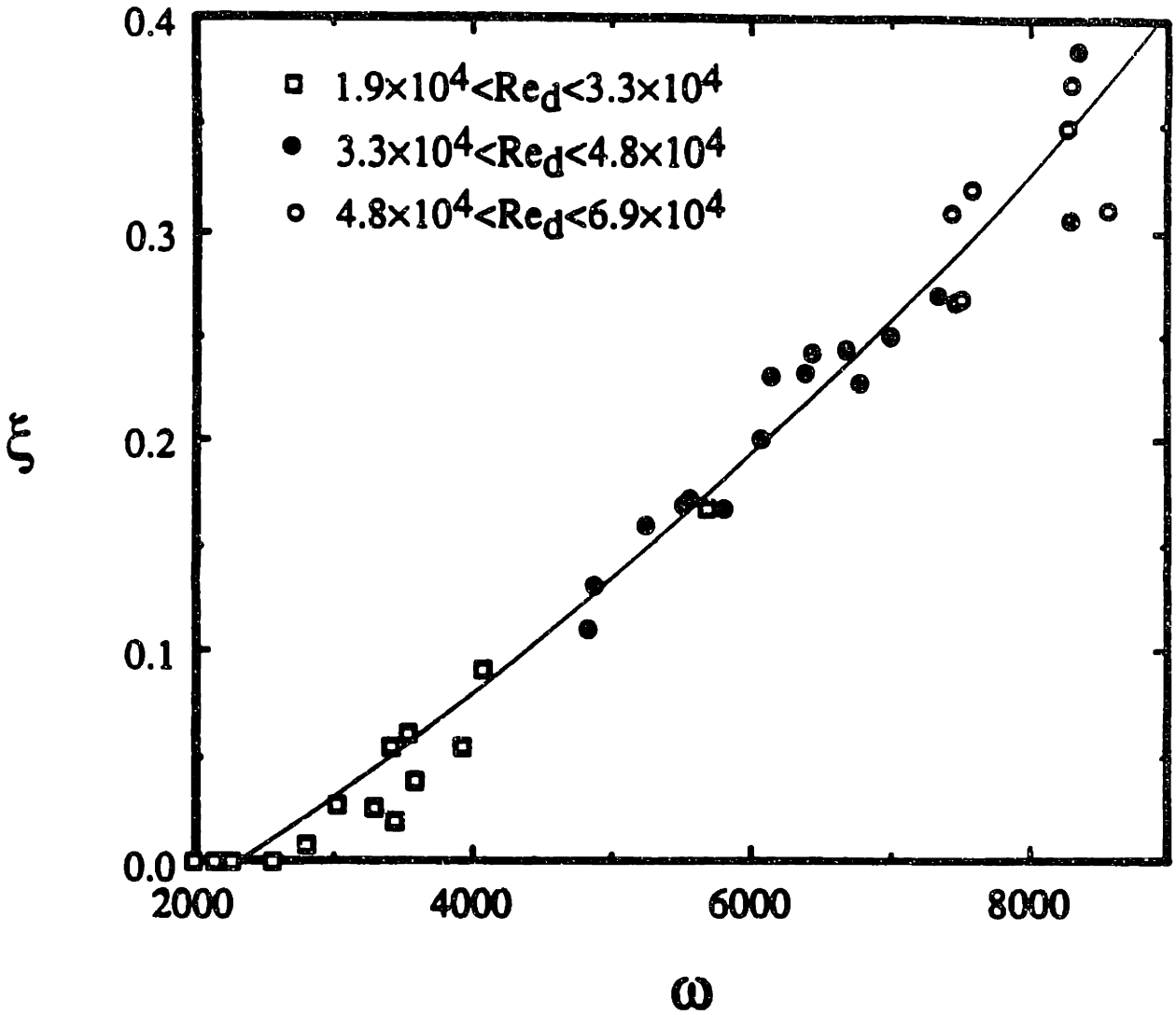

Figure 3.7: The fraction of incoming mass splattered, ξ, as function of ω; — curve fit.

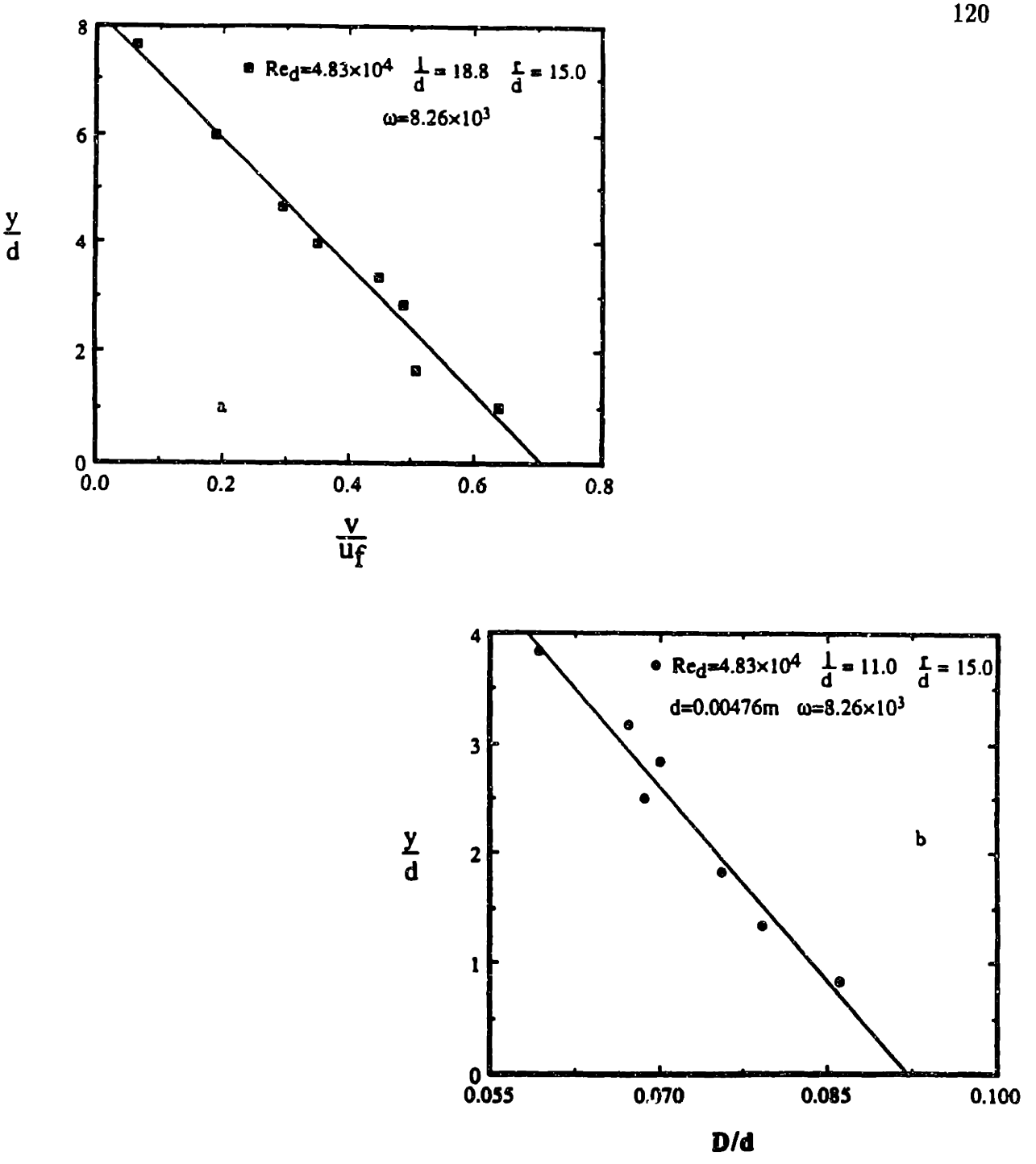

Figure 3.8: (a) Droplet radial velocity profile above plate; (b) Droplet diameter profile; — curve fits.

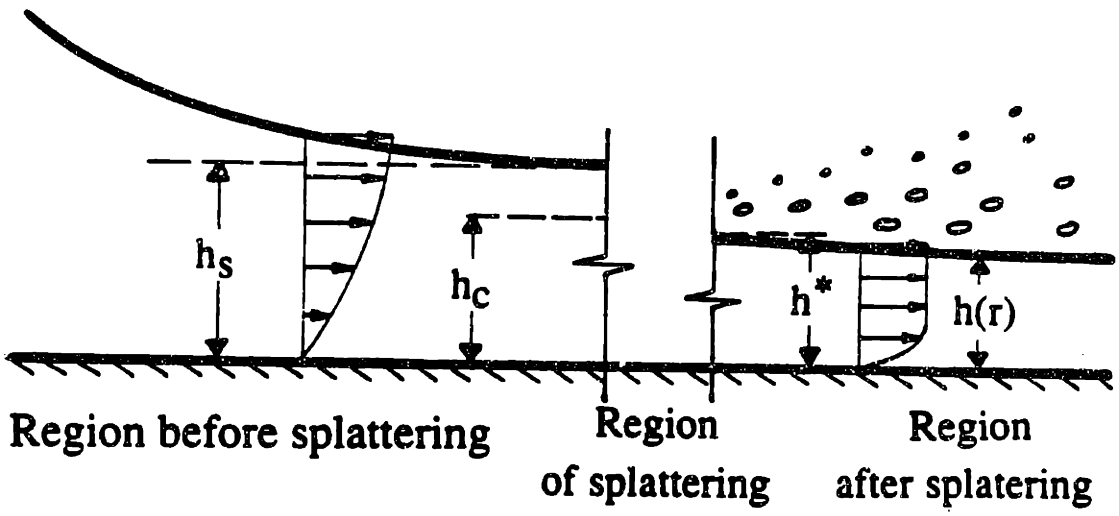

Figure 3.9: Mean flow field during splattering (schematic).

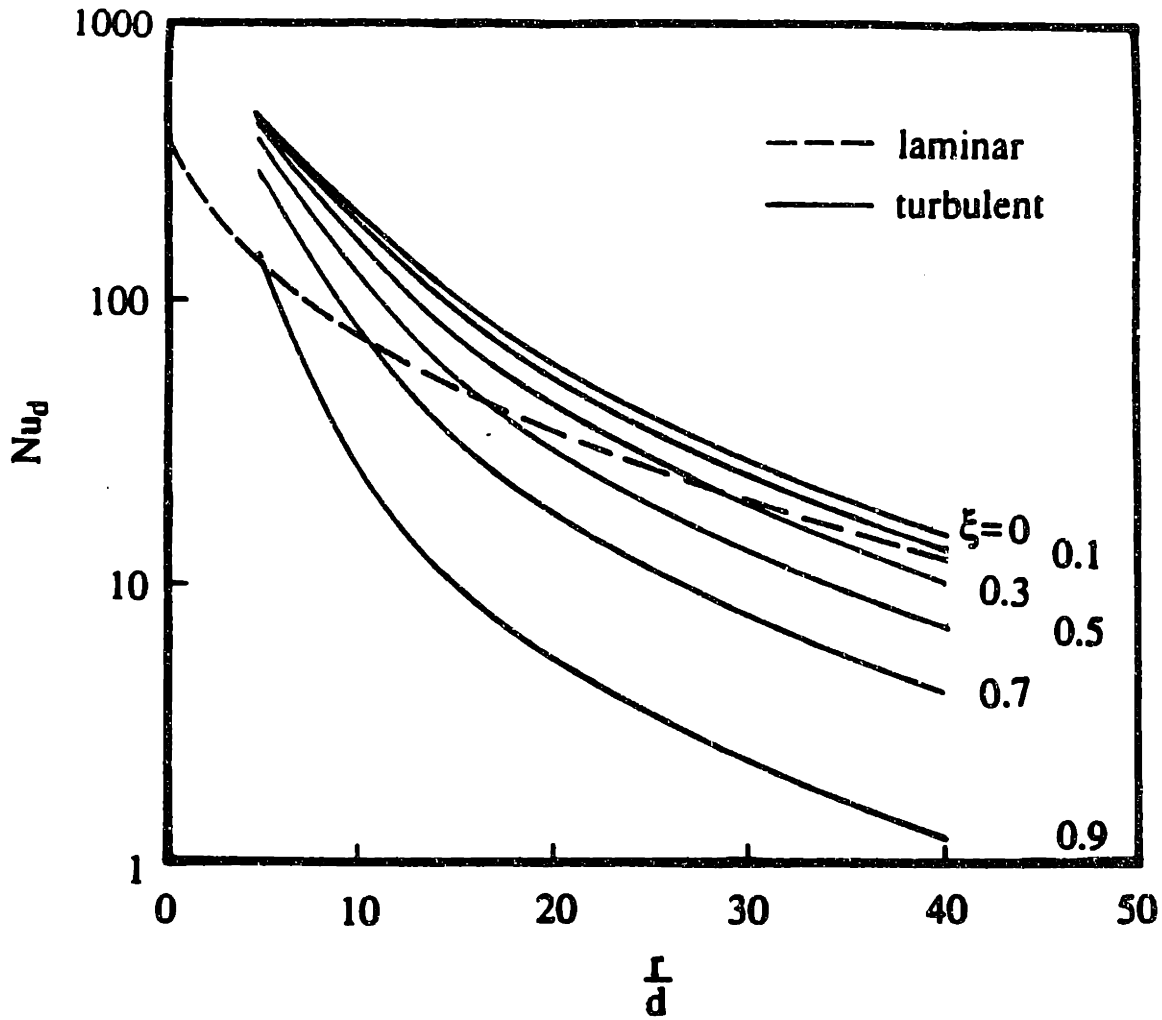

Figure 3.10: Estimated Nusselt number for region after splattering as a function of fraction of mass splattered: Eqn. 33 —; laminar results (present) - - -.

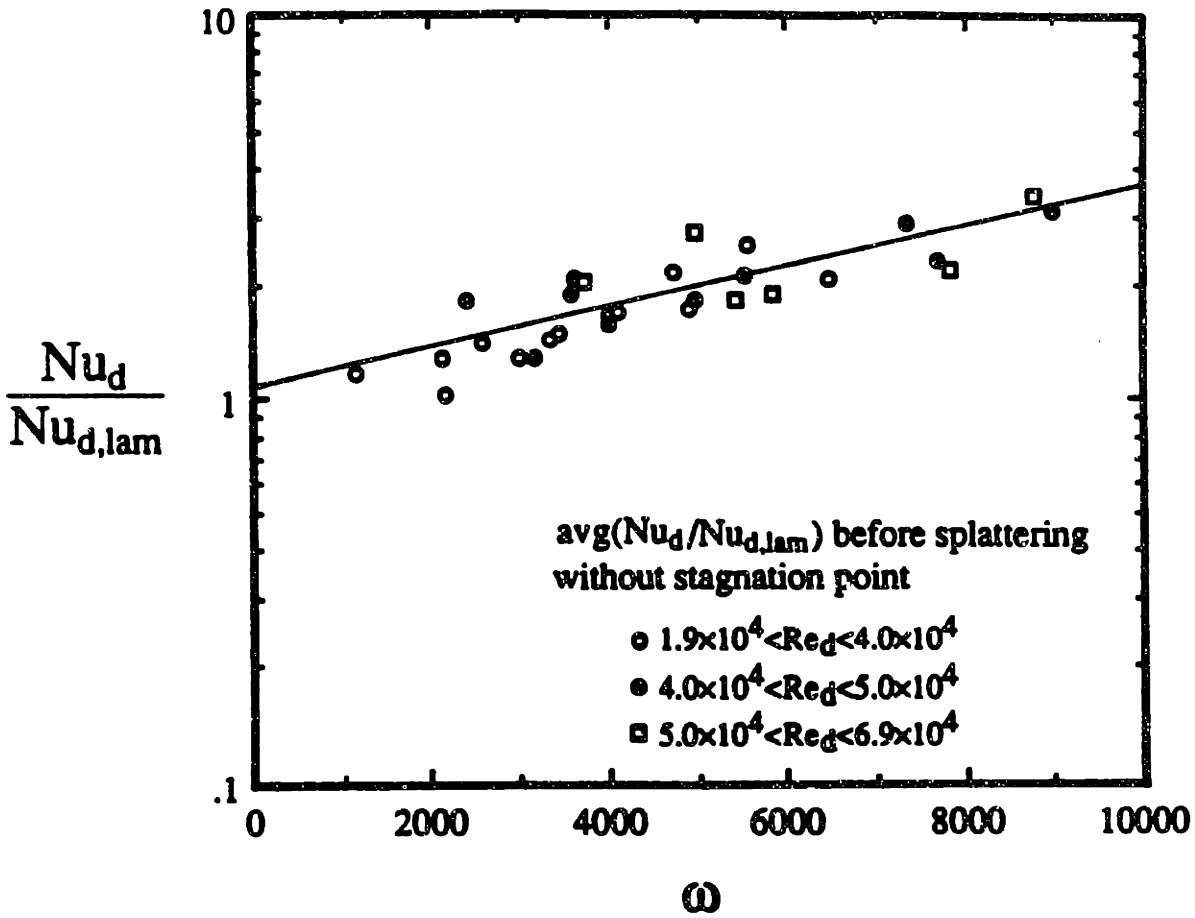

Figure 3.11: Augmentation of Nu_d in boundary layer region upstream of the splattering radius as a function of ω. Turbulent results normalized with laminar results from Chapter 2.

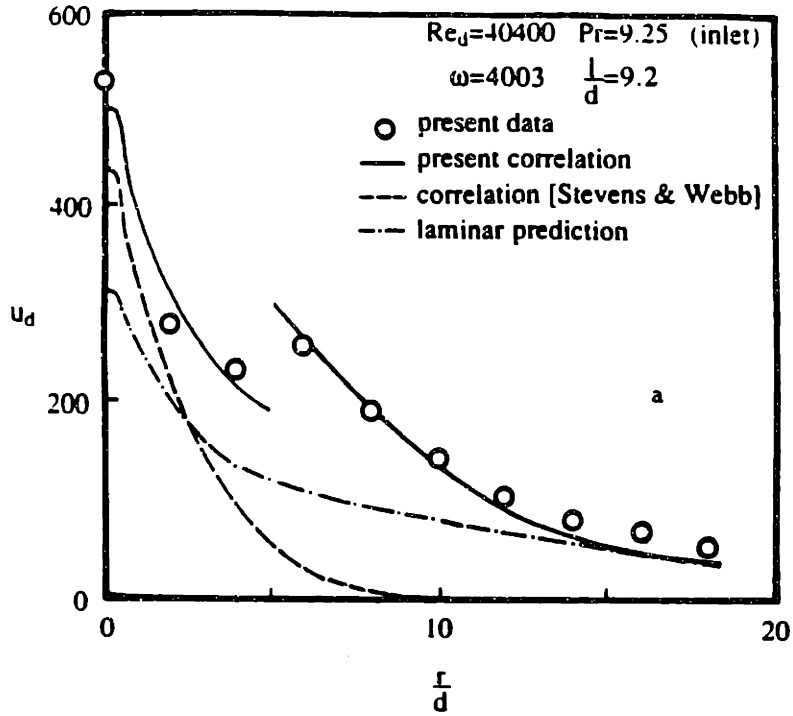

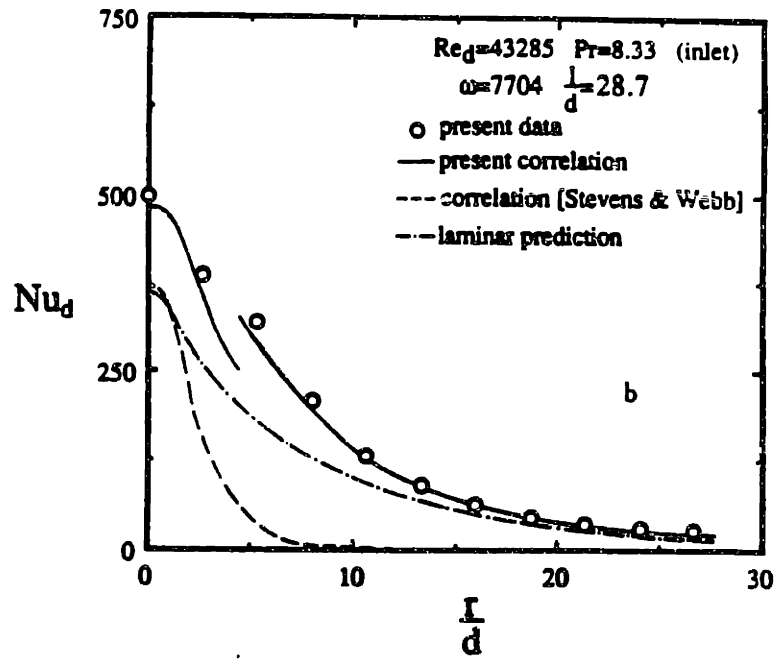

Figure 3.12: Comparison of measurements to the present model: — from Eqn. 3.33 and Figure 5-9; the present laminar theory

Chapter 4

THE CIRCULAR HYDRAULIC JUMP

4.1 Introduction

When a downward-flowing jet of liquid strikes a flat surface, it normally spreads out in a thin layer which experiences a sudden increase in depth farther downstream (Fig. 4.1). Watson (1964) provides three different models for calculating the position of the hydraulic jump, one inviscid model and two viscous models which differ depending on whether the flow upstream of jump is laminar or turbulent. In his models, he assumed that both upstream and downstream flows were unidirectional and applied the same momentum balance normally used for planar flow (*see* Introduction), in which the thrust of pressure is balanced by the momentum loss due to jump, taking

into the viscous effect on the upstream sheet thickness and momentum:

$$2\pi r_j \left(\int_o^h \rho u^2 dz + \int_o^h p dz \right) = 2\pi r_s \left(\int_o^s \rho u^2 dz + \int_o^s p dz \right) \tag{4.1}$$

$$\bar{u}_h = \frac{1}{h} \int_0^h u(r,y) dy = \frac{u_f d^2}{8rh} \tag{4.2}$$

The inviscid model gives the jump radius, r_j, as

$$\frac{r_j s^2 g d^2}{4Q^2} = \frac{1}{\pi^2} - \frac{g s d^2}{8Q^2} \tag{4.3}$$

where s is downstream depth and Q is the total flow rate. For viscous theory the solution for the hydraulic jump depends on which region, region 2 or region 3, the radial position of the jump is in. For laminar flow, if the jump occurs in region 2, then the following equation applies:

$$\frac{r_j s^2 g d^2}{4Q^2} + \frac{d^2}{8\pi^2 r_j s} = 0.10132 - 0.1297 (\frac{2r_j}{d})^{\frac{2}{3}} R^{-\frac{1}{2}} \tag{4.4}$$

where R is the Reynolds number defined by Watson, which is $\frac{2Q}{d\nu} = (\pi/2)\mathrm{Re}_d$. If the jump occurs in region 3, then the following equation applies:

$$\frac{r_j s^2 g d^2}{4Q^2} + \frac{d^2}{8\pi^2 r_j s} = \frac{0.01676}{\left(\frac{2r_j}{d}\right)^3 R^{-1} + 0.1826} \tag{4.5}$$

For turbulent flow in the liquid film, Watson used a assumption due to Glauert (1956) based on the Blasius drag law and assumed the eddy viscosity, ϵ, was of the form

$$\epsilon = (const.) u_f^{\frac{3}{4}} \delta^{\frac{3}{4}} F^6(\frac{z}{\delta}) \tag{4.6}$$

in which he further assumed that the velocity could be expressed by multiplication of functions of r and of z/δ

$$u = U(r) F(\frac{z}{\delta}) \tag{4.7}$$

Equation 4.6 is valid in the region near the wall, but Watson argued that since $\frac{\partial u}{\partial z} \geq 0$ everywhere in the present problem, it seems reasonable to use this relation throughout the layer. For a jump occurring in region 2, he gave

$$\frac{r_j s^2 g d^2}{4Q^2} + \frac{d^2}{8\pi^2 r_j s} = \frac{1}{\pi^2} - \frac{\left[560\pi(A - \frac{2}{9})\right]^{\frac{1}{6}}}{40\pi^2}\left(\frac{2r_j}{d}R^{-\frac{1}{6}}\right)^{\frac{9}{7}} \tag{4.8}$$

and for a jump occurring in region 3, he gave

$$\frac{r_j s^2 g d^2}{4Q^2} + \frac{d^2}{8\pi^2 r_j s} = \frac{200}{81.14^{\frac{1}{7}}(\pi A)^{\frac{9}{7}}}\left[\left(\frac{2r_j}{d}R^{-\frac{1}{6}}\right)^{\frac{9}{7}} + \frac{40(1-2A)}{(7\pi)^{\frac{1}{7}}(2A)^{\frac{5}{7}}}\right]^{-1} \tag{4.9}$$

The model proposed by Watson is based on the assumption that the flow field is either laminar or turbulent at all radii throughout the liquid sheet (an assumption shown to be invalid in Chapter 2). Comparing his data to his prediction, he found that his prediction agreed well with experiments around $s/r_j = 0.1$. For higher or lower of s/r_j, the data deviated form prediction.

From the present experimental observations, immediately after the jump the liquid on the free surface flows backward (Figure 4.2) and rolls down. Thus, the velocity immediately after jump is not unidirectional, and the assumption of uniform velocity or parabolic downstream velocity profiles clearly disagrees with this phenomena. Moreover, the Glauert relation is valid only in the region near the wall, and applying it to the whole liquid sheet causes additional error in the prediction. Furthermore, the liquid sheet is initially laminar and becomes turbulent only at large radii downstream.

Olsson and Turkdogan (1966) measured the free surface velocity (*see* Chapter 2) and the sheet depth in both supercritical and subcritical regions. They estimated the kinetic energy converted into free surface energy for jump. The energy loss during a

jump was measured to be about 20 to 50 percent of the total energy.

Ishigai *et al* (1977) observed various types of jumps, which were classified according to the upstream film Froude number defined by $\frac{u_f}{\sqrt{gh}}$:

1. Fr < 2 water surface is smooth and transparent. The jump is stable.

2. 2 < Fr < 7 the jump becomes S-shaped.

3. 7 < Fr < 15 the jump becomes round and its width is very narrow.

4. 15 < Fr the front face of the hydraulic jump collapses and air is caught up in the water. The jump is unstable.

Ishigai *et al.* simplified the balance between the pressure thrust and momentum assuming that the velocity after jump is uniform over the film thickness. His comparison between model and measured jump radii showed increasing disagreement at large jump radii, or large Froude number.

Nakoryakov *et al.* (1977) measured the wall shear stresses by an electrodiffusion method. The measurement showed that the friction changed sign twice and in the jump region took a negative value. Instead of the conventional definition of hydraulic jump, they defined the jump radius as the distance from the jet center where the friction was minimal. They also mentioned that the jump radius could be calculated setting the velocity of disturbance propagation, $\sqrt{gh}$, on shallow water equal to the jet velocity. They claimed that the jump radius calculated from $u = \sqrt{gh}$ is about the same as that found by electrodiffusion method. However, for such thin liquid film (the smallest jet diameter was 3.4mm) the capillary waves should be more important than

the gravitational waves assumed by Nakoryakov *et al.*. In addition, the axisymmetric wave speed is not a constant, but depends on the local velocity and sheet thickness.

Bouhadef (1978) analysed the supercritical and subcritical flows using an integral method. He measured the velocity distribution after jump, but he did not report an eddy under the jump. His measurements showed that the surface velocity close to the jump in subcritical region was much lower than the mean velocity and close to zero, and that it increased with radius. The velocity distribution gradually became close to parabolic further downstream in the subcritical zone.

Streeter and Wylie (1979) described the phenomena accompanying large scale hydraulic jumps, which typically occur at the base of dams or in tidal bores on rivers. For large jump height a roller develops on the inclined surface of thickening liquid sheet. The surface of the jump is very rough and turbulent. Air is drawn into the liquid. For small height, the form of the jump changes to a standing wave pattern. Further discussion of planar jumps is given by Peterka (1963).

Craik *et al.* (1981) described observations of the jump when a jet hit a glass tray, which was dry initially. As the jet filled the tray and the downstream depth increased, they observed that the initially stable jump became wavy, and then became unstable. The unstable jump changed from fluctuations to bubble entrainment as downstream depth increased further. Their data showed the same trends as Watson's when compared to Watson's prediction.

Errico (1986) found that the eddy under the jump shrank as outer depth increased and shrank faster than the jump radius. As the eddy disappeared, oscillations began

at the jump started. Strong oscillations commenced at $\frac{Q}{2\pi r_j \nu} = 147$. With low flow rates or for small outer depth, the closed eddy under the jump maintains a fast flow in the top portion of the downstream flow. The momentum loss occurs over the considerable length of the closed eddy. As the outer depth increases, the eddy shrinks and dissipation occurs over a shorter and shorter length.

Stevens and Webb (1989) gave a correlation for the hydraulic jump

$$\frac{r_j}{d} = 0.0061 Re_d^{0.82} \tag{4.10}$$

However, the downstream condition of their experiment was not specified or varied. Since the hydraulic jump location always depends on downstream conditions, this result must be regarded as instructive but a specific to their apparatus.

In the present chapter, several different types of jump are identified. They are a single jump without roller, a single jump with roller, a jump with double roller, and an unstable jump. These jumps occur as a sequence of bifurcations as the downstream depth is increased. For very small jump height, no roller develops. This kind of roller is stable and has smooth surface, which is much different from the roller for large height described by Streeter and Wylie. In this case the surface tension stabilizes the free surface. With a further increase of the jump height, a double roller appears in place of single roller. If the height exceeds a certain value, surface tension cannot compensate the liquid potential and liquid falls back to the subcritical region, entraining air into the liquid. We call this an unstable jump. In this region, the jump becomes less stable. The balance of viscous, potential, surface tension and inertial forces controls the instability of the hydraulic jump.

The upward-flowing jet (Figures 4.3 and 4.4) does not appear to have been considered previously. For the upward jet, the gravitational force is inverted. For this case the hydraulic jump is impossible, instead the liquid sheet is terminated by a Rayleigh-Taylor instability with liquid dripping and drip down as droplets. Figure 4.4 shows the droplets dripping from a glass plate that was used as the target of an upward jet. The photos were taken from above the glass plate. The droplets are separated by a certain wavelength which is related to Rayleigh-Taylor instability. It is known that a horizontal plane interface between two stationary fluids with a density difference, in which the density of the upper liquid is larger than that of lower one, is unstable to any small disturbance with a wavelength greater than the critical wavelength. Rayleigh-Taylor instability is related to many phenomena, such as boiling, condensation, sublimation, melting, etc. There have been papers concerning the original theory of Taylor (1950), which have added more parameters to the model, such as surface tension (Bellman *et al.* 1954), viscosity (Dhir *et al.* 1973), temperature gradients in the layers (Hsieh, 1972), and their combinations (Plesset *et al.* 1974, Taghavi *et al.* 1980). These theories discuss the instabilities of a horizontal interface between two fluid layers. For phenomena involving curved interfaces, such as rising bubbles (Taylor *et al.* 1944, Batchelor 1987), various stability criteria have been proposed.

The present experimental observation shows that, after the jump, dripping of liquid droplets driven by Rayleigh-Taylor instability dominates the phenomena. A correlation for the jump radius is given based on Rayleigh-Taylor instability theory.

4.2 Experiments

The circular jet experiments are in two parts: downward jets and upward jets. For downward jets, the experiment arrangements (*see* Chapter 2) insured that the incoming jets were laminar. The arrangement of this experiment is shown in Figure 4.5. The main components of the apparatus are the water supply, pump, pressure vessel and the target plate. The water goes from the supply tank to the pressure vessel, then exits the vessel through the orifice and strikes the target. The water from the target plate is then drained into a nearby sink. The pressure vessel is used to calm the flow before it exits through the orifice plate at the bottom of the tank. The strike plate is 4 inches from the end plate. A piece of stainless steel honeycomb (hexagonal, 1/4 inch passage diameter, 3 inch long) is situated 4 inch below the strike plate to damp and dissipate turbulence upstream of the orifice plate. The lower cap plate of the vessel is made out of aluminum and is used to hold interchangeable orifice plates.

The target plate is located under the orifice and is supported by a frame. Between the target and the frame, adjustable screws were inserted to adjust the height of target and to ensure that an even flow is obtained by keeping the plate horizontal. The target plate is a circular piece of 3/4 inch thick aluminum with an outer diameter of 12 inch. A 11.75 inch diameter circular depression is placed in the center of the plate with a depth of 0.5 inch high. Circular sheets of plexiglass are used as inserts in the target plate to provide variable lip height for any given flow.

The experimental apparatus can be run at different conditions by adjusting the two globe valves, by changing the strike plate inserts or by changing the orifice size.

Each test consists of recording the pressure, jump height, jump radius, insert height, orifice size and distance between from the plate to the orifice. The jump height is determined by using a point gauge, which is a micrometer in a stand. The jump radius is measured using graduated marks made in the surface of the strike plate at 1/4 inch radial intervals. The orifice sizes are 1/8 and 1/4 inch in diameter. The measured values are presented in Tables 4.1, 4.2, 4.3, 4.4.

The planar jet experiment set up (Figure 4.6 included a tank and a cylindrical plenum, with a slot on one end of the plenum. An adjustable gate on the slot set the gap of the slot. The water supply went though the tank to the plenum. A drain on a wall of the tank kept the water level constant. The water out of the slot flowed along a horizontal plate with a smaller width than that of the slot. Two moveable plastic glass walls were put on both sides of the plate. The leading edge of the walls were positioned just at the position of the jump and left both sides of plate open before the hydraulic jump to avoid wave generation by the wall which was otherwise found to distort the hydraulic jump.

The hydrogen bubble technique was used to visualize the flow field beneath the planar jump. The hydrogen bubbles were produced by using a platinum wire as an anode and an aluminium foil along the bottom of the channel as a cathode. The voltage was supplied by a rectifier; the circuit is shown in Figure 4.7. The circuit could generate pulses or continuous bubbles.

For upward jets, the pressure tank was inverted. A glass plate was used as the target. For each run of the experiments, photos were taken from above the glass

plate. The measurements were taken from the photos. The orifice sizes are 1/8 and 1/4 inch in diameter. The pressure in the vessel is read off the pressure gauge at the top of the tank.

From the measured quantities, all the variables of interest are calculated. For the jump height uncertainty is about 1.5% to 3%, which change was due to the surface disturbance. The larger incoming jet velocity, the larger the disturbances. The uncertainty for We_d is between 1.6% and 3.1% and, that for Froude number is less than 4%.

4.3 Discussion

4.3.1 Downward jets

Several types of jump can be identified and they are a sequence of bifurcations (Figure 4.8): (a) single jump without roller. (b) single jump with roller. In this case the pressure thrust creates a single roller on the surface and a boundary separation eddy along the wall. (c) double roller. Instability of the single roller flow leads to a double roller flow. (d) unstable jump. In this case the pressure thrust is too large to be balanced by surface tension, the jump becomes less stable. In this region, air is drawn into the liquid. With increasing jump height, two stages can be observed. In the first, the lower roller of the double roller draws a lot of air, in the second, the two rollers merge and whole jump draws a lot of liquid.

Another important characteristic of the roller is that there is a vortex under the

roller. The vortex indicates the separation of the boundary layer and the change of sign of the wall stress.

Both the roller and the vortex were confirmed by our hydrogen bubble experiments. The observations of rollers and vortices confirmed the complexity of the flow field in circular hydraulic jumps. The flow immediately after the jump was not unidirectional and showed very complicated patterns. Although the vortex beneath the jump requires special tools to be observed, the surface rollers of the jump can be seen with the naked eye.

Figure 4.1 is a photo of a single jump. The free surface is smooth and the jump is cuspate, which is considerably different from the standard hydraulic drawing shown in Figure 1.2. Instead of a turbulent, tumbling fluid mass falling over itself as in the typical hydraulic jump drawing, the free surface of the jump is very smooth and curved. Hydraulic jump research has long focused on dams and spillways. The thickness of liquid sheet of the supercritical liquid sheet is typically more than several inches thick (the subcritical sheet being thicker still) and surface tension is entirely irrelevant in these cases. For the circular jet shown in the photo, the thickness of the liquid sheet is only millimeters in the subcritical region and surface tension is dynamically important. A balance between the hydrostatic pressure force behind the jump and the surface tension force along the surface of the jump gives

$$\rho g h \sim \sigma / R \tag{4.11}$$

where R is the radius of curvature of the roller. The radius of curvature at the jump is about one half of the jump height, h. Surface tension can balance the hydrostatic

pressure behind the jump under the following condition:

$$h \sim \sqrt{\frac{2\sigma}{\rho g}} \tag{4.12}$$

For water, the thickness h is of millimeter order when the gravitational pressure force and surface tension are in balance. Surface tension stabilizes surface, because the film is thin. The result is an increase of the adverse pressure gradient along the wall and the appearance of the vortex beneath the jump. This vortex educed by the present hydrogen bubble visualization and by the experiments of Nakoryakov *et al.* (1978) and Errico (1986). The vortex shows the complexity of the flow field after a hydraulic jump, and it causes more momentum loss during the jump.

If the liquid sheet is quite thin (of millimeter order), what would happen for a planar jet? Such a flow should differ from the classical planar jump by virtue of a strong surface tension effect. Figure 4.9 is a photo of a thin planar jump. The liquid issued from a gate with a gap about 1 mm from the bottom wall. The free surface is smooth and a cusp can be seen at the jump. The similarity of circular and planar jumps for thin liquid sheets confirms that this peculiar behavior is not caused by the axisymmetric geometry, but by the thinness of the sheet and effect of surface tension. It is interesting to note that for the planar jump there is not only a roller but also an additional hump upstream of it. The flow visualization by hydrogen bubbles showed that there was vortex under the hump too(Figure 4.10). Boundary layer separation probably cause the vortex. Comparing to the circular jump case, it appears that the vortex which was in the subcritical region has moved into the supercritical region, pushed up the liquid sheet, and formed this additional hump.

Figure 4.11 shows a photo of the double jump. In this case the shape of jump becomes more irregular than the single jump. The variations can be seen in the azimuthal direction on the free surface. The variations look like cells or waves, which are not stationary but pulsate with time. This phenomena indicates the flow variation in the azimuthal direction and that the flow field is no longer axisymmetric. The distance between the two curves on the surface is not large and depends on the jet velocity. The smaller the velocity, the closer the two "jumps". Decreasing the downstream depth, the double jump goes back to a single jump. With an increase of the jump height, more and more air is trapped in the liquid, and the jump tends to be more unstable (Figure 4.12). The jump oscillates back and forth and a lot of air is trapped in the water, since the back flow catches air and then flows into the main stream.

The edge of the jump basically is circular for clear and stable incoming jets. On this circle, a certain wave pattern can sometimes be seen (Figure 4.13). In our experiments for very stable incoming jets and small jet velocity, this wave pattern is very regularly. This azimuthal instability phenomena is separated from the above vertical instability of the jump and governed by a Taylor instability produced by the density difference between the air and the water. Liquid drops tend to escape from the crest of these waves and enter the supercritical stream inside the jump. Increasing the stream velocity inside the jump, the drops seem to splash and bounce up. We can observe that on the jump edge drops bounce up and down with some regular interval and frequency. For large jet velocity, the crests of the waves are smoothed by the

high velocity of the supercritical region; this pattern becomes invisible, is covered by disturbances of the flow, and appears to be random.

The circular hydraulic jumps exhibit many structures. But the classical theory of hydraulic jumps takes a very simple mathematical form. We may ask whether the classical theory of the hydraulic jump works for circular hydraulic jumps. The circular jump can be put in the same form as the classical planar jump by defining the Froude number as:

$$\mathrm{Fr}_h = \frac{\bar{u}}{\sqrt{gh}} \tag{4.13}$$

where $\bar{u}_h$ is the mean velocity of liquid film with a thickness of h. By momentum balance and continuity, assuming that the velocity is unidirectional, and neglecting curvature effects in the jump region, we can obtain the same hydraulic jump formula for circular jump:

$$\frac{s}{h} = \frac{1}{2}\left(\sqrt{1 + 8\mathrm{Fr}_h^2} - 1\right) \tag{4.14}$$

The formulas for circular proposed by various investigators, including Watson, can generally be expressed by the above equation except for variations in the assumed velocity distributions, the methods of calculating the thickness of liquid sheet, the use of inviscid or viscous models, and the assumption of laminar or turbulent flow*.

Figure 4.14 puts the data on coordinates of the ratio of downstream depth over upstream depth versus the upstream Froude number. The circular hydraulic jumps asymptotically approach the classical theory at low Froude number and low ratio of downstream to upstream depth. The hydraulic jump is impossible for $Fr_h \leq 1.0$.

*Bouhadef took into account of the thickness variation of both supercritical and subcritical sheets. There are some sign errors in his equations.

For high Froude numbers, the axisymmetric jumps deviate increasingly from the classical theory, Equation 4.14, which is represented by a solid line. In addition to the deviation, the scattering of axisymmetric jump data increase with the Froude numbers or the ratios of the downstream and upstream depth. The scatter implies that must be other dimensionless group or groups, which should be included in the analysis of axisymmetric hydraulic jumps.

The parameters which would be introduced only for jump with thin supercritical liquid sheet and not for jumps with thick sheet may be identified from a dimensional analysis.

It is instructive to examine the planar inviscid flow and the planar viscous flow to see what parameters would differ in these two cases. For a planar jump the flow is thick enough the viscosity can be neglected. Then, for two dimensional inviscid flow, the upstream film thickness and downstream film thickness are independent of traveling distance, or the horizontal coordinate. The parameters involved in a planar jump are

$$F(u_h, h, u_s, s, g, \rho) = 0 \tag{4.15}$$

From the continuity, we have

$$u_h h = h_s s \tag{4.16}$$

and we can eliminate u_s, then we get

$$F(u_h, h, s, g, \rho) = 0 \tag{4.17}$$

This gives two dimensionless groups and we may write as

$$\frac{s}{h} = \bar{F}\left(\frac{u_h}{\sqrt{\rho g h}}\right) \tag{4.18}$$

Intuitively, the only parameter introduced in viscous flow is viscosity and the above two dimensionless groups plus Reynolds number is enough to describe the viscous case. But this intuition obviously misses some other important factors. Viscosity is important only for very thin liquid sheets, in which the boundary layer thickness is comparable to the liquid sheet thickness. Therefore, the thickening of liquid sheet due to the viscosity cannot be neglected. The thickness of liquid sheet is no longer independent of the horizontal coordinate, x, and becomes a function of horizontal coordinate both for upstream and downstream. Usually, we know the thickness of the liquid sheet, h_1, and the velocity u_h, at a certain upstream position, let us say $x = x_1 = 0$, and the thickness of the sheet, h_2, at a certain downstream position, $x = x_2$. In fact, if we know the diameter and Reynolds number of the incoming jet (or Re_d and Fr_d), we can calculated h for any radius in the supercritical region upstream of the jump.

As mentioned above, surface tension is no longer negligible for a hydraulic jump on thin liquid film. The order of magnitude of the thickness length scale, at which the surface tension becomes important, may be estimated as $\sqrt{\frac{\sigma}{\rho g}}$. For the case of a hydraulic jump, the length scale is the difference of downstream depth and upstream depth. This difference is usually close to the downstream depth, since the upstream depth is normally much smaller than the downstream depth. Coincidentally, the order of magnitude of the liquid sheet thickness, at which the surface tension becomes

important, is similar to that of the free surface wave length, at which surface tension waves become comparable to gravitational waves.

From the above argument, we may have the following parameters for a hydraulic in a thin with viscous liquid sheet:

$$F(u_h, h_1, x_j, x_2, h_2, g, \rho, \sigma, \mu) = 0 \tag{4.19}$$

Thus, the location of the jump depends on:

$$\frac{x_j}{h_1} = \bar{F}\left(\mathrm{Fr}, \mathrm{We}, \mathrm{Re}, \frac{x_2}{h_1}, \frac{h_2}{h_1}\right) \tag{4.20}$$

where

$$\mathrm{Fr} = \frac{u_h}{\sqrt{g h_1}} \tag{4.21}$$

$$\mathrm{We} = \frac{\rho u_{h_1}^2 h_1}{\sigma} \tag{4.22}$$

$$\mathrm{Re} = \frac{\rho u_{h_1} h_1}{\mu} \tag{4.23}$$

Six dimensionless groups involved in the thin film hydraulic jump rather than two for thick sheet hydraulic jump. Similarly, six dimensionless groups are required for an axisymmetric hydraulic jump. If the initial conditions are set at the nozzle, we exchange h_h with diameter of incoming jet, d, and x_s with r_s, which is the diameter at which the sheet thickness is s:

$$\frac{r_j}{d} = F\left(\mathrm{Fr}_d, \mathrm{We}_d, \mathrm{Re}_d, \frac{s}{d}, \frac{r_s}{d}\right) \tag{4.24}$$

There have been some investigations which tried to fit axisymmetric jet data into the classical hydraulic model, using only the ratio of downstream depth over upstream depth and upstream Froude number. The above explains why they were not successful: more dimensionless groups should have been considered.

Some questions have arisen from using Equation 4.14 for circular jumps. The formula requires the downstream depth. In the planar case, the downstream depth is constant except the jump region, in which the surface is rough and unstable. For circular jumps, the liquid sheet thickness is not constant, especially for a large downstream depth. However, in most references, the downstream depth, s, was not given for a specific downstream position. Because Equation 4.14 does not take into account the momentum loss during the jump, the downstream depth considered should be the depth immediately after the jump. As mentioned above, the roller and vortex beneath the jump make the flow non-unidirectional and very complex. The unidirectional velocity profile assumption does not apply.

If the subcritical liquid sheet depth is given for a position not immediately after the jump, the momentum loss between the jump and this given position must be taken into account. In this case, the momentum balance (Figure 4.15) becomes

$$2\pi r_j \left(\int_o^h \rho u^2 dz + \int_o^h p dz \right) = -D + 2\pi r_s \left(\int_o^s \rho u^2 dz + \int_o^s p dz \right) \tag{4.25}$$

where D is the drag force exerted by the wall on the fluid in a downstream direction, and

$$\bar{u}_h = \frac{1}{h} \int_0^h u(r,y) dy = \frac{u_f d^2}{8rh} \tag{4.26}$$

Rearranging and we get the upstream Froude number

$$\mathrm{Fr}_h = \frac{u_f d^2}{8r\sqrt{gh^3}} \tag{4.27}$$

The Froude number in subcritical region is, similar,

$$\mathrm{Fr}_s = \frac{u_f d^2}{8r\sqrt{gs^3}} \tag{4.28}$$

We rearrange and nondimensionalize the above equation to yield:

$$\left(\frac{\mathrm{Fr}_s}{\mathrm{Fr}_h}\right)^{4/3}\left(\frac{1}{2}+\mathrm{Fr}_h^2\right)=\left(\frac{1}{2}+\mathrm{Fr}_h^2\right)-\frac{D}{\rho g s^2} \tag{4.29}$$

From the above dimensional analysis, the drag must be a function of Reynolds number, Weber number, and $(r_s - r_j)/d$. The dependence of the drag term on other dimensionless groups must be found.

Figure 4.16 shows the dimensionless total momentum loss, which is $\frac{D}{\rho g s^2}$ divided by the terms on the right hand side of equation. The figure shows that the momentum loss can be a very large portion of the total momentum. The loss increases with Reynolds number and Weber number, especially, when the jump was close to the weir at the edge of the target plate where the flow is deflected by the weir. It should be noticed that the highest depth in the subcritical region was taken as the downstream depth, s, and the velocity was assumed positive in the radius direction.

The downstream momentum loss is not negligible for thin film hydraulic jump. The downstream condition need to be considered in the jump predictions. The experiments by Nakoryakov *et al.* (1978) showed that not only the downstream lid height but also the shape of the disk edge had effects on the position of the jump; the jump radius is larger with the round-edge plate than with the sharp-edged plate. This is another evidence that the downstream drag affects the jump position.

In Figure 4.17 the different types of jump are shown for different Reynolds numbers. The horizontal axis is the Weber number. If the types of jump, which are single, double, and unsteady jump, are solely determined by the Weber number, the different region of jump would be divided by the lines normal to the horizontal axis. But the

figure shows that it is not the case. The borders of different types of jump are at some angle to the Weber number axis. This implies that the changing of different types of jumps is not only function of the Weber number, but also of Reynolds number.

4.3.2 Upward jets

Since the thickness of the liquid sheet is very thin, the viscosity is important for the velocity development along r direction. For flow without disturbances and in the region not near the stagnation point a viscous similarity solution was given by Watson (1964). However, for simplification of the problem we may neglect the viscosity when we analyze the actual wavelength in the thick dripping region. This is justified by the result of Taghavi (1980), which shows that if the dimensionless viscosity parameter

$$M = \frac{\sigma^{\frac{3}{4}}}{\nu g^{\frac{1}{4}} (\rho_l - \rho_v)^{\frac{3}{4}}} \tag{4.30}$$

is greater than 100, the viscosity effect can be neglected in Taylor unstable layers (for water M is much larger than 100).

The rate of liquid inflow to the dripping region, Q, must equal to the rate of removal by droplets. Making an analogy to film boiling (Lienhard and Wong, 1964), the rate of liquid removal by droplets is

$$Q = (volume\ of\ droplet)\,(number\ of\ droplets/cycle)\,(cycle/second) \tag{4.31}$$

We may make the following assumptions:

1. The thick ring of liquid at the outer edge of the sheet undergoes Taylor instability.

2. The flow in the thick dripping region is inviscid. This assumption is valid since the velocity gradient is small.

3. The both phases, liquid and gas, are of infinite depth.

4. The droplet radius is proportional to the most dangerous wavelength λ_d, say, λ_d/C_1, where C_1 is a constant, and λ is calculated from Taylor theory for a plane layer.

5. The frequency of droplet release is proportional to the growth rate corresponding to the most dangerous wavelength, say, $C_2 s/2\pi$, where C_2 is a constant.

From Taylor instability theory (Taylor 1950), the most dangerous wavelength is

$$\lambda_d = 2\pi\sqrt{\frac{3\sigma}{(\rho_f - \rho_g)g}} \tag{4.32}$$

and the corresponding growth rate is

$$growth\ rate = \left(\frac{4(\rho_f - \rho_g)^3 g^3}{27(\rho_f + \rho_g)^2 \sigma}\right)^{\frac{1}{4}} \tag{4.33}$$

Then we have

$$volume\ of\ droplet = \frac{4\pi}{3}\left(\frac{\lambda_d}{C_1}\right)^3 \tag{4.34}$$

and

$$number\ of\ droplets\ per\ cycle = 2\left(\frac{2\pi r_j}{\lambda_d}\right) \tag{4.35}$$

where the coefficient 2 is the number of droplets per wave per cycle, and

$$cycle/sec = \frac{C_2}{2\pi}(growth\ rate) \tag{4.36}$$

Combining them we obtain

$$Q = Cr_j\left(\frac{\sigma^3}{(\rho_f - \rho_g)(\rho_f + \rho_g)^2 g}\right)^{\frac{1}{4}} \tag{4.37}$$

where

$$C = \frac{32}{3} 2^{\frac{1}{3}} 3^{\frac{1}{4}} \frac{C_2}{C_1^3} \tag{4.38}$$

If ρ_f is much larger than ρ_g, equation (4.37) can be simplified to

$$Q \simeq C r_j \left(\frac{\sigma^3}{g\rho^3} \right)^{\frac{1}{4}} \tag{4.39}$$

Since

$$Q = \frac{\pi}{4} d^2 u_f \tag{4.40}$$

we have

$$u_f d \left(\frac{g\rho^3}{\sigma^3} \right)^{1/4} = C_1 (\frac{r_j}{d}) \tag{4.41}$$

The above equation does not fit the data very well. The reason may be that it was derived without considering the effect of the axisymmetric stretching of the liquid drips (*see also* Batchelor, 1987). Our observations showed that stretching alters the wavelength and growth rate because the drips move radially as they grow. The jet nondimensional drip radius has some relation to those effects. To take it into account, we use the nondimensional groups in another form:

$$\frac{u_f d g^{1/4} \rho^{3/4}}{\sigma^{3/4}} = C_1 \left(\frac{r_j}{d} \right)^{C_2} \tag{4.42}$$

Our experiments gave

$$C_1 = 0.199 \ \textit{and} \ C_2 = 1.67 \tag{4.43}$$

which fit the data to a mean square deviation in r_j/d of 0.13.

Figure 4.18 shows a comparison of the data from the upward jet with the correlation previously mentioned. For very low flow rates the data deviate from the correlation.

For large jet velocity or large Froude number, the effect of gravity on liquid sheet is negligible. But for small jet velocity or small Froude number, this effect is unnegligible. Figure 4.19 shows the measured wavelength. For small r_j/d, the wavelength is close to the most dangerous wavelength. But for large r_j/d, the wavelength becomes smaller than the most dangerous wavelength.

4.4 Conclusions

Immediately after hydraulic jump, a back flow can occur on upper part of the liquid sheet. This back flow makes the velocity distribution nonuniform.

The downward hydraulic jump shows four different patterns. The vertical instability of jump is a sequence of bifurcations. They are jump without roller, with single roller, with double roller, and unstable jump. For the unstable jump two stages can be identified, which are the lower roller of the double roller drawing air and whole jump drawing air. This series of bifurcations is associated with the ability of surface tension to stabilize the jump.

The azimuthal instability is governed by Taylor instability.

For upward jets, Taylor instability dominates the phenomena, in which the droplets drip down at certain wavelength. The wavelength of the droplets is somewhat smaller than the prediction of Taylor instability theory.

The radius of dripping can be estimated by Equation 4.42.

REFERENCES

Batchelor, G. K., "The Stability of a Large Gas Bubble Rising through Liquid," *J. Fluid Mech.,* vol.184, pp.399-422, 1987.

Bellmann, R. and Pennington, R.H., "Effects of Surface Tension and Viscosity on Taylor Instability," *Q. Appl. Math.,* Vol.12, pp.151-162, 1954.

Birkhoff, G. and Zarantonello, E.H., *Jets, Wakes, and Cavities*, New York: Academic Press, 1957.

Bouhadef, P.M., "Étalement en couche mince d'un jet liquide cylindrique vertical sur un plan horizontal," *Journal de Mathematiques et de Physique appliquées (ZAMP),* Vol.29, 1978.

Craik, A.D.D., Latham, R.C., Fawkes, M.J., and Gribbon, P.W.F., "The Circular Hydraulic Jump," *J. Fluid Mech.,* Vol.112, pp.347, 1981.

Dhir, V. K. and Lienhard J. H., "Taylor stability of viscous fluids with application to film boiling," *Int.J.Heat Mass Transfer* 16, 2097-2109, 1973.

Errico, M., "A Study of the Interaction of Liquid Jets with Solid Surfaces," Ph.D. Thesis, University of California, San Diego, 1986.

Glauert, M.B., *Boundary Layer Research* (ed. H. Görtler), Berlin: Springer, 1958.

Hsieh, D. Y., "Effects of heat and mass transfer on Rayleigh-Taylor instability," *J. Bas. Engng*, 156-162, 1972.

Ishigai, S., Nakanishi, S., Mizuno, M., and Imamura, T., "Heat Transfer of the Impinging Round Water Jet in the Interference Zone of Film Flow along the Wall," *Bulletin of the JSME,* Vol.20, No.139, pp.85-92, 1977.

Lienhard, J. H. and Wong, P. T. Y., "The Dominant Unstable Wavelength ad Minimum Heat Flux during Film Boiling on a Horizontal Cylinder," *J. Heat Transfer,* Vol.86, pp.220-226, 1964.

Lin, C.C., 1945, *Quart. Appl. Math.*, Vol.16, pp.153.

Nakoryakov, V.E., Pokusaev, B.G., and Troyan, E.N., "Impingement of an Axisymmetric Liquid Jet on a Barrier," *Int. J. Heat Mass Transfer,* Vol.21, pp.1175-1184, 1978.

Olsson, R.G., and Turkdogan, E.T., "Radial spread of a liquid stream on a horizontal plate," *Nature*, Vol.211, No.5051, pp.813-816.

Plesset, M. S. and Whipple, C. G., "Viscous effects in Rayleigh-Taylor instability," *Physics Fluids* 17, 1-7 (1974).

Peterka, A.J., "Hydraulic Design of Stilling Basins and Energy Dissipators," *U.S. Dept. Interior, Bur. Reclamation, Engr. Monograph 25*, 1963.

Stevens, J. and Webb, B. W., "Local Heat Transfer Coefficients under an Axisymmetric, Single-Phase liquid Jet," *J. Heat Transfer*, Vol.113, pp.71, February, 1991.

Streeter, V. L. and Wylie, E. B., *Fluid Mechanics,* 7th ed., New York, McGraw-Hill, 1979.

Tagahvi-Tafreshi, K. and Dhir, V.K., "Taylor Instability in Boiling, Melting and Condensation or Evaporation", *Int. J. Heat Mass Transfer*, Vol.23, pp.1433-1445, 1980.

Taylor, G. I. and Davies, R. M. "The rate of rise of large volumes of gas in water," Reproduced in *Underwater Explosions Research*, vol.2, Office of Naval Research, Washington, 1950.

Taylor, G.I., "The Instability of Liquid Interfaces When Accelerated in a Direction Perpendicular to Their Planes–Part I", *Proc. Royal Soc.*, Vol.A-201, pp.192-196, 1950.

Watson, E.J., "The radial spread of a liquid over a horizontal plane," *J. Fluid Mech.*, Vol.20, pp.481-499, 1964.

Table 4.1: Hydraulic jump data for water.

$\mathrm{Re}_d = 4.45 \times 10^4$		
We	r_j/d	s/h
6.09	6.08	104.3
4.77	11.37	88.4
4.67	12.32	82.5
4.61	14.0	70.7
4.24	14.96	59.3
3.97	16.49	48.53
3.83	16.0	48.82
3.61	17.13	41.91
3.39	18.73	34.89
3.13	18.25	33.38
2.88	19.53	27.8
3.00	19.69	28.83
2.66	18.57	27.72
2.08	21.77	17.56
2.52	19.21	23.10

Table 4.2: Hydraulic jump data for water.

$\mathrm{Re}_d = 6.10 \times 10^4$		
We	r_j/d	s/h
6.18	7.86	127.1
5.15	13.71	85.79
4.83	14.82	72.36
4.51	15.73	62.34
4.53	15.93	52.64
4.18	17.14	42.76
3.82	18.45	35.45
3.53	20.07	27.13
3.28	21.89	28.55
3.22	22.08	23.81
2.98	22.97	20.43

Table 4.3: Hydraulic jump data for water.

$Re_d = 7.47 \times 10^4$		
We	r_j/d	s/h
5.51	8.97	124.3
5.41	13.7	90.39
4.88	14.72	74.44
4.52	17.14	57.09
4.58	16.94	58.64
4.31	17.24	54.02
3.91	18.56	44.73
3.91	19.16	42.73
3.68	20.67	36.69
3.58	21.58	33.81
3.18	22.29	28.86
3.01	23.59	25.49
$Re_d = 8.62 \times 10^4$		
We	r_j/d	s/h
5.36	8.64	122.75
4.90	14.65	75.46
4.42	17.05	56.84
3.70	19.84	39.55
3.11	23.27	27.22
4.65	16.65	61.53
4.29	18.24	50.88
4.09	19.53	44.19
3.54	20.01	37.57
3.41	21.33	33.41
3.39	23.37	29.72
2.86	24.81	23.26

Table 4.4: Hydraulic jump data for water.

$Re_d = 9.88 \times 10^4$		
We	r_j/d	s/h
5.76	8.87	136.73
5.14	15.5	74.39
4.92	17.75	60.99
4.51	18.35	53.74
4.07	19.66	47.65
3.79	20.16	43.51
3.79	22.08	36.32
2.90	24.15	25.01
$Re_d = 11.8 \times 10^4$		
We	r_j/d	s/h
6.10	9.67	136.6
4.70	17.84	59.01
4.54	19.14	52.65
4.16	22.09	40.89
4.16	21.38	42.43
3.70	23.37	34.03

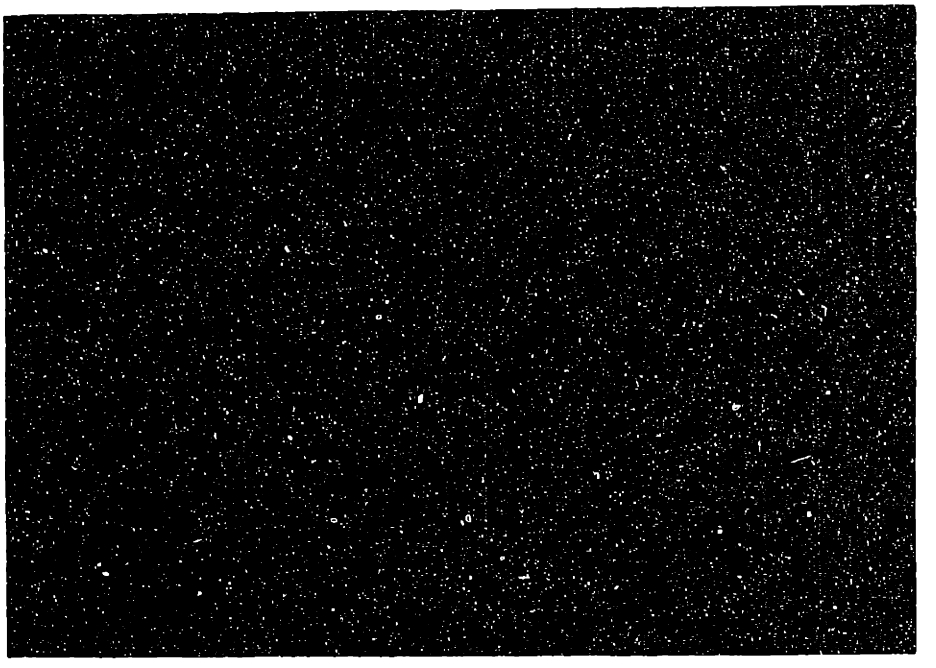

Figure 4.1: Hydraulic jump for a downward jet at d=4.96 mm (this low-speed jet was driven by gravity).

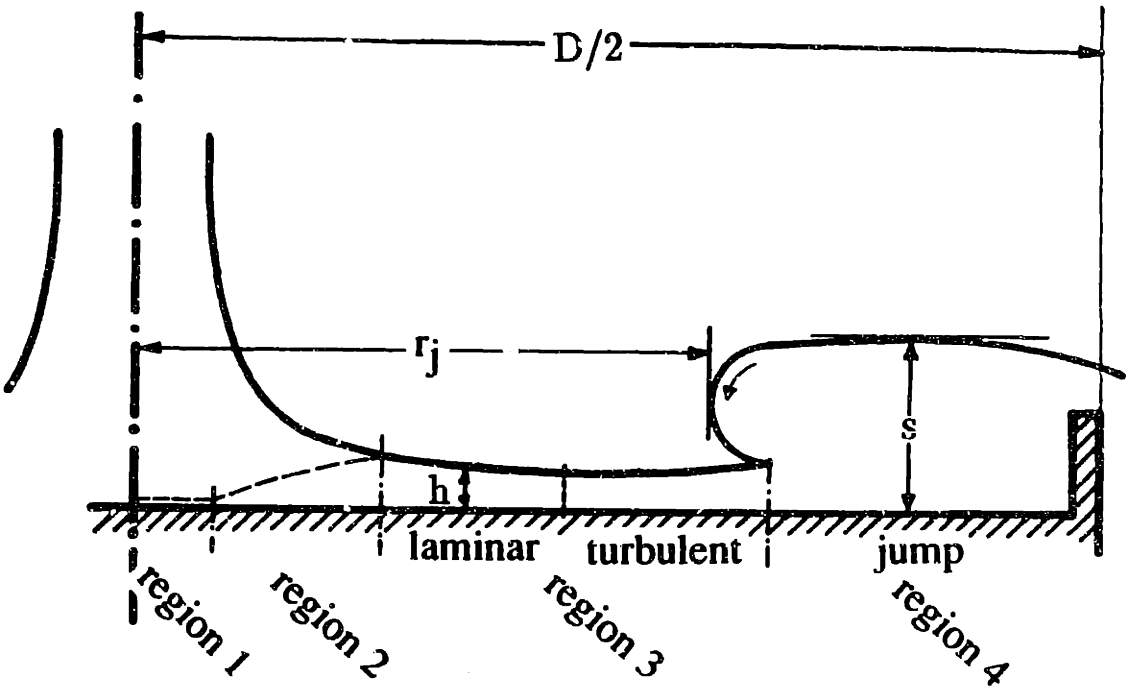

Figure 4.2: Region map for the downward-flowing jet.

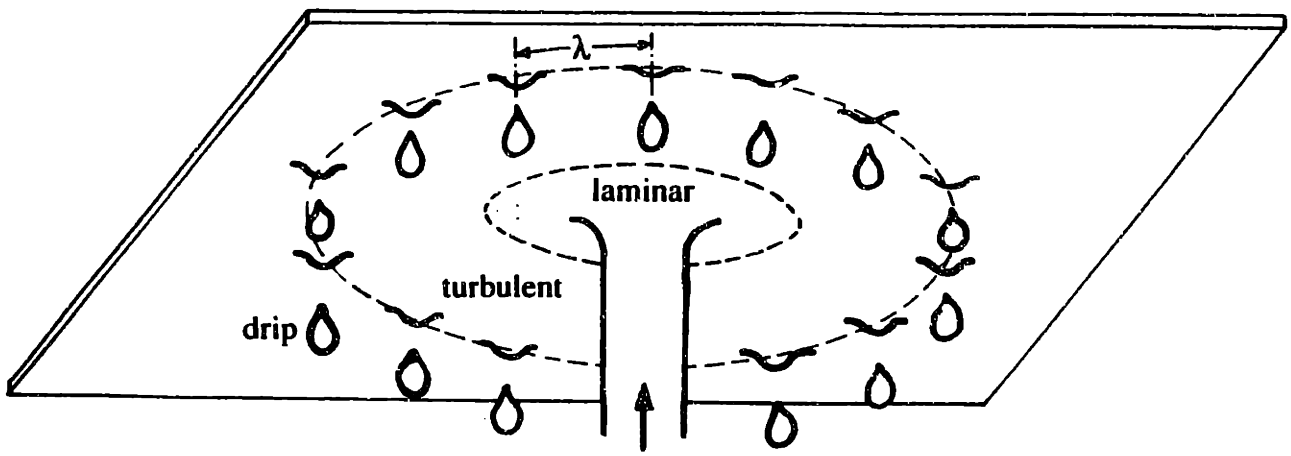

Figure 4.3: Upward jet.

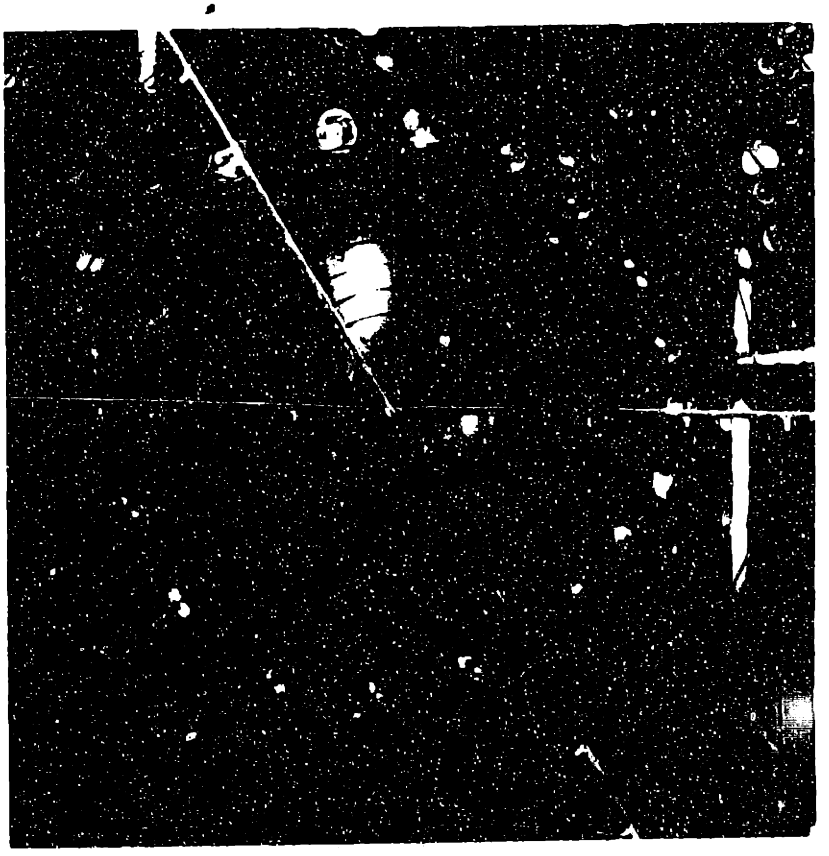

Figure 4.4: Rayleigh-Taylor instability for a upward water jet at u_f=18.9m/s and d=4.96mm.

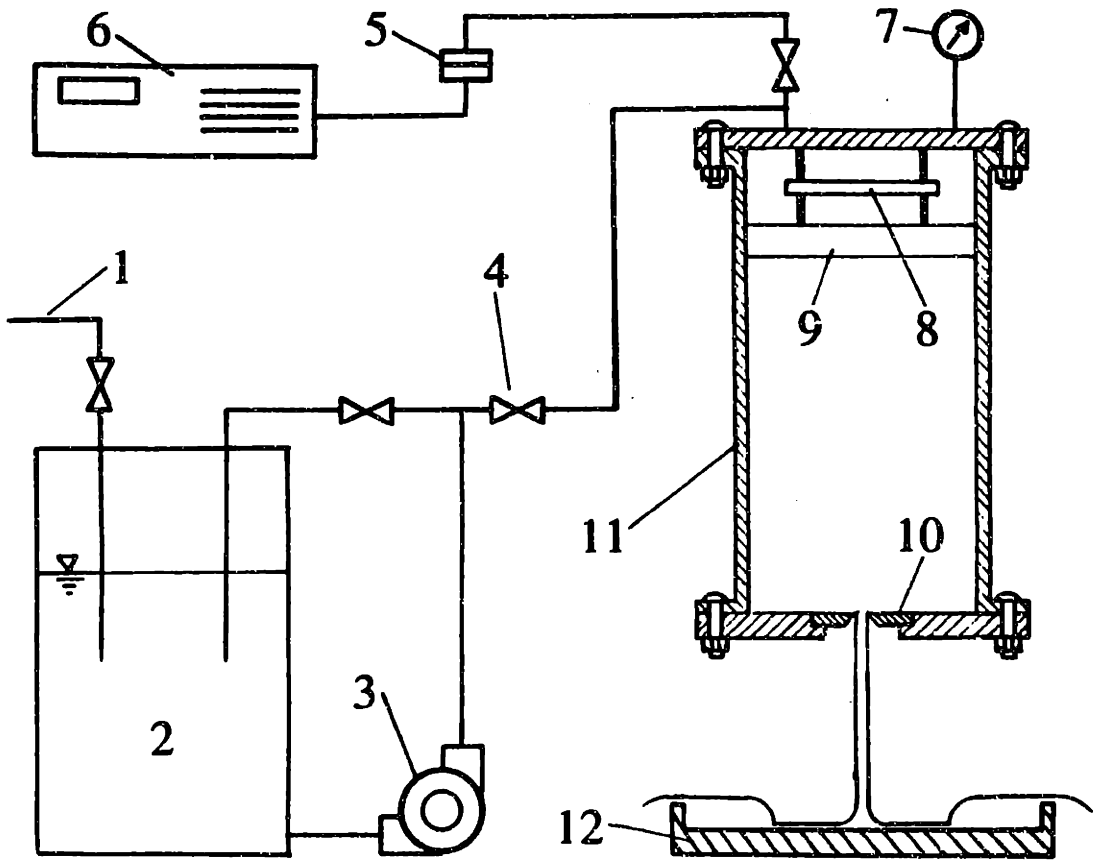

Figure 4.5: Experimental setup 1. water supply; 2. water tank; 3. pump 4. control valve; 5. pressure transducer; 6. digital voltmeter; 7. pressure gage; 8. strike plate; 9. honeycomb; 10. removable orifice; 11. pressure tank; 12. target plate

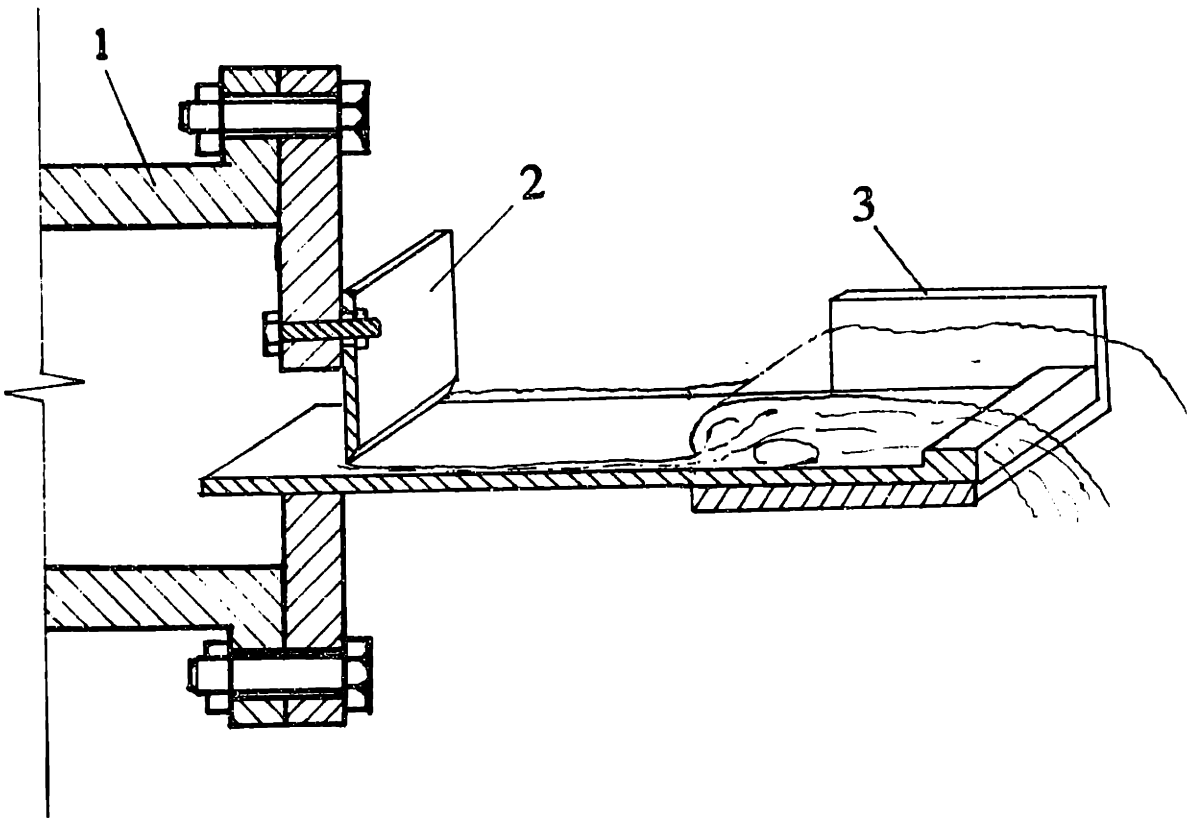

Figure 4.6: Experimental setup for the planar hydraulic jump 1. pressure tank; 2. adjustable gate; 3. moveable wall

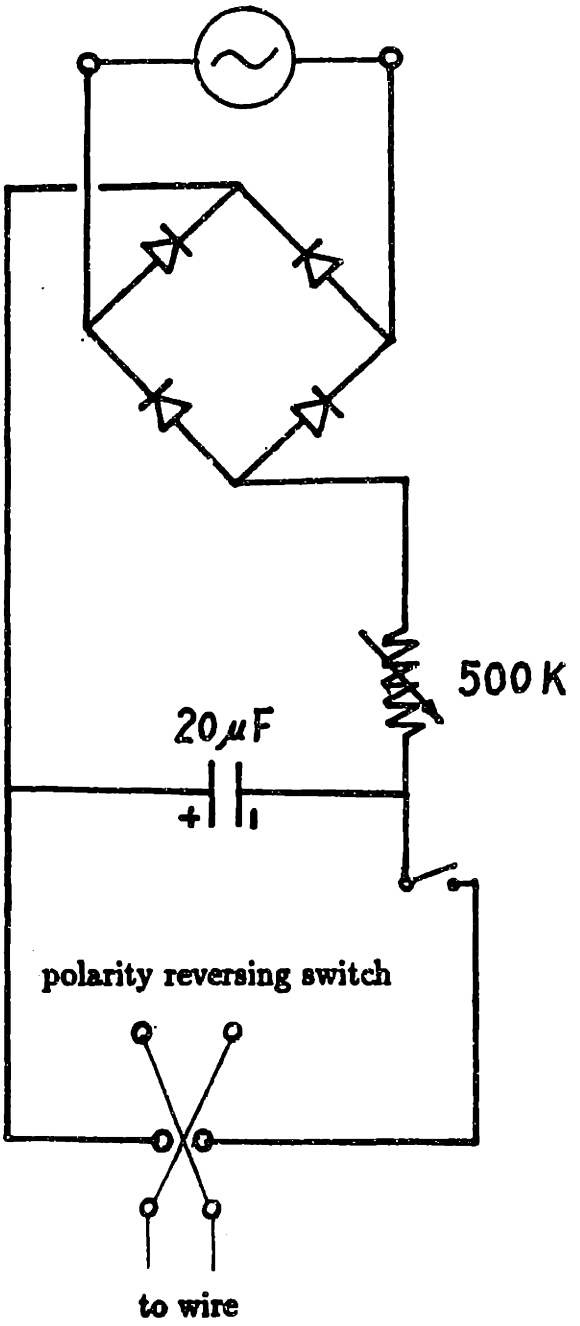

Figure 4.7: The circuit used for hydrogen bubble generation.

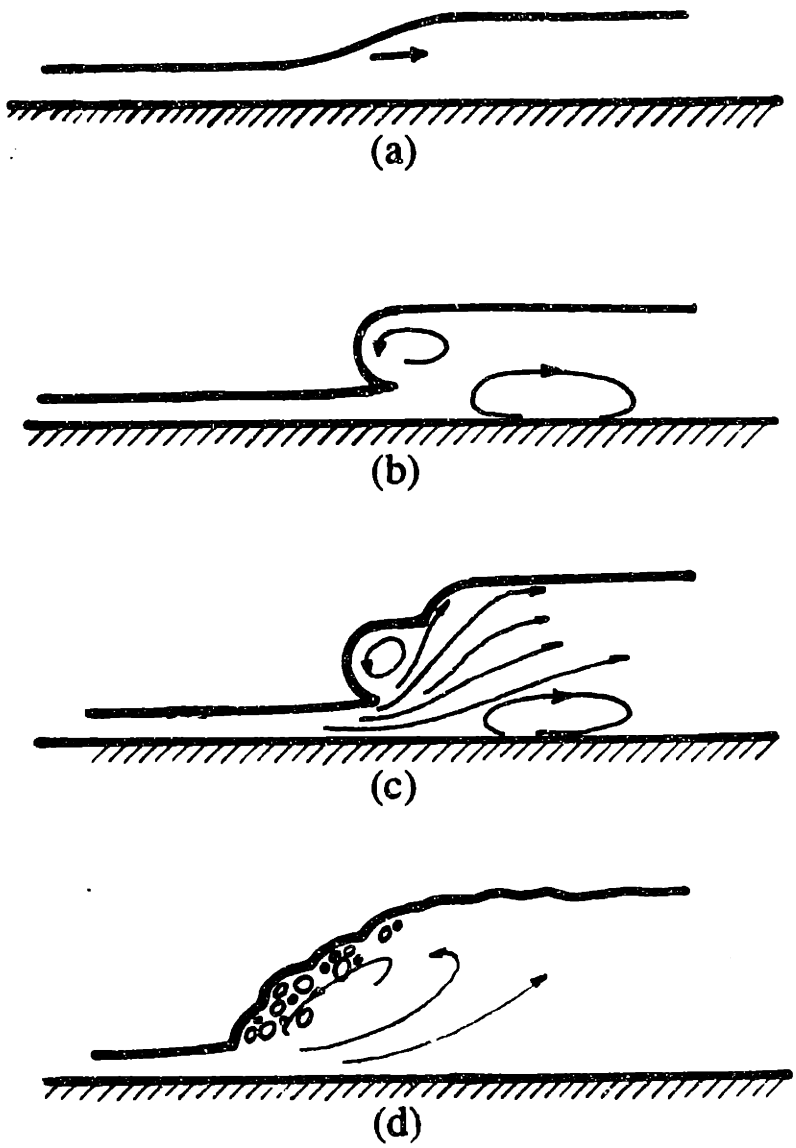

Figure 4.8: Instability of the jump (a) jump without roller; (b) jump with single roller; (c) jump with double roller; (d) unstable jump with turbulent flow and air entrainment

Figure 4.9: Planar hydraulic jump constructed by thin water film issued from a gate with 1.9mm height

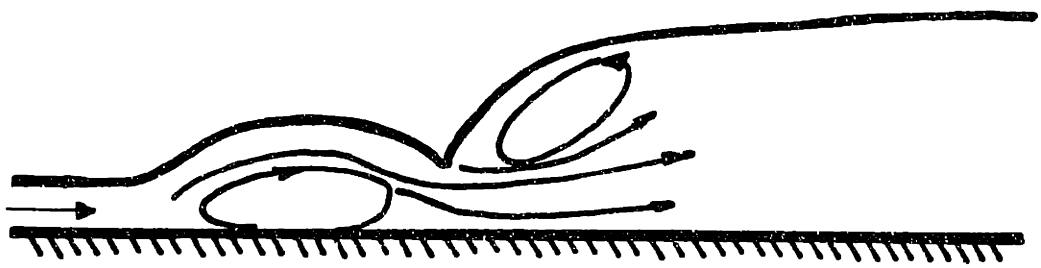

Figure 4.10: The hump and the vortex preceding the jump for thin planar flow.

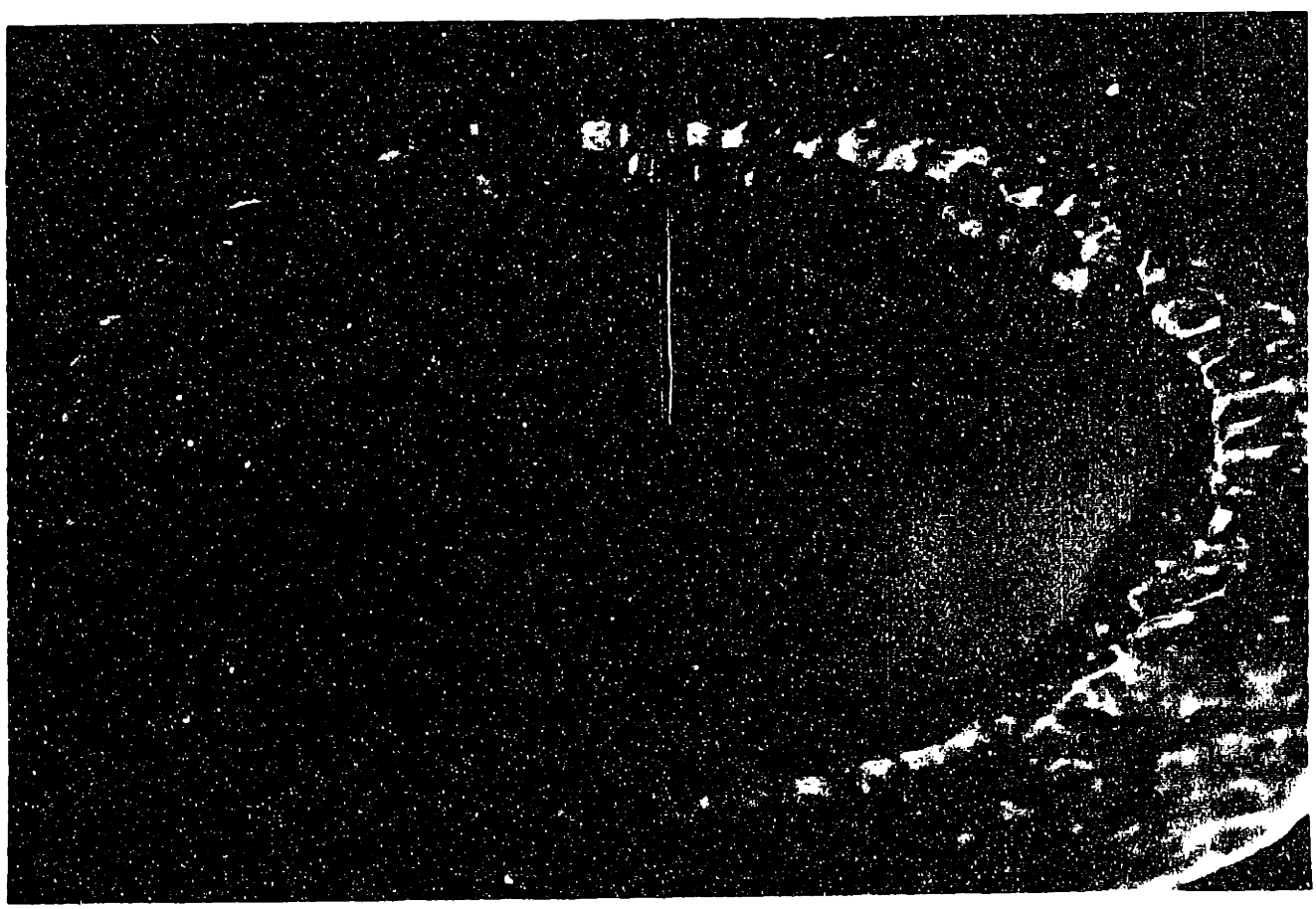

Figure 4.11: Jump with double roller at $Re_d = 51,500$, d=4.96mm, and $r_j = 90.3$ (depth of 9.2mm beyond hydraulic jump).

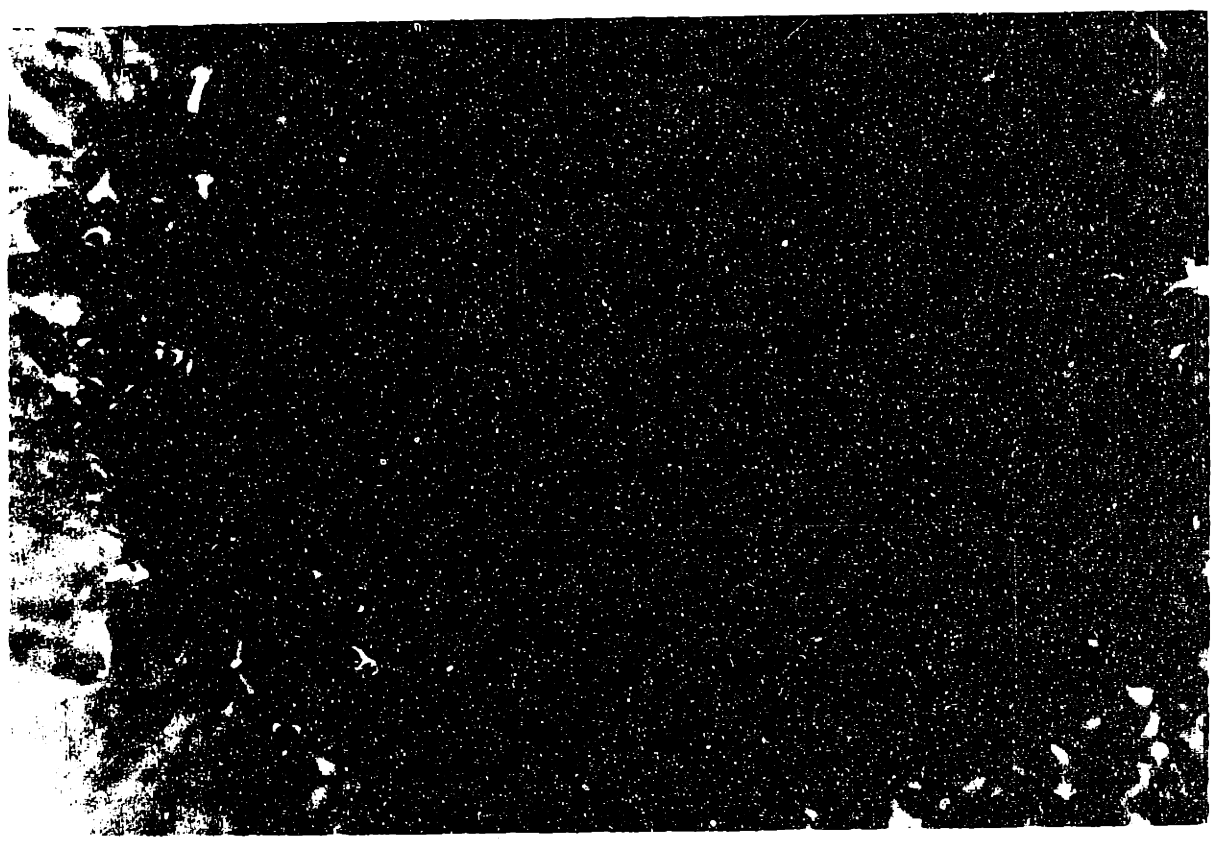

Figure 4.12: Unstable water jump at $Re_d = 45,500$ and d=4.96mm (depth of 13.2mm beyond hydraulic jump).

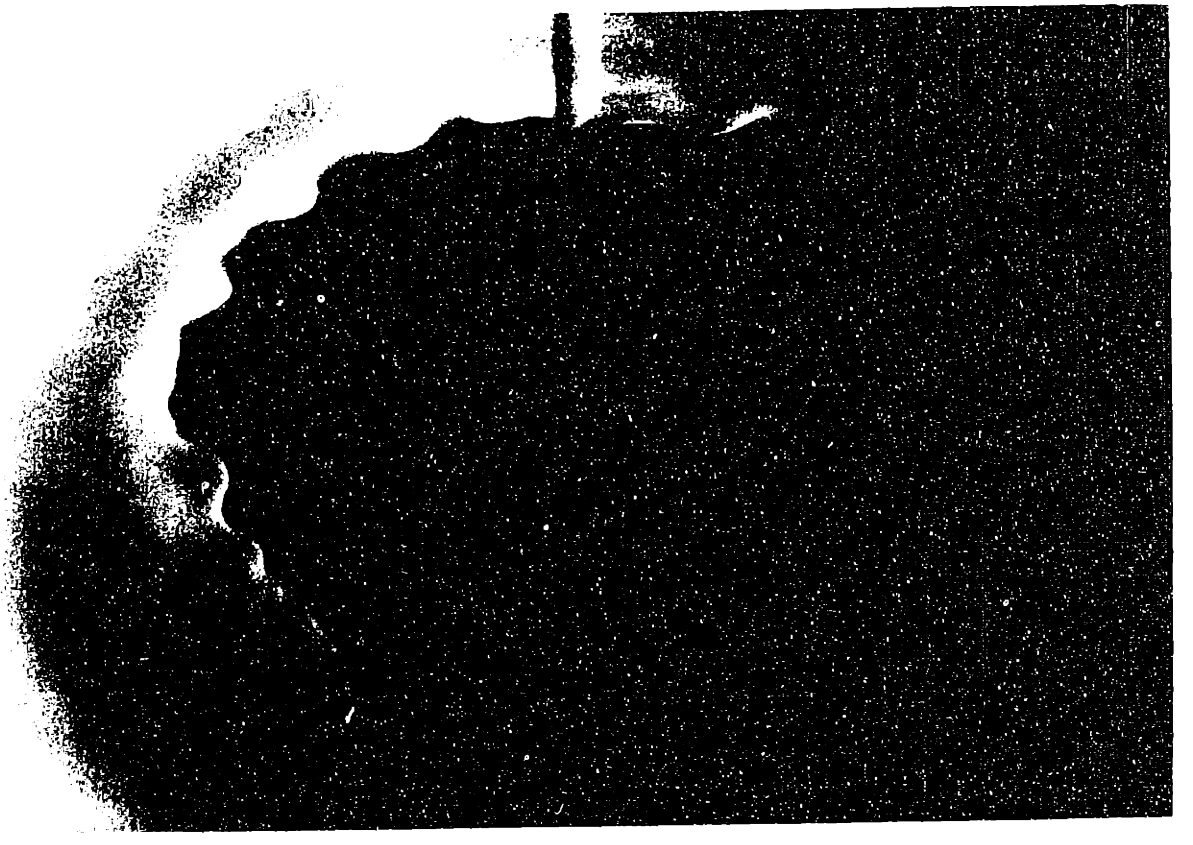

Figure 4.13: Wave pattern on the edge of jump (this low-speed jet was driven by gravity).

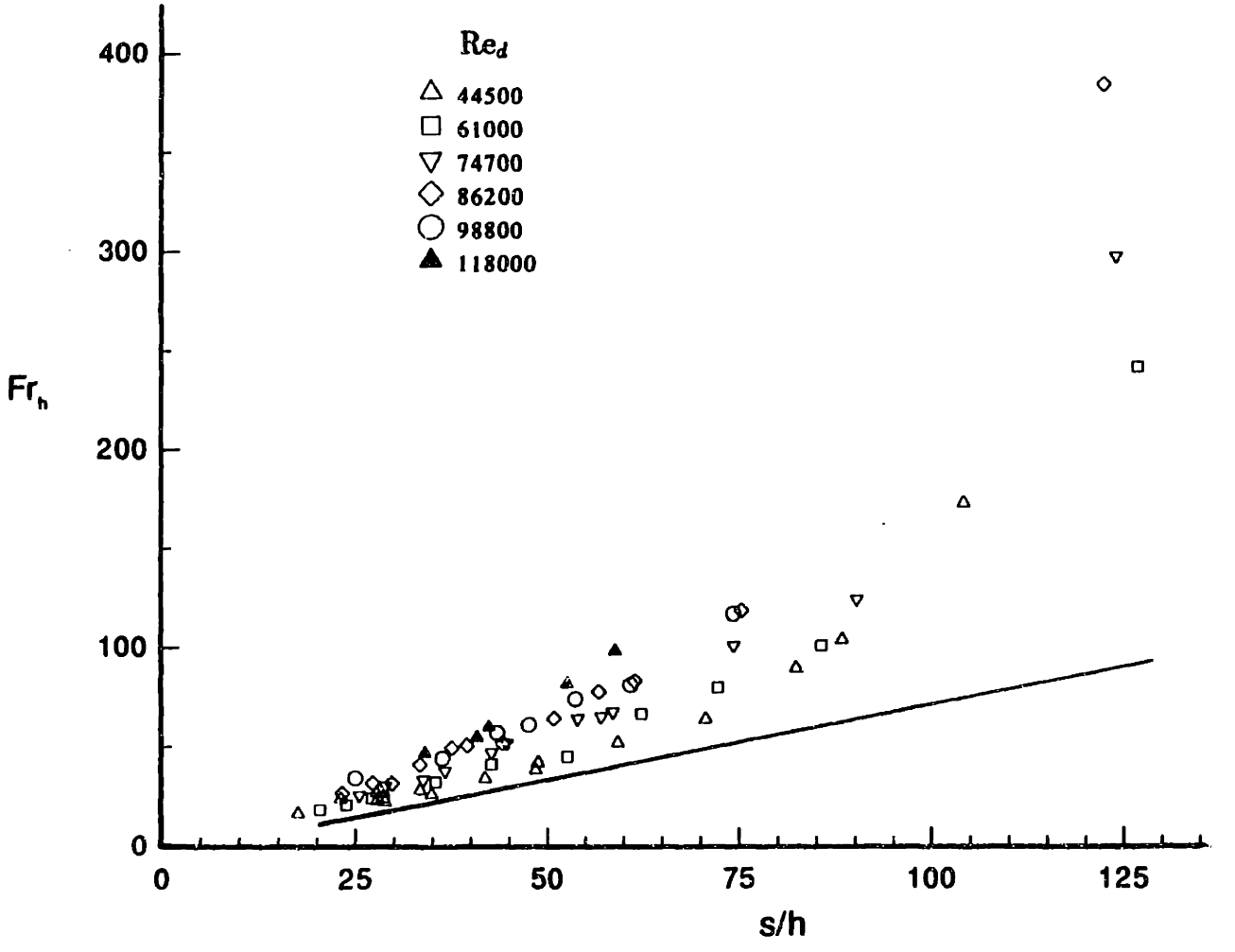

Figure 4.14: Plot of data as Froude number and ratio of downstream over upstream depth: —— Equation 4.12.

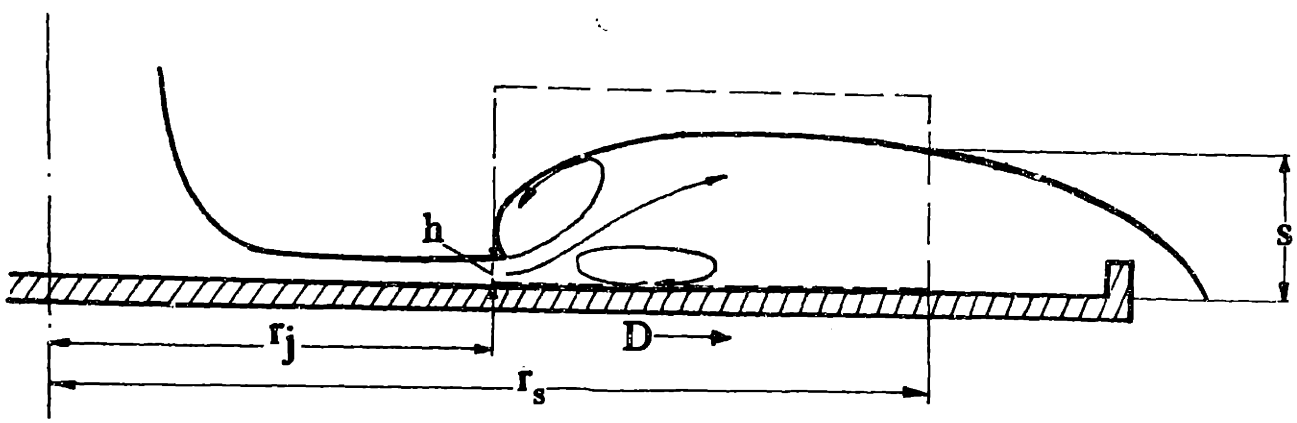

Figure 4.15: The control volume for the momentum balance

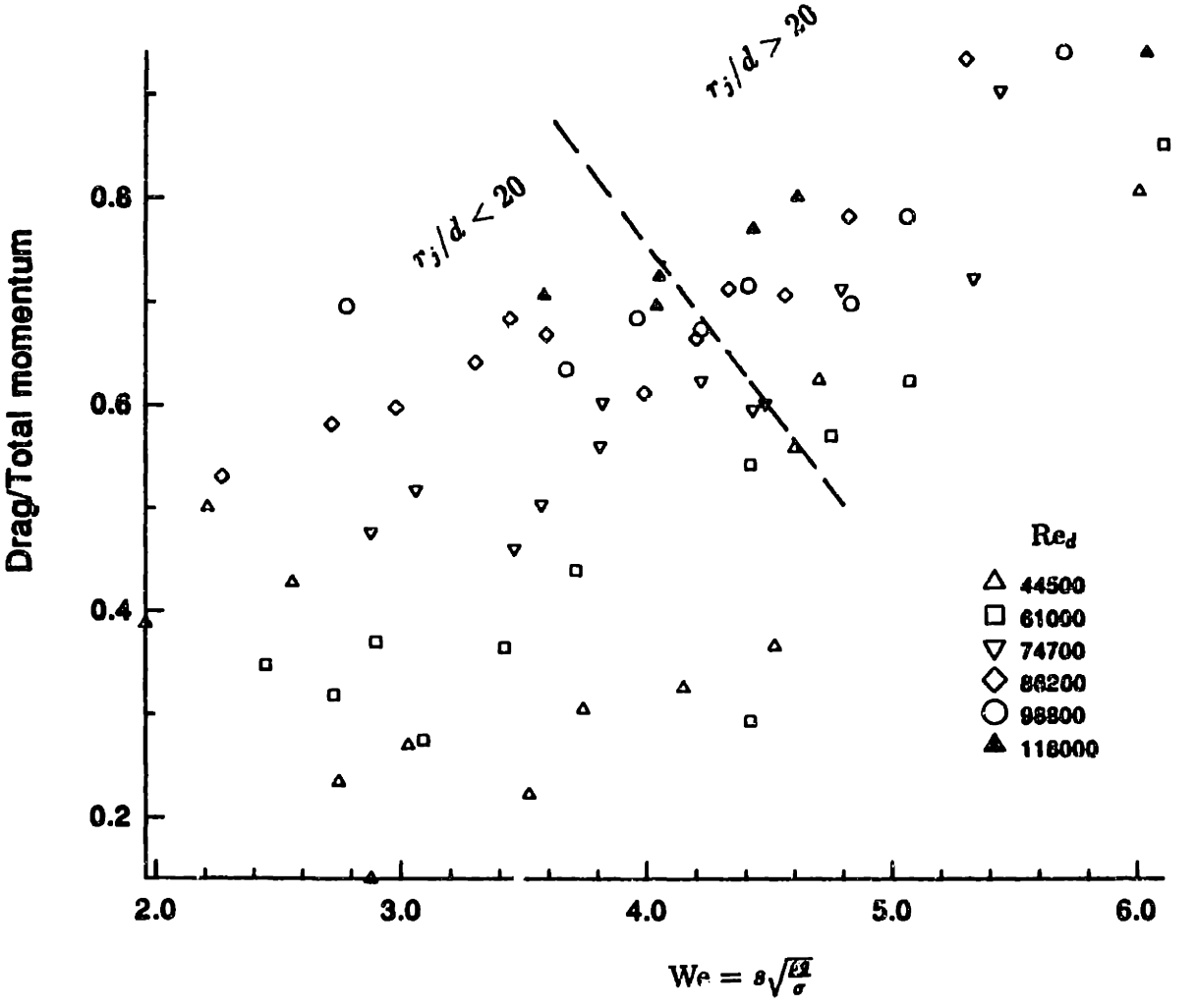

Figure 4.16: Plot of total momentum loss as a function of Weber number, and Reynolds number (0.5D/d=30.1)

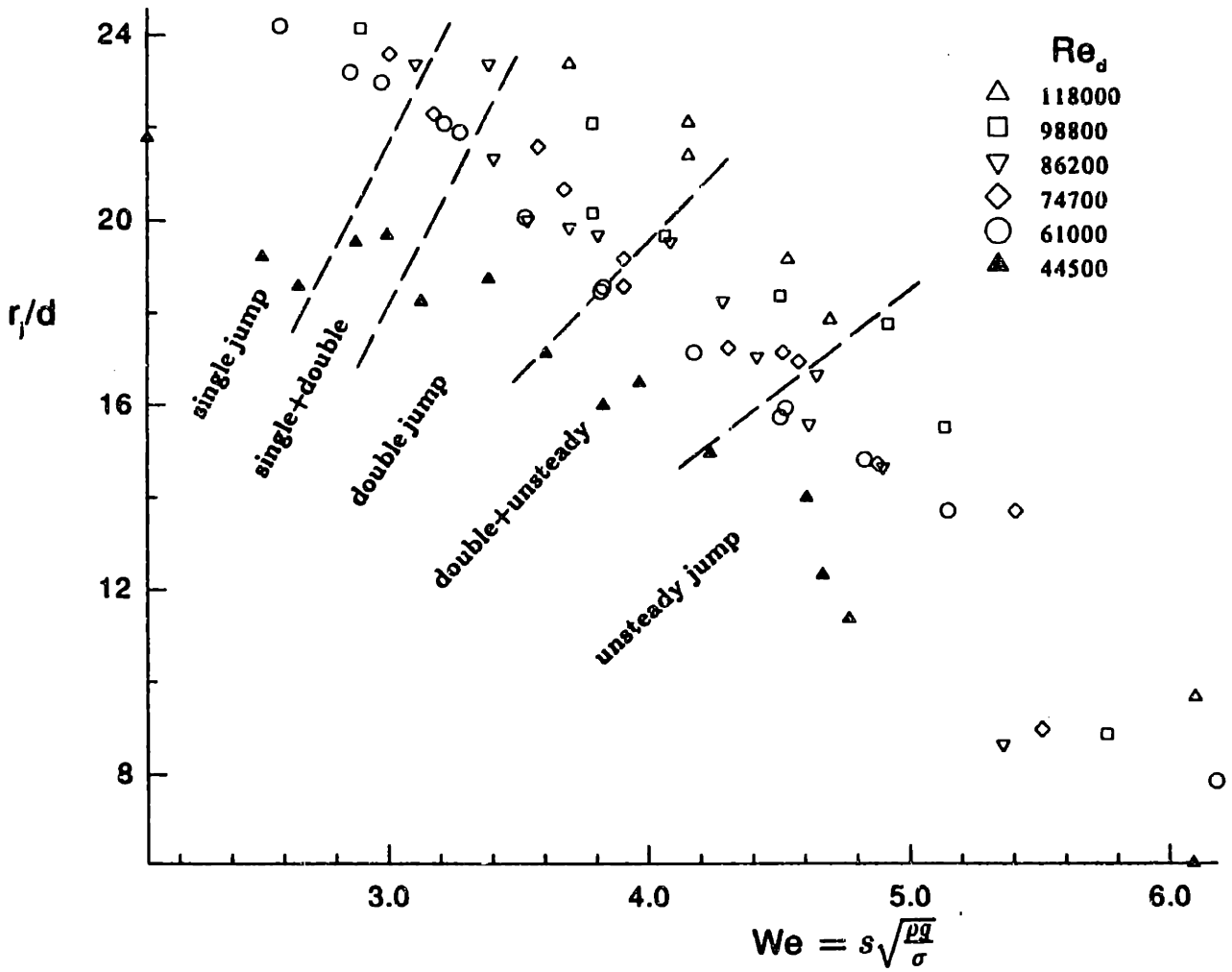

Figure 4.17: Plot of data as Weber number and dimensionless jump radius.

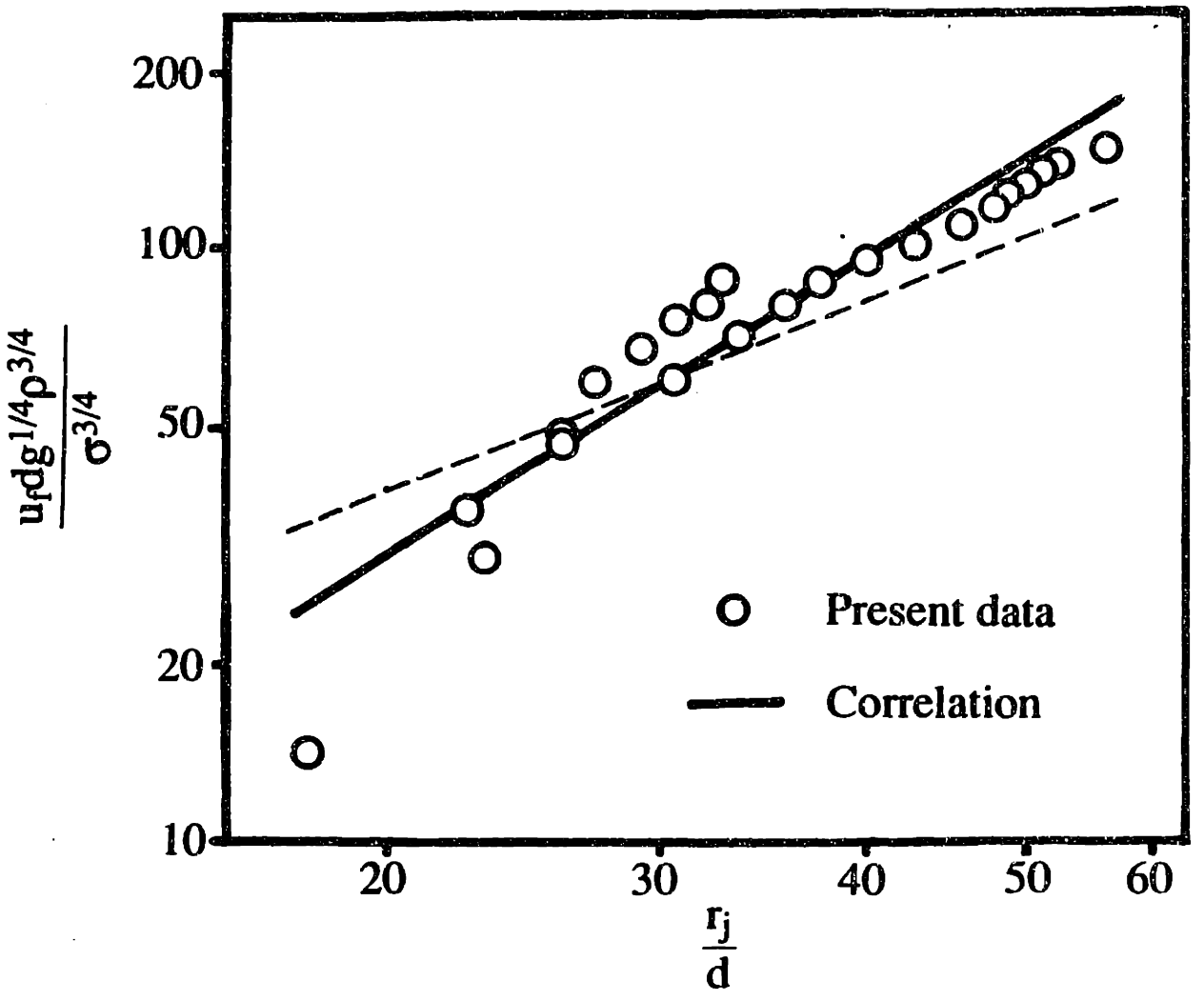

Figure 4.18: Comparison between the data and the correlations for upward jets: — — Equation 4.39; - - - Equation 4.40 .

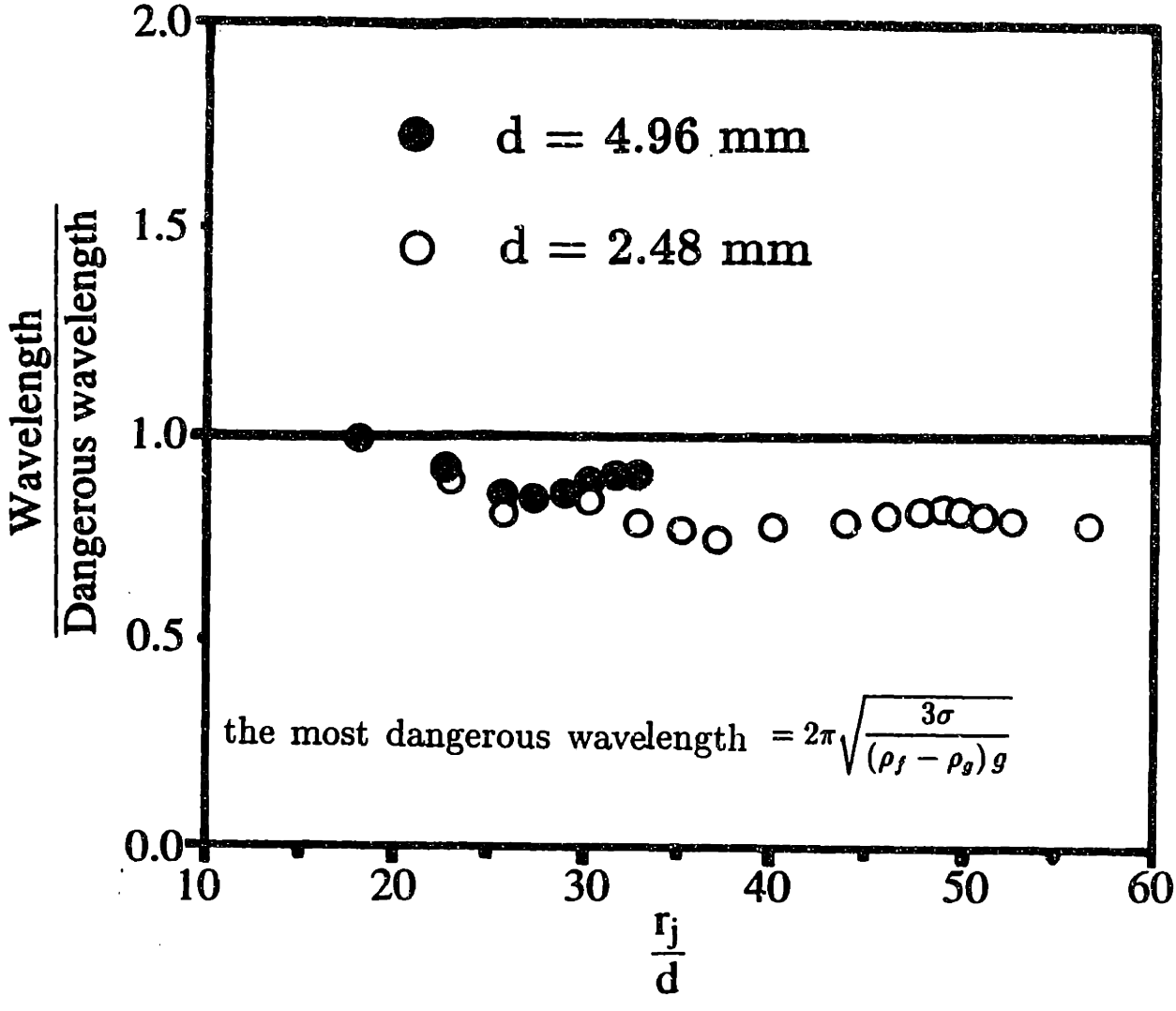

Figure 4.19: Wavelength variation with r_j/d.

Chapter 5

STAGNATION POINT HEAT TRANSFER

5.1 Introduction

The stagnation zone of an impinging jet is characterized by an extremely thin thermal boundary layer. While this produces a very large heat transfer coefficient, it also sensitizes the stagnation zone cooling efficiency to various parametric influences which would be less important for a thicker thermal boundary layer. In this paper, we examine some such effects, with a particular emphasis on those which alter the radial velocity gradient in the stagnation zone. Surface tension influences are our primary focus.

The stagnation point flow field has been studied extensively for submerged jets. The theory for the submerged jet is based on an infinite flow-field assumption, in which

the partial differential equations are transformed to ordinary differential equations by using a similarity coordinate (Schlichting, 1979 and White, 1974). For an unsubmerged jet, the free surface between the two phases imposes an additional boundary condition and greatly complicates the calculation of the inviscid flow above the wall boundary layer; numerical solution is required. The influence of the free surface on the near wall flow field should be more pronounced at small Weber number, when surface tension affects the flow; this may occur in particular for small diameter jets.

A number of numerical methods have been developed for free surface problems, and they generally fall into two classes (Crank, 1984). In the first class, the solution is obtained for the problem as originally formulated in the physical plane. After computation of approximate trial solutions, the free boundary is adjusted numerically to an improved free boundary. Various methods have been sought to avoid some of the difficulties associated with trial free boundary methods by interchanging the dependent variable with one or more of the independent variables. In the second class, the problem is recast by introducing some suitable change of coordinates, and the transformed problem is solved numerically like a fixed boundary problems.

To avoid solving the full Navier-Stokes equations, the stagnation flow can be divided into an inviscid flow and a boundary layer. The inviscid flow, which provides the freestream condition need for the near wall viscous flow, represents the primary computational problem. Schach (1935) employed an integral equation method, which was developed from Green's theorem. Shen (1962) expended the velocity potential in a series using Legendre polynomials. The free streamline boundary condition was

satisfied in an average manner. An iteration scheme was suggested, but it lacked a method for successively correcting the approximated free streamline position and it was not actually carried out. Strand (1964) expanded the velocity potential in Bessel functions. The free-streamline boundary condition was satisfied by discrete points. None of those solutions considered the surface tension.

In the following, a series solution which includes surface tension is constructed. An iteration scheme for the free surface is carried out using a correction function. The solution is given in terms of Legendre functions and satisfies the free-surface boundary conditions in an approximate manner, whose accuracy improves as more terms are retained.

Many heat transfer experiments on submerged jet impingement have been performed, but fewer consider unsubmerged jets. Nakoryakov *et al.* (1978) measured the Nusselt number for mass transfer beneath an impinging jet at high Schmidt number with uniform wall concentration. They did not directly test a relation for the stagnation zone transport. Instead, they used a relation for Nu to calculate their jet velocities. The relation they used seems to be quite close to that suggested above, although its origin remains obscure (it does not appear in the reference they cite). Nakoryakov *et al.* also measured wall shear stress in the stagnation zone, but the calibration of their stress probe was similarly based on an assumed value of $\partial u/\partial r$.

Stevens and Webb (1989) used a pipe-type nozzle producing turbulent incoming jets, and their measured Nusselt numbers are in the same general range, although a bit higher, than the present data. They represented their stagnation zone results by

a correlation which accounts for the Reynolds number dependence of the stagnation velocity gradient with a dimensional correlating factor of u_f/d

$$\mathrm{Nu}_d = 2.67\,\mathrm{Re}_d^{0.67}\left(\frac{z}{d}\right)^{-1/30}\left(\frac{u_f}{d}\right)^{-1/4}\mathrm{Pr}^{0.4} \tag{5.1}$$

where z is the distance of their nozzle from the heater. This correlation shows a somewhat different dependence on jet diameter and velocity than is found for the present laminar jets. Stevens and Webb present a second correlation for the radial variation Nu_d which does not represent the present data well at the large radii of interest to us, although it does represent their own data very well for r/d less than about 5.

Jiji and Dagan (1988) examined the characteristics of arrays of jets. Heat transfer coefficients for jet Reynolds numbers of 6240 and 12580 were reported. Stevens and Webb (1989) used tube-type nozzles and presented stagnation zone results as a correlation which included the dimensionless distance of their nozzle from the target plate and the dimensional ratio of jet velocity and diameter in addition to Reynolds and Prandtl numbers. In this chapter, data for uniform laminar jets and data for fully-developed turbulent jets are presented. Present results are compared with those of previous investigations. The influence of nozzle-to-target separation and velocity profile are discussed. The overall understanding of liquid jet stagnation-point heat transfer is summarized.

5.2 Analysis

The flow field is separated into an outer, inviscid irrotational flow and a near wall viscous boundary layer. The inviscid flow is determined as a potential flow with a surface tension along the free streamline. The resulting radial velocity distribution along the wall is used as the freestream flow in the subsequent boundary layer calculation. Gravitational effects are neglected.

5.2.1 Inviscid Impinging Jet Flow

For an inviscid, axisymmetric, and irrotational jet (Figure 5.1), the governing equation is

$$\nabla \cdot \vec{v} = 0 \tag{5.2}$$

with a velocity potential, ϕ,

$$\vec{v} = \nabla \phi \tag{5.3}$$

The boundary condition along the inlet to the computational domain is

$$\vec{v} = known = u_f \tag{5.4}$$

In present computation, the inlet velocity is assumed to be uniform (and thus irrotational) and purely downward. The potential influence of surface tension on free jets velocity has been considered by Lienhard and Lienhard (1984) who showed that

$$u_f = C_v u_0 = C_v \sqrt{\frac{2P_0}{\rho}} \tag{5.5}$$

for sharp-edged orifices, with P_0 the gauge stagnation pressure in the plenum and ρ the liquid density. They further showed that the velocity coefficient, C_v, was essentially equal to unity. Thus, we take the inlet velocity to be

$$u_f = u_0 \equiv \sqrt{\frac{2P_0}{\rho}} \tag{5.6}$$

as if our jet had issued from a plenum through a sharp-edged orifice and completed its contraction. The inlet is located one diameter above the target plate.

Along the free streamline, the velocity vector is obtained using Bernoulli's equation and the condition of no flow through the liquid surface. The velocity normal to the surface is

$$v_n = 0 \tag{5.7}$$

The velocity tangent to the streamline is

$$v_t = \sqrt{\frac{2P_0}{\rho} - 2\frac{\sigma\kappa}{\rho} + 4\frac{\sigma}{\rho d}} \tag{5.8}$$

where κ is the curvature of the free surface and d is the jet diameter. The Bernoulli constant is evaluated at the inlet and has the same value, $P_0+2\sigma/d$, for all streamlines. Along the target plate and the axis of symmetry

$$v_n = 0 \tag{5.9}$$

The boundary condition along the outlet is

$$\vec{v} = known \tag{5.10}$$

Schach's results (1935) show that the velocity is essentially uniform and parallel to the target plate for a radius larger than 1.25 diameter. In present computation, the

outlet is placed at $r/d = 1.25$ and the outlet velocity is assumed uniform and parallel to the target. From Bernoulli's equation, the outlet speed is

$$v_t = \sqrt{\frac{2P_0}{\rho} + 4\frac{\sigma}{\rho d}} \tag{5.11}$$

neglecting the free surface curvature along the outlet.

If the above equations and boundary conditions are to be solved, a choice of physical coordinate system is required. Cylindrical coordinates (Strand, 1964) have the advantage that the boundary conditions at inlet and outlet are simplified, since the inlet and outlet coincide with one of the coordinate planes. However, concurrent difficulties occur because the free surface derivatives in these coordinates become either infinite or zero at the inlet and outlet. While those derivatives are irrelevant for the zero surface tension case, they are essential when surface tension is included. Spherical coordinates (Shen, 1962) avoid the above problems and while preserving the simplicity of the mathematical expressions. We adopt spherical coordinates with radius r and polar angle θ. The origin is placed at the stagnation point with the polar axis along the vertical axis of symmetry; the free surface radius is $R(\theta)$.

Dimensionless velocity is defined relative to the inlet velocity:

$$\vec{v}^* = \frac{\vec{v}}{u_0} \tag{5.12}$$

The coordinates r and R are nondimensionalized as

$$r^* = \frac{r}{2d} \tag{5.13}$$

$$R^* = \frac{R}{2d} \tag{5.14}$$

The factor 2 is included to make the dimensionless radius less than unity in the do ain of computation so as to guarantee the convergence of the series in Equation 5.24. In addition, we scale the velocity potential and the surface curvature as

$$\phi^* = \frac{\phi}{2d\,u_0} \tag{5.15}$$

$$\kappa^* = 2d\,\kappa \tag{5.16}$$

The magnitude of the surface tension pressure relative to the dynamic pressure is characterized by the Weber number

$$\mathrm{We}_d = \frac{\rho u_0^2 d}{\sigma} \tag{5.17}$$

In terms of the velocity potential, the dimensionless equation of motion is

$$\nabla^2\phi^* = \left[\frac{1}{r^{*2}}\frac{\partial}{\partial r^*}\left(r^{*2}\frac{\partial}{\partial r^*}\right) + \frac{1}{r^{*2}\sin\theta}\left(\frac{\partial}{\partial\theta}\sin\theta\frac{\partial}{\partial\theta}\right)\right]\phi^* = 0 \tag{5.18}$$

The boundary condition along the inlet is

$$\left(\frac{\partial\phi^*}{\partial n^*}\right)_{inlet} = \frac{\partial\phi^*}{\partial r^*}\cos\theta - \frac{1}{r^*}\frac{\partial\phi^*}{\partial\theta}\sin\theta = -1 \tag{5.19}$$

The boundary condition along the outlet is

$$\left(\frac{\partial\phi^*}{\partial n^*}\right)_{outlet} = \frac{\partial\phi^*}{\partial r^*}\sin\theta + \frac{1}{r^*}\frac{\partial\phi^*}{\partial\theta}\cos\theta = \sqrt{1 + 4/\mathrm{We}_d} \tag{5.20}$$

Along the free surface, the boundary conditions are

$$\left(\frac{\partial\phi^*}{\partial n^*}\right) = \frac{1}{\sqrt{(\frac{1}{R^*}\frac{dR^*}{d\theta})^2 + 1}}\left(\frac{\partial\phi^*}{\partial r^*} - \frac{1}{r^{*2}}\frac{\partial\phi^*}{\partial\theta}\frac{dR^*}{d\theta}\right) = 0 \tag{5.21}$$

$$\left(\frac{\partial\phi^*}{\partial t^*}\right) = \frac{1}{\sqrt{(\frac{1}{R^*}\frac{dR^*}{d\theta})^2 + 1}}\left(\frac{1}{r^*}\frac{\partial\phi^*}{\partial r^*}\frac{dR^*}{d\theta} + \frac{1}{r^*}\frac{\partial\phi^*}{\partial\theta}\right) = \sqrt{1 + 4/\mathrm{We}_d - \kappa^*/\mathrm{We}_d} \tag{5.22}$$

κ^* is the dimensionless curvature of the free surface which is given by:

$$\kappa^* = \frac{R^*\left(\frac{d^2R^*}{d\theta^2} - R^*\right) - 2\left(\frac{dR^*}{d\theta}\right)^2}{\left[R^{*2} + \left(\frac{dR^*}{d\theta}\right)^2\right]^{3/2}} + \frac{\frac{\cot\theta}{r^*}\frac{dR^*}{d\theta} - 1}{\left[R^{*2} + \left(\frac{dR^*}{d\theta}\right)^2\right]^{1/2}} \tag{5.23}$$

5.2.2 Inviscid Flow Solution Procedure

The solution of Laplace's equation in spherical coordinates is

$$\phi^*(r^*, \theta) = \sum_{n=0}^{\infty} A_{2n} r^{*2n} P_{2n}(\cos\theta) \tag{5.24}$$

where $P_{2n}(\cos\theta)$ is Legendre function of $2n$ order. Legendre function automatically satisfies the boundary conditions along the target and the axis of symmetry.

The coefficients A_{2n} cannot be determined by conventional orthogonal function methods. Therefore, an alternative procedure must be sought. If the jet boundary can be located, we may pursue the problem as follows.

Assume $f_n(\theta)$ is an arbitrary continuous function of θ, and multiply both sides of boundary conditions by f_n. Substitute ϕ^* from Equation 5.24 into the equations and integrate along the boundaries to obtain a set of nonlinear algebraic equations for A_{2n}. By solving the set of algebraic equations, the coefficients A_{2n} can be calculated. However, at the beginning, the location of the free boundary of the jet is unknown and unlikely to coincide with a coordinate line. To proceed, we may assume a jet free boundary and integrate the equations along this assumed boundary; then we may correct the previous boundary and repeat the computation until the solution converges, satisfying both the basic equation and the boundary conditions. The problem is to construct a scheme to correct the free surface.

Shen (1962) suggested an iteration scheme, but he did not carry it out. The basic idea of the iteration was:

1. Assume a jet boundary $R^{*(0)}$; determine first $N/2$ of $A_{2n}^{(0)}$ by solving the set of equations.

2. Assume the improved jet boundary is

$$R^{*(1)} = \sum_{m=0}^{N/2} B_{2m} P_{2m}(cos\theta) \tag{5.25}$$

   and substitute into the set of equations.

3. These unknown B_{2m} can be determined by first substituting $A_{2n}^{(0)}$ for A_{2n} and $\sum_{m=0}^{N/2} B_{2m} P_{2m}(cos\theta)$ for $R^*(\theta)$ and solving this set of nonlinear algebraic equations simultaneously. With $A_{2n}^{(1)}$ thus determined, the new jet boundary is obtained.

4. Repeat the computation until the solution converges and the right jet boundary is found.

Shen's scheme did not give a method to correct the previous boundary and was difficult to carry out by computer. We suggest an alternative method to locate the free boundary, as represented by the function $R^* = R^*(\theta)$. The condition for determining the position of free surface is a flux condition that the total flow rate over any jet cross-section must be the same, that is

$$\int_0^{R^*(\theta)} 2\pi \frac{d\phi^*}{d\theta} dr^* = Q^* \tag{5.26}$$

for any r^*, or

$$\int_0^{\theta(R^*)} 2\pi \frac{d\phi^*}{dr^*} r^* d\theta = Q^* \tag{5.27}$$

for any θ. We integrate the total flow rate over a cross-section. If the flow rate is larger than Q^*, we pull in the free boundary (Figure 5.2). If the flow rate is smaller than Q^*, we push out the free boundary. Then, the correction function is

$$R^{*(n+1)}(\theta) = R^{*(n)}(\theta)[1 + \beta(Q^* - \int_0^{R^{*(n)}(\theta)} 2\pi \frac{d\phi^*}{d\theta} dr^*) \frac{1}{Q^*}] \tag{5.28}$$

where β is a relaxation factor. The convergence of the iteration strongly depends on the value of β. In the present computation, β was chosen between 0.03 to 0.2. Similarly, we can get

$$\theta^{(n+1)}(R^*) = \theta^{(n)}(R^*)[1 + \beta(Q^* - \int_0^{\theta^{(n)}(R^*)} 2\pi r^* \frac{d\phi^*}{dr^*} d\theta) \frac{1}{Q^*}] \tag{5.29}$$

In the computation, discrete points on the free surface are chosen to be corrected by the above two equations. For points near inlet and the outlet the second correction equation is used; for the other points the first one is used, to achieve better convergence. The points which represent the shape of free surface then are fitted into an equation. This fitted equation is substituted back into the set of original equations to calculate a new set of coefficients of A_{2n}. In principle, it is not necessary to curve-fit the points; the equation could be discretized instead. In the present calculation the first method curve-fit is used, because the calculation is simplified significantly.

5.2.3 Boundary Layer Solution

For the boundary layer, cylindrical coordinates are more convenient than spherical coordinates, since the boundary layer is very thin and no singularity arises as for the free surface. The basic equations for axisymmetric flow are

$$\frac{\partial(ur)}{\partial r} + \frac{\partial(vr)}{\partial y} = 0 \tag{5.30}$$

$$u\frac{\partial \vec{v}}{\partial r} + v\frac{\partial \vec{v}}{\partial y} = -\frac{1}{\rho}\nabla p + \nu\nabla^2\vec{v} \tag{5.31}$$

with the energy equation

$$u\frac{\partial T}{\partial r} + v\frac{\partial T}{\partial y} = \alpha\frac{\partial^2 T}{\partial y^2} \tag{5.32}$$

In these equations, r represents the radial distance from the stagnation point and y the vertical distance from the target plane.

The velocity just outside the boundary layer can be obtained from Equation (5.24)

$$U(r) = \sum_{n=0}^{\infty} 2nA_{2n}r^{2n-1}P_{2n}\left(\cos(\theta = \pi/4)\right) \tag{5.33}$$

Very close to the stagnation point only the first term in the above equation need be considered. The solution of the boundary layer equations can be obtained using a standard similarity transformation, from which the Nusselt number at the stagnation point is obtained as:

$$\mathrm{Nu}_d = G(\mathrm{Pr})\mathrm{Re}_d^{1/2}\sqrt{2\frac{d}{u_0}\frac{\partial U}{\partial r}} \tag{5.34}$$

where (White, 1974)

$$G(\mathrm{Pr}) \approx \begin{cases} \frac{\sqrt{2\mathrm{Pr}/\pi}}{1+0.804552\sqrt{2\mathrm{Pr}/\pi}} & \mathrm{Pr} \leq 0.15 \\ 0.53898\mathrm{Pr}^{0.4} & 0.15 < \mathrm{Pr} < 3.0 \\ 0.60105\mathrm{Pr}^{1/3} - .050848 & \mathrm{Pr} \geq 3.0 \end{cases} \tag{5.35}$$

The effect of the Weber number, or surface tension, on Nusselt number is implicit in the above equation through its effect on the dimensionless velocity gradient. This solution can be extended to radii beyond the stagnation point by adapting the series solution of Scholtz and Trass (1970).

5.3 Experiments

Experimental measurements of Nu_d were performed. The experimental apparatus consists of three parts: a water jet loop, a refrigerating system, and an electrical heating system. Details of the heater, instrumentation, and error analysis are given in Chapter 2

Laminar jets were produced using a sharp-edged orifice at the base of a plenum in which upstream disturbances were carefully damped. The turbulent jets were produced using straight tubes long enough to guarantee fully-developed turbulent flow.

The Nusselt number is based on the difference between the wall temperature at the stagnation zone and the temperature of the incoming jets. To ensure that the liquid free surface temperature is not too high, so that evaporation effects could be neglected (*see* Appendix B) and to increase the accuracy of the experiments, the

water was cooled to near 4°C. A narrow, high-power heated target was employed at fluxes of up to 300 kW/m^2 so as to further increase the resolution of the measured temperature difference. For each thermocouple measurement, a number of values were taken to eliminate random error. These measured values were averaged to get the actual temperature for the calculations. The uncertainty in Reynolds number is ±5% and in Nusselt number it is less than ±10%.

5.4 Results

Validation of the flow field solution is based on a comparison to existing results for infinite Weber number (Schach, 1935). The essential contribution of the flow field solution to the subsequent stagnation point heat transfer analysis is the streamwise velocity gradient which enters the Nusselt number

$$B = 2\frac{d}{u_0}\frac{dU}{dr} \tag{5.36}$$

For the present solutions, B is 1.83 for infinite Weber number. This value differs from Schach's value of 1.76* by only 3%, corresponding to a difference of about 1.5% in Nusselt number. While both the present solution and Schach's result are approximate, the good agreement between the two results lends a measure of confidence to the present procedure.

*Schach's figures 9 and 10 are a bit garbled. This often quoted value is obtained from his $\partial v/\partial z$ and continuity.

5.4.1 Calculated Flow Field and Velocity Profiles

Figure 5.3 shows the free surface shape and non-dimensional velocity distribution, $\frac{v}{\sqrt{2P_0/\rho}}$, for infinite Weber number. The free surface streamline deflects much sooner than do the interior streamlines. The radius of curvature of the free surface, in the plane of the axis of symmetry, is smaller than the jet radius. The velocity field is almost normal to a line at angle $\theta = \pi/6$ through stagnation point; in contrast, the line of normal flow for planar jets is $\theta = \pi/4$. The free surface for axisymmetric jet deflects only much closer to the target than for the planar case.

Free surface deflection is caused by the increased pressure near the stagnation point. The above characteristics are also seen in Figure 5.4, which shows the calculated non-dimensional pressure distribution, p/P_0. The pressure is a maximum at the stagnation point and decreases steadily with increasing radius. In the region $r < 0.25d$, the non-dimensional pressure is larger than 0.75; by $r/d = 0.66$, the pressure is less than 10% of the stagnation pressure.

5.4.2 The Role of Weber Number

Figure 5.5 shows the calculated free surface shape as a function of Weber number. The free surface deflection is progressively reduced as Weber number decreases. This is because surface tension provides an additional restoring force which balances the higher pressure near the stagnation region.

As previously shown by Lienhard and Lienhard (1984), a circular orifice will choke

when

$$\mathrm{We}_d = \frac{\rho u_o^2 d}{\sigma} \approx 8 \tag{5.37}$$

where orifice diameter, d_o, is related to jet diameter by

$$d = d_o \sqrt{C_c} \tag{5.38}$$

with $C_c = 0.611$ for orifices and $C_c \approx 1$ for pipes. Under these conditions, surface tension forces prevent a steady flow from the upstream plenum.

Figure 5.6 shows the velocity and pressure variation along the target plate at different Weber numbers. The smaller the Weber number, the faster the velocity grows with radius and the quicker the pressure drops along the plate. As Weber number decreases, the stagnation pressure rises, presumably as a result of surface-tension pressure rise across the free liquid surface.

Figure 5.7 and Table 5.1 show the effect of Weber number on the velocity gradient at stagnation point. The dimensionless gradient, B, at the stagnation point increases as Weber number decreases. Because the surface curvature changes from concave (along the incoming jet) to almost flat (in the far field), surface tension pressure decreases radially and produces a net increase in the momentum of the outflowing liquid. As the Weber number decreases from infinity to 12.7, the dimensionless velocity gradient increases by 26%. Since the Nusselt number is proportional to the square root of the velocity gradient, the Nusselt number goes up about 13%. For common cooling applications with water, the Weber number is usually more than several hundred, and Weber number effects will be negligible. For low velocity, small diameter jets, however, such effects may have some importance.

It is estimated by the momentum integral (*see* Appendix B) from boundary layer growth ideas that the stagnation zone is confined to the region $r/d \leq 0.787$. Figure 5.6 shows that the linear rise of velocity, expected for true stagnation point flow, occurs only for $r/d < 0.25$, although it may provide a useful approximation to r/d as large as 0.75.

Figure 5.8 shows the present experimental results for laminar water jets. The jet issued from a sharp-edge orifice with an orifice-to-target separation of more than 6 diameters to guarantee a uniform velocity distribution. The Weber number is in the range $2100 < \mathrm{We} < 34000$, for which our calculations show surface tension to be unimportant. The measured Nusselt numbers are in good agreement with the analysis for an infinite Weber number. Nevertheless, the stagnation point data show a small, systematic drop with decreasing diameter; for the smallest diameter jet, the deviation exceeds the estimated uncertainty. This suggests the presence of another, unidentified parametric effect which scales with jet diameter. The possibility that they resulted from surface tension effects was a partial motivation for this study. Viscous effects in the *outlet* region of the stagnation flow remain a possible cause, in so far as they provide additional resistance to the flow and may decrease the stagnation velocity gradient.

Table 5.2 shows the Nusselt number formulae obtained from Equation 5.34 when the values of B from other investigations are employed or when different expressions for $G(\mathrm{Pr})$ are used. In general, they differ little from the present results.

5.4.3 The Role of Velocity Profile

Our calculations have assumed a uniform velocity distribution for the incoming jet flow. In many cases, the velocity profiles of jets issuing from nozzles are not uniform. A jet flowing from a long pipe, in which the flow is fully developed, has a parabolic velocity profile if it is laminar or a one-seventh power law profile if it is turbulent. For many other cases, the velocity profiles may lie between a parabolic and a uniform profile for a laminar jet, or a between a one-seventh power law and uniform profile for a turbulent jet.

Previous investigations have shown that the radial velocity gradient at the stagnation point is much larger for a parabolic velocity profile than for uniform profile. Prediction and experiments by Scholtz and Trass (1970) showed that the velocity gradient B for an axisymmetric, parabolic-profile jet was a factor of four greater than for a uniform profile; this doubles the stagnation point Nusselt number (Table 5.2). Sparrow and Lee (1975) showed that, for two-dimensional cases, the asymptotic velocity gradient as the nozzle is moved away from the plate is almost four times as large for a a parabolic profile as for a flat profile. Note that the asymptotic value is reached at a small separation distance for a parabolic profile and at a large separation distance for a uniform profile.

The basic assumption in all such analyses is inviscid incoming flow. Without viscosity, the initially zero free-surface velocity of a nonuniform profile will not increase to the bulk velocity after the jet issues from its nozzle. Thus, for example, Sparrow and Lee (1975) concluded that the velocity gradient is relatively insensitive to sep-

aration distance within the $0.5d$ to $3d$ range of separation for a nonuniform initial profile. However, the absence of a wall shear stress at the free jet surface implies ongoing acceleration of the near surface liquid as the jet travels from nozzle to target.

Scriven and Pigford (1959) pointed out that the surface velocity was not constant, and analyzed its behavior. Duda and Vrentas (1967) performed numerical studies of the evolution of the free surface velocity. Davies and Makepeace (1978) studied the streamwise surface "ages" for different type of nozzles. Their experiments showed that the downstream distance at which the surface velocity approached the mean velocity depended strongly on the nozzle type and Reynolds number. For laminar jets of pure water, the measured surface velocities approach half the mean velocity at only about $3d$ from the outlet and reached 90% of mean velocity at about $20d$; these results were of the same order as the numerical results of Duda and Vrentas for initially parabolic jets at $Re = 2200$. For turbulent jets at Reynolds numbers of 18800, their data showed that the free surface velocity reached the 90% of mean velocity in only 1.5 jet diameter, much more rapidly than the $25d$ reported by Rupe (1962) for turbulent jets at Re=30000.

The parabolic and uniform profiles are the two extreme velocity distributions for jets and should provide upper and lower bounds on the stagnation velocity gradients. The former applies short distance from a pipe nozzle and the latter for a sharp edge-nozzle or for a pipe nozzle well-separated from the target, for which the nonuniform velocity profiles have already relaxed to a nearly uniform velocity. In any case, the assumption of a nonuniform velocity distribution should be tempered with a knowledge

of the nozzle-to-target separation.

5.4.4 The Effect of Separation Distance

Two factors appear to contribute to the effect of nozzle-to-target separation. As just noted, one is the relaxation of the initial distribution. The other is the deflection of the free streamline by target plate, which occurs only when the nozzle is very close to the target plate. For planar jets, Sparrow and Lee (1975) show that the Nusselt number goes up about 7% when the dimensionless separation, l/d, moves from ∞ to 1.5 for a uniform velocity distribution; the Nusselt number increases by 3% as the nozzle moves from l/d of ∞ to 0.5 for a parabolic initial velocity distribution. Larger increases occur when the nozzle is moved closer to the target plate. For axisymmetric jets, as mentioned above, the deflection of free streamline occurs even nearer the plate than for planar jets, and for l/d greater than 1, the effect of deflection is appears to be negligible.

The initial velocity distribution has much stronger effect on heat transfer than the deflection of free streamline. However, the liquid velocity profile relaxes steadily toward the the mean velocity, v_m, owing to internal shear stresses. From the discussion of the previous section, existing predictions and experiments suggest that an initially parabolic velocity relaxes rapidly toward a uniform profile. Within a few diameters from the nozzle the parabola will be partially dissipated; for a distance of more than 20 diameter, the distribution is essentially flat rather than parabolic. The parabolic initial velocity profile is important only for relatively small separation distances. For

a turbulent flow, the free surface velocity catches up the mean velocity even faster than for the laminar case. Again, the data of Davies and Makepeace (1978) show that the free surface velocity reaches 90% of mean velocity only in about 1.5 jet diameters. Apparently, for turbulent jets, the local mean velocity profile can be considered flat when the separation distance is greater than 1.5 diameters.

5.4.5 The Effect of Jet Turbulence

For a turbulent jet, it is instructive to rewrite the Weber number in term of the Reynolds number

$$\mathrm{We} = \left(\frac{\rho u_j d}{\mu}\right)^2 \frac{\mu^2}{\rho\sigma d} = \mathrm{Re}_d^2 \frac{\mu^2}{\rho\sigma d} \tag{5.39}$$

Since the Reynolds number is greater than 2400 for most turbulent jets, the Weber number is usually large (except for very small diameter jets), and direct surface tension effects in the stagnation point can be neglected.

While the turbulent mean velocity profile may play some role for small nozzle-to-target separations, the primary influence on heat transfer in the stagnation zone appears to be free-stream turbulence. This effect is well-known for submerged flow (Kestin, 1966) and has been experimentally demonstrated for liquid jets by the present experiments. The fluctuations in the freestream flow tend to disrupt the already thin stagnation boundary layer, increasing heat transfer by about 50% (Figure 5.9b, Table 5.2). For planar turbulent jets, experimental data by Wolf, Viskanta, and Incropera (1990) also showed that heat transfer enhancement at the stagnation line was as much as 79% relative to a laminar jet.

In addition to turbulence, capillary disturbances on the jet surface play an important role in the stability of the downstream liquid film. However, these surface disturbances have little or no effect on the stagnation point heat transfer. Figure 5.9 shows the ratio between the measured Nusselt number and $\mathrm{Re}_d^{1/2}\mathrm{Pr}^{1/3}$ against a nondimensional group ω, which characterizes the surface disturbances (*see* Chapter 3):

$$\omega = \mathrm{We}_d \exp\left(\frac{0.971}{\sqrt{\mathrm{We}_d}}\frac{l}{d}\right) \tag{5.40}$$

The stagnation zone heat transfer appears to be essentially independent of ω. This is not surprising given that the stagnation zone is well separated from the free surface and its capillary disturbances. However, the turbulent stagnation zone heat transfer is still much higher than for a laminar impinging jet. Turbulent disturbances are not directly separated from capillary disturbances in this presentation. However, as mentioned previously, variations in outlet turbulence intensity show only a weak additional dependence on Reynolds number beyond the u_f dependence of ω, and viscous damping of turbulence during travel to the plate may well be offset by growth of the fluctuating capillary disturbances to the fluid flow. Indeed, Figure 5.9b shows the augmentation factor to be essentially independent of jet Reynolds number in this range of Re_d and ω. The stagnation zone Nusselt number for the present experiments is represented by the following expression to an accuracy of about $\pm 10\%$:

$$\mathrm{Nu}_d = 1.24\,\mathrm{Re}_d^{1/2}\mathrm{Pr}^{1/3} \tag{5.41}$$

This equation should apply for any Prandtl number greater than 3, although the present experiments, for $7 < \mathrm{Pr} < 11$, do not verify the Pr range.

5.4.6 The Influence of Wall Properties

The stagnation region is characterized by a very thin thermal boundary layer. Wall roughness greater than several microns in height can be expected to influence Nu_d at high Reynolds number by partially perforating the thin boundary layer. These effects are presently under study in our laboratory.

Finite wall conductivity effects – conjugate heat transfer – is also an issue owing to the very large heat transfer coefficients in the stagnation region. For example, a 0.1 mm thick stainless steel target will have a Biot number $Bi = ht/k_w \approx 1$ under a 4 mm water jet at a Reynolds number of 80,000. Allowance for wall thermal resistance should usually be made when designing jet cooling systems.

5.5 Conclusions

The influence of surface tension on stagnation point heat transfer beneath an impinging liquid jet has been analytically studied. The effect of jet velocity profile and nozzle-to-target separation are also discussed. Various past results for the stagnation point Nusselt number are summarized.

- Surface tension affects the stagnation point velocity gradient and Nusselt number for We_d less than about 100. The increase in Nusselt number is about 15% at a Weber number of 12.7. For most industrial cooling applications, however, We_d is too large for this effect to be of significance.

- The dimensionless stagnation-point velocity gradient obtained for $We_d \rightarrow \infty$ is $B = 1.832$, is good agreement with the results of Schach (1935) and others.

- Stagnation point Nusselt number formulae for this and previous investigations are summarized in Table 2. Those results include both laminar and turbulent jets with both uniform and nonuniform velocity profiles; most have experimental validation. For laminar jets, the results differ principally in the method of correlating Prandtl number effects; more data is needed at very high and very low Prandtl number.

- Two formulae for stagnation-point heat transfer which agree well with data are that of Liu *et al.* (1991) for uniform laminar jets ($Nu_d = 0.797 Re_d^{1/2} Pr^{1/3}$) and that of Lienhard *et al.* (1991) for fully-developed turbulent jets ($Nu_d = 1.24 Re_d^{1/2} Pr^{1/3}$).

- Nusslet number can be significantly increased by a nonuniform velocity profile at the nozzle exit if the nozzle is very close to the target. However, existing evidence suggests that nonuniform velocity profiles rapidly become uniform after the fluid leaves the nozzle, and that the influence of a nonuniform profile diminishes rapidly as the nozzle-to-target separation is increased.

REFERENCES

Crank, J., *Free and Moving Boundary Problem,* Oxford, Clarendon Press, 1984.

Davies, J.T. and Makepeace, R.W., "Measurement of the Surface Ages of Water Jets," *AIChE Journal,* Vol.24, No.3, pp.524-530, May 1978.

Duda, J.L. and Vrentas, J.S., "Fluid Mechanics in Laminar Liquid Jets," *Chem. Eng. Sci.,* 22, 866 (1956).

Kestin, J, The effect of free-stream turbulence on heat transfer rates, *Adv. Heat Transfer,* 3. 1-32, 1966.

Jiji, L.M. and Dagan, Z., 1988, "Experimental Investigation of Single-Phase Multijet Impingement Cooling of an Array of Microelectronic Heat Source," *Cooling Technology for Electronic Equipment,* Hemisphere, New York.

Lienhard V, J.H., and Lienhard, J.H., "Velocity Coefficients for Free Jets from Sharp-Edged Orifices," *J. Fluid Engr.,* Vol.106, pp.13-17, 1984.

Miyazaki, H., and Silberman, E., "Flow and Heat Transfer on a Flat Plate Normal to a Two-Dimensional Laminar Jet Issuing From a Nozzle of Finite Height," *Intl. J. Heat Mass Transfer,* Vol.15, pp.2097-2107, 1972.

Nakoryakov, V.E., Pokusaev, B.G., and Troyan, E.N., "Impingement of an Axisymmetric Liquid Jet on a Barrier," *J. Heat Transfer,* Vol.21, pp.1175-1184, 1978.

Rupe, J.H., "On the Dynamic Characteristics of Free Liquid Jets," *Jet Propulsion Lab. Tech. Rept. No. 32-207,* 1962.

Schach, W., "Umlenkung eines kreisförmigen Flussigkeitsstrahles an einer ebenen Platte senkrecht zur Strömungsrichtung," *Ing.-Arch.*, vol.6, 51-59, 1935.

Schlichting, *Boundary Layer Theory,* 7th ed. New York: McGraw-Hill, 1979.

Scholtz, M.T. and Trass, O., "Mass Transfer in a Nonuniform Impinging Jet," *AIChE Journal,* pp.82-96, January 1970.

Scriven, L.E., and Pigford, R.L., "Fluid Dynamics and Diffusion Calculations for Laminar Liquid Jets," *AIChE Journal,* 5, 397, 1959.

Shen, Y.C., "Theoretical Analysis of Jet-Ground Plane Interaction," *IAS Paper No. 62-144,* 1962.

Sparrow, E.M. and Lee, L., "Analysis of Flow Field and Impingement Heat/Mass Transfer Due to a Nonuniform Slot Jet," *J. Heat Transfer,* pp.191-197, May 1975.

Stevens, J. and Webb, B.W., "Local Heat Transfer Coefficients Under an Axisymmetric, Single-Phase Liquid Jet," *J. Heat Transfer,* Vol. 113, pp.71-78, 1991.

Strand, T., "On the Theory of Normal Ground Impingement of Axi-Symmetric Jets in Inviscid Incompressible Flow", *Am. Inst. Aeron. Astronaut. Paper No.64-424,* 1964.

White, F. M., *Viscous Fluid Flow,* McGraw-Hill Book Company, New York, 1974.

Wolf, D.H., Viskanta, R., and Incropera, F.P., "Local Convective Heat Transfer from a Heated Surface to a Planar Jet of Water with a Nonuniform Velocity Profile," *J. Heat Transfer,* Vol.112, pp.899-905, November 1990.

Table 5.1: Velocity gradients at stagnation point during jet laminar impingement.

Investigators	$\frac{d}{u_j}\frac{\partial U}{\partial r}$	flow type	inlet velocity profile	l/d	We
Miyazak (1972)	0.951	planar	uniform	0.5	∞
	0.457	planar	uniform	1.5	∞
parrow and	0.964	planar	uniform	0.5	∞
Lee (1975)	0.445	planar	uniform	1.5	∞
	0.393	planar	uniform	∞	∞
	1.74	planar	parabolic	0.25	∞
	1.51	planar	parabolic	1.5	∞
Scholtz (1970)	2.32	circular	parabolic	0.5	∞
	0.903	circular	uniform	1.0	∞
Schach (1935)	0.88	circular	uniform	1.5	∞
Shen (1962)	0.743	circular	uniform		∞
Strand (1964)	0.958	circular	uniform	1.0	∞
Present	0.916	circular	uniform	1.0	∞
	0.981	circular	uniform	1.0	46
	1.06	circular	uniform	1.0	21
	1.16	circular	uniform	1.0	12.7
Present data	0.88	circular	uniform	> 6	> 2100

Table 5.2: Axisymmetric stagnation point Nusselt number expressions for various investigations.

Investigators	Nu_d	Velocity gradient & initial distribution
Scholtz and Trass (1970)	$0.727\,Re_d^{1/2}Pr^{0.361}$ $1<Pr<10$ l/d=1.0	Strand (1964) uniform laminar
Scholtz and Trass (1970)	$1.648\,Re_d^{1/2}Pr^{0.361}$ $1<Pr<10$ l/d=0.5	Inviscid vortex eqn., parabolic
Nakoryakov *et al.* (1978)	$0.753\,Re_d^{1/2}Pr^{1/3}$	Schach (1935) uniform laminar
Liu *et al.* (1991) Eqn. 5.33	$0.797\,Re_d^{1/2}Pr^{1/3}$ $Pr>3$ $l/d > 1.5$	Schach (1935) uniform laminar
Eqn. 5.33	$0.813\,Re_d^{1/2}Pr^{1/3}$ $Pr>3$ $l/d = 1$	Present (We $\rightarrow \infty$)
Eqn. 5.33	$0.832\,Re_d^{1/2}Pr^{1/3}$ $Pr>3$ $l/d = 1.5$	Strand (1964) uniform laminar
Eqn. 5.33	$0.733\,Re_d^{1/2}Pr^{1/3}$ $Pr>3$ $l/d = 1.5$	Shen (1962) uniform laminar
Lienhard *et al.* (1991)	$1.24\,Re_d^{1/2}Pr^{1/3}$ $Pr>3$ $l/d > 1.5$	Correlation, turbulent
Stevens and Webb (1991)	$2.6\,Re_d^{0.667}Pr^{0.4}(\frac{d}{l})^{0.0336}(\frac{d}{u_f})^{0.237}$	Correlation, turbulent

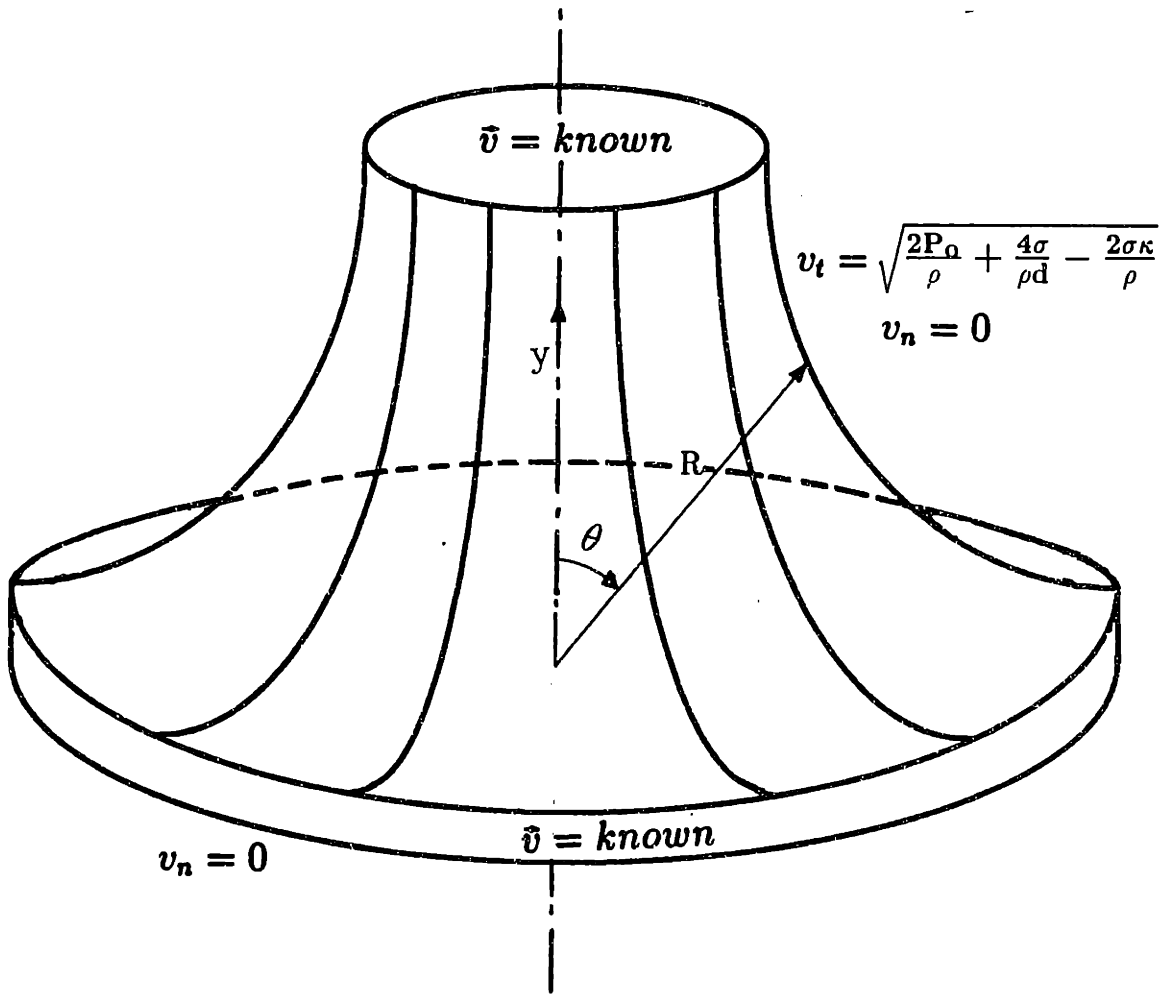

Figure 5.1: Computational domain and boundary conditions.

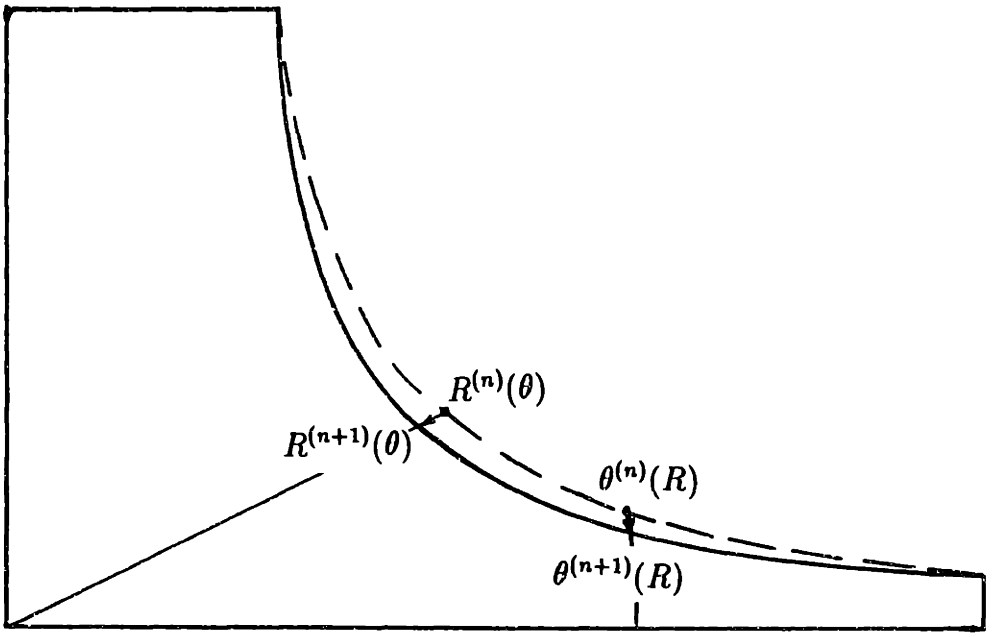

Figure 5.2: Free surface iteration.

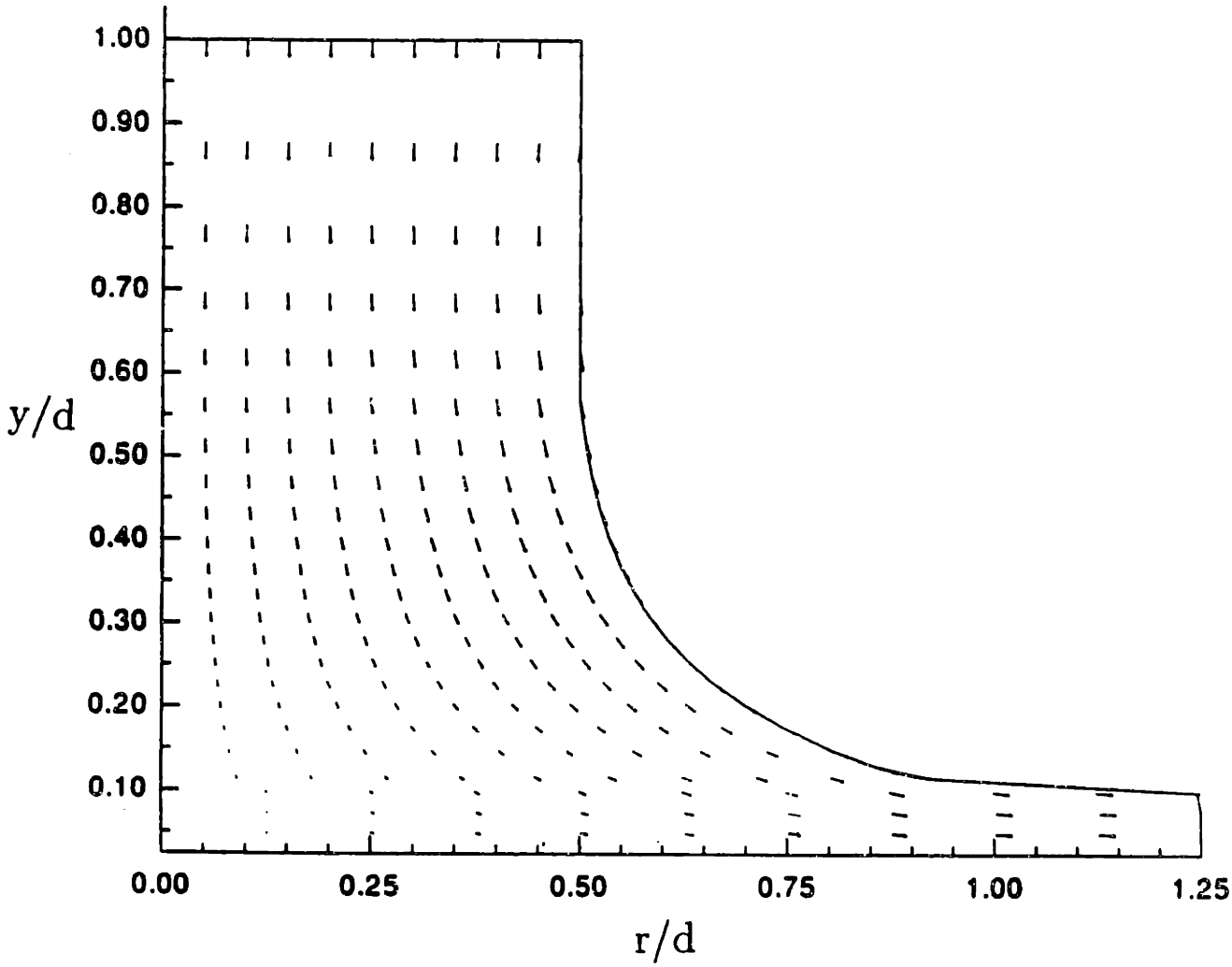

Figure 5.3: The velocity field for $We_d \to \infty$.

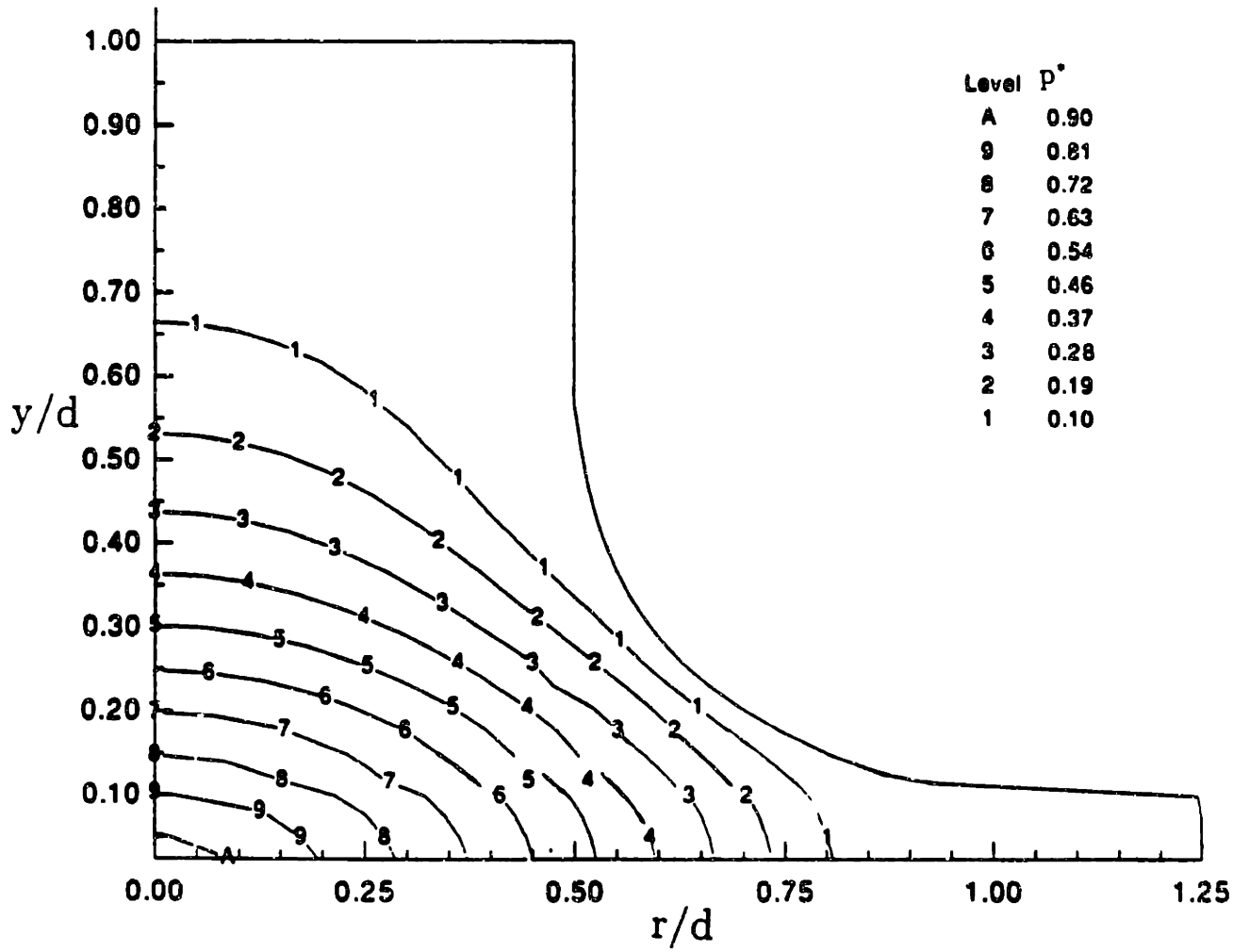

Figure 5.4: The pressure distribution, $p^* = p/P_0$, as $We_d \to \infty$ for P_0 the stagnation pressure.

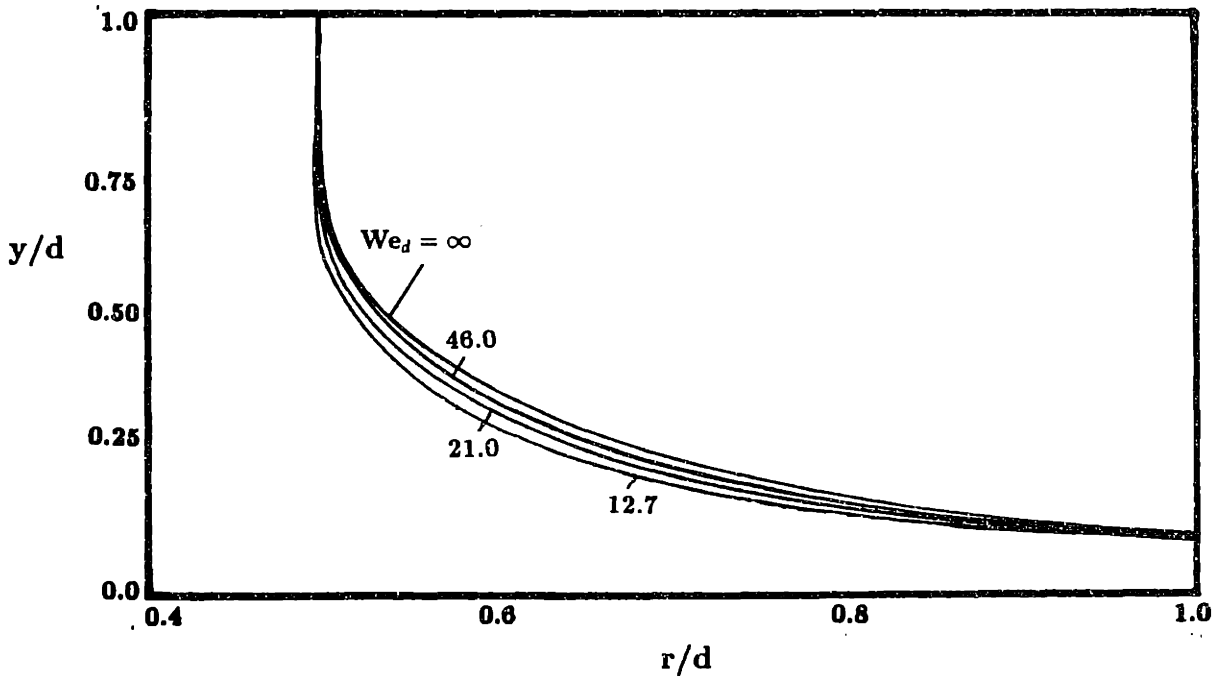

Figure 5.5: The free surface shape for several values of Weber number.

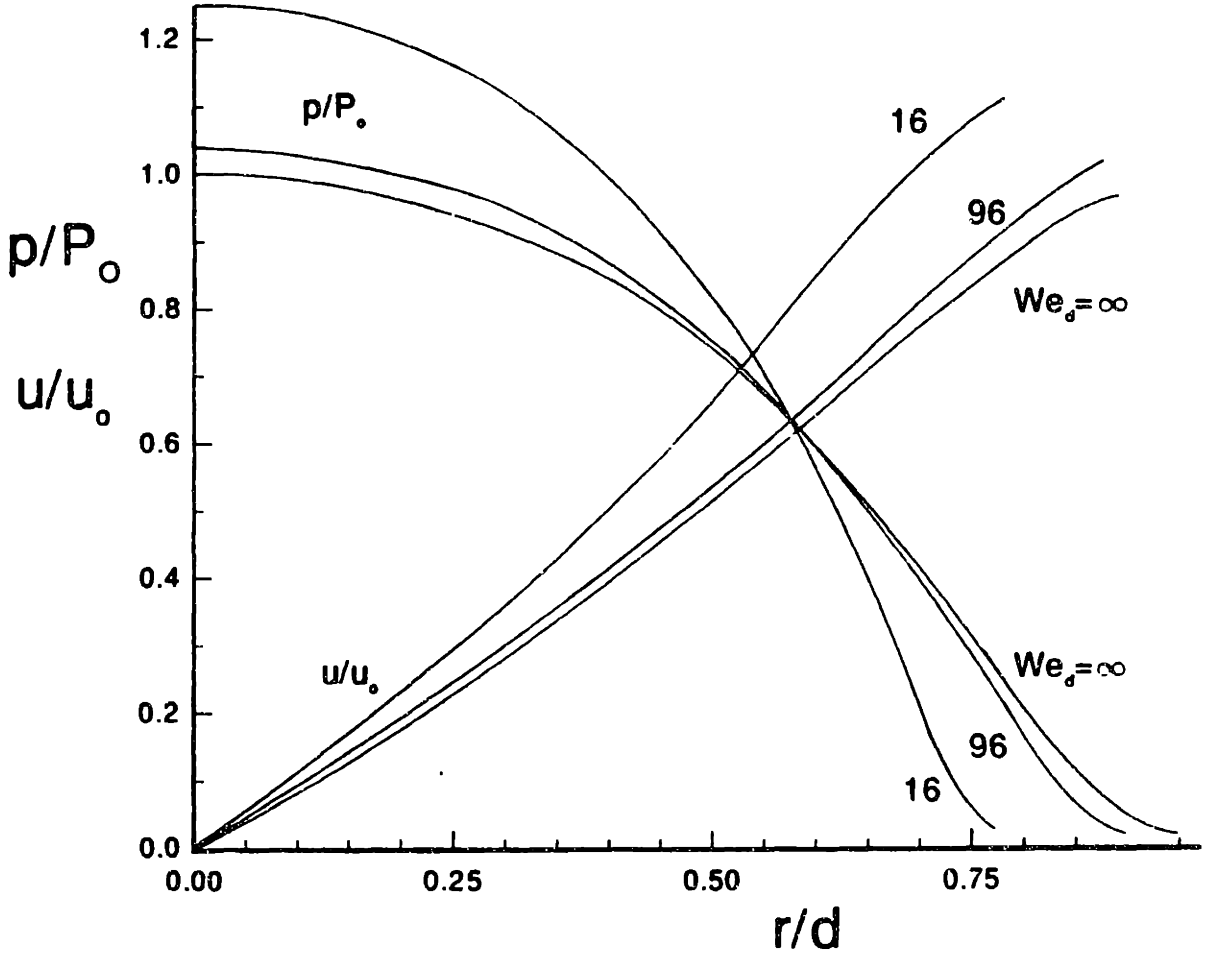

Figure 5.6: Velocity and pressure variation along the target plate ($y/d = 0$) for several values of Weber number.

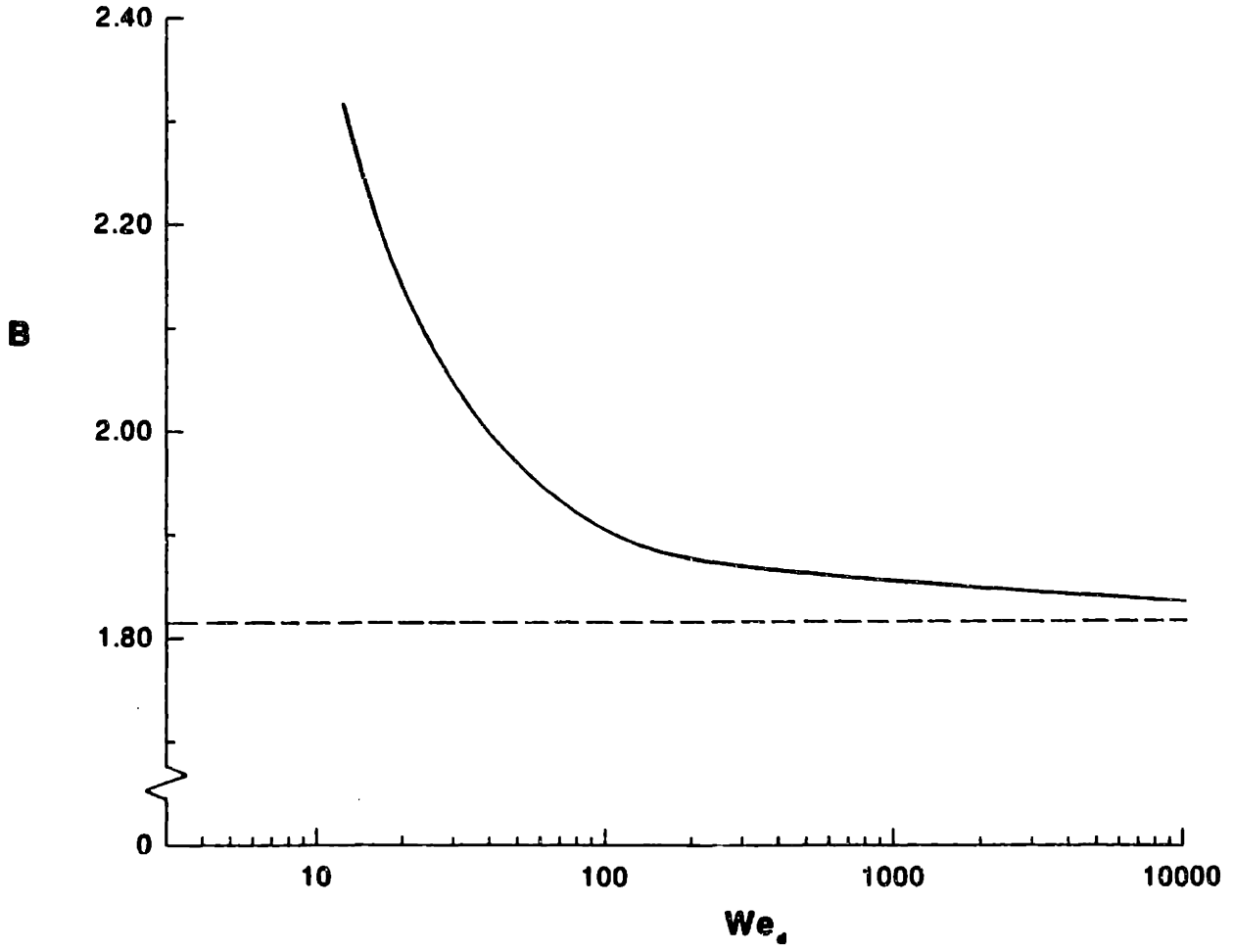

Figure 5.7: Effect of Weber number on stagnation point velocity gradient. ($B = \frac{d}{u_0}\frac{\partial U}{\partial r}$).

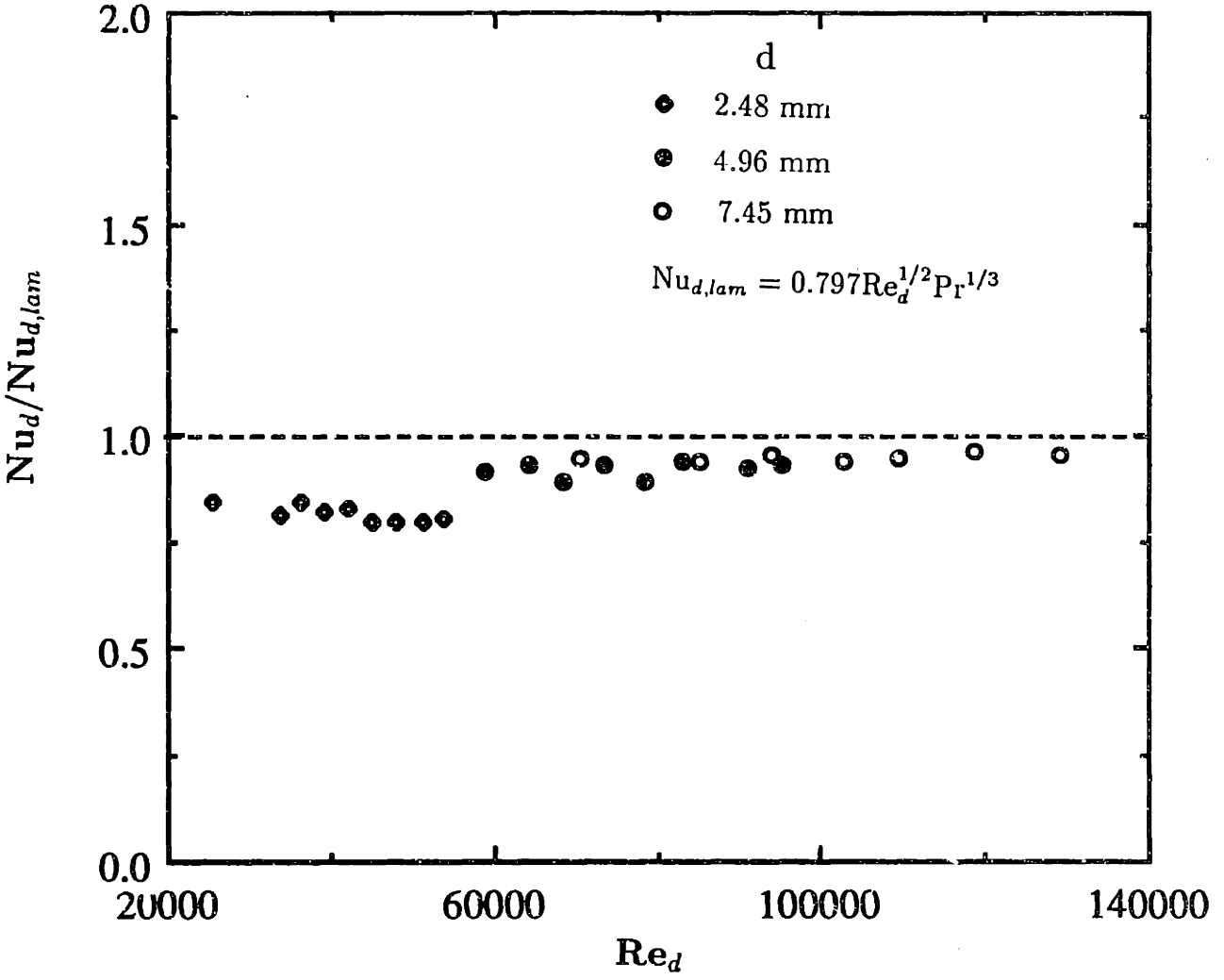

Figure 5.8: Experimental data for laminar jets of various diameters with $We_d > 2100$.

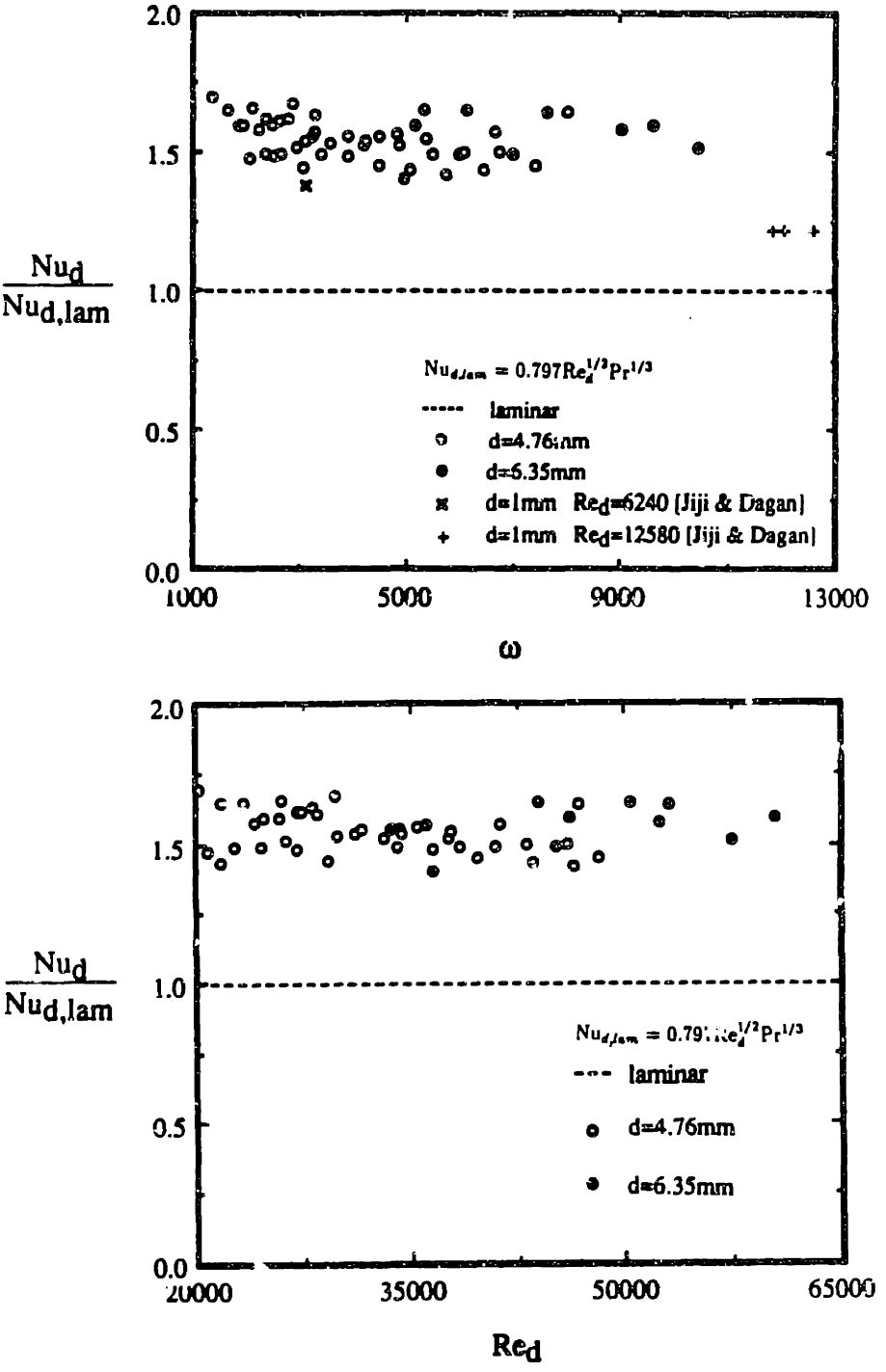

Figure 5.9: Stagnation zone Nusselt number for fully-developed turbulent jets relative to laminar theory.

Chapter 6

EXTREMAL HEAT FLUX REMOVAL BY JET IMPINGEMENT

6.1 Introduction

The previous chapters show that the stagnation zone of an impinging liquid jet is very attractive, since extremely high heat transfer coefficients occur in the stagnation zone and the flow is very easily created. In addition to these facts, some investigators have already achieved very high heat fluxes using liquid jet impingement (Monde and Katto, 1978).

Modern technology is demanding operation at higher and higher power densities. Cooling in controlled nuclear fusion demands very reliable, high heat flux design.

During the plasma disruption in a Tokamak, which lasts about 0.1 to 3 ms, from 7 to 200 GW/m^2 heat flux is released. Under this condition the wall must melt and evaporate. Steady cooling at rate of more than 10 MW/m^2 is required for the design (Nariai, 1990). In the advanced neutron source, the heat flux released from the fuel is as high as 17 MW/m^2. Other state of the art technologies also require strategies to handle extremely high heat fluxes, far higher than those accomplished to date. Previously-studied, high flux, experimental configurations have included jet impingement on a disk, axial tube flow with and without generated swirl, and crossflow over a cylinder. Subcooled boiling through tubes has to date achieved much higher heat fluxes than those reported for jet impingement. The value of the highest heat flux, which we can locate* is $337 MW/m^2$, achieved in axial tube flow, by Ornatskii and Vinyarskii (1965). Subcooled water ($\Delta T_{sub} = 180K$) flowed through a 0.5mm diameter and 14mm long tube under 31.3 atmosphere inlet pressure at velocity 90 m/s under a nonuniform heat flux; the critical heat flux as high as 337 MW/m^2. Other extremely high heat flux results for water are shown in Table 6.1. Most of the information on heat fluxes in tube flow comes from Nariai's paper (1990). Most of the extremely high heat fluxes were achieved by subcooled boiling through small tubes, either smooth or internally augmented. In order to increase the critical heat flux, smaller and shorter tubes are usually required.

The highest heat flux previously achieved by liquid jet impingement (Monde and Katto, 1978) was $18 MW/m^2$. A water jet from a nozzle of 2.0 mm diameter impacted

*Boyd *et al.* (1984) reported another highest heat flux, 347 MW/m^2 by Thompson and Harkee. We could not locate them so far and unable to cite it directly

on an electrically heated disk of diameter 11.3mm. The jet velocity was 26 m/s and subcooling was 20 °C. The nozzle was a converging pipe. The authors claimed that the nozzle was able to make a circular liquid jet having laminar flow within that range of jet velocity, but they reported that the liquid was splattered from the target and that the splattered mass could be as high as 90% depending on the heat flux. A dimensional analysis was carried out to provide coorelations for the critical heat fluxes. They argued that because the thermal conductivity and the specific heat of liquid had no effect on burnout, they were not needed in the analysis.

Katto and Shimizu (1979) investigated the critical heat flux by impinging jets for R-12. They found that at low system pressure the critical heat flux increased with velocity, but at high pressure the critical heat flux was independent of velocity. They further proposed that the critical heat flux behavior of an impinging jet could be divided into four regions:

1. *D-region:* the critical heat flux takes place only due to the deficiency of liquid supply as compared with the heat load. It is situated in the range of low jet velocity.

2. *V-region:* in this region, the critical heat flux increases with the incoming jet velocity.

3. *I-region:* in this region, the critical heat flux is independent of the incoming jet velocity.

4. *HP-region:* this region probably exists at very high pressure, because a similar

region exists for the forced convection boiling in tubes.

The boundary between D-region and V-region is determined by:

$$\frac{\sigma}{\rho_l u_f^2 D} = 6.50 \times 10^{-2} \tag{6.1}$$

The boundary between V-region and I-region is determined by:

$$\frac{\sigma}{\rho_l u_f^2 D} = 1.64 \times 10^{-5} \tag{6.2}$$

The boundary of the HP-region is suggested to be

$$\rho_l / \rho_g = 6.0 \tag{6.3}$$

They also gave correlations for the critical heat flux for each region other than the HP-region.

Monde (1987) did experiments at comparatively higher pressures from 0.6 to 2.8 MPa for R-12 and gave a correlation for the HP-region, in which the critical heat flux rises again with an increase in the jet velocity.

Gambill and Lienhard (1989) summarized some experimental results of highest heat fluxes. They showed that the highest heat fluxes achieved so far are an order lower than the estimation by Schrage (1953). Schrage (1953) had estimated the highest heat flux which could be achieved in a phase-transition process. He assumed that all molecules leaving a liquid vapor interface never return to it, in other words, that no collisions occur in vapor phase, so that the heat flux is simply the sum of the latent heats of all molecules leaving the interface per unit area per unit time. This model leads to

$$q_{max} = \rho_g h_{fg} \sqrt{RT/2\pi} \tag{6.4}$$

Gambill and Lienhard (1989) represented the data they collected in a dimensionless form suggested by Schrage's estimate of highest heat flux:

$$\phi = \frac{q_{max}}{\rho_g h_{fg} \sqrt{RT/2\pi}} = f(p_r) \tag{6.5}$$

The data for the reduced pressure range $0.004 < p_r < 0.10$ appear to be consistently bounded by $\phi = 0.1$. At higher pressure, the highest existing values of ϕ fall off roughly as $(p_r)^{-2}$.

As pointed out by Gambill and Lienhard (1989), the above mentioned experimentalists have taken particular pains trying to push the heat flux to its limit. but the heat fluxes achieved so far are still far from the heat flux estimated by Schrage. This is especially true for jet impingement for which the previously achieved highest heat flux is an order lower than that for tube flow. The present work tried to check experimentally the heat flux limit for jet impingement set by the above mentioned correlations, to check the idea of a heat flux limit (such as given Schrage's estimate for phase change heat transfer), and attempts to achieve heat fluxes in the range beyond 100 MW/m^2 by using liquid jet impingement. Our attention will go toward identifying basic phenomena accompanying cooling at such enormous fluxes.

Our discussion will show that despite the high heat flux limits predicted by theoretical considerations, the strongest constraints come from practical problems, especially from material limitations.

6.2 Experiments

The experiments require the solution of some difficult problems. Most experimental heaters are designed for much lower fluxes. Electrical heaters (Samant and Simon, 1984) having a substrate serving as both the heater surface and as a resistance thermometer, will not work. To get a heat flux of $1GW/m^2$, we need to deliver $1KW$ to an area of only $1mm^2$. We have the problem of supplying this power to such small area. A heater with tiny area must have very lower electrical resistance in order to convert kilowatts of power into thermal energy, but at the same time, the leads and connection between the leads and heater must have an even lower electrical resistance, in comparison to the resistance of the heater. The configuration of the heater and the arrangement of the connections are very difficult problems since the heating must remain.

At high heat fluxes, any finite thermal resistance to heat flow can produce a substantial temperature difference. The heater must be very thin, even for a material with exceptionally high thermal conductivity. Because a high heat flux heater requires very efficient cooling of the heater surface to minimize the surface temperature, any damage or corrosion of the thin heater will cause large error in the experiments.

Thus, the electrical heating is not good choice for the experimental design. Other alternatives include optical heating, laser heating, and plasma arc heating. All of these methods have the same feature of projecting energy beams onto a surface. The benefits are to avoid the arrangement of leads and connections to the thin heater as well as possible erosion problem. Bhunia and Lienhard (1990) designed an optical

heater and estimated its cost. They showed that even though optical heating was possible, it was not economical. Based on economic considerations, we chose plasma arc heating. The experimental arrangement (Figure 6.1) is to heat a metal plate from one side with a plasma arc and to cool the metal from the other side with an impinging liquid jet. The plasma arc was produced by AIRCO-3A/DDR245 plasma welder with 21.8 kW power.

In such an arrangement, the calorimetry becomes extremely difficult. Thermocouple measurement, for example, has substantial some problems. On the liquid jet side, the thermocouples would disturb the fluid flow. Contact resistance between thermocouples and plate could not be tolerated due to the large temperature increase at large flux. On the plasma arc side, the arc would melt the thermocouple. Even if the thermocouples were placed far from the arc, solution of the inverse conduction problem would be difficult owing to the large gradients. Direct measurements of surface temperature are not feasible in such circumstances.

Non-contact measurements, such as infrared sensors, collect the radiation from the surface with a focused sensor which converts the signals to temperatures. On the jet side, the liquid phase on the plate and the splattering of the jet preclude an accurate measurement. On the plasma arc side, the strong radiation from the arc makes the measurement impossible. Since both contact and non-contact measurements are not promising, we chose fusible temperature indicators as the basis of the calorimetry.

Fusible temperature indicators used are metals and alloys which have known melting temperatures (Table 6.2). A very thin layer of metal or alloy with a specific

melting temperature was coated on the jet side of the plate. If the wall temperature on this side was beyond the melting temperature, the coating was melted and washed away by the high speed jet. Otherwise the coating stayed on the plate. By repeating the experiment with different coatings, while holding other variables fixed, we determined upper and lower bounds of the temperature. Figure 6.2 shows the arrangement of the experiments and the temperature indicator on the plate. The jet and the arc struck on either side of the plate, respectively, during the experiments.

Because the high heat flux raises the temperature on the arc side, a portion of the plate under the arc is melted and finally reaches a steady state. The border of the melting pool is an isotherm which gives the melting temperature of the plate material. After steady state is reached, we stop the arc and the jet, and take the plate as a sample.

Several steps are needed to locate the melting temperature isotherm. First, we mark the plate with a line going through the center of the melting pool. Then cut the plate in half, making sure to leave enough room near the centerline for polishing. The polishing start progresses rough polishing to fine polishing until the cross section becomes a mirror surface. In order to see the crystal structure of the metal, to identify the border of the melting pool, the surface must next be etched properly. We will not go into the details of etching procedure and recipes of the etching solutions. The relevant materials can be found in many handbooks and reference books on materials science. After etching, the sample's crystal structure can be examined and photographed.

Figures 6.3 and 6.4 shows a photo of a sample under a microscope. The material is a steel plate. The two different crystal structures can be easily identified. The crystal structures are closely related to the cooling history of the material. In the melting pool, the metal was first melted by the plasma arc and then was quickly quenched by the jet on the other side of plate after the arc was stopped. Since the cooling rate is so large and the temperature drop is so fast, the resulting crystal structure is martensite. The material that did not melt remains its original crystal structure. The isotherm of melting temperature is easily located between the two different crystal structures.

After we located the isotherm of the melting temperature and the upper bound and lower bound temperatures on the liquid side of the plate, we could put those information into a computer to calculate the heat flux that went through the plate. This was done by the axisymmetric conduction calculation offered by the computer code NEKTON. A result of the calculation is shown in Figures 6.5 and 6.6. Figure 6.5 gives the isotherm contours, which show the temperature distribution in the plate. The temperature changes are concentrated in the center area of the plates. Beyond a radius of four plate thicknesses from the stagnation point, the temperature difference almost negligible. Figure 6.6 shows the heat flux distribution along the plate wall on the jet side. The heat flux was normalized as

$$q^* = \frac{qt}{k(T_{melt} - T_w)} \tag{6.6}$$

Since the plasma arc was concentrated at the center of the plate, the heat flux quickly decreases with radius. Based on the upper bound temperature and the lower bound

temperature on the jet side of plate, we also made a upper bound and lower bound on the heat flux for each sample plate. The measured values are presented in Tables 6.3 and 6.4.

The jet was produced by a high head pump supplying a large plenum. The plenum flow was stabilized by a momentum dissipating plate and honeycomb at its inlet; the plenum use a high pressure cylindrical tank, which was 0.19 meter in diameter and 1.4 meter long. A sharp-edged nozzle was made of a 3.18 cm diameter plug and screwed into the head plate of the pressure tank (Figure 6.7). The pressure was measured by a pressure gauge connected to the pressure tank. The pressure ranged from 2.06 to 8.95 MPa psi in the experiments. The jet velocity was calculated from the pressure measurement using the Bernoulli equation. The estimated uncertainty for Re_d is 5%, less than 2% for the thickness of the plate, and 1.4% for the melting point of the fusible temperature indicators. Because the temperature on the jet side was bounded by two temperatures, the uncertainty of the heat fluxes were mainly determined by the upper and lower temperature bounds. Since the melting temperature of the plate, 1371°Cfor steel, was relatively high, the uncertainty for heat fluxes was $\pm$19% for the samples with largest temperature difference between the upper and lower bounds. The Nusselt number strongly depends on the temperature difference between the wall temperature and the incoming jet temperature; its uncertainty was 64% for the samples with largest temperature difference between upper and lower bounds, and 29% for those with smallest temperature difference.

6.3 Discussion

6.3.1 Stagnation zone heat transfer

The stagnation zone heat transfer is very attractive, because it is very easy to set up. If we also allow the liquid to boil, we know that the heat flux is roughly the sum of convective heat flux and boiling heat fluxes (Rohsenow and Griffith, 1955). Jet impingement at the stagnation zone is a very promising arrangement to achieve extremely high heat fluxes. The present data are compared to other experimental data for extremely high heat fluxes in Table 6.1. The amount of data for extremely high heat fluxes, which are above 10 MW/m^2, is still very limited, especially data above 100 MW/m^2. For jet impingement, the present data are the only ones in the range above 100 MW/m^2 range.

The present data proves that the jet impingement is very promising method to deal with high cooling rates. It is important to notice that most of the previously-existing data in Table 6.1 are critical heat fluxes, which are the limiting cases for given conditions. The present data are not critical heat fluxes. Figure 6.8 shows the experimental data for a fixed jet velocity with different wall temperatures. The data are given by their lower bounds and their upper bounds. The symbol at the left end of a solid line is the upper bound of heat flux corresponding to the lower bound of the wall temperature, and the symbol at the right end of a solid line is the lower bound of heat flux corresponding to the upper bound of the wall temperature. For the cases when the lower bounds of wall temperatures is only known as the

incoming jet temperature, the data are presented by dashed lines with symbols for upper bound heat fluxes. Using different temperature indicators, the heat fluxes still showed increase with increase of wall temperature. There is still room to push heat fluxes higher, if better materials can be obtained. Thus, the limiting factors are different for our data and the rest of the data. The limiting factor of material will be discussed later.

Katto and Shimizu (1979) divided the critical heat flux behavior of jet impingement into four regions. High speed jets fall in either the I-region or the HP-region. The HP-region is for the cases $\rho_l/\rho_g > 6.0$ and will be discussed later. The present experimental conditions were in the I-region:

$$\frac{\sigma}{\rho_l u_j^2 D} < 1.64 \times 10^{-5} \tag{6.7}$$

where D is the diameter of target disc. In this region, the critical heat fluxes are independent of the jet incoming velocity. Katto gave a correlation for the critical heat fluxes:

$$\frac{q_{max}}{\rho_g h_{fg}\sqrt{\sigma/(\rho_l D)}} = 1.18\left(\frac{\rho_l}{\rho_g}\right)^{0.614} \tag{6.8}$$

Because the present heat transfer is confined to the stagnation zone, the diameter of stagnation zone, which is about 1.574 d (*see* Appendix B), should replace the disk diameter. In Figure 6.9 the data are plotted as heat flux versus stagnation point pressure. The solid line is the pool boiling critical heat flux and the dot-dash line represents Equation 6.8. The present data, which are not critical heat fluxes, are higher than the prediction of Equation 6.8. Katto and Shimizu's prediction (1979) was based on their experiments with the disk diameter of 0.01 m and nozzle

diameter of 0.002m. The disk diameter was much larger than the nozzle diameter. The nozzle was claimed to be designed to make laminar circular liquid jet within the range of jet velocity of the experiments (Monde and Katto, 1978). However, a converging nozzle, which was their nozzle type, cannot by itself damp the turbulence from upstream. McCarthy and Molloy (1974) discussed the influence of nozzle design. Monde and Katto's photos (1978) showed that their jets had serious splattering. Their measurements also showed that the splattered mass was as high as 90%. The splattering effects on the heat fluxes must be taken into account.

In Chapter 3, the splattering mass is characterized and depends on the dimensionless group ω, which describes the effects of velocity on the splattering. For a disk larger than the diameter where splattering occurs, the mass and momentum remaining in liquid sheet are reduced, and liquid supply for the phase change is limited by the splattering. The boundary between the V-region and I-region marked by Equation 6.7 is simply a function of the Weber number, which characterizes the splattering for a fixed separation of nozzle and target. For larger Weber number, the splattering becomes important and may compensate for the effects of increasing velocity on the heat fluxes. However, for the stagnation region, splattering has no effects on the heat flux, which is the case for present data.

In Figure 6.10 the data shows the increasing trend of heat flux with velocity. This set of data has lower bound temperatures of 190°C corresponding to the upper bound of heat flux and upper bound temperature of 400°C corresponding to the lower bound of heat fluxes. From Figure 6.8, the heat fluxes increases with a higher power of

temperature than unity. This indicates clearly the involvement of phase change. But the saturation pressure corresponding 190°C is $1.23 \times 10^6 N/m^2$, which is stagnation pressure for a jet with incoming velocity of about $50m/s$. However, data with jet velocities of more than $50m/s$ indicate that phase change is involved. The reason of this is the instability of jets. We stabilized the jets significantly by turbulence damping in the plenum (momentum strike plate and honeycomb). But for jets at very high velocity, the shear stress with air causes breakup of the jets. Ohnesorge (McCarthy *et al.*, 1974) divided the jet breakup into three regions:

1. The jet breaks up into large reasonably uniform drops (Rayleigh type breakup).

2. The jet breaks up into drops with a wide size distribution.

3. Secondary atomization occurs.

The secondary atomization of a high speed jet is caused by the ambient atmosphere. As the jet speed increases, more air is entrained into the jets. Therefore, the stagnation point pressure was not constant. On one hand, reducing stagnation pressure is a disadvantage. In some rage, increasing pressure will increase the critical heat flux of pool boiling. The pressure fluctuation limits the ability of high speed jet to maintain the high critical heat flux. On the other hand, the fluctuation of stagnation point pressure has advantages. The pressure fluctuation reduces the wall temperature required by phase change, as shown by the data. The entrained air provides the original seeds for nucleation, which reduces the nucleation barrier. To seed an impinging flow with small gas bubbles simply by entrainment has favorable effects on the jet

impingement heat transfer (Serizawa *et al.*, 1990), and is a interesting area requiring further investigation.

In Figure 6.11 the measured Nusselt numbers are compared to the convective Nusselt numbers. The shaded area represents the Nusselt number calculated from the convective heat transfer. Since the viscosity and Prandtl number are temperature dependent, the two bounds on Nusselt number were calculated using lower bound and upper bound temperatures and shown on the figure. The comparison shows that the convective heat transfer is an important portion of the total heat flux and that the convective heat fluxes are the same order of the total heat fluxes.

To understand mechanism of heat transfer it is worthwhile to look at the heating process of a jet and to follow a hypothetical particle in the jet (Figure 6.12 and 6.13). From point *a* to *b* in the figures, the particle enters the stagnation zone, is pressurized and experiences essentially no heat transfer. On an s-h chart it basically travels an isotherm. From *b* to *c*, the particle is influenced by heat transfer from the wall; it is heated very rapidly. The residence time from *b* to *c* under a fast jet is on the order of 10^{-5} second. Because the pressure goes down in the radial direction along the wall, the particle is rapidly depressurized. This forces the particle to go through a boiling or phase transition process. The process is approximately like going from the saturation state to the spinodal limit, at which point the liquid state becomes unstable. At that point the heated liquid must vaporize. What follows can be either homogeneous boiling or bubble nucleation, forming on wall and penetrating to the boundary layer almost immediately. Either mechanism creates very efficient phase

transition heat removal. However, the heat was removed when the liquid was heated, not after it boils.

From the data, we may conclude that what happens is probably bubble nucleation rather than homogeneous boiling. If homogeneous boiling occurs at certain radius due to depressurization, the heat transfer within that radius would be pure convection heat transfer, and for the Reynolds number used, the heat fluxes should be lower than the data shown in the figure.

Although homogeneous boiling is unlikely to have happened, the bubble nucleation requires a certain time to occur under a certain temperature excess. In a time span on the order of 10^{-5} second, much larger temperature excess is required for nucleation. But if we consider the liquid on the wall, which has velocity close to zero, the residence time is long enough to start nucleation. It is not quite clear what the dynamics of a bubble are under such a fast flow, but it is clear that the bubbles cannot become too large due to the very thin boundary layer and subcooled free flow, and that the bubbles would have difficult remaining on the wall due to the pressure gradient and high shear stress exerted on them

For high pressure, $\rho_l/\rho_g > 0.6$, Monde (1987) proposed a correlation, which showed the heat fluxes increased again with the velocity:

$$\frac{q_{max}}{\rho_g h_f g u_f} = 0.172 \left(\frac{\rho_l}{\rho_g}\right)^{1.27} \left(\frac{2\sigma}{\rho_l u_f^2 (D-d)}\right)^{0.28} (1 + D/d)^{-1.01} \qquad (6.9)$$

Before we check the limitations of the heat transfer correlation for high pressure, let us consider a process which is above the critical point pressure. As we look at an s-h chart, we see that it is possible to pressurize and heat the liquid above the critical

state. Then the working fluid is gradually depressurized and the "phase transition" will proceed smoothly. The whole fluid ends up as vapor, but the process finishes without going through the two phase region. The whole process may be treated as convective heat transfer with variable properties, including density, conductivity, thermal capacity, and viscosity. From the s-h chart, we can see that the latent heat becomes smaller with increasing saturation pressure. The latent heat finally disappears as the pressure reaches the critical point. The latent heat plays decreasing role in the phase transition process and finally its role is simply replaced by convection. The question is which mode, swift phase transition or smooth phase transition, is more efficient. The heat transfer coefficient for stagnation point flow of a $2mm$ diameter water jet at critical state is about $5\times10^5 W/m^2K$. However, pool boiling of water at 85 atm. with $10K$ superheat has roughly the same heat transfer coefficient. Therefore, in this sense, simply increasing jet velocity (or in other words, increasing stagnation pressure) does not necessarily mean the increasing the heat transfer coefficient. When increasing the stagnation pressure, the heat transfer coefficient increases first and then decreases. An optimum point of the heat transfer coefficient is thus expected.

From the above discussion, in any model of heat transfer of high speed jet impingement, the convective heat transfer must be taken into account. In their dimensional analysis, Monde and Katto (1978) argued that the thermal conductivity and the specific heat of the liquid had no effect on burnout, and these were not included in the parameter list of their analysis. However, heat transfer from convection is very important in high speed jet heat transfer. It will be dominant when the pressure goes

up to the critical pressure, since the latent heat becomes smaller and smaller.

The thermal boundary layer thickness in stagnation zone of a jet is on the order of

$$\delta_t \sim d\mathrm{Re}_d^{-1/2}\mathrm{Pr}^{-1/3} \tag{6.10}$$

For a water jet with a diameter of millimeters, δ_t is less than micron thick for $\mathrm{Re}_d > 10^5$. In this case, the thermal boundary layer is in the same order of the microlayer beneath bubbles. The phase change in the bubbles will not be responsible for the high heat transfer coefficient. However, the bubble generation and departure do provide a periodic fluctuation of the thermal boundary layer, and the air entrained into the jet provides another source of oscillation. We propose the following model, in which the convection process with an oscillatory velocity rather than phase change is considered responsible for the high heat transfer coefficient. For a periodic boundary layer with high frequency, we have the skin friction (Lighthill, 1954):

$$\tau = \tau_o + \mu u_{oscil}\left(\frac{\omega}{\nu}\right)^{1/2} \tag{6.11}$$

where τ_o is the skin friction without oscillation, u_{oscil} is oscillatory velocity component, and ω is the oscillatory frequency. The oscillatory velocity component is assumed to be proportional to the bubble growth rate, dR/dt. In high speed jets, the bubble departure radius is not likely to be at the balance point between buoyancy force and surface tension, since the drag force is much stronger than buoyancy force and must be balanced by surface tension:

$$\sigma D_{depart} \sim C_D \rho u_f^2 D_{depart}^2 \tag{6.12}$$

where D_{depart} is the bubble departure diameter, C_D is drag coefficient, which is function of Re_d depending on Reynolds number. This gives an estimate of bubble departure diameter, which is very small:

$$D_{depart} \sim \frac{\sigma}{C_D \rho u_f^2} \tag{6.13}$$

where C_D is a function of the Reynolds number base on the bubble diameter. We may assume:

$$C_D = C\left(\frac{u_f D_{depart}}{\nu}\right)^m = C\left(\frac{u_f \sigma}{C_D \rho_l u_f^2 \nu}\right)^m \tag{6.14}$$

Rearrange and we get

$$C_D = C^{1/(m+1)}\left(\frac{\sigma}{\nu \rho_l u_f}\right)^{m/(m+1)} \tag{6.15}$$

Therefore, bubble growth is controlled by initial force:

$$\frac{dR}{dt} \sim \left(\frac{\Delta T \rho_g h_{fg}}{\rho_l T_{sat}}\right)^{1/2} \tag{6.16}$$

The frequency is assumed to be proportional to

$$\omega \sim \frac{dR/dt}{D_{depart}} \tag{6.17}$$

For water the Prandtl number is close to unity, and the Reynolds-Colburn analogy can be used:

$$\frac{\mathrm{Nu}_d}{\mathrm{Re}_d \mathrm{Pr}^{1/3}} = \frac{2\tau}{\rho_l u_f^2} \tag{6.18}$$

Substituting the expressions for ω and u_{oscil} into τ, and using the Reynolds-Colburn analogy we find

$$\mathrm{Nu}_d = 1.24 \mathrm{Re}_d^{1/2} \mathrm{Pr}^{1/3} + C'\left(\frac{\sigma}{\nu \rho_l u_f}\right)^{\frac{m}{2(m+1)}}\left(\frac{\Delta T \rho_g}{T_{sat} \rho_l}\right)^{3/2}\left(\frac{\rho_l^{1/2} d h_{fg}^{3/4}}{\sigma^{1/2} \nu^{1/2}}\right) \tag{6.19}$$

where C' is undetermined constant and m is the Reynolds number dependence of the drag coefficient. We need to determine what values should be used in the above correlation. We mentioned above that the jet was disintegrated for the present experimental range. The entrainment of air caused the pressure fluctuation. In the above correlation, the characteristic pressure, $(P_o + P_{atm})/2$ was used to determine the saturation temperature. The Reynolds number based on the bubble diameter fell in the range of 10^5, assuming the bubble diameter is the departure diameter. In this Reynolds number range the drag coefficient should be approximately constant, but a curve fit of present data gives m=-0.44. This may be because the drag for the "bubbles" of the entrained air was different from that for the vapor bubbles. For smaller Reynolds number, the drag coefficient becomes a function of Reynolds number (White, 1974). The curve-fit result is shown by the dashed line in Figure 6.9.

It is important to note that the data shown in the figure is not the critical heat flux of forced convective boiling and that the heat flux can still be higher at the same condition except as it may be limited by increasing wall temperature and wall failure. The forced convective process is able to accommodate even higher heat fluxes, if materials which have better properties, conductivity, and mechanical strength, can be found.

6.3.2 Practical limits of high heat flux

In the following, we do not attempt to exhaust the possible arrangements of heat transfer modes, but just to illustrate some heat flux limits for simple configurations.

Through these simple configurations, we try to pinpoint the major problems at extremely high heat fluxes.

For a radiator mounted on a spacecraft, whose surface is assumed to be black, the radiative heat flux is determined by the Stefan-Boltzmann law of thermal radiation:

$$q \cong \sigma T_w^4 \tag{6.20}$$

where σ is the Stefan-Boltzmann constant ($5.669 \times 10^{-8} W/m^2K^4$). Supposing that we choose tungsten as the radiator material because its melting temperature is as high as $3600K$: the maximum heat flux we can get is $9.52\mathrm{MW/m^2}$. Therefore, the heat flux limit for the pure radiation is well marked by $10\mathrm{MW/m^2}$.

Because most situations involve containers or heat exchangers, the conduction can not be avoided. Taking tungsten as an example which has both high melting temperature and conductivity, the maximum heat flux for $1mm$ thick plate is on the order of $500MW/m^2$.

In practice the maximum heat flux for boiling heat transfer is much lower than the heat flux limit suggested by Schrage (1953). If we allow the surface temperature to go up to the melting temperature of the material, the maximum heat flux of film boiling has the same order of magnitude as that of radiation because the heat flow mainly goes through the vapor blanket by radiation. This heat flux may be well below the critical heat flux of boiling. The analytical expression for the critical heat flux of pool boiling, which is in good agreement with experimental data, is (Lienhard and Dhir, 1973):

$$q = 0.419 h_{\rho g} \rho_g \left(\frac{\sigma g (\rho_l - \rho_g)}{\rho_g^2} \right)^{1/4} \tag{6.21}$$

The critical heat flux for water is in the order of 1MW/m^2 at the atmospheric pressure. At elevated pressure the critical heat flux goes up and then goes down, and ite maximum is less than 5 MW/m^2. The heat flux in nucleate boiling is limited by the stability requirements of the interface between the vapor film and liquid and has nothing to do with Schrage's estimate from kinetic theory. This implies that it is impossible to reach Schrage's limit without overcoming the stability barrier.

However, boiling from an area, in which dimensions are much smaller than the most unstable wavelength, can overcome the barrier, even though the heat flux still cannot reach Schrage's estimate. Mechanisms other than Helmhotz stability, for example the stability of microconvection (Boyd, 1984), control the maximum heat fluxes. We know that there is a microlayer under bubbles during nucleate boiling. The typical thickness of the microlayer, t_{ml}, is about micron. The conduction limit through this microlayer is

$$q = C_{ml} k_l \frac{\Delta T}{t_{ml}} \tag{6.22}$$

where the subscript ml stands for microlayer and C_{ml} takes into account that the microlayer only occupies a fraction of the heating surface and a fraction of a unit time due to the periodic behavior of bubbles. If the temperature is allowed to go up to $3000K$, then this flux is in the hundreds of megawatts range.

Convective heat transfer seems to be the only heat transfer mode that does not face any barrier to increasing heat flux. The heat flux for convection may be determined in terms of the thickness of thermal boundary layer, the temperature difference, and the conductivity of working fluid. The thickness of thermal boundary

layer, unlike the thickness of solid walls which usually take some mechanical stresses, can be reduced as much as we like. But the thermal boundary layer grows in the flow direction unless a strong favorable pressure gradient exists. The best we can do is probably to sit at the entrance of a channel flow or at the stagnation point of a blunt body. From previous chapter, we have the Nusselt number at the stagnation zone under a turbulent liquid jet is:

$$\mathrm{Nu}_d = 1.24\mathrm{Pr}^{1/3}\mathrm{Re}_d^{1/2} \tag{6.23}$$

By increasing the Reynolds number, we increase the heat flux for a given ΔT as much as desired. This suggests that for any combination of heat transfer modes involving convection, the proper arrangement of convection can incorporate the required heat fluxes within a tolerable temperature range. This is the basic reason that we are interested jet impingement heat transfer at stagnation zone.

6.4 Conclusions

- The stagnation point heat transfer of jet impingement is very efficient way to cool a high power density source.
- The maximum heat flux for jet impingement is not limited by the jet liquid side, but the conduction in the target plate plate. Choosing a better material, the higher heat fluxes can be achieved.
- The V-region for the stagnation point heat transfer of a jet still depends on the velocity. The heat transfer coefficient increases with Reynolds number in this

region. For large area, the splattering is probably responsible for the reported independence of heat fluxes on jet velocity.

- For high speed jets, the convection heat flux is an important portion of the total heat flux. The convection heat transfer needs to be considered in the heat transfer models.

- The stagnation zone heat transfer of jet impingement can be modeled as an oscillatory flow.

REFERENCES

Bhunia, S.K. and Lienhard V, J.H., "Design of a High Power Density Radiant Heater Using a Non-imaging Optical Concentrator," *Report,* MIT, 1991.

Boyd, R.D., "Subcooled Flow Boiling Critical Heat Flux (CHF) and Its Application to Fusion Energy Components. Part II: A Review of Micro-convective, Experimental and Correlational Aspects," *Fusion Technology,* Vol.7, Jan. 1985.

Gambill, W.R. and Lienhard, J.H., "An Upper Bound for the Critical Boiling Heat Flux," *J. Heat Transfer,* Vol.111, pp.815-818, August, 1989.

Katto, Y. and Shimizu, M., "Upper Limit of CHF in the Saturated Forced Convection Boiling on a Heated Disk with a Small Impinging Jet," *J. Heat Transfer,* Vol.101, pp.265-269, May 1979.

Lienhard, J.H. and Dhir, V.K., "Extended Hydrodynamic Theory of the Peak and Minimum Pool Boiling Heat Fluxes," *NASA CR-2270,* July 1973.

Lighthill, M.J., *Proc. R. Soc. Lond.,* ser.A, Vol.224, PP.1-23, 1954.

McCarthy, M.J. and Molloy, N.A., "Review of Stability of Liquid Jets and the Influence of Nozzle Design," *The Chemical Engineering Journal*, Vol.7, pp.1-20, 1974.

Monde, M. and Katto, Y., "Burnout in High Heat-Flux Boiling System With an Impingement Jet," *Int. J. Heat Mass Transfer*, Vol.21, pp295-305, 1978.

Monde, M., "Critical Heat flux in Saturated Force Convection Boiling on a Heated Disk with an Impinging Jet," *J. Heat Transfer*, Vol.109, pp.991-996, November 1987.

Nariai, H., "High Heat Flux Boiling Heat Transfer", *Topical Workshop: Research of Boiling Heat Transfer, Heat Transfer Society of Japan*, The University of Tokyo, July 20, 1990.

Ornatskii, A.P. and Vinyarskii, L.S., "Critical Heat Transfer in the Forced Motion of Underheated Water-Alcohol Mixtures in Tubes of Diameter 0.5mm," *High Temp.*, Vol.3, No.6, pp.881-882, 1965.

Ornatskii, A.P. and Vinyarskii, L.S., "Heat Transfer Crisis in a Forced Flow of Underheated (Subcooled) Water in Small-Bore Tubes," *High Temp.*, Vol.3, No.3, pp.400-406, 1965.

Rohsenow, W.M. and Griffith, P., "Correlation of Maximum Heat Flux Data for Boiling of Saturated Liquids," *AIChE-ASME Heat Transfer Symp., Louisville, KY.*, 1955.

Samant, K.R. and Simon, T.W., "Using Thin-Film Technology to Fabricate a Small-Patch Boiling Heat Transfer Test Section," *ASME Pub. HTD-Vol.31*, 1984.

Schrage, R.W., *A theoretical Study of Interphase Mass Transfer*, Columbia University Press, New York, 1953.

Serizawa, A., Takahashi, O., and Kawara, Z., "Heat Transfer from High Temperature Surface by Two-Component Bubbly Flow Impinging Jet Using a Liquid Metal or Metals," *9th Int. Heat Transfer Conf.*, Jerusalem, Israel, 1990.

Thompson, B. and Macbeth, R.V., "Boiling water heat transfer – burnout in uniformly heated round tubes: A compilation of world data with accurate correlations," *AEEW-R 356,* 1964.

White, F.M., *Viscous Fluid Flow,* McGraw-Hill Book Company, New York, 1974.

q_{max}, MW/m^2	method	d^1, mm,	P^2, MPa	v^3, m/s	ΔT_{sub}, K	data[4]	material	Reference
40.1-321.	jet (not CHF)	1.9	1.03-4.98	64.3-134.	166.-242.	30	steel	Present
208.8-337.0	straight tube (Nonuniform q)	0.5	3.13	90	60-180	7	Cu Alloy	Ornatskii *et al.* (1965)
29.1-224.5	straight tube	0.4-2.0	1.12-7.2	10-90	36-195	28	Cu Alloy	Ornatskii *et al.* (1965)
51.4-173	tube (slot vortex)	4.85-6.35	2.4-6.5	8.05-29.9	16-70	11	Inc. *etc.*	Gambill *et al.*
90.9-130.0	straight tube	3.05	1.31-1.61	46.9-61.9	161.9-170.2	3	SUS	Schaefer *et al.*
8.7-117.8	tube (Inconel tape)	3.45-10.2	0.1-3.8	4.5-47.5	0-144.4	40	Nickel	Gambill *et al.*
5.58-81.3	tube (constantan tape)	1.6	0.4-1.4	4-25	22.3-71.4	25	Cu	Drizius *et al.*
23-80	tube (spiral vortex)	6.4-7.6	0.75-3.0	3.4-8.4	0-83	10	Cu *etc.*	Gambill *et al.*
14-66	straight tube	1-3	0.1	20		31		Nariai (1990)
42.9	straight tube	11.68	3.0	45.2	167.7	1	SUS	Mayersak *et al.*
1.5-18.26	jet impingement	2.0	0.1	3.9-26.0	10-30	98	copper	Monde & Katto (1976)

Table 6.1: The parameters of previous and present extremely high heat flux experiments for water: 1. Jet diameter or tube internal diameter; 2. Jet stagnation pressure or tube inlet pressure; 3. Bulk velocity of jet or tube flow. 4. Data points.

Table 6.2: The metals and alloys used as fusible temperature indicators.

Composition, wt%	Melting point, °C
Zn ~ 100	419.5
Pb Sn 90 10	298.9
Pb Sn 80 20	277.2
Pb Sn 40 60	238.0
Pb Sn 40 60	190.0

Table 6.3: Stagnation point heat transfer data for high speed water jets.

u_f, m/s	q, MW/m^2	
	lower bound back temperature < 419.5°C	upper bound back temperature > 190 °C
134.	186.	231.
130.	151.	187.
128.	138.	170.
123.	63.1	78.3
120.	106.	130.
117.	104.	129.
117.	64.5	80.0
114.	97.0	120.
111.	95.7	119.
111.	93.9	116.
111.	90.4	112.
108.	87.5	108.
105.	104.	129.
105.	86.1	107.
105.	79.6	98.6
102.	76.5	94.8
102.	73.1	90.6
102.	67.3	83.4
90.96	61.8	76.6
81.4	56.2	69.6
78.8	55.3	68.5
64.3	40.1	49.6

Table 6.4: Stagnation point heat transfer data for a high speed water jet.

$u_f = 129 m/s$			
upper bound q		lower bound q	
ΔT, °C	q	ΔT, °C	q
284.9	327.	405.5	295.
263.2	186.	405.5	168.
284.9	177.	405.5	160.
224.0	153.	405.5	131.
176.0	132.	405.5	108.
14.5	108.	176.0	93.
14.5	93.6	176.0	81.5

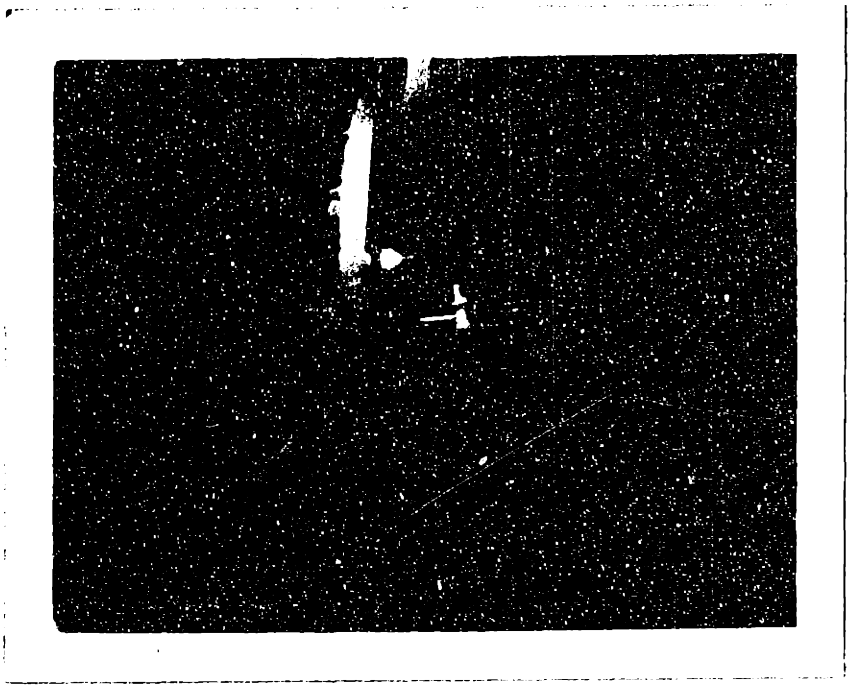

Figure 6.1: The cooling experiment of high speed jet (heating source is a plasma arc).

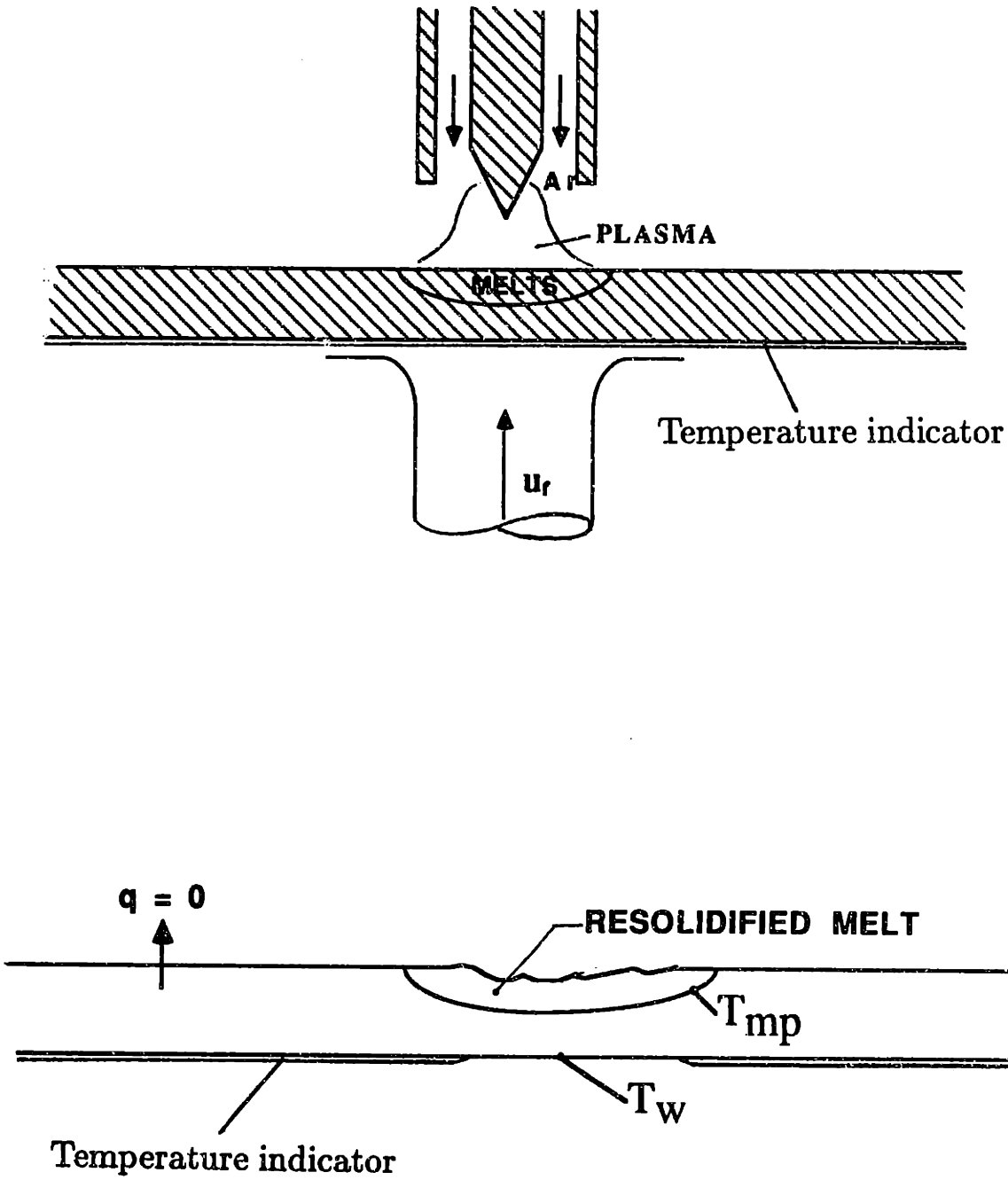

Figure 6.2: The melting pool and the temperature indicator on a target plate. (Not to scale)

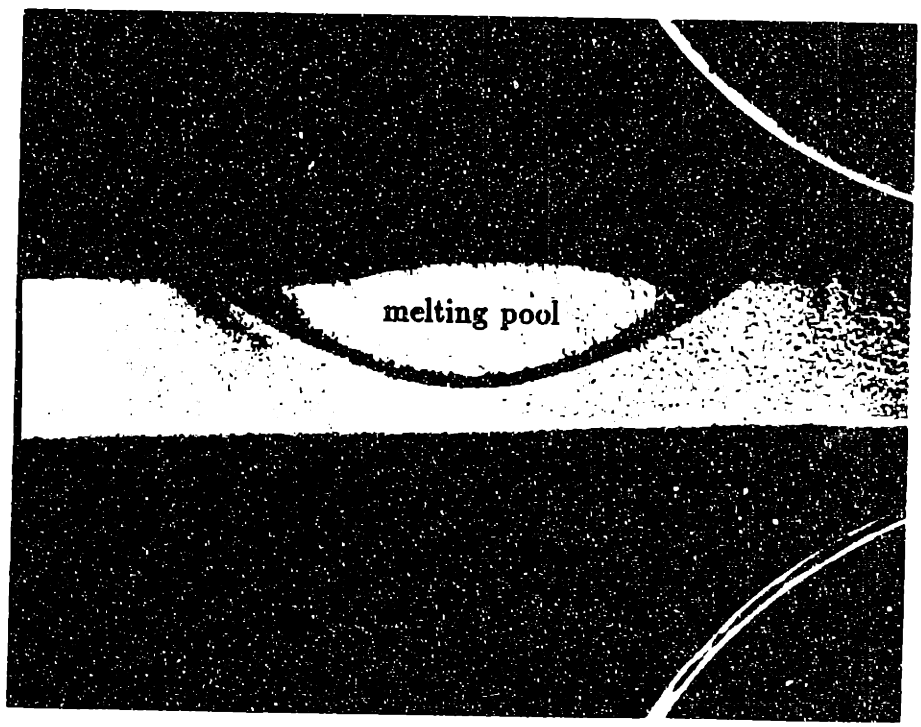

Figure 6.3: The melting pool on a sample plate.

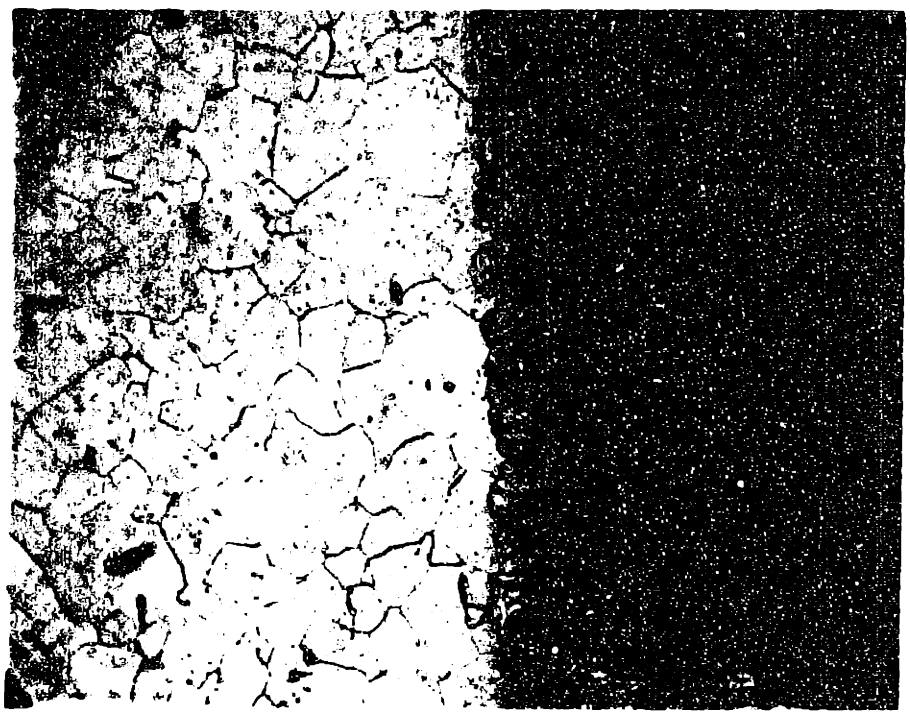

Figure 6.4: The crystal structure of the resolidified melting-pool (right) and the unmelted region (left).

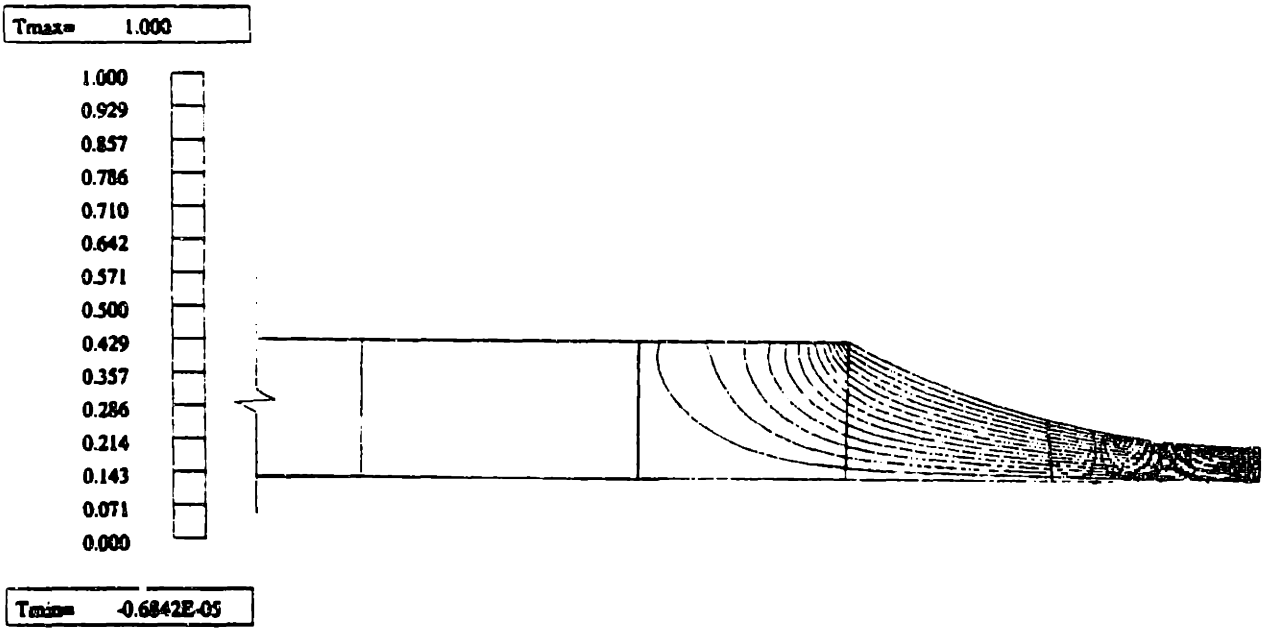

Figure 6.5: The numerical calculation of the isotherms for a sample.

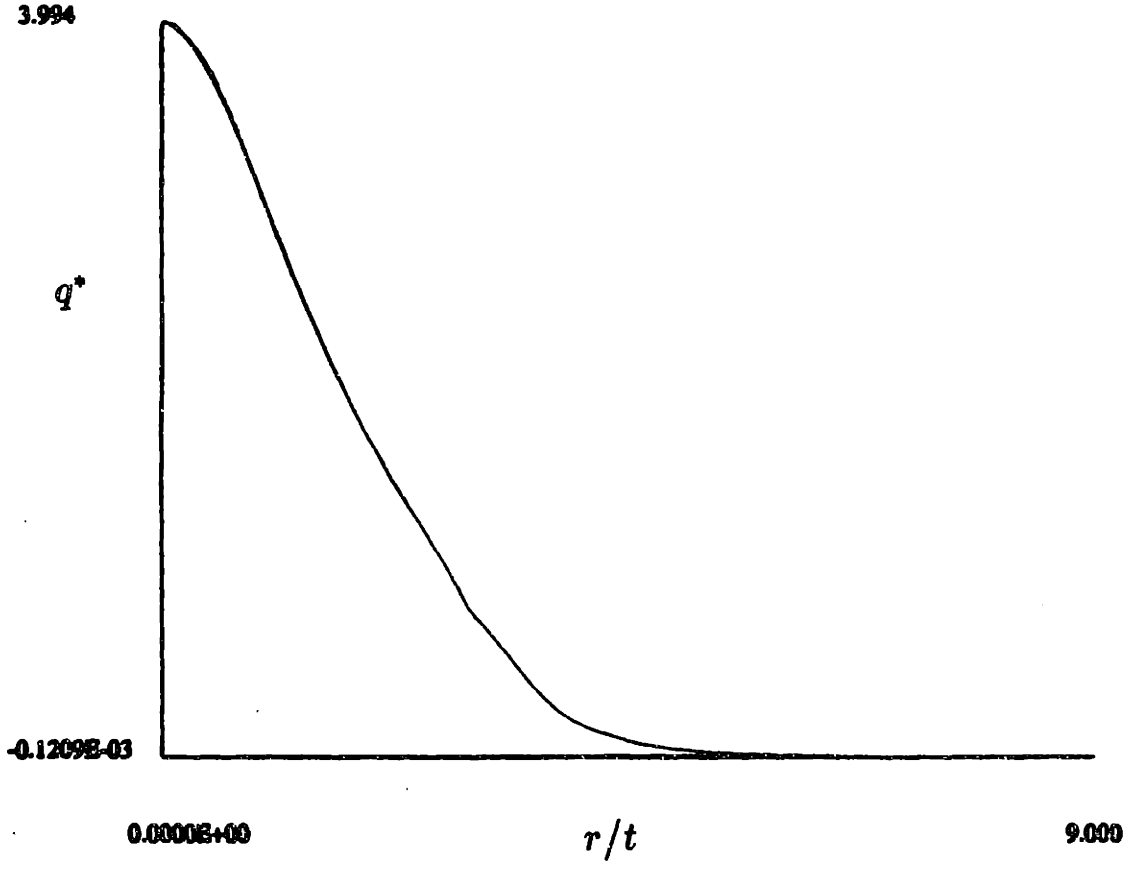

Figure 6.6: A numerical calculation of the heat flux for a sample: $q^* = \frac{qt}{k(T_{melt}-T_w)}$.

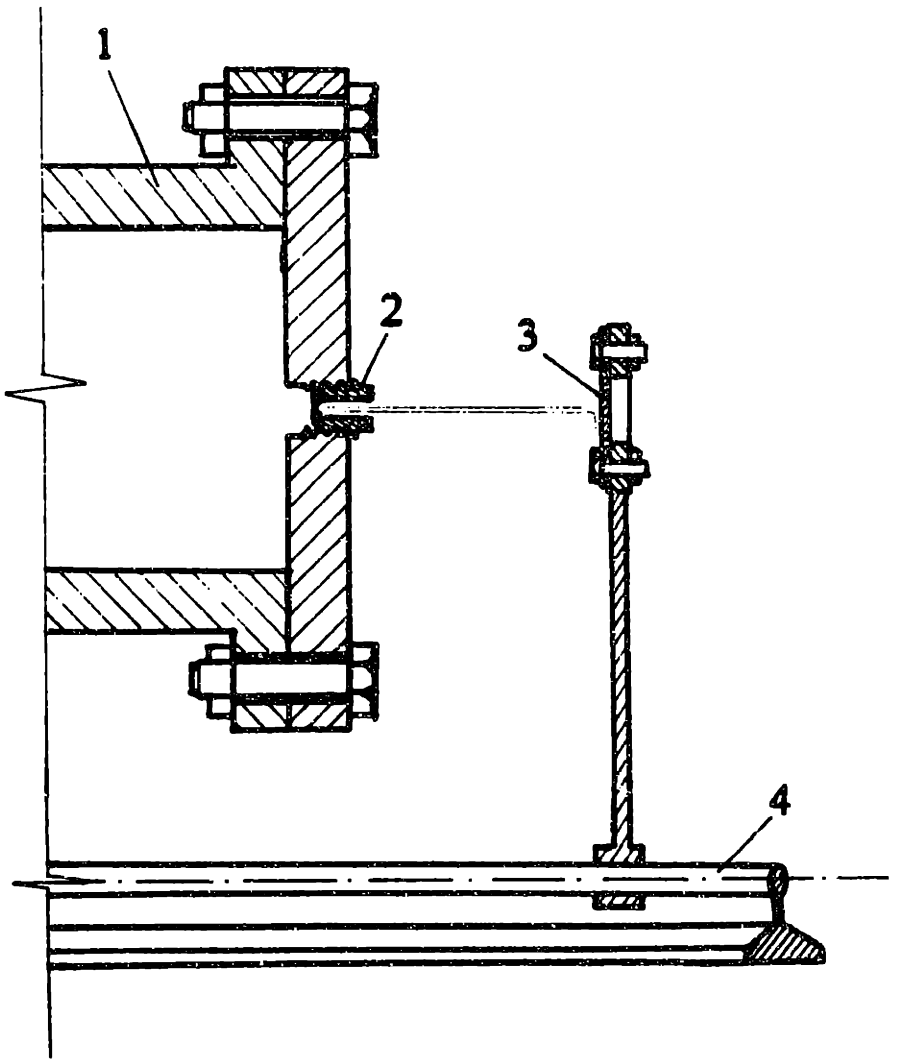

Figure 6.7: The high pressure tank with the jet nozzle: 1. High pressure tank; 2. Nozzle plug; 3. Target plate 4. Horizontal rail bearing.

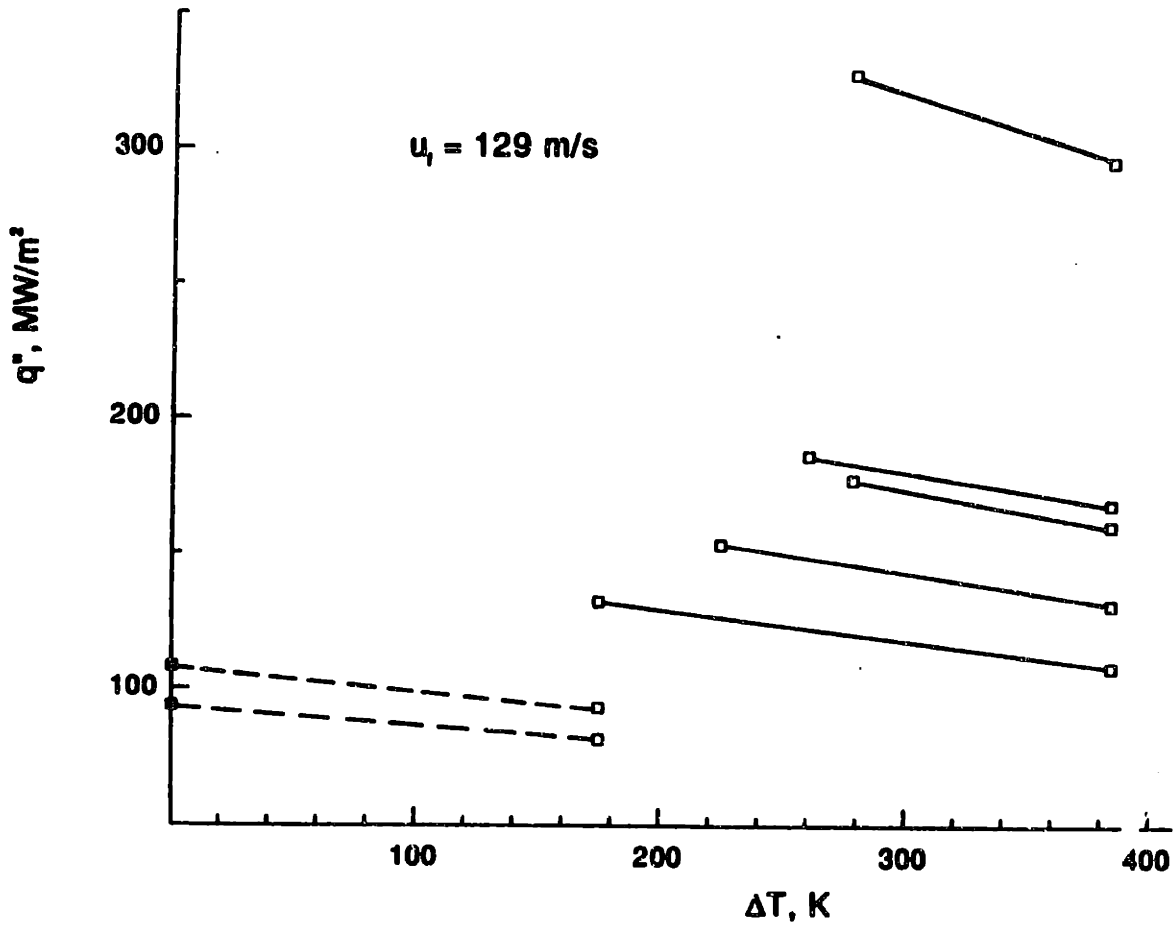

Figure 6.8: Plot of data as heat flux versus temperature.

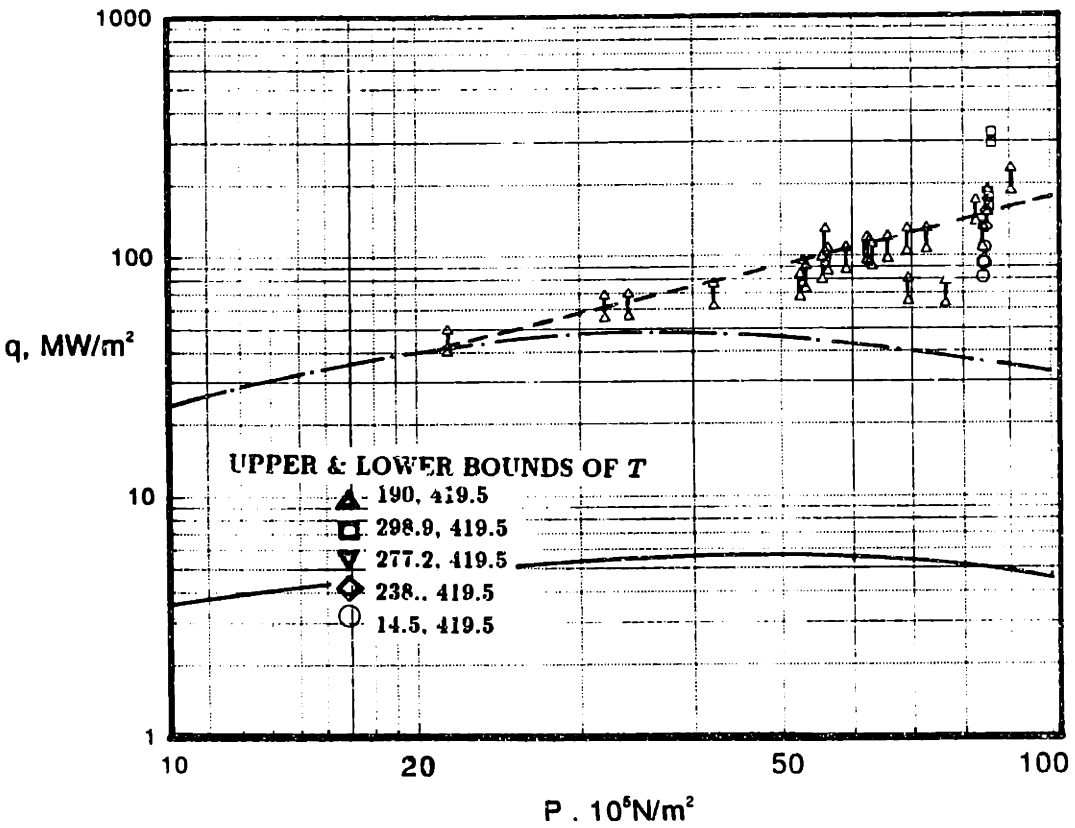

Figure 6.9: Plot of data as heat flux versus stagnation pressure: Pool boiling CHF — —; Equation 6.8 – · – · –; Present correlation – – –..

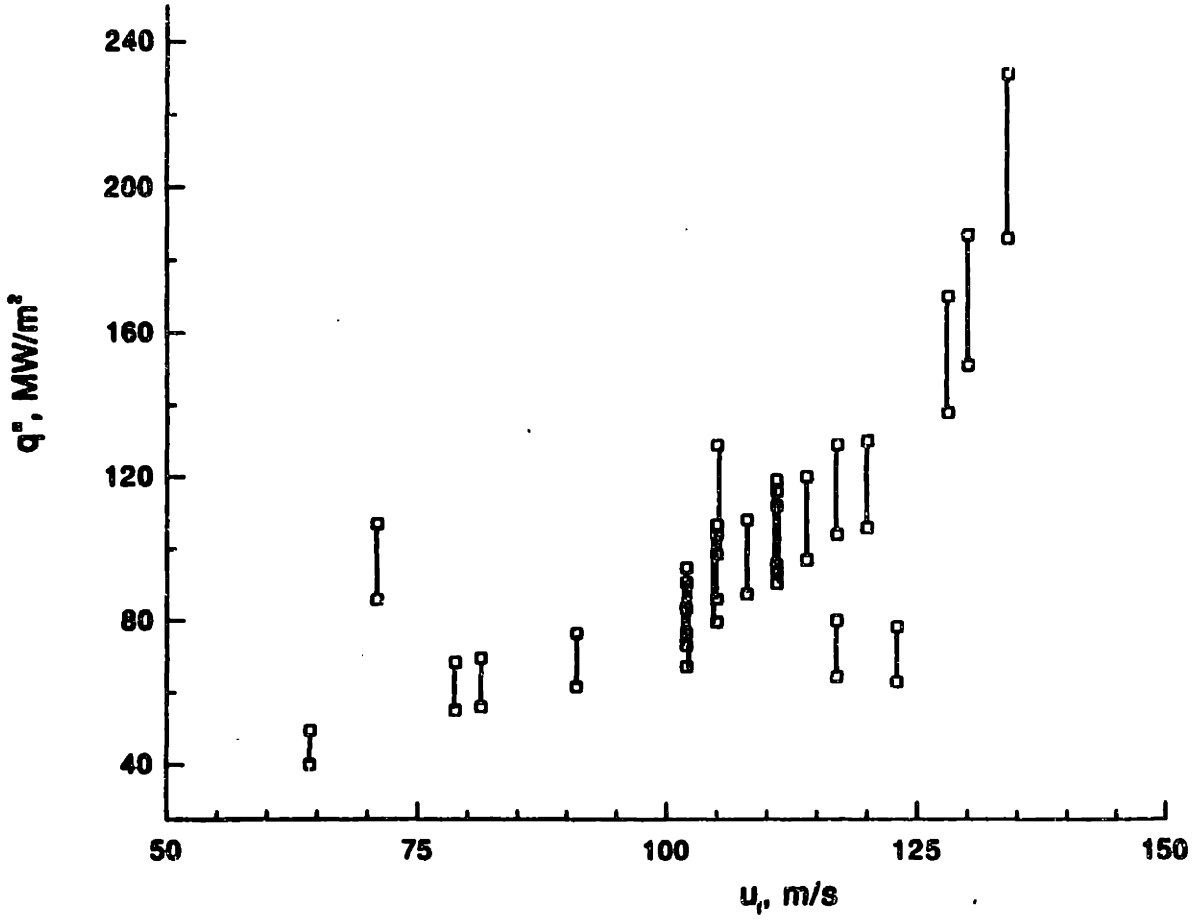

Figure 6.10: Plot of data as heat flux versus jet velocity.

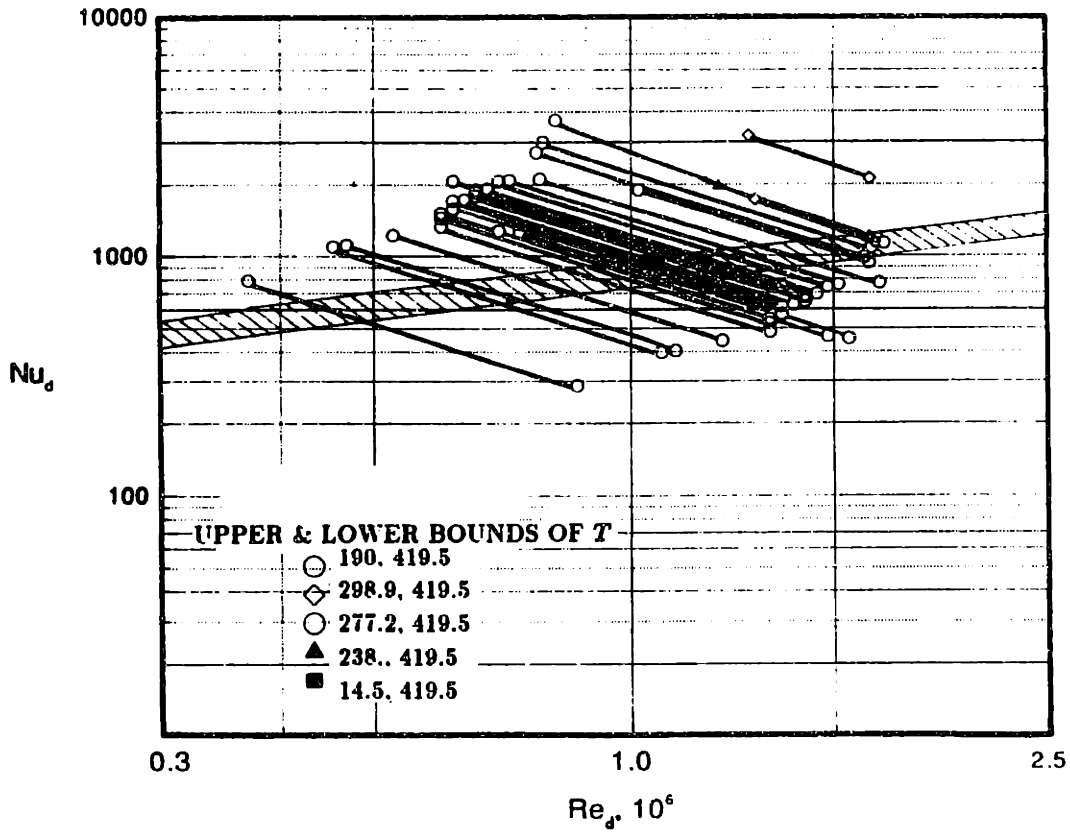

Figure 6.11: Plot of data as Nusselt number versus Reynolds number.

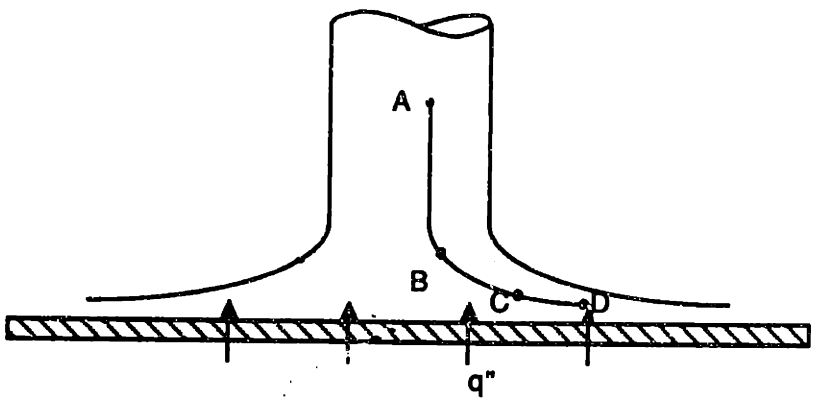

Figure 6.12: The path of a liquid particle in a jet.

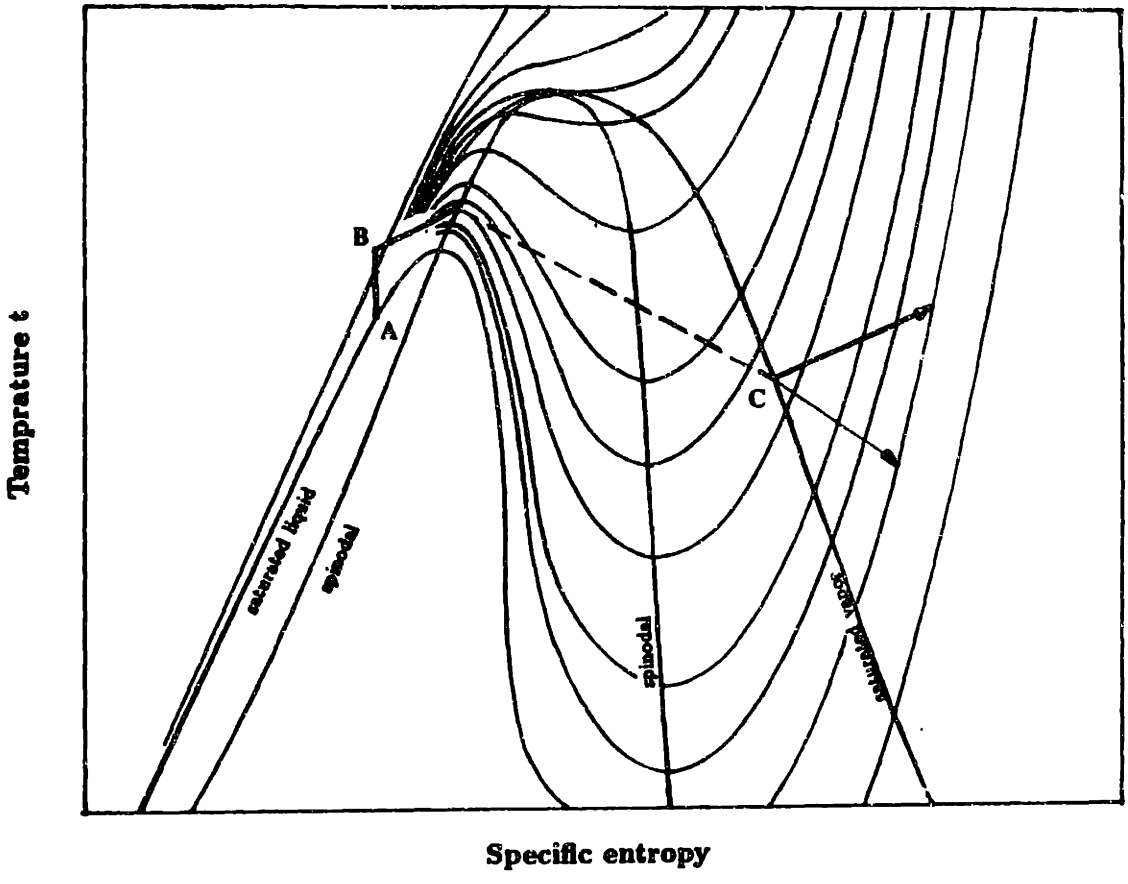

Figure 6.13: The path of the liquid particle on a s-h graph.

Chapter 7

DESIGN TIPS FOR JET IMPINGEMENT COOLING

7.1 Single phase cooling design

Economic gain is an important goal in engineering design. When a single jet is used to cool a constant heat flux target, the priority is to guarantee that the highest temperature is below the maximum tolerable temperature and then to optimize the costs of material and energy.

When an area with certain radius, R, and heat flux, q_w, is required to be cooled below a certain temperature, T_{max}, the working fluid, the incoming jet temperature, the jet diameter, and the jet velocity need to be determined. The choice of working fluid is determined by special chemical, electrical, and

environmental considerations. Table 7.1 gives the thermophysical properties for some common coolants.

Once the working fluid and incoming jet temperature have been decided, turbulent flow or laminar flow must be specified. First, we must guess a jet diameter and velocity. In practical applications, space requirement limits the possibility of using large tanks to damp the upstream turbulence, and only pipe-type nozzle are likely to be used. For high Reynolds number, the incoming flow must be turbulent. For low Reynolds number, the incoming flow must be laminar.

If the space does allow the installation of a large damping tank, then we need to calculate the dimensionless group $\mathrm{We}_d \exp \frac{0.971l}{d\sqrt{\mathrm{We}_d}}$. From Equation 3.12

$$\xi = -0.0935 + 3.41 \times 10^{-5}\omega + 2.25 \times 10^{-9}\omega^2 \tag{7.1}$$

, the fraction of incoming mass splattered can be calculated. Then we can go to the laminar and turbulent correlations, and compare the Nusselt numbers for laminar and turbulent flow and choose the flow with larger Nusselt number at $r = R$. If only the total heat flow is considered, the comparison should be based on the average Nusselt number instead of the local one. Because the jet diameter and velocity are only guesses now, we still need to go back to check if they are the best combination.

After choosing the flow type, no matter whether you have laminar or turbulent jet, the similar procedures can be followed to determine the jet diameter and velocity for incoming jet. The following is an example for a laminar jet.

– Assume R is located in Region 2. Then the Nusselt number based on jet diameter is

$$\mathrm{Nu}_d = 0.632\mathrm{Re}_d^{1/2}\mathrm{Pr}^{1/3} \tag{7.2}$$

– The Reynolds number, $\frac{u_f d}{\nu}$, is determined by both jet diameter and velocity. The jet diameter and velocity can be determined by optimizing the pumping power, which can be expressed as

$$P_{total} = (\eta_{pump} + \eta_{pipe})\rho g Q H \tag{7.3}$$

$$= \frac{\pi}{8}\rho d^2 u_f^3(\eta_{pump} + \eta_{pipe}) \tag{7.4}$$

$$= C\frac{\mathrm{Nu}_d^6}{\mathrm{Pr}^3}\left(\frac{R^3\nu^3}{d^3\rho_l^2 d}\right)(\eta_{pump} + \eta_{pipe}) \tag{7.5}$$

$$= C\frac{q^6 d^2 R^3 \nu^3}{(T_{max} - T_f)^6 k^6 \rho_l^6}(\eta_{pump} + \eta_{pipe}) \tag{7.6}$$

where η_{pump} is the efficiency of the pump and η_{pipe} is the friction coefficient for pipes. The above equation seems to imply that the best combination of jet diameter and velocity is occurs by reducing diameter as small as possible. However, the η_{pump} and η_{pipe} are functions of velocity and diameter, which depends on the pump and pipe system designs.

Second, Region 2 is limited by:

$$\frac{R}{d} \leq 0.1773\mathrm{Re}_d^{1/3} = 0.1773\left(\frac{u_f d}{\nu}\right)^{1/3} \tag{7.7}$$

. Based on the jet diameter and velocity to check if the edge of heating area is located in region 2.

- Assume R is located in Region 3, Region 4, or the turbulent region. Repeat the above procedure to find the jet diameter and velocity based on Equations 2.3, 2.5, and turbulent correlation.
- Compare the pumping powers for different combinations of diameter and velocity, and choose the best combination which consumes minimum power.

If the incoming jet is turbulent jet, the general procedure is the same as the above. For the area before jet splattering, refer to Figure 3.11 for the augmentation factor.

Compare the calculated jet diameter and velocity with the guessed diameter and velocity. If their agreement is not satisfactory, repeat the whole procedure.

7.2 Design problem for high cooling rate

For high heat fluxes, which are those above 10 MW/m^2, many problems still require further research. In future commercial fusion reactors, a steady state cooling rate of more than 10 MW/m^2 is expected. For safety, the maximum cooling rate must be much higher than 10 MW/m^2 and the operation must be very reliable over a long period. At extreme high heat flux, the conduction through the solid wall rather than the cooling fluid becomes the main limiting factor. The wall not only experiences a very high heat flux, but also a very large mechanical stress introduced by jet momentum and thermal strain. Fracture of components due to fatigue is the most common cause of service failure, where

cyclic stressing is taking place. With static loading of a ductile material, plastic flow precedes final fracture, but with fatigue, the crack is initiated from points of high stress concentration, and then spreads or propagates under the influence of the load cycles until it reaches a critical size when fast fracture of the remaining cross-section takes place. Life testing under high heat fluxes is crucial in order to get data for the reliability of the materials used.

There are currently a wide variety of sophisticated finite element computer codes available to predict the stresses and displacements of high heat flux components. But accurate failure analysis remains very difficult. Structure failure can be caused by following modes (Abdou *et al*, 1984):

- Tensile plastic instability (ductile rupture)
- Compressive instability (bucking)
- Brittle fracture
- Excessive deformation

In general, the models for predicting these types of failures are not well understood. In the following, rankings of materials (which are confirmed by our practical experience) are listed as a guide for choosing materials at high heat fluxes under jet impingement.

The thermophysical properties for some metals are in Table 7.2. The materials having high melting points are tungsten, rhenium, tantalum, molybdenum, and iridium. But rhenium and iridium are to expensive (Column 5) to use. The

thermal expansion is related to the thermal stress. Metals with small thermal expansion are molybdenum, tungsten, iridium, rhenium, and chromium. The thermal conductivity is well-known for the top metals (Silver, Gold, aluminum, tungsten, and molybdenum). If we look at this list, we may identify tungsten and molybdenum as the most promising metals (Figure 7.1).

Fracture toughness is also very important. The data for this property are very limited, and we have had trouble finding for these metals. The present experiments comparing tungsten, molybdenum, and tantalum demonstrated that even though tungsten had a very high yield stress, but it was very brittle. Molybdenum had lower yield stress, but can took higher heat fluxes than tungsten. Therefore, the fracture toughness must be considered in making a material selection.

7.2.1 Material properties limiting heat fluxes by conjugate heat transfer for jet impingement and conduction

Stress dominated by jet momentum

In combined convection by a impinging jet and conduction through a plate, material properties provide the main constraint on heat flux. For a circular disk with a central load F and without thermal stress, the maximum normal stress is

$$\sigma_{max,l} > C\frac{3F}{2\pi t^2} \tag{7.8}$$

where F is equal to the jet total momentum $\frac{\pi}{4}\rho u_f^2 d^2$, and $C = \frac{3}{2\pi}$ for edge clamped and $C = \frac{3}{2\pi}(1+\nu)\ln\frac{R}{r}$. Since the load is

$$F = \frac{\pi}{4}d^2\rho_l u_f^2 = \frac{\pi}{4}\mathrm{Re}_d^2\frac{\nu^2}{\rho_l} \tag{7.9}$$

and

$$\Delta T = qt/k_{solid} \tag{7.10}$$

and knowing q as function of u_f and other working fluid properties, we can eliminate u_f and t. Taking convection as a example, rearrange to find

$$A\frac{q^6 d^2}{\Delta T_l}\sigma_{max}(k\Delta T)^2 \tag{7.11}$$

where

$$A = \frac{\nu^2}{k_l^4\rho \mathrm{Pr}^{4/3}} \tag{7.12}$$

where $\Delta_l T$ is the temperature difference between the wall and liquid. For the same d and Δ_l, in the first term only working fluid properties are involved. Changing the working fluid can increase or decrease the stress. Better working fluid has smaller value of A (Figure 7.2).

On the right we have a term determined by material properties. This term suggests that the material with higher yielding stress, higher conductivity, and higher melting point will be better (Figure 7.3).

Stress dominated by the thermal stress

The maximum thermal stress for a circular disk (free support) with a temperature difference between center and average temperature, ΔT is

$$\sigma_{max} > \frac{\alpha E}{(1-\nu)}\Delta T \tag{7.13}$$

Considering

$$\Delta T = qt/k_{solid} \tag{7.14}$$

and we have

$$q_{max} \sim \Delta T \frac{\sigma_{max}(1-\nu)k_{solid}}{E\alpha} \tag{7.15}$$

for the same disk thickness, t.

When the stress is dominated by thermal stress, the following group can be used to rank the materials for the same temperature gradient (same t and ΔT):

$$\frac{\sigma_{max}(1-\nu)k_{solid}}{E\alpha} \tag{7.16}$$

Figure 7.4 (Abdou *et al*, 1984) shows a comparison of the above values for different materials. Molybdenum has the highest values among metals, which is consistent with our experiments mentioned in previous chapter.

7.2.2 Thermoelastic stability

The above discussion is based on the assumptions that deflections of the plate are small compared with the plate thickness, so that the linear strain-displacement

relations are valid, and that the influence of membrane forces on the transverse deflection can be ignored in equilibrium considerations. Under high speed jets concentrated at the center of a plate, the transverse deflection may be not small compared to the plate thickness, since the latter is usually small under high heat fluxes. Considering a theory proposed by von Kármán (Hetnarski, 1986), and assuming a linear temperature distribution across a circular plate of diameter D, in which the thermal stress is dominant, the critical thermal force gives the buckling instability condition:

$$\frac{3D^2(1+\nu)\alpha\Delta T}{2t^2} = C \tag{7.17}$$

where C is constant which is equal to 4.20 for a simple supported plate and 14.7 for a clamped plate.

7.2.3 Fouling and erosion on liquid side

For a heat transfer surface, fouling usually deteriorates the performance significantly. Jet impingement cooling can effectively ease the fouling problem, which is one of the advantages of jet impingement. Jet impingement is, in fact, one of the technologies of cleaning surfaces (Errico, 1986). However, instead of fouling, jet impingement has a corrosion-erosion problem, especially for high speed jets (Field 1983; Abdou *et al.*, 1984). In addition, at extremely high heat fluxes, surface erosion is a critical lifetime issue that directly affects cooling performance. The long-term corrosive effects of jet impingement on target materials

needs to be investigated further.

Resolving the problem of extremely high heat fluxes using jet impingement has many issues in common with the problem of high heat flux materials and components research in fusion devices (Abdou, 1984). Many of these problems require extensive long-term development.

REFERENCES

Abdou *et al.*, (DOE Office of Fusion Energy Task Group on High Heat Flux Material and Component Development), "Magnetic Fusion Energy Plasma Interactive and High Heat Flux Components," Vol.2, UCLA, 1984.

Errico, M., "A Study of the Interaction of Liquid Jets with Solid Surfaces", Ph.D. Thesis, University of California, San Diego, 1986.

Field, J.E. *et al.*, "On Erosion by Liquid and Solid Impact," *Proc. 6th Int. Water Jet Conf.*,, pp.9, 1983.

Hetnarski, R.B., *Thermal Stresses I,* Vol.I, Elsevier Science Publishers B.V., 1986.

Property	PERFLOURINATED LIQUID DESIGNATION FC-87	L-1402	FC-72 FC-86	FC-84	FC-77 FC-75 FC-104	FC-43	R-113	Water
Boiling point, degrees C	30	51	52	82	100	172	48	100
Liquid density, ρ_l, kg/m^3	1633	1825	1593	1575	1500	1845	1511	958
Vapor density, ρ_v, kg/m^3	11.58	11.25	12.68	13.26	14.31	18.35	7.40	0.59
Dynamic viscosity, μ, kg/m sec	4.20E-04	5.20E-04	4.50E-04	4.20E-04	4.50E-04	3.90E-04	5.03E-04	2.70E-04
Specific heat, c, J/kg K	1088	1050	1098	1130	1172	1255	979	4184
Heat vaporization, h_{fg}, J/kg	87927	104675	87927	79653	83740	71179	146234	2357044
Therm conductivity, k, W/m K	5.51E-02	5.96E-02	5.46E-02	5.25E-02	5.70E-02	6.50E-02	7.02E-02	6.93E-01
Surface tension, σ, N/m	8.90E-03	1.09E-02	8.50E-03	7.70E-03	8.00E-03	4.50E-03	1.47E-02	5.85E-02
Therm coef expan, β, K^{-1}	1.90E-03	1.60E-03	1.60E-03	1.50E-03	1.40E-03	1.20E-03	1.70E-03	2.00E-04
Dielectric const	1.71	1.77	1.72	1.71	1.75	1.68	2.60	78.00
Average molecular weight, gm/mole	288	299	338	388	438	670	187	18

Table 7.1: Thermophysical Properties of Selected Coolants (Danielson *et al.*)

Table 7.2: Thermophysical Properties of some metals.

Metal	Melting point (°C)	Thermal expansion, /°C (per °C×10^6)	Modulus of elasticity (Pa, ×10^9)	Thermal conductivity (W/m°C)	Price /gold
Aluminum	658.6	23.86	70.3	221.	.00029
Iron	1536	11.7	210.	72.8	.000059
Iridium	2454	6.8	535.	58.6	3.29
Chromium	1900	8.1	186.	69.1	.00196
Molybdenum	2656	4.9	329.	145.	.0274
Rhenium	3167	8.0	518.	71.2	2.89
Rhodium	1966	8.3	378.	87.9	3.57
Silver	960	19.0	73.1	419.	.0259
Tantalum	3000	6.6	186.	54.4	0.143
Tungsten	3370	4.45	359.	201.	.0031
Gold	1063	14.2	79.3	293.	1.00

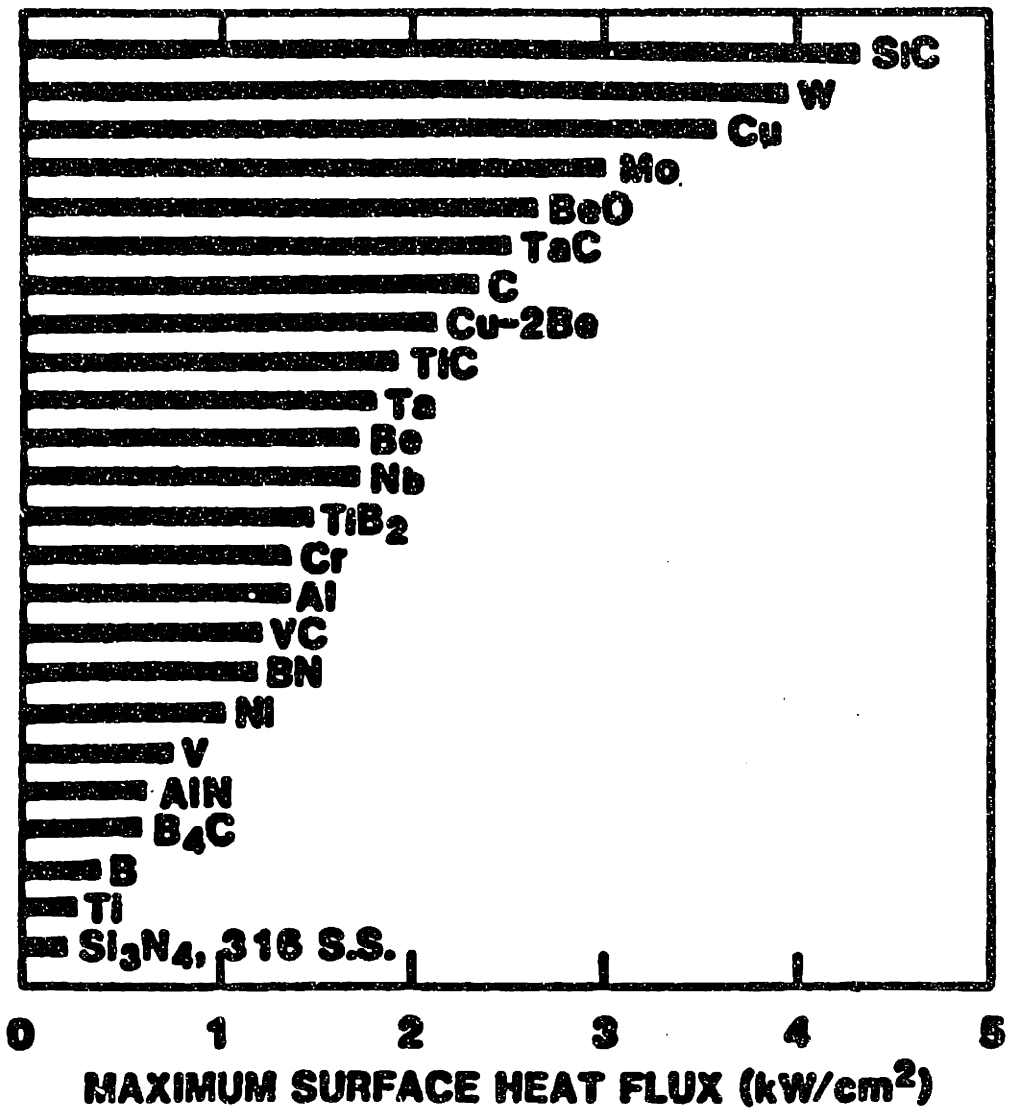

Figure 7.1: Maximum heat flux needed to melt the surface of a 1 cm thick plate cooled on its backside to 100°C during steady-state conditions (Abdou *et al.*, 1984)

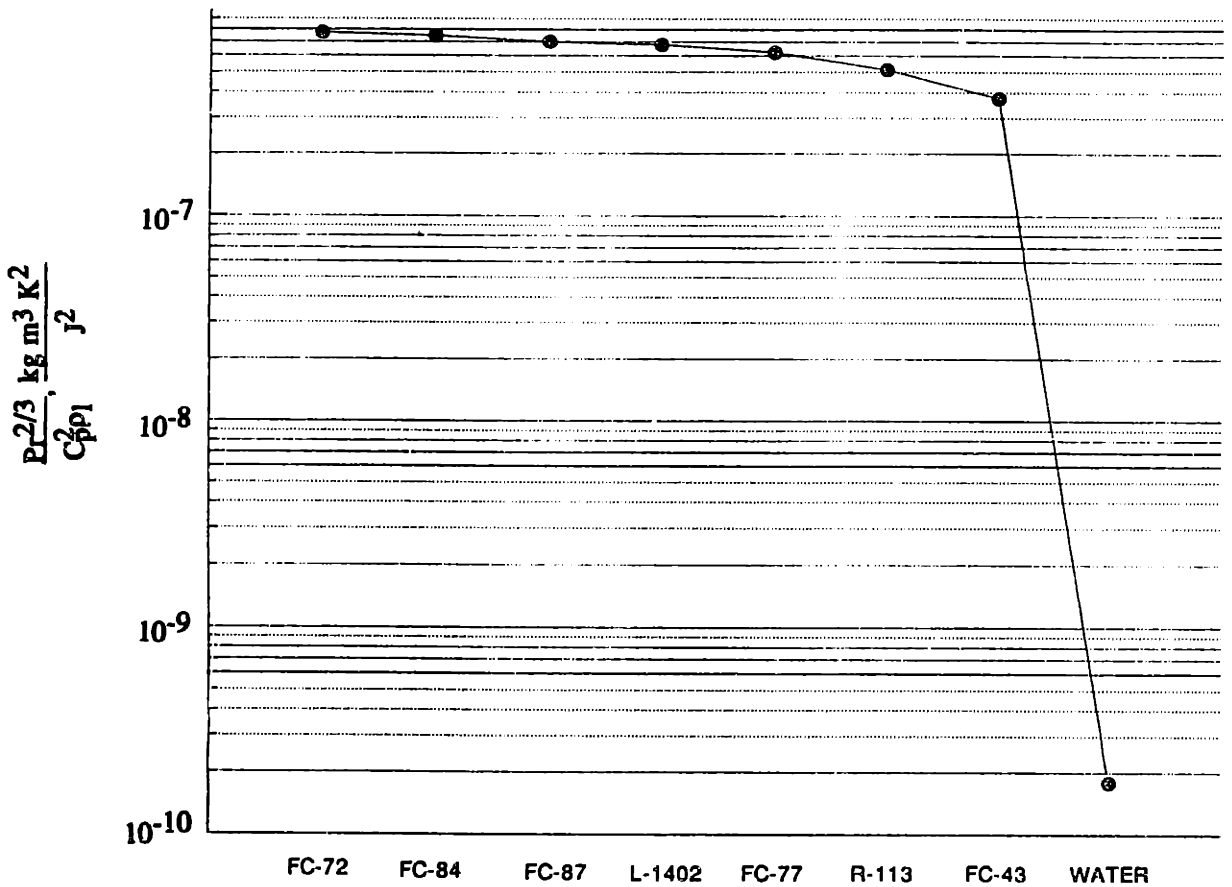

Figure 7.2: Values of A for selected coolants: $A = \frac{Pr^{2/3}}{C_p^2 \rho_l}$

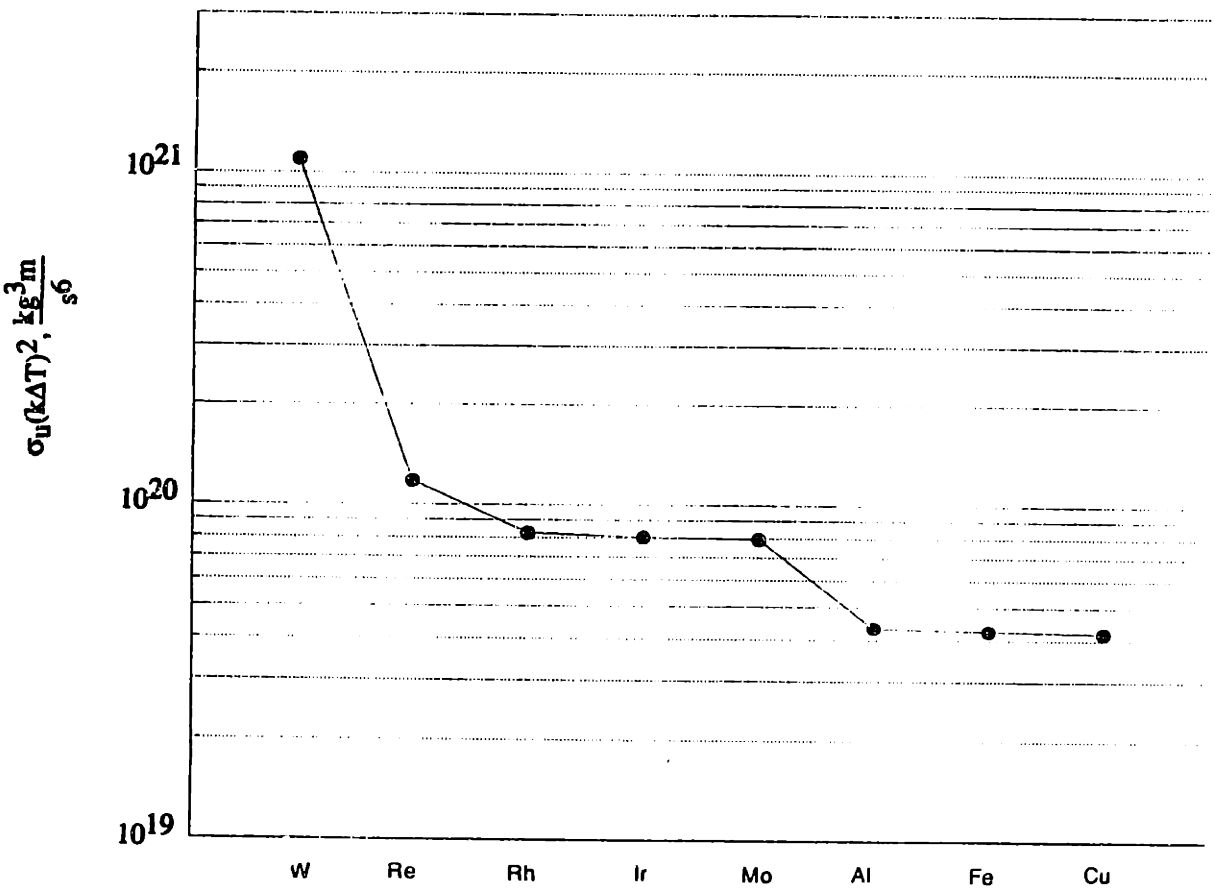

Figure 7.3: Values of $\sigma_u(k\Delta T)^2$ for selected metals.

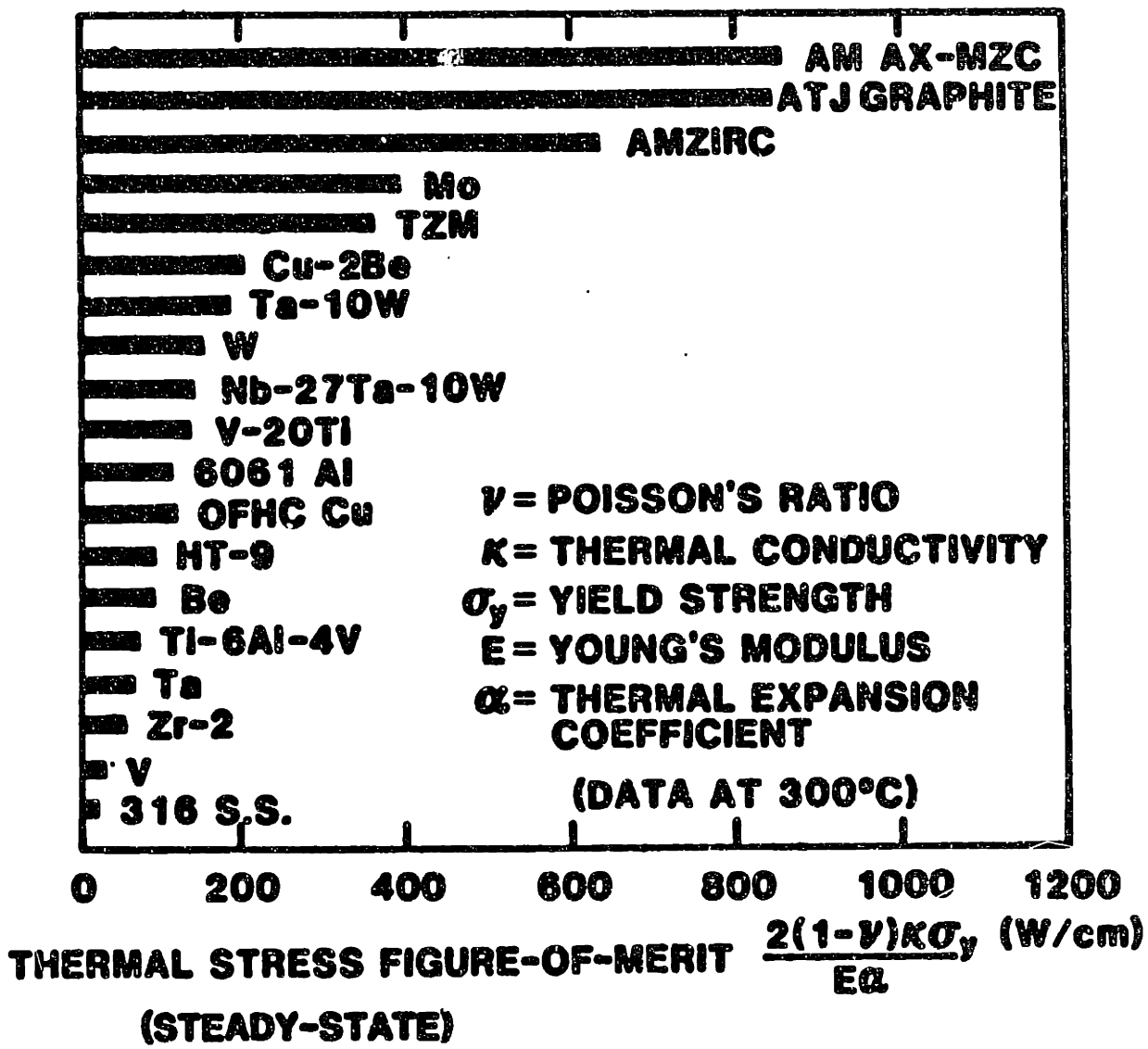

Figure 7.4: Thermal stress figure-of-merit for steady-state heating. Large values imply that greater heat fluxes can be removed steady-state without yielding the material (Abdou *et al.*, 1984).

Appendix A

Limit of Classical Conductivity Theory

Thermal conductivity theory is well established by elaborate classical statistics and quantum statistics for a state not far from the equilibrium state. Conduction electrons cause the large heat conductivity of metals. Heat conduction by vibrations of the lattice is rather small by comparison to the electron contribution, especially when the resistance is mainly due to impurities or imperfections of metals (Ziman, 1960). The classical statistical theory of the conduction of electricity and heat in metals is due to Lorentz (1916). He attributed both effects to the motion of free electrons and treated the electron gas in the metal by classical Maxwell-Boltzmann statistics. Sommerfeld (1933) modified the Lorentz theory by introducing quantum statistics. In classical theory, the conductivity

of metal can be expressed (Lindsay 1941):

$$k = \frac{16\pi^3\kappa^3 T^2 m}{9h^3}\gamma_1 l(\gamma_1) \tag{A.1}$$

where κ is Boltzmann's constant, h is Planck's constant, m is the electron mass, γ_1 is the Fermi potential, and l is the mean free path of electron gas. Taking the ratio of thermal conductivity, k, to electric conductivity, k_e, times temperature, T, we have the well-known Wiedemann-Franz Law with the standard Lorentz number, $k/(k_e T)$, as:

$$\frac{k}{k_e T} = \frac{\pi^2}{3}\frac{\kappa^2}{e^2} \tag{A.2}$$

The predicted ratio of the thermal conductivity to the electric conductivity

$$\frac{k}{k_e} = 7.15 \times 10^{10} \tag{A.3}$$

agrees well with experiments.

The basic assumption behind the theory is that of a state not far from the equilibrium. However, an extremely high heat flux, as we mentioned previously, can be on the order of 1 GW/m^2 for a steady state heat flux and much higher for unsteady heat flux. This indicates a huge temperature gradient within the metal. Thus, we need to check the validity of the above assumptions.

If a metal is not affected by external influences, the distribution function f_0 will remain unchanged at any particular place in the metal. However, the situation will be different when a temperature gradient is applied to the metal.

Considering an imaginary line normal to the temperature gradient in the metal, the velocities of electrons on the left of the line are different from those on the

right of the line. Supposing that the temperature on the left is larger than that on the right, the electrons on the left have larger velocity than those on the right. At any moment there are more chances for the electrons on the left to cross the line than electrons on the right. Therefore, an electric field is introduced within the metal, even though the circuit is open and the current is zero.

Under the above mentioned electric field, electrons are accelerated along the direction of electric field, or in other words, in the direction opposite the temperature gradient. Consider the electrons at a given instant t in a small volume $d\tau$ of the metal at the point x, y, z and with velocity components in the interval $v_x, v_x + dv_x$, etc. At the time $t + dt$, if there were no collisions, these electrons would be displaced to the same volume around the point $(x + v_x dt, y + v_y dt, z + v_z dt)$ and their velocity components would become $v_x + eE/m\, dt, v_y, v_z$. Note that we are assuming that the applied field acts only along the x axis. Now because of collisions, a certain number of electrons having velocity components in the interval in question at time t will have passed out of the interval by $t + dt$ and a certain number of electrons will have their velocity components brought into the interval. The difference of these two number is denoted by

$$(b - a)d\tau dv_x dv_y dv_z \tag{A.4}$$

When a steady state is established, we shall have

$$f(x + v_x dt, y + v_y dt, z + \frac{eE}{m} dt, v_y, v_z) = f(x, y, z, v_x, v_y, v_z) + (b - a)dt \tag{A.5}$$

where f is the generalized distribution function in the presence of the external

field. The above equation leads to

$$b - a = v_x \frac{\partial f}{\partial x} + \frac{eE}{m} \frac{\partial f}{\partial v_x} \tag{A.6}$$

Assume that the distribution function as altered by the temperature gradient can be expressed in term of the original distribution function f_0 and a correction term

$$f = f_0 + v_x \chi(x, v_x, v_y, v_z) \tag{A.7}$$

Substitute into equation A.6 to yield (Lindsay, 1941)

$$v_x \left(\frac{\partial f_0}{\partial x} + v_x \frac{\partial \chi}{\partial x} \right) + \frac{eE}{m} \left(\frac{\partial f_0}{\partial v_x} + \chi + v_x \frac{\partial \chi}{\partial v_x} \right) = nR^2 v \chi \int (v_x' - v_x) \cos \beta d\omega \tag{A.8}$$

In classical theory the correction term, χ, is assumed small. $v_x \frac{\partial \chi}{\partial x}$ is negligible compared to $\frac{\partial f_0}{\partial x}$ and $\chi + v_x \frac{\partial \chi}{\partial v_x}$ negligible compared to $\frac{\partial f_0}{\partial v_x}$.

However, if the temperature gradient is very large and the electric field introduced by the temperature gradient is very strong, χ may be not small and may instead be comparable to $\frac{\partial f_0}{\partial v_x}$. In the following we try to modify the classical theory and make a bound on the temperature gradient, above which the classical theory of thermal conductivity does not hold any more. In other words, the conductivity depends on not only the local temperature, but also on the temperature gradient. In order to make a bound on the temperature gradient, the correction term χ is assumed comparable to $\frac{\partial f_0}{\partial v_x}$. The term involving the derivatives of χ may be of the same order as χ. But here we do not attempt give a solution of thermal conductivity under a strong temperature gradient;

instead we try to give a sufficient condition for the breakdown of the classical theory. Then we may leave $v_x\frac{\partial\chi}{\partial x}$ and $v_x\frac{\partial\chi}{\partial v_x}$ out. The correction term, $\bar{\chi}$ can be written as:

$$\bar{\chi} = -\frac{l}{v}\left(\frac{\partial f_0}{\partial x} + \frac{eE}{mv}\frac{\partial f_0}{\partial v_x}\right) \tag{A.9}$$

Based on these assumptions and the expression for $b - a$ (Lindsay, 1968), we have

$$\chi = -\frac{l}{v}\left(\frac{\partial f_0}{\partial x} + \frac{eE}{mv}\left(\frac{\partial f_0}{\partial v_x} + \frac{v}{v_x}\chi\right)\right) \tag{A.10}$$

Rearrange to yield

$$\chi = -\frac{l}{v}\frac{1}{(1+\frac{eEl}{mvv_x})}\left(\frac{\partial f_0}{\partial x} + \frac{eE}{mv}\frac{\partial f_0}{\partial v}\right) \tag{A.11}$$

Later, the integration of χ will go from negative infinity to positive infinity. Notice that the distribution for a strongly degenerate Fermi-Dirac gas remains practically constant for a very considerable range of values of the velocity v from zero up. Since the value of $\frac{eEl}{m}$ is small, the range of velocity which makes $\frac{El}{mvv_x} \gg 1$ is very small and can be left out of the integration to avoid the singularity, which will be removed because it multiplies higher order of velocity in integration. We linearize the above equation into

$$\chi = -\frac{l}{v}\left(1 - \frac{eEl}{mvv_x} + (\frac{eEl}{mvv_x})^2\right)\left(\frac{\partial f_0}{\partial x} + \frac{eE}{mv}\frac{\partial f_0}{\partial v}\right) \tag{A.12}$$

The heat flux (or the total rate of transfer of kinetic energy per unit area per second) is

$$q = \frac{mm}{2}\int\int_{-\infty}^{\infty}\int v_x^2 v^2 \chi dv_x dv_y dv_z \tag{A.13}$$

We proceed to spherical coordinates:

$$q = \frac{2\pi m}{3}\int_0^\infty v^6 \bar{\chi} dv + 2\pi m \int_0^\infty \left(\frac{leE}{m}\right)^2 v^2 \bar{\chi} dv \tag{A.14}$$

The first integration on the right is just the one in classical theory. We need to evaluate the second integral. Substitute the expression for $\bar{\chi}$ into the second integral to give

$$2\pi m \int_0^\infty \left[\left(\frac{eE}{m}\right)^2 l^3 v \frac{\partial f_0}{\partial x} + \left(\frac{eE}{m}\right)^3 l^3 \frac{\partial f_0}{\partial v}\right] dv \tag{A.15}$$

Nondimensionalize velocity v by letting:

$$u = \frac{mv^2}{2kT} \tag{A.16}$$

$$A = \frac{kT}{m} \tag{A.17}$$

and then we can write

$$\int_0^\infty l^3 v \frac{\partial f_0}{\partial x} dv = \int_0^\infty A l^3 \frac{\partial f_0}{\partial x} du \tag{A.18}$$

and

$$\int_0^\infty l^3 v \frac{\partial f_0}{\partial v} dv = \int_0^\infty l^3 \frac{\partial f_0}{\partial u} du \tag{A.19}$$

The distribution function f_0 is given by the Fermi-Dirac expression

$$f_0(x, v_x, v_y, v_z) = \frac{2m^3}{h^3} \frac{1}{1 + e^{-\gamma_1} e^{m(v_x^2+v_y^2+v_z^2)/2\sigma T}} \tag{A.20}$$

or simply

$$f_0 = \frac{2m^3}{h^3} \frac{1}{1 + e^{-\gamma_1 + u}} \tag{A.21}$$

where both γ_1 and T vary with x Then we have

$$\frac{\partial f_0}{\partial x} = -\frac{\partial f_0}{\partial u}\left(\frac{\partial \gamma_1}{\partial x} + \frac{u}{T}\frac{\partial T}{\partial x}\right) \tag{A.22}$$

Substitute the above expression into Equation A.15 and rearrange:

$$2\pi m \int_0^\infty \left[A\left(\frac{eE}{m}\right)\left(l^3\frac{\partial \gamma_1}{\partial x}\frac{\partial f_0}{\partial u} + l^3\frac{u}{T}\frac{\partial T}{\partial x}\frac{\partial f_0}{\partial u}\right) - \left(\frac{eE}{m}\right)^3 l^3\frac{\partial f_0}{\partial u}\right] du \tag{A.23}$$

The mean free path of electrons, l, is a function of velocity u. Define

$$\int_0^\infty l^3 u^m \frac{\partial f_0}{\partial u} du = B_m \tag{A.24}$$

and recall that the first integral in Equation A.14 is

$$\frac{4\pi\kappa T}{3m} A_2 \left(eE - \kappa T\frac{\partial \gamma_1}{\partial x} - \kappa\frac{\partial T}{\partial x}\frac{A_3}{A_2}\right) \tag{A.25}$$

the first approximations to A_2 and A_3 are

$$A_2 = \frac{2\kappa T}{m}\frac{2m^3}{h^3}\gamma_1^2 l(\gamma_1) \tag{A.26}$$

$$A_3 = \frac{2\kappa T}{m}\frac{2m^3}{h^3}\gamma_1^3 l(\gamma_1) \tag{A.27}$$

Then the heat flux can be expressed as:

$$\begin{aligned} q = \; & \tfrac{4\pi\kappa T}{3m} A_2 \left[eE - \kappa T\tfrac{\partial \gamma_1}{\partial x} - \kappa\tfrac{\partial T}{\partial x}\tfrac{A_3}{A_2}\right] + \\ & \tfrac{4\pi\kappa T}{3m} A_2 \left[\tfrac{3}{\kappa T m}(eE)^3\tfrac{B_0}{A_2} - \tfrac{3}{2m}(eE)^2\left(\tfrac{\partial \gamma_1}{\partial x}\tfrac{B_0}{A_2} + \tfrac{1}{T}\tfrac{\partial T}{\partial x}\tfrac{B_1}{A_2}\right)\right] \end{aligned} \tag{A.28}$$

If the terms in the second bracket are negligible, we recover to the classical result, which is represented by the terms in the first bracket. The electric field, E, is a function of temperature gradient. If any term in the second bracket is comparable to the terms in the first bracket, the conductivity is not only a function

of temperature, but also a function of temperature gradient. Comparing the terms without derivatives, we have a condition, under which the conductivity is only a function of temperature:

$$\frac{3e^2E^2}{2m\kappa T}\frac{B_0}{A_2} \ll 1 \tag{A.29}$$

Similarly comparing the terms with $\frac{\partial \gamma_1}{\partial x}$, and with $\frac{\partial T}{\partial x}$, respectively, we have:

$$\frac{3e^2E^2}{2m\kappa T}\frac{B_0}{A_2} \ll 1 \tag{A.30}$$

$$\frac{3e^2E^2}{2m\kappa T}\frac{B_1}{A_3} \ll 1 \tag{A.31}$$

The first and second conditions are the same.

To evaluate B_m, we may expand $l^n u^m$ in a power series:

$$u^m l = \sum_{j=0}^{\infty} C_j u^{j+m} \tag{A.32}$$

and

$$l^3 u^m = \sum_{i}^{\infty}\sum_{j}^{\infty}\sum_{k}^{\infty} C_i C_j C_k u^{i+j+k+m} \tag{A.33}$$

Taking the first approximation (Lindsay, 1968), we have

$$B_o \approx -\left(\frac{2m^3}{h^3}\right) l^3(\gamma_1) + \ldots \tag{A.34}$$

Substituting the expressions for B_m and A_n into the three conditions, we finally end up with one condition:

$$\frac{3}{4}\left(\frac{eEl}{\kappa T}\right)^2 \frac{1}{\gamma_1} \ll 1 \tag{A.35}$$

The approximation for γ_1 is

$$\gamma_1 = \left(\frac{3n}{4\pi}\right)^{2/3} \frac{h^2}{2m\kappa T} \tag{A.36}$$

where n is the number conduction electrons per unit volume and the electric field is given by:

$$eE = \frac{4\pi^2}{3}\left(\frac{4\pi}{3n}\right)^{2/3} \frac{m\kappa^2 T}{h^2}\frac{\partial T}{\partial x} \tag{A.37}$$

Substituting into the condition, we obtain the condition for which the influence of the temperature gradient is negligible:

$$\frac{\partial T}{\partial x} \ll \frac{\sqrt{3}}{4\pi^2}\left(\frac{3n}{4\pi}\right)^{4/3} \frac{h^4}{4m^2k^2T} \tag{A.38}$$

Taking silver as a example, $n = 5.9 \times 10^{28} m^{-3}$, $l \sim 5 \times 10^{-10} m$, and taking $T = 300K$, we have

$$\frac{\partial T}{\partial x} \ll 1.18 \times 10^{16} K/m \tag{A.39}$$

For a 1 cm thick plate, the heat flux is about 5×10^{20} W/m^2. The conductivity in steady-state situations unlikely to be encountered in real materials and can be regarded to be independent of temperature gradient.

REFERENCES

Lindsay, R.B., *Introduction to Physical Statistics,* Dover Publications, Inc., 1968.

Lorentz, H.A., *Theory of Electrons,* New York, 1916.

Sommerfeld, A. and Bethe, H., *Handbuch der Physik*, 1934.

Ziman, J.M., *Electrons and Phonons*, Oxford University Press, 1960.

Appendix B

Integral Solutions of Heat Transfer by a Laminar Jet

Many investigations have dealt with convective heat transfer by submerged jet impingement (gas jets in gases or liquid jets in liquids), but studies of free liquid jets (travelling through gases) are much less common, particularly those presenting theoretical analyses of the heat transfer by liquid jets. The reason may be the complexity of the local phenomena.

When a liquid jet strikes a flat surface, it spreads radially in a thin film. This film is responsible for convective heat removal form the surface. Following Watson (1964), we subdivide the jet impingement flow into four regions:

1. *The stagnation zone.*

2. *The boundary layer region.* In this region, the viscous boundary layer

thickness is less than the liquid sheet thickness, so that the liquid on the surface is unaffected by wall friction.

3. *The fully viscous sheet.* In this region, the boundary layer thickness is the same as the sheet thickness. The viscous influence extends through the entire liquid film, from the wall to the free surface.

4. *The hydraulic jump.* An abrupt increase of liquid sheet thickness occurs, and in this region the liquid velocity is much lower than in the upstream region.

Sharan (1984) applied the momentum integral method to analyze regions 2 and 3 and obtained results in good agreement with those of Watson.

McMurray *et al.* (1966) studied convective heat transfer to impinging *plane* jets from uniform heat flux walls. They observed the heat transfer to be subdivided into an impingement zone and a zone of uniform parallel flow. To fit their data, they based heat transfer correlations on the stagnation flow in the impingement zone and on the flat plate boundary layer in the uniform parallel flow zone. They obtained results in the form

$$\mathrm{Nu}_x = f(\theta, \eta, \mathrm{Re}_x, \mathrm{Pr}) \tag{B.1}$$

where θ is the angle of impingement and η is jet velocity normalized with that just outside the boundary layer, u/u_f.

Chaudhury (1964) solved the axisymmetric energy equation for a constant wall temperature condition in the fully viscous region, where a similarity solution

of the momentum equation is available. The solution was expressed as a series expansion.

Metzger *et al.* (1974) experimentally studied the effects of Prandtl number on heat transfer by liquid jets. They used a uniform surface temperature boundary condition at the test surface. They presented only surface average values of the Stanton number, determined from measurement of the total heat flux, the test surface temperature, and the jet adiabatic wall temperature. No local measurements or analytical results were given. Their correlations are based on data for oil and water; for water, their correlation represents 95% of the data for disk radii of up to 6.6 jet diameters to within $\pm 25\%$. The possible effect of evaporation resulting from apparently high liquid surface temperatures was not documented.

Carper *et al.* (1978,1986) studied the heat transfer from a rotating disk struck by a liquid jet. The papers show that disk rotation enhances the heat transfer

In this appendix, an integral method is used to predict the Nusselt number for constant heat flux and to examine the distance required to reach liquid saturation temperatures (relevant to the boiling jet problem).

The heat transfer regions are more complicated than those of the flow field because more parameters are involved. We shall assume that the Prandtl number is greater than unity, $Pr > 1$, as is the case for most liquids. The heat transfer regions can then be subdivided as follows (*see* Figure B.1).

1. *The stagnation zone.*

2. $\delta < h$ *region*: Within this region, the velocity outside the viscous boundary layer is undisturbed and approximately equal to the jet velocity, u_f.

3. $\delta = h$ *and* $\delta_t < h$ *region*: Within this region, the temperature outside the thermal boundary layer is not affected by the heat transfer, but the thermal boundary layer is affected by the viscous retardation of the momentum boundary layer.

4. $\delta = h, \delta_t = h$, *and* $T_w < T_{sat}$ *region*: In this region, the thermal boundary layer has reached the surface of the liquid sheet, and the temperature of the liquid surface increases with radius. Our analysis below shows that this region cannot exist for Pr > 4.859.

5. *The boiling region:* This region may include regions of nucleate boiling, burnout, and dry surface if the heat flux is high enough. Since boiling might occur at any wall temperature beyond T_{sat}, depending on heater finish and other factors, we will refer to the entire region for which $T_w > T_{sat}$ as the boiling region. We avoid all detailed consideration of nucleation incipience in the present work.

6. *The hydraulic jump:* In this region the heat transfer deteriorates dramatically. If the jet is directed upward, the hydraulic jump is very different than for the downward-directed jet and is associated with a Rayleigh-Taylor instability (*see* Chapter 4).

We do not treat region 5 or region 6 hear. It must be noted that the all of the above regions may not exist at the same time, and that the last two may occur in a different sequence. For example, boiling incipience may take place in any region, and it can change the region map. The hydraulic jump may even occur in region 2 for low heat flux.

We note in passing that for Pr < 1, region 2 and region 3 will instead be:

1. $\delta < h$ *region:* Since Pr < 1, the viscous boundary layer is thinner than the thermal boundary layer.
2. $\delta_t = h$ *and* $\delta < h$ *region:* In this region, the thermal boundary layer has reached the surface while the viscous boundary layer has not.

For the constant wall temperature problem, the region map would be simpler since we know in advance whether or not boiling occurs. In the present paper, we consider the regions 2, 3, and 4 without boiling for a uniform wall heat flux with Pr > 1.

B.1 Integral Solutions for the Heat Transfer: $Pr > 1$

B.1.1 Region 2

Sharan (1984) shows that treating the flow as purely radial is a very good approximation. We assume that in the regions beyond region 1, a purely radial

flow occurs. In these regions, the integral energy equation is given by

$$\frac{d}{dr}\int_0^{\delta_t} ru(T-T_f)\,dy = \frac{q}{\rho c_p}r \tag{B.2}$$

where T is the liquid temperature profile, T_f is the subcooled incoming jet temperature, q is the uniform wall heat flux, u is the radial liquid velocity profile, and other terms are defined in the nomenclature. We approximate the profiles in equation (B.2) as:

$$T - T_w = (T_f - T_w)\left[\frac{3}{2}\frac{y}{\delta_t} - \frac{1}{2}\left(\frac{y}{\delta_t}\right)^3\right] \tag{B.3}$$

$$u = u_{max}\left[\frac{3}{2}\frac{y}{\delta} - \frac{1}{2}\left(\frac{y}{\delta}\right)^3\right] \tag{B.4}$$

for T_w the wall temperature and $u_{max} = u_f$ the constant liquid surface speed in region 2. For $\mathrm{Pr} > 1$, we neglect $3\delta^3/280{\delta_t}^3$ relative to $3\delta/20\delta_t$ and integrate to obtain

$$\frac{27}{80}\,\mathrm{Re}_d\mathrm{Pr}\,\frac{1}{\mathrm{Nu}_r^3}\left(\frac{r}{d}\right)^2\frac{r^2}{\delta d} = \frac{1}{2}\left(\frac{r}{d}\right)^2 + C_2 \tag{B.5}$$

where $\mathrm{Nu}_r = qr/k(T_w - T_f)$ and $\mathrm{Re}_d = u_f d/\nu$.

For $d/2 \ll r$, Sharan shows that the initial boundary layer thickness can be neglected. We have the same situation for the thermal boundary layer and may use Sharan's expression for δ

$$\delta = 2.679\left(\frac{rd}{\mathrm{Re}_d}\right)^{1/2} \tag{B.6}$$

Thus, we find

$$\mathrm{Nu}_r = 0.632\,\mathrm{Re}_d^{1/2}\mathrm{Pr}^{1/3}\left(\frac{r}{d}\right)^{1/2} \tag{B.7}$$

At $r = r_o$, the viscous boundary layer reaches the surface of the liquid sheet, which is the border of region 2. Sharan gives

$$r_o = 0.1773\,\mathrm{Re}_d^{1/3} d \tag{B.8}$$

The size of the stagnation zone may be estimated by calculating the radius at which the stagnation boundary layer and the region 2 boundary layer have the same thickness (*viz.* $2.107\,d\,\mathrm{Re}_d^{1/2} = 2.679(r\,d/\mathrm{Re}_d)^{1/2}$; White, 1974; Sharan, 1984). The result is:

$$\frac{r_m}{d} = 0.787 \tag{B.9}$$

Similarly, Stevens and Webb found the stagnation region beneath a turbulent jet to reach to roughly $r/d = 0.75$. This crude estimate shows that the stagnation zone is very small. Its primary importance is that it possesses the maximum local heat transfer coefficient (lowest wall temperature) in the flow. It contributes little, however, to overall heat removal or downstream Nusselt numbers as may be seen from the full integral result for region 2 which does not neglect the stagnation zone heat flow as does eqn. (B.7):

$$\mathrm{Nu}_d = \left(\frac{\frac{27}{80}\mathrm{Re}_d \mathrm{Pr} \frac{r}{\delta}}{\frac{1}{2}\left(\frac{r}{d}\right)^2 + C_2} \right)^{1/3} \tag{B.10}$$

At $r = r_m$, the Nusselt number should equal the stagnation zone Nusselt number; thus,

$$C_2 = -0.2535 \tag{B.11}$$

The error in Nu_d caused by neglecting the stagnation zone is less than 10% for $r/d > 2.3$.

B.1.2 Region 3

The significant difference between this region and region 2 is that in this region the velocity at the liquid surface, u_{max}, is not constant. Watson (1964) and Sharan (1984) show

$$u_{max} = \frac{A}{hr} = \frac{1}{5}\frac{u_f d^2}{hr} \tag{B.12}$$

where

$$A = \frac{u_f d^2}{5} \tag{B.13}$$

and

$$h = 0.1713\left(\frac{d^2}{r}\right) + \frac{5.147}{\mathrm{Re}_d}\left(\frac{r^2}{d}\right) \tag{B.14}$$

In this region, the energy equation is again equation (B.2), but u_{max} is now a function of r and h and $\delta = h$. Integration with equations (B.3), (B.4), and (B.12), neglecting higher order terms as before, gives

$$\frac{3}{100}\mathrm{Re}_d\mathrm{Pr}\frac{1}{\mathrm{Nu}_r}\left(\frac{\delta_t}{h}\right)^2\frac{r}{d} = \frac{1}{2}\left(\frac{r}{d}\right)^2 + C_3 \tag{B.15}$$

With

$$\mathrm{Nu}_r = 3r/2\delta_t \tag{B.16}$$

from equation (B.3), substitution of equation (B.14) into equation (B.15) and subsequent rearrangement then yields

$$\mathrm{Nu}_r = \frac{0.407\,\mathrm{Re}_d^{1/3}\mathrm{Pr}^{1/3}(r/d)^{1/3}}{\left[0.1713\left(\frac{d}{r}\right)^2 + \frac{5.147}{\mathrm{Re}_d}\frac{r}{d}\right]^{2/3}\left[\frac{1}{2}\left(\frac{r}{d}\right)^2 + C_3\right]^{1/3}} \tag{B.17}$$

From equation (B.8), at $r = r_o$

$$\mathrm{Nu}_r = 0.632\,\mathrm{Re}_d^{1/2}\,\mathrm{Pr}^{1/3}\left(\frac{r_o}{d}\right)^{1/2} \tag{B.18}$$

Solving equations (B.17 - B.18) for C_3 produces

$$C_3 = \frac{0.267(d/r_o)^{1/2}}{\left[0.1713\left(\frac{d}{r_o}\right)^2 + \frac{5.147}{\mathrm{Re}_d}\frac{r_o}{d}\right]^2 \mathrm{Re}_d^{1/2}} - \frac{1}{2}\left(\frac{r_o}{d}\right)^2 \tag{B.19}$$

At $r = r_1$, the border of region 3, we have $\delta_t = h$. To locate r_1, we use equations (B.16) and (B.15) to find

$$\frac{2}{100}\,\mathrm{Re}_d\mathrm{Pr}\left(\frac{h}{d}\right) = \frac{1}{2}\left(\frac{r}{d}\right)^2 + C_3 \tag{B.20}$$

Then, using equation (B.14) and rearranging, we get

$$\left(\frac{r_1}{d}\right)^3 + p\left(\frac{r_1}{d}\right) + s = 0 \tag{B.21}$$

where we define

$$p = \frac{-2C_3}{(0.2058\,\mathrm{Pr} - 1)} \qquad s = \frac{0.00686\,\mathrm{Re}_d\mathrm{Pr}}{(0.2058\,\mathrm{Pr} - 1)} \tag{B.22}$$

Since C_3 is usually less than zero, equation (B.21) has real, positive roots when

$$s < 0 \tag{B.23}$$

This condition is satisfied only for*

$$\mathrm{Pr} < 4.859 \tag{B.24}$$

*Our previous paper gave this value as 4.86. If the higher-order terms in the integral analysis are retained, the value becomes 5.23, which is 7% higher than the previous one.

This is a very interesting result. It means that for Pr > 4.859 the thermal boundary layer can never reach the surface of the liquid sheet before subcooled boiling occurs: the increase of h owing to viscous retardation is more rapid than the growth of the thermal boundary layer.In this case, region 4 cannot exist. The situation is shown schematically in Figure 3.

For Pr < 4.859, equation (B.21) yields

$$\frac{r_1}{d} = \left\{-\frac{s}{2} + \left[\left(\frac{s}{2}\right)^2 + \left(\frac{p}{3}\right)^3\right]^{1/2}\right\}^{1/3} + \left\{-\frac{s}{2} + \left[\left(\frac{s}{2}\right)^2 - \left(\frac{p}{3}\right)^3\right]^{1/2}\right\}^{1/3} \tag{B.25}$$

With this and equation (B.14), we can calculate the liquid sheet thickness, h_{r1}, at $r = r_1$. The wall temperature can be determined from the expression

$$T_w = T_f + \frac{q\,r}{k\,\mathrm{Nu}_r} \tag{B.26}$$

Since boiling might occur for any wall temperature which exceeds the saturation temperature, depending on heater surface finish and other factors, we exclude any case for which $T_w > T_{sat}$ from subsequent considerations.

B.1.3 Region 4

For Pr < 4.859, after the thermal boundary layer reaches the surface, the surface temperature increases with radius. If we neglect the heat transfer from the liquid surface, the energy equation may be written

$$\frac{d}{dr}\int_0^h ruT\,dy = \frac{q}{\rho c_p}\,r \tag{B.27}$$

We assume the temperature profile to be

$$T - T_w = (T_{f4} - T_w)\left[\frac{3}{2}\frac{y}{h} - \frac{1}{2}\left(\frac{y}{h}\right)^3\right] \tag{B.28}$$

where the surface temperature in region 4, T_{f4}, is a function of r. Substituting equations (B.4), (B.12), and this temperature distribution into equation (B.27), we obtain

$$A\left(\frac{5}{8}T_{f4} + \frac{13\,qh}{140\,k}\right) = \frac{q}{\rho c_p}\frac{r^2}{2} + C_4 \tag{B.29}$$

The constant may be found by evaluating this expression at $r = r_1$, where $T_{f4} = T_f$ and $h = h_{r1}$:

$$C_4 = A\left(\frac{5}{8}T_f + \frac{13\,q\,h_{r1}}{140\,k}\right) - \frac{q}{\rho c_p}\frac{r_1^2}{2} \tag{B.30}$$

Since $T_{f4} = T_w - 2qh/3k$,

$$\mathrm{Nu}_r = \frac{0.25\,(r/d)}{\frac{1}{\mathrm{PrRe}_d}\left(1 - \frac{r_1^2}{r^2}\right)\left(\frac{r}{d}\right)^2 + 0.130\frac{h}{d} + 0.0371\frac{h_{r1}}{d}} \tag{B.31}$$

and

$$T_w = T_f + \frac{q}{k}\left[0.518\,h + \frac{4\alpha(r^2 - r_1^2)}{u_f\,d^2} + 0.149\,h_{r1}\right] \tag{B.32}$$

From equation (B.32) we can find r_2, the point at which T_w exceeds the saturation temperature, and beyond which subcooled boiling might occur. We exclude consideration of the region $r > r_2$ from this paper.

B.1.4 Calculations

To use these results in calculating Nu_r and $T_w(r)$, a numerical iteration is most expedient. In particular, the viscosity varies strongly with temperature for

most liquids, and properties must be evaluated at the local average temperature across the film. The some of the different expressions for each region are also quite complex. The flowchart in Figure B.3 shows the general procedure for using the analytical results of this section to determine the distribution of Nusselt number and wall temperature. This procedure was used in obtaining the calculated results presented in Section 4 below.

B.2 Integral Solutions for the Heat Transfer: $Pr < 1$

The region map changes for small Prandtl number (*see* Figure 2.2b):

Region 1l. *The stagnation zone.*

Region 2l. $\delta_t < h$ *region*: Neither the thermal nor viscous boundary layer reach the free surface; surface temperature and velocity, T_{sf} and u_{max} are the inlet temperature and velocity, T_f and u_f.

Region 3l. $\delta_t = h$ *and* $\delta < h$ *region*: The thermal boundary layer has reached the free surface. The surface temperature increases with radius, but the velocity outside the viscous boundary layer is still the jet velocity, u_f.

Region 4l. $\delta = h, \delta_t = h$, *and* $T_w < T_{sat}$ *region*: In this region, the viscous boundary layer has reached the surface of the liquid sheet, and the velocity of the liquid surface decreases with radius.

The integral energy equation may be used to estimate the Nusselt number:

$$\frac{d}{dr}\int_0^{\delta_t} ru(T - T_f)\,dy = \frac{q_w}{\rho c_p}\,r \tag{B.33}$$

In region 2l, we approximate the velocity and temperature profiles as:

$$T - T_w = (T_f - T_w)\left[\frac{3}{2}\frac{y}{\delta_t} - \frac{1}{2}\left(\frac{y}{\delta_t}\right)^3\right] \tag{B.34}$$

$$u = u_{max}\left[\frac{3}{2}\frac{y}{\delta} - \frac{1}{2}\left(\frac{y}{\delta}\right)^3\right] \quad y < \delta$$
$$= u_f \quad y \geq \delta \tag{B.35}$$

These profiles satisfy no slip at the wall, have no shear or heat flux at the free surface (*i.e.* negligible evaporation), and match the local wall temperature. Integration of equation (B.33) with these profiles yields:

$$\mathrm{Nu}_d = \left[\frac{\frac{9}{16}\mathrm{Re}_d\mathrm{Pr}\left(\frac{r}{d}\right)\left(1 - \phi + \frac{1}{10}\phi^2 - \frac{1}{140}\phi^4\right)}{\frac{1}{2}\left(\frac{r}{d}\right)^2 + C}\right]^{1/2} \tag{B.36}$$

where

$$\phi = \frac{\delta}{\delta_t} = 1.786\mathrm{Nu}_d\left(\frac{r}{d\mathrm{Re}_d}\right)^{1/2} \tag{B.37}$$

and C is a constant used to match to the stagnation zone. (*see* Chapter 5) If we assume that at the match point r_m, $\mathrm{Nu}_d = \mathrm{Nu}_{d,m}$ and $\phi = \phi_m$, then

$$C = \frac{9}{16}\frac{\mathrm{Re}_d\mathrm{Pr}}{\mathrm{Nu}_{d,m}^2}\left(\frac{r_m}{d}\right)\left(1 - \phi_m + \frac{1}{10}\phi_m^2 - \frac{1}{140}\phi^4\right) - \frac{1}{2}\left(\frac{r_m}{d}\right)^2 \tag{B.38}$$

If δ/δ_t is very small and C is also negligible (as shown in §4.4), equation (B.38) can be further simplified to:

$$\mathrm{Nu}_d = 1.06\mathrm{Re}_d^{1/2}\mathrm{Pr}^{1/2}\left(\frac{d}{r}\right)^{1/2} \tag{B.39}$$

Region 2l ends where the thermal boundary layer reaches the surface of the liquid sheet at $r = r_{T0}$:

$$\frac{r_{T0}}{d} = \frac{0.1984\mathrm{Re}_d^{1/3}\mathrm{Pr}^{1/3}}{\left(1 - 0.7107\mathrm{Pr}^{1/2}\right)^{2/3}} \tag{B.40}$$

In region 3l, $\delta_t = h$ and the temperature of the liquid surface, T_{sf}, is an increasing function of r. The temperature profile in this region is:

$$T - T_w = (T_{sf} - T_w)\left[\frac{3}{2}\frac{y}{h} - \frac{1}{2}\left(\frac{y}{h}\right)^3\right] \tag{B.41}$$

At r_{T0}, the beginning of region 3l, $\mathrm{Nu}_d = \mathrm{Nu}_{d,T0}$, $h = h_{T0}$, and $\delta = \delta_{T0}$, where h and δ can be computed from Sharan's equations (1984):

$$\frac{h}{d} = 0.125\left(\frac{d}{r}\right) + 1.005\left(\frac{r}{\mathrm{Re}_d d}\right)^{1/2} \tag{B.42}$$

$$\frac{\delta}{d} = 2.679\left(\frac{r}{\mathrm{Re}_d d}\right)^{1/2} \tag{B.43}$$

Integration of equation (B.33) from $r = r_{T0}$ with equations (B.35) and (B.41) gives

$$\left(\frac{\mathrm{Nu}_d}{2(1-\frac{3}{8}\Delta)}\right)^{-1} = \frac{r}{\mathrm{Re}_d \mathrm{Pr} h}\left(1 - \left(\frac{r_{T0}}{r}\right)^2\right) + \frac{4}{3}\frac{h}{d}\left(\frac{5}{8} - \frac{3}{20}\Delta^2 + \frac{3}{280}\Delta^4\right)$$
$$- \frac{4}{3}\frac{h_{T0}}{d}\left(\frac{5}{8} - \frac{3}{20}\Delta_{T0}^2 + \frac{3}{280}\Delta_{T0}^4\right) + 2\frac{r_{T0}h_{T0}}{rh}\left(1 - \frac{3}{8}\Delta_{T0}\right)\frac{1}{\mathrm{Nu}_{T0}} \tag{B.44}$$

where $\Delta = \delta/h$. If the terms in Δ are neglected, this simplifies to

$$\mathrm{Nu}_d = \frac{2}{\frac{r}{\mathrm{Re}_d \mathrm{Pr} h}\left(1 - \left(\frac{r_{T0}}{r}\right)^2\right) + 0.833\frac{h}{d} - 0.833\frac{h_{T0}}{d} + 2\frac{r_{T0}h_{T0}}{rh}\frac{1}{\mathrm{Nu}_{T0}}} \tag{B.45}$$

Region 4l begins at $r_0 = 0.1773 d\,\mathrm{Re}_d^{1/3}$, where the viscous boundary layer reaches the surface; here, the surface velocity decreases with radius. Sharan's integral analysis (1984) shows that

$$u_{max} = \frac{1}{5}\frac{u_f d^2}{hr} \tag{B.46}$$

where

$$h = 0.1713\left(\frac{d^2}{r}\right) + \frac{5.147}{\mathrm{Re}_d}\left(\frac{r^2}{d}\right) \tag{B.47}$$

(Equation (B.47) is in good agreement with Watson's expression for h, which is based on velocity profile of the similarity solution.) The velocity profile is equation (B.35) with $\delta = h$ and u_{max} from equation (B.46), while the temperature profile is still equation (B.41). At $r = r_0$, $h = h_0$ and $\mathrm{Nu}_d = \mathrm{Nu}_{d,0}$. Integration of equation (B.33) from $r = r_0$ yields

$$\mathrm{Nu}_d = \frac{0.25}{\frac{1}{\mathrm{Re}_d\mathrm{Pr}}\left(\frac{r^2}{d^2} - \frac{r_0^2}{d^2}\right) + 0.130\left(\frac{h_0}{d} - \frac{h}{d}\right) + 0.25\frac{1}{\mathrm{Nu}_{d,0}}} \tag{B.48}$$

.

B.3 Results and Comparisons

In this section, we consider the predictions by integral method in detail. In our analysis, the evaporation from the liquid surface was neglected. This assumption should be carefully checked in any practical situation, since evaporative heat loss can become a significant fraction of the wall heat flux. Evaporation will tend to cool the liquid at the surface and reduce the rate of wall temperature increase (lowering Nu_r), even if only a very small amount of the liquid film is vaporized. The rate of evaporation increases rapidly with the surface temperature of the liquid; in dry air it will rise by a factor of 29 as the surface temperature increases from 5°C to 65°C. Some estimates are in order for the present data.

The evaporative heat flux from the liquid surface can be calculated as

$$q_e = h_{fg}\, g_m (m_w - m_\infty) \tag{B.49}$$

where h_{fg} is the latent heat of vaporization, m_w is the mass fraction of water vapor at the liquid surface, m_∞ is the mass fraction of water in the environment, and the mass transfer coefficient, g_m, is calculated from the Lewis analogy

$$g_m = \frac{\hat{h}}{c_p}\left(\frac{\mathrm{Pr}}{\mathrm{Sc}}\right)^{2/3} \tag{B.50}$$

with $\hat{h}$ the estimated local heat transfer coefficient from the moving liquid to the air. For 15°C water, a wall heat flux of 12.4×10^4 W/m^2, and $u_f = 24$ m/s, the ratio of evaporative heat flux, q_e, to wall heat flux, q, is shown in Figure B.4.

The heat flux by evaporation decreases rapidly with r/d. For $r/d > 20$, it is less than 5% of the wall heat flux, and it is never more than about 12% . The rapid decrease in q_e is due in part to the rapid slowing of the liquid surface velocity in region 3. While the evaporation is greatest in region 2, it has no effect on wall temperature until the surface and wall thermal boundary layers meet further downstream. The overall effect of evaporative cooling probably remains negligible in the present case because the overall reduction in liquid bulk temperature is only a few percent of the increase produced by wall heating. However, the same estimation procedure shows, for example, that for a surface temperature of 45°C, evaporation would become comparable to a wall flux of 12.4×10^4 W/m^2 and cannot be neglected.

Figure B.5 shows a comparison of our prediction to the *plane* jet data of McMurray *et al.* (1966). The most significant difference is that, for the axisymmetric jet, Nu_r reaches a maximum and then decreases with radius, but that for the plane jet it does not. This is because the liquid layer thickness produced by the plane jet of McMurray *et al.* was so large that the viscous boundary layer never reached the liquid surface. Thus, the differences are not surprising: McMurray's experiment remains in region 2 throughout. Before the boundary layer reaches the surface, the plane and axisymmetric jets show the same variation with Reynolds number, although for the axisymmetric jet the coefficient is 0.632 while for the plane jet it is 0.47, 25% lower.

Figure B.6 compares the *average* Nusselt number for our uniform wall heat flux predictions to that for the uniform wall temperature axisymmetric jet experiments of Metzger *et al.* (1974). The average Nusselt number for a uniform wall heat flux is generally larger than that for a uniform wall temperature. Average Nusselt numbers for the uniform wall flux plane jet data of McMurray *et al.* are also shown. Although the local Nusselt number for the plane jet is smaller than for the axisymmetric jet in region 2 and part of region 3, the average Nusselt number for the plane jet is generally larger than that for the axisymmetric jet. In region 2, the average Nusselt number for the plane jet is twice as large as the local Nusselt number, but that for the axisymmetric jet is 4/3 the local one. This switch in size relates to the different areas involved in planar and axisymmetric averaging.

CONCLUSIONS

The heat transfer phenomena beneath an impinging circular jet can be divided into different regions by taking account of the development of the viscous and thermal boundary layers and the possible occurrence of nucleate boiling or a hydraulic jump. These regions may appear in different combinations, depending the jet Reynolds number, temperature levels, wall heat flux, and liquid physical properties. The radial variation of Nusselt number, Nu_r, is interpreted in terms of the development of the thermal boundary layer, and an integral analysis is presented for each of the convective regions.

The analysis shows that if $Pr > 4.859$, the thermal boundary layer never reaches the surface of the liquid film because the growth of the thermal boundary layer is slower than the thickening of the liquid film caused by viscous retardation.

The prediction shows that Nu_r reaches a maximum at some radius away from the point of impact and then decreases as the radius increases further. Both the magnitude and radial position of the maximum Nusselt number increase with Reynolds number. The wall temperature rises steadily away from the stagnation point.

Evaporative heat loss should be carefully examined for any practical application. In situations with significant evaporation, the wall temperatures at large radius will be lower than the present predictions, although the evaporation rate will decline with increasing radius as a result of decreasing liquid surface velocity.

For the present experiments, the evaporation effect is small.

The average Nusselt number for a constant heat flux is generally larger than for a constant wall temperature. Although the local Nusselt number for the plane jet is smaller than that for an axisymmetric jet in region 2 and part of region 3, the average Nusselt number for a plane jet is generally larger than that for an axisymmetric jet.

REFERENCES

Carper, H.J. and Deffenbaugh, D.M., 1978, "Heat transfer from a rotating disk with liquid jet impingement," *Proc. Sixth Intl. Heat Transfer Conf.*, Vol.4, Toronto, pp.113-118.

Carper, H.J., Saaveda, J.J., and Suwanprateep, T., 1986, "Liquid jet impingement cooling of a rotating disk," *J. Heat Transfer*, Vol.108, pp.541.

Chaudhury, Z.H., 1964, "Heat transfer in a radial jet," *J. Fluid Mech.*, Vol.20, pp.501-511.

Errico, M., 1986, "A study of the interaction of liquid jets with solid surfaces," Doctoral dissertation, University of California at San Diego, Chapter 3.

McMurray, D.C., Myers, P.S., and Uyehara, O.A., 1966, "Influence of impinging jet variables on local heat transfer coefficients along a flat surface with constant heat flux," *Proc. Third Intl. Heat Transfer Conf.*, Vol.2, Chicago, pp.292-299.

Metzger, D.E., Cammings, K.N., and Ruby, W.A., 1974, "Effects of Prandtl number on heat transfer characteristics of impinging liquid jets," *Proc. Fifth Intl. Heat Transfer Conf.*, Vol.2, Tokyo, pp.20-24.

Sharan, A., 1984,"Jet-disc boiling: burnout predictions and application to solar receivers," Master's thesis, University of Houston.

Watson, E.J., 1964, "The radial spread of a liquid over a horizontal plane," *J. Fluid Mech.*, Vol.20, pp.481-499.

White, F.M., *Viscous Fluid Flow,* McGraw-Hill Book Company, New York, 1974.

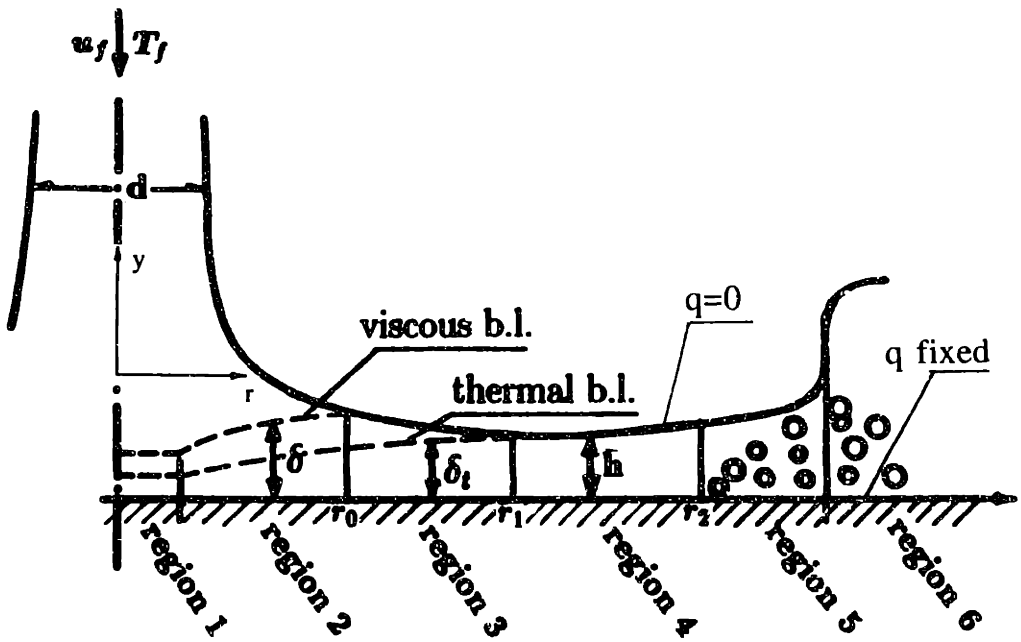

Figure B.1: Region map for the downward-flowing jet.

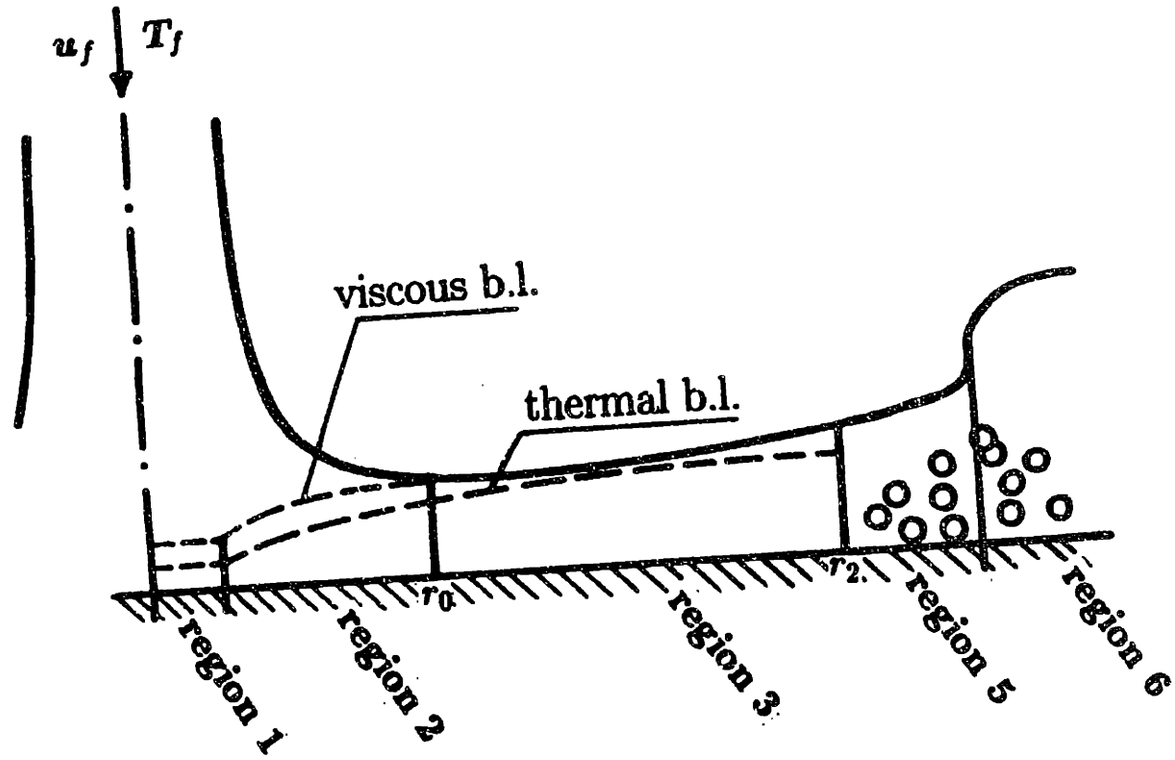

Figure B.2: Region map for Pr > 4.859.

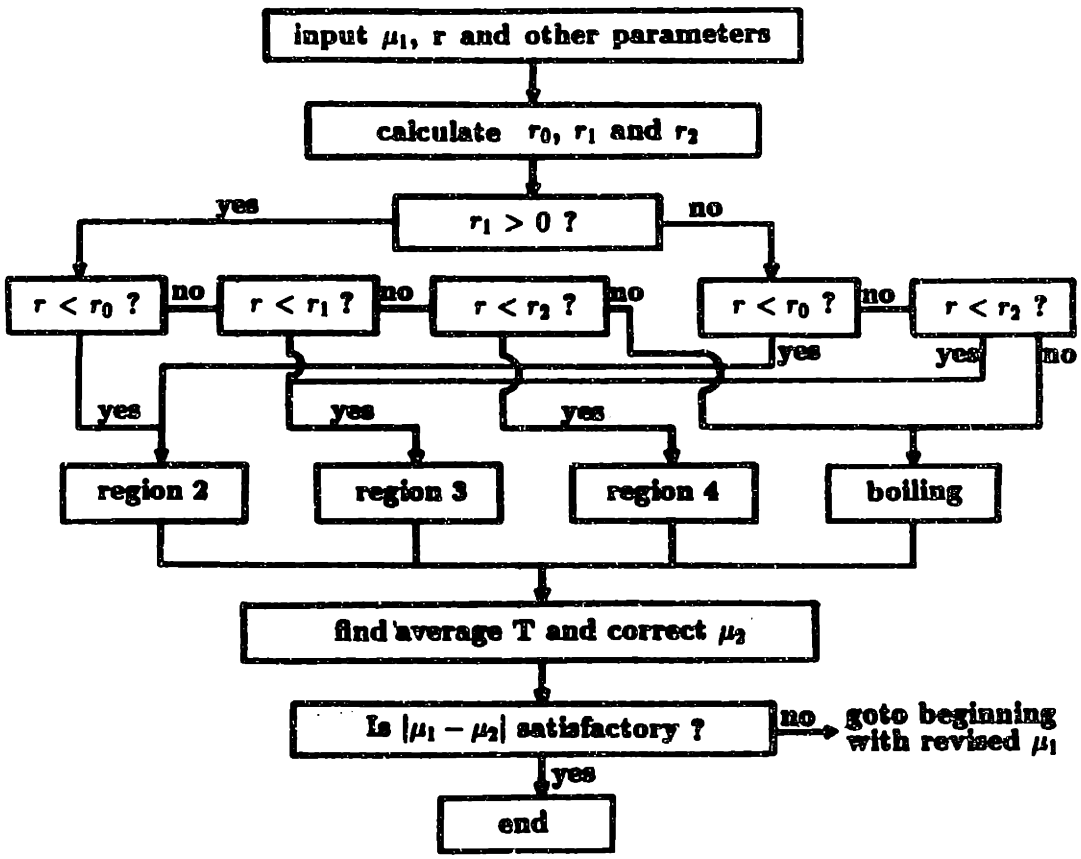

Figure B.3: Calculation procedure for integral predictions.

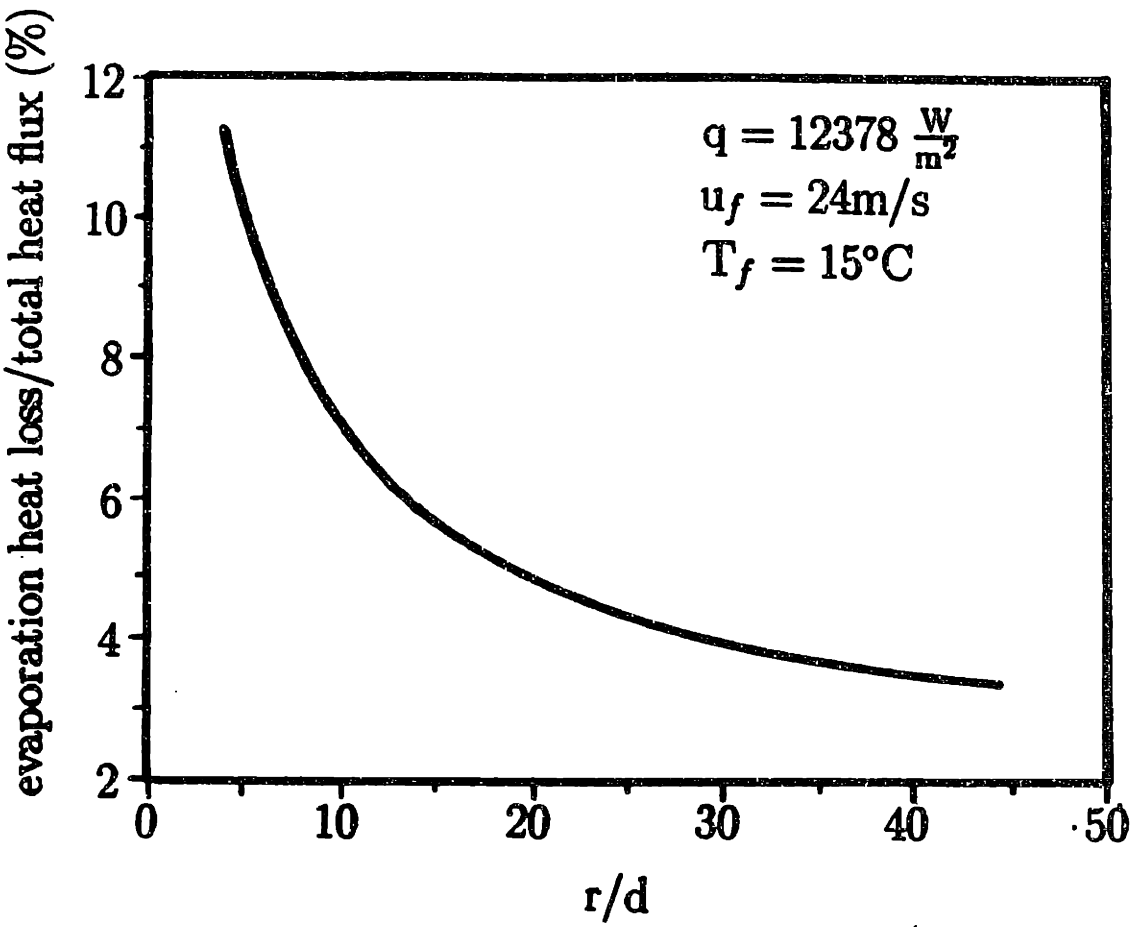

Figure B.4: Estimated evaporative heat loss at $Re_d = 6.24 \times 10^4$.

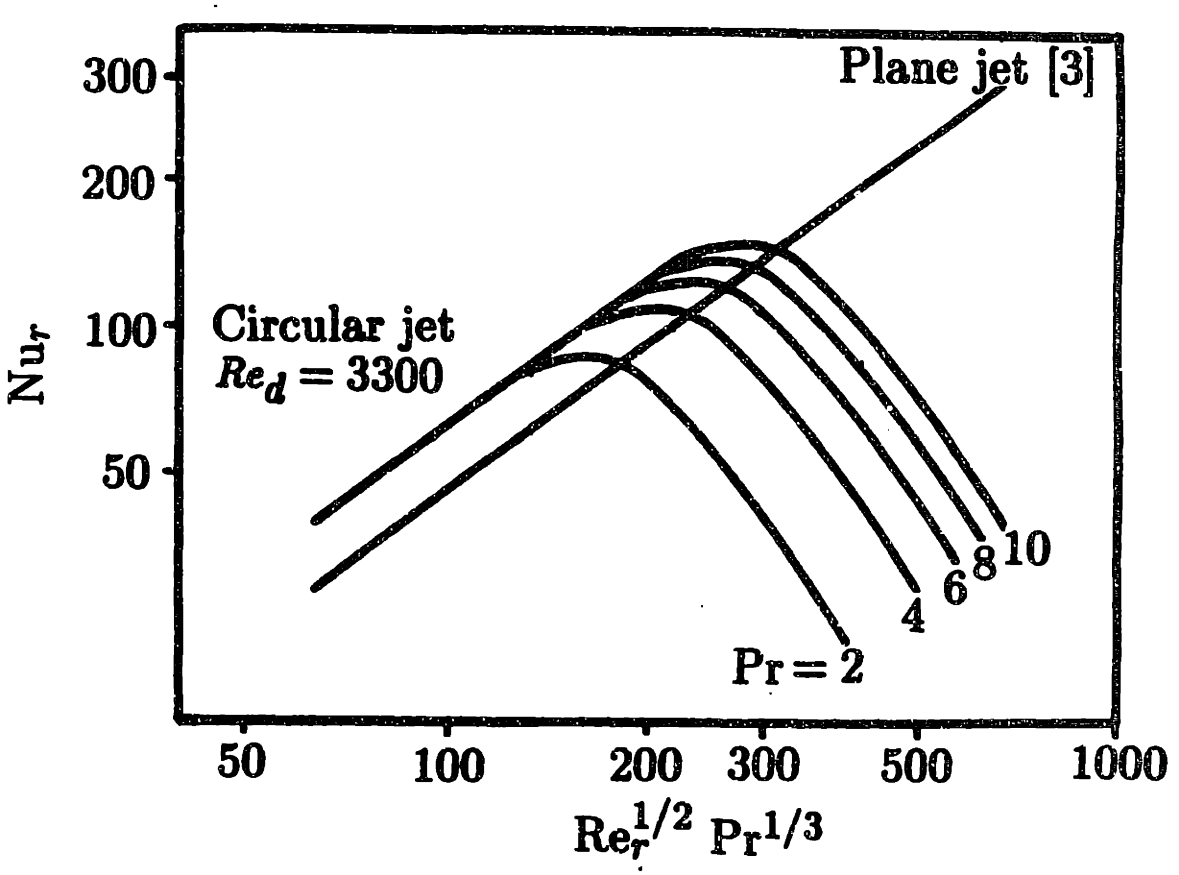

Figure B.5: Comparison of predicted local Nusselt number for circular jets to local Nusselt number correlation for plane jets.

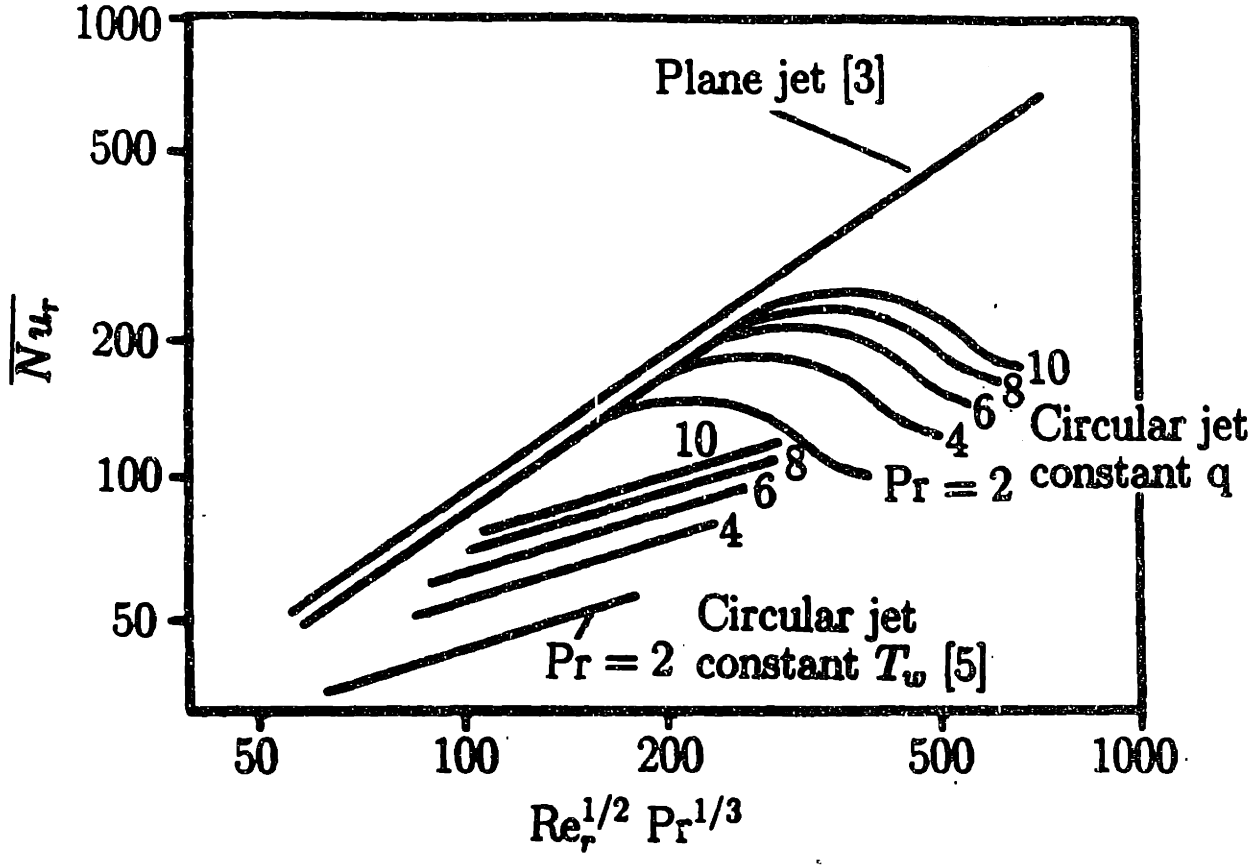

Figure B.6: Comparison of predicted average Nusselt number for uniform flux to correlation for uniform wall temperature in circular jet impingement and to correlation for uniform flux plane jet impingement.